

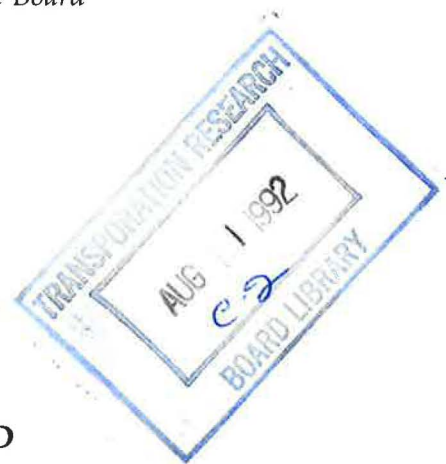
TRANSPORTATION RESEARCH RECORD

No. 1336

Soils, Geology, and Foundations

Foundation Engineering: Seismic Design, Drilled Shafts, and Other Issues

A peer-reviewed publication of the Transportation Research Board



TRANSPORTATION RESEARCH BOARD
NATIONAL RESEARCH COUNCIL
WASHINGTON, D.C. 1992

Transportation Research Record 1336
Price: \$22.00

Subscriber Category
IIIA soils, geology, and foundations

TRB Publications Staff
Director of Publications: Nancy A. Ackerman
Senior Editor: Naomi C. Kassabian
Associate Editor: Alison G. Tobias
Assistant Editors: Luanne Crayton, Norman Solomon
Production Coordinator: Karen W. McClain
Office Manager: Phyllis D. Barber
Production Assistant: Betty L. Hawkins

Printed in the United States of America

Library of Congress Cataloging-in-Publication Data
National Research Council. Transportation Research Board.

Foundation engineering: seismic design, drilled shafts, and other issues.

p. cm.—(Transportation research record ISSN 0361-1981;
no. 1336)

Papers from the Transportation Research Board's 71st Annual Meeting along with related papers.

ISBN 0-309-05174-6

1. Roads—Foundations. 2. Bridges—Foundations and piers.

3. Soil mechanics. 4. Earthquake resistant design. I. National Research Council (U.S.). Transportation Research Board.

II. Series.

TE7.H5 no. 1336

[TE210]

388 s—dc20

[625.7'33]

92-19391

CIP

Sponsorship of Transportation Research Record 1336

GROUP 2—DESIGN AND CONSTRUCTION OF TRANSPORTATION FACILITIES

Chairman: Charles T. Edson, New Jersey Department of Transportation

Soil Mechanics Section

Chairman: Michael G. Katona, Tyndall AFB

Committee on Transportation Earthworks

Chairman: Richard P. Long, University of Connecticut
Loren R. Anderson, Arnold Aronowitz, Jerome A. Dimaggio, Said M. Easa, Eugene C. Geiger, Raymond L. Gemme, John B. Gilmore, Robert D. Holtz, Ilan Juran, Philip C. Lambe, Victor A. Modeer, Jr., K. Jeff Nelson, T. Skep Nordmark, Subal K. Sarkar, Cliff J. Schexnayder, Walter C. Waidelich

Committee on Foundations of Bridges and Other Structures

Chairman: Richard S. Cheney, Federal Highway Administration
Secretary: Richard P. Long, University of Connecticut
Gregg Batchelder Adams, Roy H. Borden, Jean-Louis Briaud, Joseph A. Caliendo, Ronald G. Chassie, Murty S. Devata, Albert F. Dimillio, Victor Elias, Richard L. Engel, George G. Goble, Robert C. Houghton, Alan P. Kilian, John F. Ledbetter, Jr., Larry Lockett, James H. Long, Randolph W. Losch, William J. Lytle, Thom L. Neff, Peter J. Nicholson, Gary M. Norris, Michael Wayne O'Neill, John L. Walkinshaw, Gdalyah Wiseman, James L. Withiam

Geology and Properties of Earth Materials Section

Chairman: Robert D. Holtz, University of Washington

Committee on Engineering Geology

Chairman: Jeffrey R. Keaton, Sergeant Hauskins & Beckwith
Robert K. Barrett, William D. Bingham, Scott F. Burns, Jerome V. De Graff, Carol J. Hammond, Steve M. Lowell, Stanley M. Miller, Harry L. Moore, Stephen F. Obermeier, A. Keith Turner, Duncan C. Wyllie

G. P. Jayaprakash, Transportation Research Board staff

Sponsorship is indicated by a footnote at the end of each paper. The organizational units, officers, and members are as of December 31, 1991.

Transportation Research Record 1336

Contents

Foreword	v
<hr/>	
Numerical Simulation of Reinforced Soil Structures During Blast Loads	1
<i>M. Yogendrakumar and R. J. Bathurst</i>	
<hr/>	
Dynamic Centrifuge Modeling of Sound Walls Supported on Concrete Cantilever and Mechanically Stabilized Earth Retaining Structures	9
<i>David Soon, John A. Casey, Bruce L. Kutter, and Karl M. Romstad</i>	
<hr/>	
Response of Tension Piles to Simulated Seismic Motion in Saturated Fine Sand	17
<i>Michael W. O'Neill, Cumaraswamy Vipulanandan, and Mauricio Ochoa</i>	
<hr/>	
Dynamic Centrifuge Modeling of Geotechnical Structures	24
<i>Bruce L. Kutter</i>	
<hr/>	
Overview of Evaluation of Pile Foundation Stiffnesses for Seismic Analysis of Highway Bridges	31
<i>Gary M. Norris</i>	
<hr/>	
Seismic Highway Bridge Design Using Spectra Specific to Washington State	43
<i>Carlton Ho and George Tsiatas</i>	
<hr/>	
Effects of Stratigraphic and Construction Details on the Load Transfer Behavior of Drilled Shafts	50
<i>Michael O'Neill, Lymon Reese, Ralph Barnes, Shin-Tower Wang, Mark Morvant, and Mauricio Ochoa</i>	
<hr/>	

Comparison of Measured and Computed Drilled Shaft Capacities Based on Utah Load Tests	57
<i>Richard Price, Kyle M. Rollins, and Edward Keane</i>	
<hr/>	
Dynamic Testing of Drilled Shafts	65
<i>Mohamad Hussein, Frank Townsend, Frank Rausche, and Garland Likins</i>	
<hr/>	
Lateral Subgrade Modulus of Sands for Deep Foundations	70
<i>Daniel O. Wong</i>	
<hr/>	
Modeling Soil Reaction to Laterally Loaded Piles	81
<i>Takaaki Kagawa</i>	
<hr/>	
Bearing Capacity Determination Method for Strip Surface Footings Underlain by Voids	90
<i>C. W. Hsieh and M. C. Wang</i>	
<hr/>	
Vertical Uplift Load-Displacement Relationship of Horizontal Anchors in Sand	96
<i>Braja M. Das and Vijay K. Puri</i>	
<hr/>	

Foreword

The increased awareness of the need for seismic considerations in the design of foundations of transportation structures and the growing use of drilled shafts for foundations of highway structures prompted three sessions at the Transportation Research Board's 71st Annual Meeting. The presentations from those sessions and other related papers are included in this Record. The 13 papers are arranged in three groups and are of interest to foundation engineers and researchers alike.

The first group, consisting of six papers, is related to seismic design of foundations. These papers present information on the use of a finite element computer program to study the dynamic response to blast loading of a reinforced soil wall and a soil slope with and without reinforcement; the basic principles of centrifuge modeling, a comparative study of mechanically stabilized earth walls and conventional reinforced concrete cantilever retaining walls, and how centrifuge studies provide a better understanding of the deformation and failure mechanisms of transportation structures; a laboratory model study of tension piles subjected to simulated seismic loading through the soil; assessment of the nonlinear variation in foundation stiffness; and development of seismic response spectra for soils for use in seismic highway bridge design.

The second group, consisting of three papers, is related to drilled shafts. These papers contain information on the effects of minor inclusions in soil layers, polymer drilling slurry, and artificial roughening of the borehole on load transfer in drilled shafts; actual load tests conducted to determine failure loads from load-settlement data; and dynamic testing of drilled shafts or driven piles.

The third group, consisting of four papers, is on issues related to other types of foundations. These papers include information on the concept of the equivalent subgrade modulus for sand in which nonlinear characteristics are implicitly taken into account; a new procedure for estimating the lateral soil springs used in the beam-on-Winkler foundation model; a method developed for analysis and design of strip surface footing underlain by a continuous circular void; and a small-scale laboratory study on the uplift capacity of horizontal rectangular anchors embedded at shallow depth in medium and dense sand.

Numerical Simulation of Reinforced Soil Structures During Blast Loads

M. YOGENDRAKUMAR AND R. J. BATHURST

A comprehensive approach to the dynamic response analysis of reinforced soil structures subjected to blast loading is presented. The method is based on an estimate of the pressure-time response at the boundaries of target structures using a two-dimensional versatile gas dynamic code (SPLIT2D). The soil-reinforcement response is simulated using a direct nonlinear approach that is implemented in the finite element computer program RESBLAST. Examples of this approach to investigate the response of a reinforced soil wall and a soil slope with and without reinforcement are presented. The results of rapid cyclic tensile loading tests are used to obtain mechanical properties used in the nonlinear reinforcement model implemented in the finite element code.

Advanced polymeric material such as geogrids and geotextiles are becoming a common reinforcing material for the construction of reinforced soil systems used in industrial and military applications (1,2). Soil retaining walls and steepened slopes are often used in military and civilian applications to protect personnel, property, and adjacent structures from accidental detonation of stored explosives, munitions, and ammunition plants and to provide blast containment of volatile liquids. As in conventional reinforced soil structures, the advantages of polymeric-reinforced soil structures lie in their cost-effectiveness, rapid construction, minimization of ground area, and high tolerance of differential settlements. Less well understood is the dynamic response of these structures to short duration excitations resulting from above-ground explosions.

Related work on the seismic response of similar structures under earthquake excitation provides a starting point for the study of resistance to air blast. For earthquake design, the stability of steepened slopes and walls is usually estimated using analytical methods that are typically extended versions of conventional limit-equilibrium methods (3,4). These methods are primarily stress based and do not consider deformations explicitly.

More recently, the finite element method of analysis has been used to study the response of reinforced soil systems to dynamic loads (5-9). These papers have focused on the response due to earthquake excitations. The choice of excitation forces in earthquake simulations is relatively straightforward. The analogous task for air blast loading requires separate analyses that are complex and at least as computational intensive as the simulation of structure response alone.

To carry out numerical simulation of blast loadings on a reinforced soil system, it is necessary to establish the pressure-time history at the boundaries of the target structure. In this

study the pressure-time history of air blast loadings was calculated using a computer package called SPLIT2D (10). The stress-deformation-time response of an example reinforced soil wall and steepened slope due to the boundary excitations predicted in the air blast simulation was carried out using the computer program RESBLAST (RESPONSE to BLAST loading) (11). RESBLAST implements a direct nonlinear method in which the nonlinear dynamic behavior of both the soil and the polymeric reinforcement are modeled. The behavior of soil in shear and the load-deformation behavior of the polymeric reinforcement are both assumed to be nonlinear, hysteretic, and to exhibit Masing behavior during unloading and reloading. A unique feature of this program is that permanent deformations are computed directly.

The retaining wall example was studied to examine the effect of magnitude of blast loading on structure response at different locations within the reinforced soil zone. The slope example was examined with and without reinforcement to investigate the influence of the polymeric reinforcement on the response of otherwise identical structures. The model parameters for the polymeric reinforcement were obtained from results of in-isolation, high-frequency, cyclic-loading tests.

METHOD OF ANALYSIS

In the current study, the procedure for computing the blast response of example target structures was carried out in two stages: first, the blast loading on the particular structure was determined using the computer program package SPLIT2D; next, the response of the structure to the boundary pressure-time loading was computed using the computer program RESBLAST.

Program SPLIT2D

SPLIT2D is a two-dimensional versatile gas dynamic code capable of solving a variety of problems involving blast, reactive flows, and interaction of shocks with obstructions. The governing equations are derived from the more general Navier-Stokes relations by eliminating the turbulence and diffusive transport terms. The resulting set of coupled partial differential relationships comprise continuity, momentum conservation, and energy conservation equations. The ideal gas equation of state relating the internal energy to the pressure and density is also used. The numerical algorithm uses an explicit time stepping algorithm. The spatial derivatives are discretized on a finite difference grid using a second-order

M. Yogendrakumar, Golder Associates Ltd., 224 West 8th Avenue, Vancouver, British Columbia, Canada V5Y 1N5. R. J. Bathurst, Department of Civil Engineering, Royal Military College of Canada, Kingston, Ontario, Canada K7K 5L0.

scheme in conjunction with the flux-corrected transport algorithm. Complicated geometries of the protective structures are set up by placing obstructions within the computational blast domain using rectangular, elliptical, and triangular shapes that can be superimposed. Similarly, regions with different initial conditions are created using these three shapes.

In this study the air blast was modeled as a planar wave front traveling horizontally until impact with the structure. The postimpact blast response in the surrounding space was determined by the magnitude and duration of the blast and the geometry of the obstruction.

Program RESBLAST

RESBLAST uses a direct nonlinear method that is implemented in a code for total stress analysis of reinforced soil structures subject to blast loading. The treatment of soil behavior under dynamic loading is based on algorithms originally implemented in program TARA-3 (12) developed by researchers at the University of British Columbia. In both programs an incremental approach has been adopted to model nonlinear behavior of soil using tangent shear and tangent bulk moduli, G , and B , respectively. The incremental displacements during the blast loading are obtained by solving the incremental dynamic equilibrium equations given in Equation 1 by a direct numerical integration method.

$$[M]\{\Delta\ddot{x}\} + [C]\{\Delta\dot{x}\} + [K]\{\Delta x\} = \{\Delta P\} \quad (1)$$

Here $[M]$ is the mass matrix; $[C]$ is the damping matrix; $[K]$ is the stiffness matrix; $\{\Delta\ddot{x}\}$, $\{\Delta\dot{x}\}$, and $\{\Delta x\}$ are incremental acceleration, velocity, and displacement vectors of the nodes relative to the base; and $\{\Delta P\}$ is the increment in blast load.

The stiffness matrix $[K]$ is a function of the current tangent moduli during loading, unloading, and reloading. The use of shear and bulk moduli allows the elasticity matrix $[D]$ to be expressed as

$$[D] = B_i[Q_1] + G_i[Q_2] \quad (2)$$

where $[Q_1]$ and $[Q_2]$ are constant matrices for the plane strain conditions considered in the analysis. This formulation reduces the computation time for updating $[D]$ whenever G , and B , change in magnitude because of straining.

Soil Model

The behavior of soil in shear is assumed to be nonlinear and hysteretic and to exhibit Masing behavior during unloading and reloading. Masing behavior is a term used in mechanics to describe the pattern of hysteretic load/unload-strain cycles having the generic shape shown in Figure 1a. The relationship between shear stress τ and shear strain γ for the initial loading phase under loading conditions is assumed to be hyperbolic and given by

$$\tau = f(\gamma) = \frac{G_{\max} \gamma}{[1 + (G_{\max}/\tau_{\max})|\gamma|]} \quad (3)$$

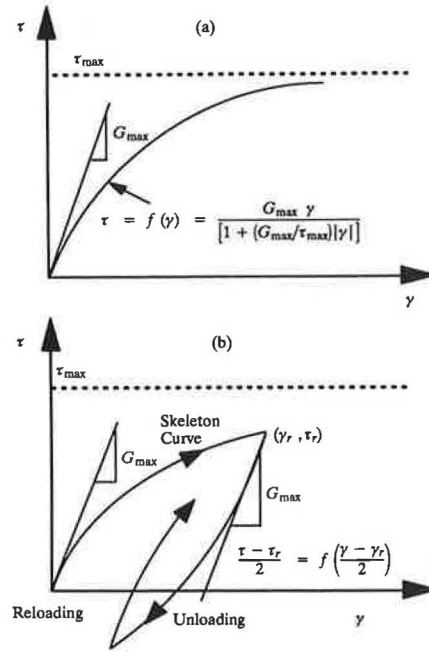


FIGURE 1 Nonlinear hysteretic loading paths for granular soil.

where G_{\max} is the maximum shear modulus and τ_{\max} is the maximum shear strength. The initial loading curve is shown in Figure 1a. The equation for the unloading curve from a point (γ_r, τ_r) at which the loading reverses direction is given by

$$\frac{\tau - \tau_r}{2} = f\left(\frac{\gamma - \gamma_r}{2}\right) \quad (4)$$

or

$$\frac{\tau - \tau_r}{2} = \frac{G_{\max} (\gamma - \gamma_r)/2}{[1 + (G_{\max}/2\tau_{\max})|\gamma - \gamma_r|]} \quad (5)$$

The shape of the unloading-reloading curve is shown in Figure 1b. The tangent shear modulus, G_t , for a point on the skeleton curve is given by

$$G_t = \frac{G_{\max}}{[1 + (G_{\max}/\tau_{\max})|\gamma|]^2} \quad (6)$$

and at a point on an unloading or reloading curve G_t is given by

$$G_t = \frac{G_{\max}}{[1 + (G_{\max}/2\tau_{\max})|\gamma - \gamma_r|]^2} \quad (7)$$

The dynamic shear modulus, G_{\max} , of the soil elements is calculated using the expression proposed by Seed and Idriss (13) as

$$G_{\max} = 21.7 K_{2\max} P_a \left(\frac{\sigma_m}{P_a}\right)^{\frac{1}{2}} \quad (8)$$

where P_a is the atmospheric pressure in units consistent with mean normal stress σ_m and G_{\max} and $K_{2\max}$ is a constant.

The response of the soil to uniform all-round pressure is assumed to be nonlinear elastic and dependent on the mean normal stress. Hysteretic behavior, if any, is neglected in this mode. The tangent bulk modulus, B_t , is expressed in the form

$$B_t = K_b P_a \left(\frac{\sigma_m}{P_a} \right)^n \quad (9)$$

where K_b is the bulk modulus constant and n is the bulk modulus exponent.

Reinforcement Model

The reinforcement is modeled using one-dimensional beam elements with axial stiffness only. Slip elements of the type developed by Goodman et al. (14) may be used to allow for the relative movements between the soil and reinforcement during dynamic loading. The behavior of relatively extensible reinforcement such as polymeric materials is assumed to be nonlinear. The relationship between axial load and axial strain for the initial loading is expressed in hyperbolic form as

$$F = \frac{D_i \epsilon_a}{[1 + (D_i/F_m)|\epsilon_a|]} \quad (10)$$

where

- F = axial load per unit width (e.g., kN/m),
- D_i = initial load modulus,
- ϵ_a = axial strain, and
- F_m = maximum axial strength.

The same model can be used to represent relatively inextensible types of reinforcement such as steel strips (elastic-perfectly plastic materials) by selecting fictitiously high F_m values and a yield stress given by the elastic limit [e.g., Yogendrakumar et al. (6)].

The details of the model parameters are shown in Figure 2. The tangent load modulus D_t on the initial loading curve is calculated as

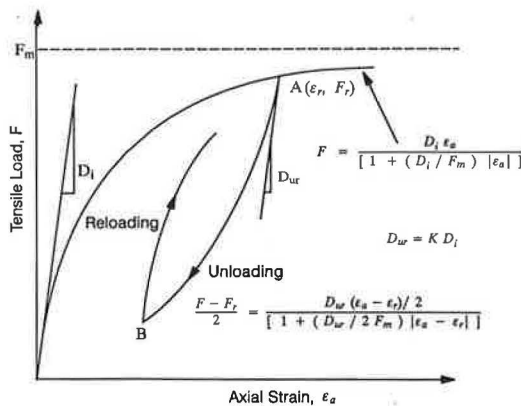


FIGURE 2 Hyperbolic load-strain relationship for polymeric material.

$$D_t = \frac{dF}{d\epsilon_a} = \frac{D_i}{[1 + (D_i/F_m)|\epsilon_a|]^2} \quad (11)$$

The unloading and reloading moduli, D_{ur} , are defined in terms of the initial load modulus as

$$D_{ur} = K D_i \quad (12)$$

where K is a constant.

The unloading and reloading paths are assumed to follow the Masing criterion. The equation for the unloading curve from point $A(\epsilon_r, F_r)$ or for the reloading curve from point B at which the loading reverses direction is given by

$$\frac{F - F_r}{2} = \frac{D_{ur} (\epsilon_a - \epsilon_r)/2}{[1 + (D_{ur}/2F_m)|\epsilon_a - \epsilon_r|]} \quad (13)$$

The shape of the unloading-reloading curve is shown in Figure 2. The tangent load modulus at a stress point on an unloading or reloading curve is given by

$$D_t = \frac{dF}{d\epsilon_a} = \frac{D_{ur}}{[1 + (D_{ur}/2F_m)|\epsilon_a - \epsilon_r|]^2} \quad (14)$$

During the analysis, compression is not allowed in the polymeric geosynthetic reinforcement.

To evaluate the accuracy of the proposed nonlinear hyperbolic reinforcement relationship, the model was used to simulate the load-deformation behavior of a typical woven polyester geogrid reinforcement during a rapid cyclic in-isolation tensile test. Figure 3 shows the experimental load-deformation curve together with the predicted response. The three model parameters D_i , F_m , and K used in the simulation were 1000 kN/m, 30 kN/m, and 1.5, respectively. The proposed model appears to simulate satisfactorily not only the initial loading curve but also the subsequent hysteresis loops during cyclic reloading. The rate of loading used in the tensile testing was limited by the capacity of the equipment. The cyclic loading frequency of 0.5 Hz is considered typical for earthquake-induced horizontal motions but is significantly less than that expected during single-pulse air blast loading. However, at the time of writing there was no rapid cyclic loading

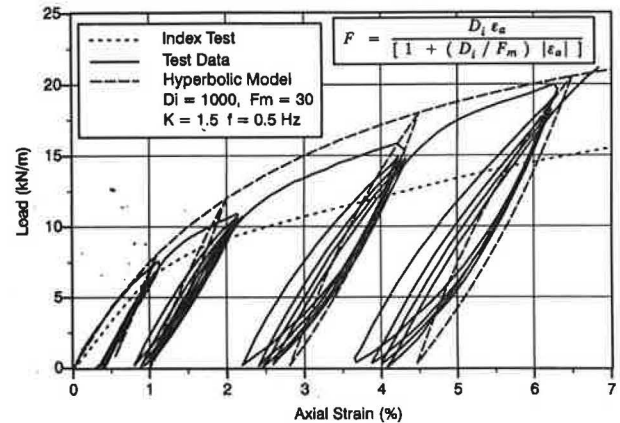


FIGURE 3 Observed and computed load-deformation behavior for woven polyester geogrid.

data available from other sources for this type of geosynthetic. Nevertheless, it is generally known that as the rate of loading of polymeric material increases, the modulus of the material increases and hence the magnitudes of deformations reported in this study are likely conservative (i.e., greater than what may be expected with stiffer modulus values).

Superimposed on Figure 3 is the result of a standard tensile test carried out according to the ASTM 4595 method of test (i.e., 10 percent axial strain/min). As may be expected, the rapid loading test gives a stiffer sample response, suggesting that conventional index test results should not be used directly in simulations modeling rapid excitation of reinforced soil structures.

FINITE ELEMENT ANALYSES

Example Reinforced Soil Wall

Program RESBLAST was used to determine the response of the example reinforced soil wall shown in Figure 4 for a variety of blast loadings. The wall is 6 m high and reinforced with polymeric geogrids 4.8 m long placed horizontally at an equal vertical spacing of 0.75 m. The elevations of the bottom and top reinforcement layers are 0.38 m and 5.63 m, respectively. The geometry of the wall and soil properties have been taken from a retaining wall reported by Richardson (15) that was reinforced with steel strips and subjected to seismic excitation from buried explosive charges. The full-scale experimental wall reported by Richardson (15) has been modeled using program TARA-3, which is the precursor to program RESBLAST. The predicted dynamic tie forces and accelerations at locations in this wall have been reported by the authors earlier (9). The predicted performance was in good agreement with the measured values.

The program RESBLAST models the reinforced soil system as an assemblage of quadrilateral soil elements and one-dimensional beam elements. The finite element representation of the reinforced soil system shown in Figure 4 consisted of 90 soil elements and 32 beam elements. Conventional limit equilibrium methods of design and analysis based on a tie-back wedge method of analysis for internal stability and a gravity structure approach for external stability failure modes indicated that there are adequate factors of safety against instability under static loading conditions (16,17).

Blast Pressure–Time Histories

Three RESBLAST analyses were conducted, each representing a different magnitude of blast loading. The blast loading imposed on the reinforced soil wall consisted of a planar blast wave having a magnitude specified by an overpressure ratio and originating 6 m from the front of the wall. The overpressure ratio is defined as the ratio of pressure in excess of ambient pressure (atmospheric pressure) to that of the ambient pressure. Blast waves with a duration of 10 msec and with different overpressure ratios of 3, 5, and 10 were considered in the current analyses, and the computation was continued for 40 msec to ensure return to an equilibrium state. The blast waves are designated as 3 Atm, 5 Atm, and 10 Atm on the figures, and in each case the program SPLIT2D was used to determine the blast pressure–time history at points on the face of the reinforced soil wall. Pressures were converted to forces at each boundary node by multiplying the pressures by the corresponding frontal area, and these forces were used as input to the RESBLAST program.

Figure 5 shows the velocity vector plots obtained from SPLIT2D for the 5 Atm blast wave at times 5.42 and 16.26 msec. At 5.42 milliseconds, the shock front has not struck the retaining wall (Figure 5a). Figure 5b shows the interaction of the wave front with the structure at 16.26 msec.

Figure 6 shows the blast pressure–time histories at two selected boundary nodes (Nodes 2 and 9). It can be seen that in all cases there is an instantaneous increase in pressure followed by a steady decay of pressure. At Node 2, the pressure is amplified by a factor of 3.7, 3.0, and 2.7 for the 10 Atm, 5 Atm, and 3 Atm blast wave, respectively. For each of the cases, amplification of pressures at other boundary locations on the face of the wall fall between the values at Nodes 2 and 9 in rough inverse proportion to height above the toe. As expected from shock propagation theory, the arrival time for the shock front at the wall face diminishes with overpressure ratio.

Model Parameters

Values of K_{2max} and other soil properties used in the RESBLAST analysis for the different soil zones are given in the following table. The load-strain behavior of the polymeric geosynthetic reinforcement under blast conditions is assumed

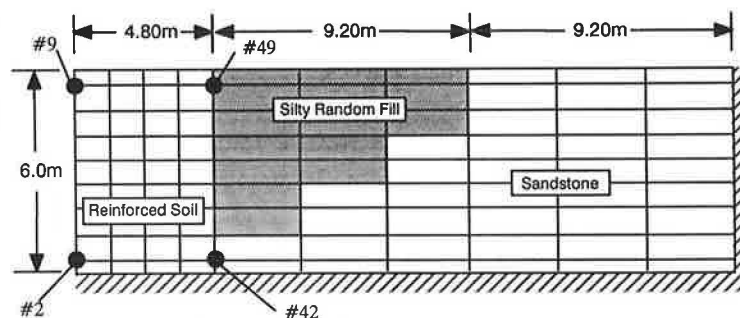


FIGURE 4 Finite element representation of example reinforced soil wall.

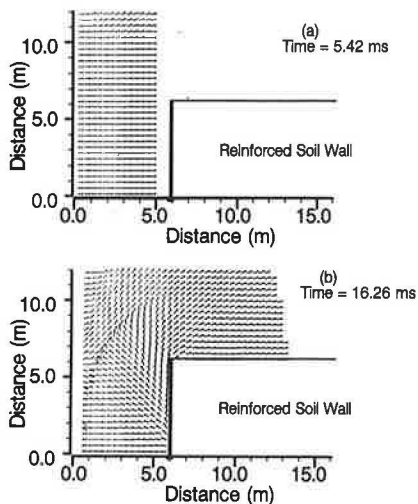


FIGURE 5 Velocity vector plots from SPLIT2D analysis, 5-Atm blast wave.

to be approximated by the hyperbolic form shown in Equation 10. The three model parameters D_i , F_m , and K were taken as 3600 kN/m, 144 kN/m, and 2.0, respectively, and were based on the results of a rapid cyclic in-isolation tensile test carried out at a frequency of 1 Hz on an HDPE uniaxial geogrid.

Type	K_{2max}	Friction Angle (deg)	Unit Weight (kN/m ³)	Poisson's Ratio
Select fill	56	38	18.8	0.35
Silty fill	50	36	17.2	0.35
Sandstone	70	38	18.8	0.35

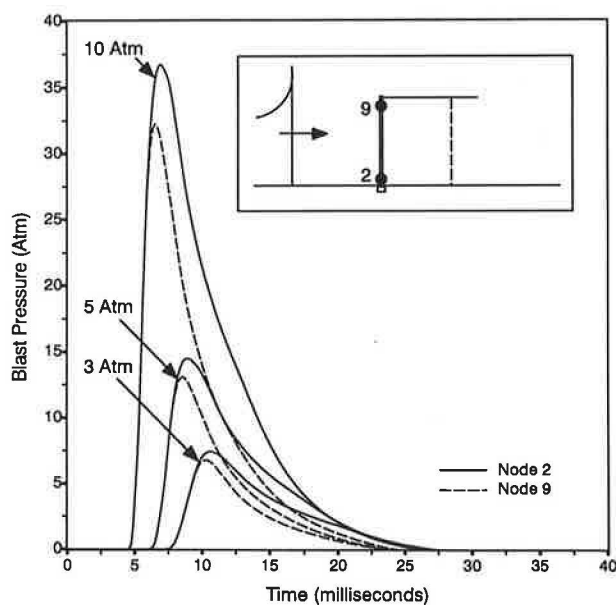


FIGURE 6 Blast pressures at Nodes 2 and 9 from different blast loadings.

Numerical Results

The horizontal displacement–time histories of Node 2, located close to the base of the wall face, and Node 42, located at the right end of the bottom reinforcement layer, are shown in Figure 7 for different blast loading conditions. The displacement responses of these two nodes are similar in shape and indicate that displacements at these locations generally increase with elapsed time and are largely irrecoverable. As expected, displacements increase with magnitude of the source detonation, and the elapsed time to peak displacement increases with distance from the blast.

Figure 8 shows the horizontal displacement–time histories of Nodes 9 and 49, respectively, for the three different blast loadings. Node 9 is located at roughly the top of the wall face, and Node 49 is located at the free end of the reinforcement layer at the same elevation. Qualitative trends identified for the lower elevation nodes are apparent in these figures, but the magnitude of the horizontal displacements of upper nodes is significantly greater (typically by a factor of 7 to 8).

The axial strain–time histories at two locations, Element 53 close to the face of the wall and Element 56 close to the free end of the near-middle reinforcement layer, are shown in Figure 9. At both locations there was a decrease in the reinforcement tensile strain as the blast loading pulse traveled through the reinforced soil mass. In the case of the 10-Atm blast wave there was evidence of a small increase in tensile strain above the static level during the structure rebound (Figure 9). The maximum peak strain in the reinforcement was about 1 percent during static and blast loading. This strain is well within the yield limit of the material on the basis of the results of rapid cyclic loading of the reinforcement sample in the laboratory and manufacturer's literature on the static load-strain-time properties of the polymeric grid material.

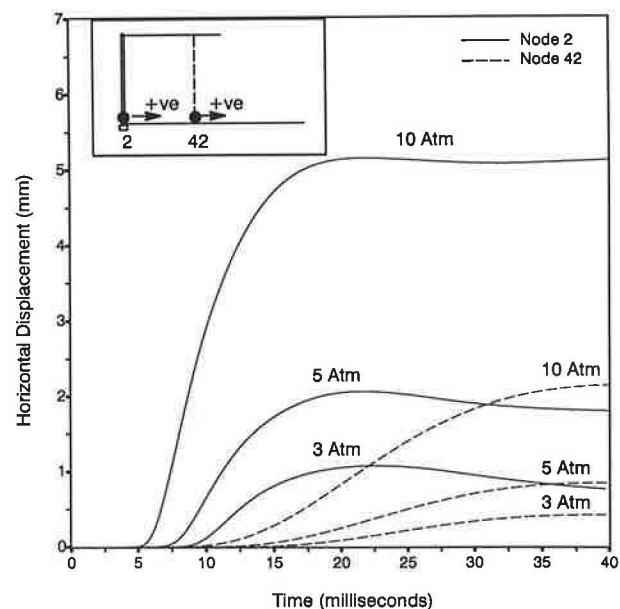


FIGURE 7 Horizontal displacement time histories of Nodes 2 and 42.

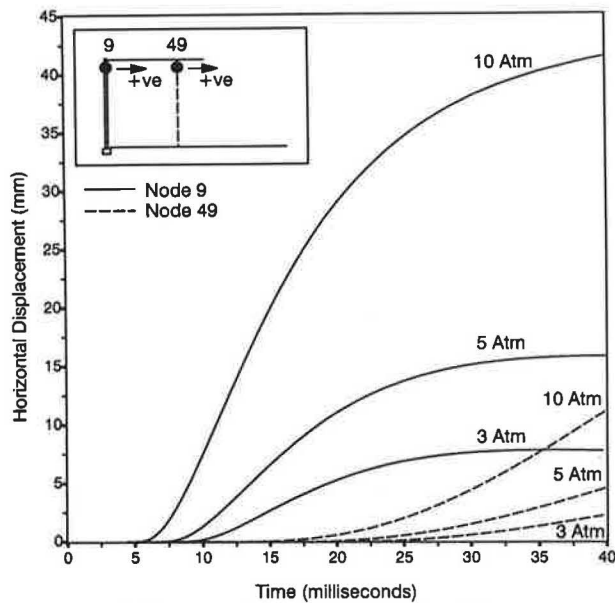


FIGURE 8 Horizontal displacement time histories of Nodes 9 and 49.

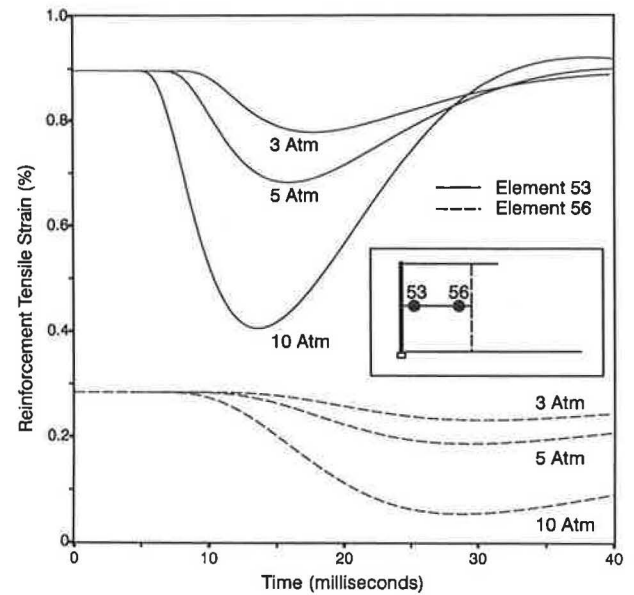


FIGURE 9 Strain time histories of Elements 53 and 56.

Example Steepened Slope

The response of reinforced and unreinforced soil slopes were computed using the RESBLAST program for a given blast loading to examine the influence of the reinforcement. The slopes were assumed to be 6 m high with a side slope of 1:1. The reinforced soil slope was lightly reinforced with 9-m lengths

of the same polymeric material used in the previous example. The reinforcement layers were placed horizontally with a vertical spacing of 1 m. The finite element representation of the reinforced soil slope shown in the inset diagram of Figure 10 consisted of 390 soil elements and 90 one-dimensional beam elements. Slip elements, which allow for relative movement between the soil and the reinforcement, were not used in this analysis since the interfacial shear stress between the soil and

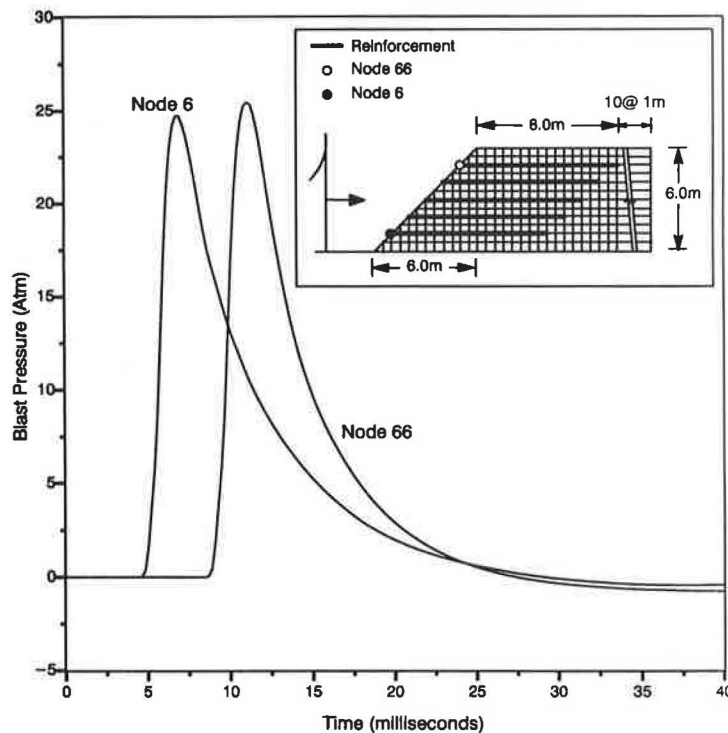


FIGURE 10 Blast pressure time history at Nodes 6 and 66.

the planar reinforcement was assumed to be too small to cause slippage.

Blast pressures caused by a planar blast wave having an overpressure ratio of 10 and a duration of 10 msec and originating at a horizontal distance of 6 m from the toe of the slope were obtained using the SPLIT2D program. Figure 10 shows the blast pressure-time histories at Nodes 6 and 66, which are located on the sloping face at elevations of 1 m and 5 m, respectively. The figure shows that the blast wave causes an average pressure amplification of 2.6 along the sloping side. As expected, the data indicate that the shock front does not arrive at every point on the slope at the same time. The ability to time phase the blast loading at the slope face is one of the distinct advantages of program SPLIT2D.

The following properties were selected for the soil in the slope: $K_b = 2950.0$, $n = 0.5$, $K_{2max} = 29.0$, cohesion = 33 kPa, angle of internal friction = 17 degrees, and unit weight = 20 kN/m³. These properties were taken from an actual reinforced embankment reported by Scott et al. (18). For the polymeric reinforcement, the three model parameters D_i , F_m , and K were taken from the previous example. A static analysis was first conducted to establish the stress-strain field before the blast loading. The program also simulated the incremental construction process of the slope.

Numerical Results

Figure 11 shows the horizontal displacement-time history at Nodes 6 and 66 for the unreinforced and reinforced slopes. Node 66 is located on the face of the structure at an elevation of 5 m close to the crest of the slope. Responses for reinforced and unreinforced cases are similar and show that there are permanent deformations in the structure at the end of loading. The comparison also shows clearly the beneficial effect of the

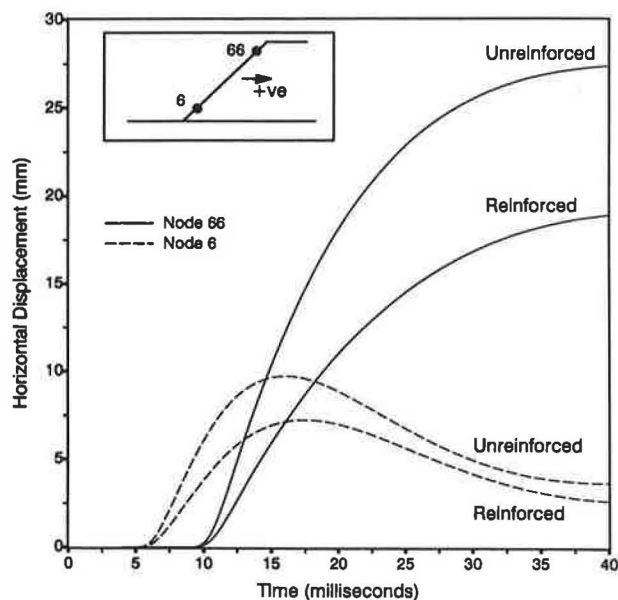


FIGURE 11 Horizontal displacement time histories of Nodes 6 and 66.

reinforcement in reducing both dynamic and permanent slope deformations.

The horizontal displacement-time histories of Node 6, located on the face of the slope at an elevation of 1 m are qualitatively different from the response recorded at the top of the slope. Here the displacement at Node 6 reaches a peak value about 12 msec after the shock front has struck. Unlike the higher elevations the soil mass attempts to follow the blast pressure-time excitation. The qualitative differences in response at different locations along the face of the slope example and previous wall example illustrate the important influence of facing geometry on structure response to blast loading.

In summary, the maximum displacement predicted at Nodes 66 and 6 in Figure 11 is reduced to about 70 to 75 percent of the value predicted at the same location in the unreinforced slope.

CONCLUSIONS

The paper has presented the results of a preliminary numerical study of the response of example geosynthetic reinforced soil wall and slope structures to air blast loading. The principal conclusions from this study can be summarized as follows:

1. Program SPLIT2D, which is a code for the prediction of air blast propagation, has proven to be useful for estimating pressure-time response at the boundaries of reinforced soil structures in proximity to aboveground detonation. The program is unique in its ability to predict the variation of pressures on reinforced soil structures and to account for the time phasing of blast loads against inclined surfaces.
2. Program REBLAST may be a useful tool for the simulation of the nonlinear behavior of the soil and polymeric reinforcement in retaining wall and steepened slope structures and for assessing their performance under blast loads in terms of deformations.
3. Rapid cyclic-tensile loading of sample geosynthetic reinforcement showed that the modulus of the geosynthetic depends on both the rate of loading and the magnitude of the accumulated strain. The reinforcement model gave a reasonable estimate of the laboratory load-strain response of the geosynthetic.
4. The lack of structure rebound predicted for the example reinforced soil wall suggests that further straining of the reinforcement beyond the static strain condition may not be a concern.
5. The predicted results for the example slope suggest that the polymeric reinforcement may improve the performance of the structure under blast loading by reducing the magnitude of dynamic and permanent soil deformations by as much as 30 percent. Greater reductions in slope deformation may have been predicted if greater value of reinforcement modulus had been used.

The results of this study are preliminary in nature. Further research is under way to investigate the influence of extensibility of reinforcement material and inclination of the slope face on air blast attenuation. A long-term goal will be the development of computationally simpler limit-equilibrium-

based methods of design and analysis to assess the stability of these structures under single pulse excitation.

ACKNOWLEDGMENTS

The funding for this study was provided by the Department of National Defence (Canada) as part of ongoing research at RMC related to the design and analysis of blast- and seismic-resistant geosynthetic reinforced soil structures. The authors would like to thank Paul Thibault of Combustion Dynamics Limited, Medicine Hat, Alberta, and David Ritzel of Defence Research Establishment, Suffield, Alberta, for their assistance with the SPLIT2D code.

REFERENCES

1. M. A. Yako and B. R. Christopher. Polymerically Reinforced Retaining Walls and Slopes in North America. *Proc., NATO Advanced Research Workshop on Application of Polymeric Reinforcement in Soil Retaining Structures*, Kingston, Ontario, Canada, June 8–12, 1987, pp. 239–283.
2. J. Ferritto, J. Tancreto, and K. Hager. *Design Procedures and Effectiveness of Reinforced Earth Berms for Enhancing Facility Survivability*. Naval Civil Engineering Laboratory, Port Huene, Calif., 1988.
3. R. Bonaparte, G. R. Schmertmann, and N. D. Williams. *Seismic Design of Slopes Reinforced with Geogrids and Geotextiles*. Technical Note. The Tensar Corporation, Morrow, Ga., 1986.
4. J. Vrymoed. Dynamic Stability of Soil Reinforced Walls. In *Transportation Research Record 1242*, TRB, National Research Council, Washington, D.C., 1989, pp. 29–38.
5. P. Segrestin and M. J. Bastick. Seismic Design of Reinforced Earth Retaining Walls—The Contribution of Finite Element Analysis. *Proc., International Geotechnical Symposium on Theory and Practice of Earth Reinforcement*, Fukuoka, Japan, Oct. 5–7, 1988, pp. 577–582.
6. M. Yogendrakumar, R. J. Bathurst, and W. D. Liam Finn. Seismic Response of Reinforced Soil Retaining Walls. *Proc., Seventh Conference of the International Association for Computer Methods and Advances in Geomechanics*, Cairns, Australia, May 6–10, 1991, pp. 907–912.
7. M. Yogendrakumar, R. J. Bathurst, and W. D. Liam Finn. Response of Reinforced Soil Walls to Earthquake Loads. *Proc., 9th Panamerican Conference*, Vina del Mar, Chile, Aug. 1991.
8. M. Yogendrakumar, R. J. Bathurst, and W. D. Liam Finn. Response of Reinforced Soil Slopes to Earthquake Loadings. *Proc., Sixth Canadian Conference on Earthquake Engineering*, Toronto, Ontario, Canada, June 12–14, 1991, pp. 445–452.
9. M. Yogendrakumar, R. J. Bathurst, and W. D. Liam Finn. Dynamic Response Analysis of a Reinforced Soil Retaining Wall. *Geotechnical Journal*, ASCE (in press).
10. *SPLIT2D—Version 4.3: A 2-D Hydrocode for Blast Loading on Arbitrary Shapes*, Combustion Dynamics Ltd., Medicine Hat, Alberta, Canada, 1990.
11. M. Yogendrakumar and R. J. Bathurst. *RESBLAST: A Computer Program to Compute the Response of 2-D Reinforced Soil Systems to Blast Loadings*. Department of Civil Engineering, Royal Military College of Canada, Kingston, Ontario, Canada, 1990.
12. W. D. Liam Finn, M. Yogendrakumar, N. Yoshida, and H. Yoshida. *TARA-3: A Program to Compute the Response of 2-D Embankments and Soil-Structure Interaction Systems to Seismic Loading*. Department of Civil Engineering, University of British Columbia, Vancouver, Canada, 1986.
13. H. B. Seed and I. M. Idriss. *Soil Moduli and Damping Factor for Dynamic Response Analysis*. Report EERC 70-10. Earthquake Engineering Research Center, University of California, Berkeley, 1970.
14. R. B. Goodman, R. E. Taylor, and T. L. Brekke. A Model for the Mechanics of Jointed Rock. *Journal of the Soil Mechanics and Foundations Division*, ASCE, Vol. 94, No. SM3, 1968, pp. 637–659.
15. G. N. Richardson. *The Seismic Design of Reinforced Earth Walls*. School of Engineering and Applied Science, University of California, Los Angeles, 1976.
16. B. R. Christopher and R. D. Holtz. *Geotextile Design and Construction Guidelines*. National Highway Institute, Washington, D.C., 1989.
17. R. J. Bathurst. Geosynthetics for Reinforcement Applications in Retaining Walls. *Proc., 44th Canadian Geotechnical Conference*, Vol. 2, Paper 74, Calgary, Alberta, Canada, Sept. 29–Oct. 2, 1991.
18. J. D. Scott, D. C. Sego, E. A. Richards, B. A. Hoffman, and E. R. Burch. Design of the Devon Geogrid Test Fill. *Geosynthetics Conference '87*, Vol. 1, New Orleans, La., 1987, pp. 157–168.

Publication of this paper sponsored by Committee on Transportation Earthworks.

Dynamic Centrifuge Modeling of Sound Walls Supported on Concrete Cantilever and Mechanically Stabilized Earth Retaining Structures

DAVID SOON, JOHN A. CASEY, BRUCE L. KUTTER, AND KARL M. ROMSTAD

The results of a model study comparing the dynamic behavior of sound walls supported on concrete cantilever (Caltrans Standard Type 1) and mechanically stabilized earth (MSE) retaining structures are presented. Different backfills representing a loose sand, a dense sand, and a cohesive material were studied. An additional test was run with the loose sand and inclined reinforcing. The models were tested on a servohydraulic shaking table mounted on a centrifuge. Realistic earthquakes with peak input base accelerations of 0.65 g to 0.75 g were simulated. The sound wall response on the MSE system involved accumulated tilting due to nonsymmetrical resistance, and in some cases lift-off and impact of the slab. The behavior of sound walls on Type 1 systems was much less sensitive to the backfill type. The MSE systems were generally more ductile than the Type 1 walls; they suffered larger permanent deformations but transmitted smaller accelerations to the sound wall. Sound wall accelerations on the Type 1 wall system were approximately twice those on the MSE system.

Mechanically stabilized earth (MSE) retaining systems are often cost-effective alternatives to conventional retaining walls. However, in areas of significant seismic activity, the dynamic behavior of sound walls superimposed on MSE systems is unknown, and design engineers have been reluctant to use systems for which there is little field or experimental data. Because of this lack of data and the policy of the California Department of Transportation (Caltrans) to encourage the use of alternative retaining systems, this research project was initiated.

Kutter, in another paper in this Record, presents a discussion of scaling laws and the advantages and disadvantages of dynamic centrifuge modeling. The disadvantages become less critical if a modeler uses the centrifuge as a tool to compare the performance of different types of structures while the grain size, boundary conditions, and loading rates are held constant. This paper presents such a study in which MSE walls are compared with conventional reinforced concrete cantilever (Type 1) retaining walls.

The models tested in this study represented 24-ft-high prototype earth retaining structures with 12-ft sound walls positioned on top of the retaining structures. The models represented a typical reinforced concrete cantilever retaining wall called a Type 1 retaining wall by Caltrans. Figure 1a shows

a schematic of the prototype Type 1 retaining wall system. The system includes a vehicle barrier and a roadway slab in addition to the reinforced masonry block sound wall. The sound wall is anchored directly to the reinforcing bars of the Type 1 retaining wall, creating a continuous structure.

The alternative soil retaining structure tested is a reinforced soil wall that Caltrans calls an MSE wall. Figure 1b is a schematic of the prototype MSE retaining wall. In this wall arrangement the vehicle barrier and sound wall are mounted on the roadway slab, which is anchored to the backfill by short piles. The MSE face plates, which serve to retain the adjacent soil, are held in place by bar mat reinforcing mesh. The reinforcing mesh (bar mat) for this prototype is made of welded rebar.

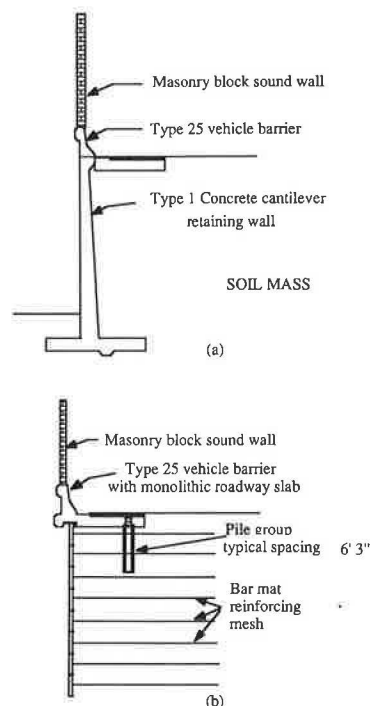


FIGURE 1 a, Type 1 retaining wall; b, MSE retaining wall.

PREVIOUS RESEARCH

Mononobe and Matsuo (1) suggested using the Coulomb sliding wedge theory, with the addition of a lateral acceleration, to predict the resultant lateral force on a gravity retaining wall subjected to an earthquake. The resultant force, which included both static and dynamic pressure, was assumed to act at $\frac{1}{3}H$ above the base. Seed and Whitman (2) later recommended that the dynamic component of the pressure resultant should be assumed to act at $0.6H$ above the base. Richards and Elms (3) suggested that permanent deformation rather than maximum pressures should be the design criterion. They applied Newmark's sliding block analysis (4) to predict wall movement. Bracegirdle (5) suggested a limit equilibrium method using a pseudolateral acceleration.

Bolton and Steedman (6) and Ortiz et al. (7) have conducted centrifuge experiments on cantilever retaining walls supporting dry cohesionless sands subjected to base motions. Richardson and Lee (8), Nagel (9), and Wolfe and Rea (10) have conducted 1-g shaking table tests on the seismic behavior of soil-reinforced walls. Later, Richardson (11) conducted a field study on a full-scale 20-ft wall to assess his earlier proposed design procedure. Kutter et al. (12) and Casey et al. (13) have presented preliminary results from this research, field data from earthquakes, and some simple analytical modeling of MSE and Type 1 systems with and without sound walls.

MODEL RETAINING WALL SYSTEMS

Model Components and Instrumentation

Figure 2a shows the general arrangement and dimensions of the MSE models. Prototype dimensions in Figure 2 are given in parentheses. A coarse wire screen was used to simulate the MSE reinforcing mats which, in the prototype, consist of a mesh of #4 rebar extending 16.8 ft (4.2 in. in model) horizontally into the soil at a vertical spacing of 3 ft (0.75 in. in the model). The total area of the longitudinal reinforcing bars was accurately scaled to that for the prototype. In the prototype MSE design, each 14.5-ft by 3-ft by 8-in.-thick concrete face plate is supported by four mats, each consisting of five 16.8-ft bars (perpendicular to the wall face) spaced at 6 in. with 2-ft-long bars spaced at 18 in. welded across the long bars. In the model, the wire screens were attached to aluminum face plates, which were scaled to simulate the mass of the prototype face plates.

In Figure 2a it can be seen that the sound wall in the model MSE system is tilted at a 9-degree angle to the vertical. This was done to ensure that the radial centripetal acceleration was acting parallel to the wall. The radial acceleration has a lateral component that, for a vertical model wall, would cause an unwarranted static overturning moment. Overturning during the seismic event is a critical failure mechanism for the sound wall of the MSE system.

Figure 2a shows seven accelerometers and three displacement transducers used to measure horizontal accelerations on the sound wall, in the backfill, at the base, and at the top face plate and horizontal deflections at the top of the sound wall, the top face plate, and the third face plate from the

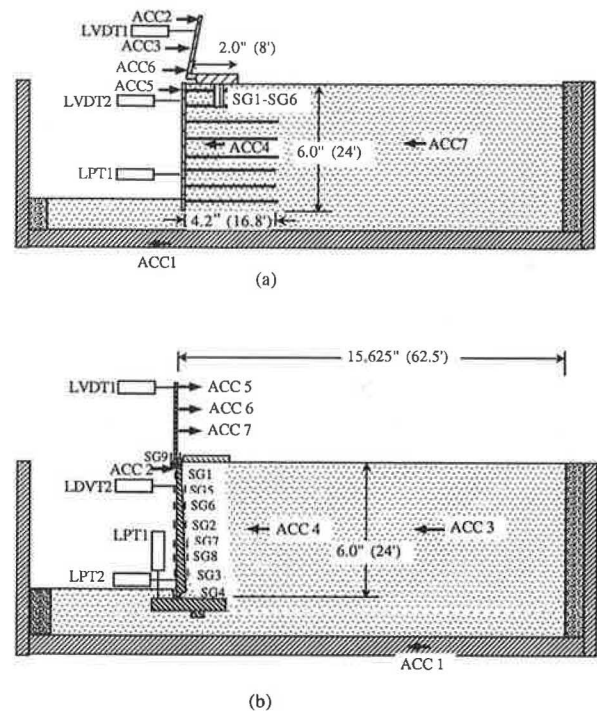


FIGURE 2 Test arrangement and instrumentation: *a*, MSE and *b*, Type 1 retaining wall models.

bottom. The MSE model system is three face plates wide (across the width of the box) and eight face plates high. The prototype roadway slab (Figure 1b) has a groove that the top face plate fits into without any connection. In preliminary model tests with this arrangement, the accelerations measured at the top face plate showed signs that the top face plate and the sound wall-slab system were making contact. Impact between the sound wall and the top face plate can cause excessively high bar mat forces and local face plate damage. To remedy this problem in later tests the model sound wall system was placed 1 ft (0.25 in. the model) behind the top face plate.

The Type 1 retaining wall model is shown in Figure 2b. The model retaining wall was machined from a solid block of aluminum. The thickness of the Type 1 model was selected to match the computed stiffness of the full-scale concrete cantilever retaining walls; the mass of the concrete wall was not scaled (most of the mass contributing to dynamic loads was assumed to come from the backfill). Because of the rigid connection between the sound wall and the retaining wall in the Type 1 system, it was not considered important to tilt the sound wall. The thickness of the model sound wall was determined by matching its scaled natural frequency to a calculated natural frequency of the prototype 8-in.-thick reinforced masonry block sound wall.

The aluminum model wall (with thickness determined by stiffness criteria) had a higher scaled bending strength than the prototype Type I system. A notch was machined at the base of the aluminum wall to provide the correctly scaled moment capacity at the critical section. Since the notch was relatively short in length, it did not significantly affect the stiffness. The base (13.25-ft prototype) and key dimensions were scaled from the prototype wall with material density

differences (aluminum model versus reinforced concrete prototype) being considered.

Figure 2b shows the location of the strain gauges, displacement transducers, and accelerometers used in the Type 1 models. The Type 1 models were instrumented with nine strain gauges to measure moments in the wall, four displacement transducers to measure deflections, and seven accelerometers to measure accelerations. Only 16 of the instruments could be monitored at once, so each model was tested with three different instrumentation combinations, each involving 16 instruments.

The roadway slabs in both systems were modeled by aluminum plates. The plates represented the mass of a 20-in.-thick concrete slab (8 ft wide) that is used in the roadway shoulder of the prototype system. In the MSE system the slab is anchored to the soil by 6-ft-long, 16-in.-diameter cast-in-place piles spaced at 6.25 ft. These piles were included in the model.

Backfill Conditions Studied

Three backfill soil conditions (denoted as loose, dense, and cohesive) were modeled. The loose backfill was Nevada sand, a fine uniform silica sand with a mean grain size of 0.15 mm and a coefficient of uniformity of 1.7. The loose model was made by spooning the sand into the box layer by layer and vibrating on a vibrating table to achieve the specified density. As commonly specified for prototype walls by Caltrans, the backfill was densified to approximately 93 percent relative compaction California Test #216 compaction test. Because of the poor compaction characteristics of this sand, however, the relative density was only 32 percent. This very loose material had a low friction angle ($\phi = 30$ degrees) and no cohesion. The loose backfill is an extreme condition that will tend to show worst-case scenarios for displacements.

The dense backfill soil was also Nevada sand, but the sand was pluviated to obtain a higher density of 101 pcf, relative density of 95 to 100 percent, and a friction angle of 45 degrees. The cohesive backfill consisted of 70 percent Nevada sand with 30 percent Yolo loam (a low-plasticity silty clay). The cohesive backfill was compacted at 12 percent water content by hand to obtain the desired density. The cohesive backfill had a friction angle of 34 degrees, cohesion of 500 psf, density of 103 pcf, and a relative compaction of 92 percent.

One other backfill condition, called loose-10°, was tested for the MSE system. For these tests, the barmats were inclined at a 10-degree angle downward into the backfill.

EXPERIMENTAL PROCEDURE

The shaker, described briefly by Kutter in another paper in this Record, has a sample container that is 11 in. by 22 in. in area and 7 in. in height. A detailed description of the centrifuge system is given by Chang (14).

Two prototype acceleration records were used to generate seven types of earthquakes. The records used were from the San Fernando (8244 Orion Blvd., 1st floor, February 9, 1971, 6:00 a.m. PST, North 00° West) and El Centro (Imperial Valley Irrigation District, May 18, 1940, 8:37 p.m. PST, South

00° East) earthquakes. Since the San Fernando record was taken inside a building, the acceleration history includes the soil-structure interactions felt at the first floor of the building. The original El Centro record, in comparison, shows free field response. The alluvial characteristics of the sites at which the accelerations were measured were chosen to match the characteristics of the Harbor Freeway construction area in Los Angeles (deep deposits of firm sandy silt, with approximate standard penetration values of 30 blows per foot).

Two typical achieved acceleration records are shown in Figures 3a and 3b. Note the extended strong motion phase of the record in the San Fernando event of Figure 3a. The strong motion phase of the original record was spliced and reattached to the end to create a long (greater than 30 sec in the prototype) duration of relatively large amplitude accelerations. The prototype acceleration records were processed by double integration, filters, and baseline corrections to create an input data file for the centrifuge shaker. These records could be multiplied by a magnification factor to provide different levels of shaking to the centrifuge models.

Figure 4 shows a comparison of the Caltrans ARS design spectra with the two output spectra from the time histories shown in Figures 3a and 3b. These spectra demonstrate that the models have been subjected to realistic earthquake records. Figure 5a shows the 2 percent damped acceleration response spectra computed using the measured base accelerations for each of the four MSE model types when subjected to the filtered El Centro motion magnified by five. The shape of each of the spectra are similar and the loose-10° and dense models appear to be receiving slightly more energy over most

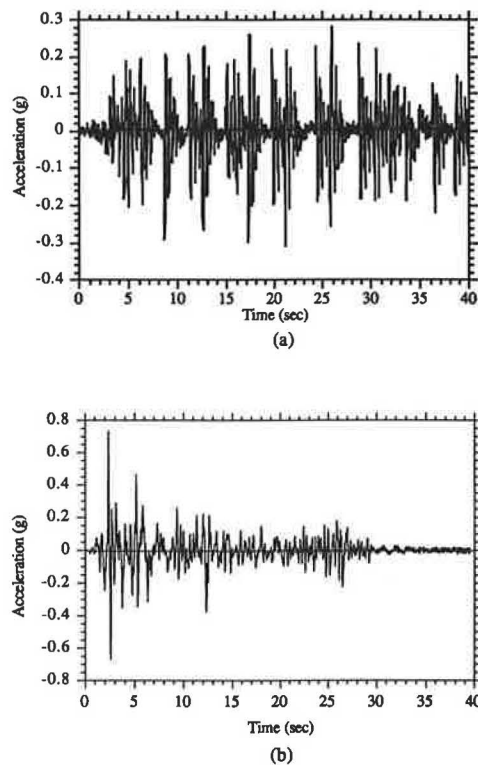


FIGURE 3 Typical achieved base acceleration: a, San Fernando $\times 4$ event and b, filtered El Centro $\times 5$ event.

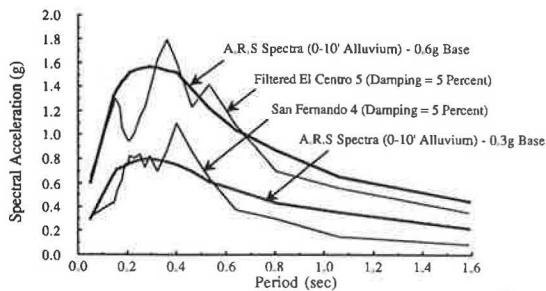


FIGURE 4 Comparison of Caltrans ARS spectral design curves and spectral accelerations from achieved base motions.

of the frequency range. The good repeatability of the base motions allows direct comparison of results. Figure 5b shows that the acceleration response spectra for the base motion during a filtered El Centro event for the Type 1 models was very similar for all three backfill types.

Six models were tested using the Type 1 retaining wall as the soil retaining structure. Four models used the loose sand, one the dense sand, and one had a cohesive backfill. A total of nine models of the MSE retaining wall were tested. Five models used the loose sand, two the dense sand, one the cohesive backfill, and one the loose sand inclined bar mats (loose-10°).

The Type 1 retaining wall systems were subjected to a total of 69 earthquakes, and the MSE retaining wall systems were subjected to 67 earthquakes. For the models used for the

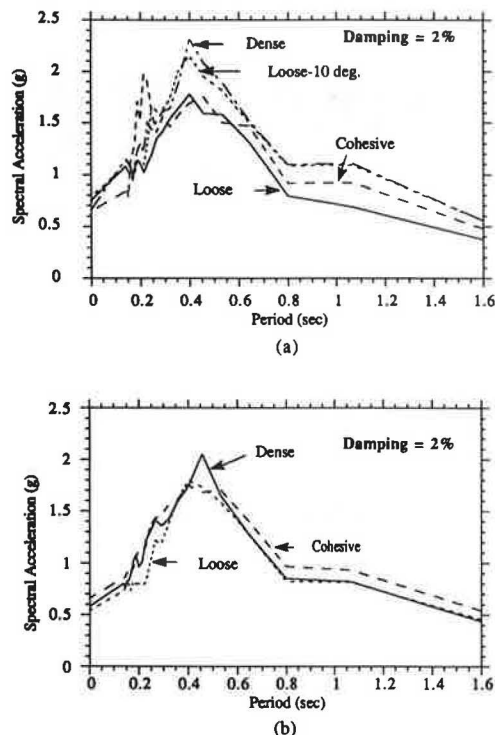


FIGURE 5 Comparison of base acceleration response spectra for a filtered El Centro $\times 5$ for *a*, MSE and *b*, Type 1 models.

comparisons, the typical earthquake sequence of the first six events was (a) filtered El Centro $\times 4$ (FEC $\times 4$), (b) El Centro $\times 2$ (EC $\times 2$), (c) old San Fernando $\times 4$ (OSF $\times 4$), (d) filtered El Centro $\times 5$ (FEC $\times 5$), (e) El Centro $\times 4$ (EC $\times 4$), and (f) new San Fernando $\times 2$ (NSF $\times 2$). The adjectives filtered, old, and new refer to different schemes used for processing the accelerations recorded in the field. Each of these events had a different input base motion. The numbers in the list are an indicator of the intensity of the events.

DISPLACEMENT BEHAVIOR

Permanent Wall Movement Comparisons

Figure 6a presents displacement time histories at the top of the MSE retaining wall (just below the sound wall) for all four backfill conditions for the filtered El Centro $\times 5$ base motion. Plotted below these motions is the corresponding time history of accelerations at the base of the model for the dense model. The base acceleration time history input motions to the other three models were very similar, as evidenced by the acceleration response spectra in Figure 5a. The first large acceleration pulse of approximately 0.6 g produced a significant permanent displacement at the top of the retaining wall for each of the models. The loose model continued to move out significantly during the first 6 sec compared with the other three models. The 10-degree sloping reinforcement reduced the total permanent displacement by a factor of almost four compared with the horizontally placed reinforcement. The total displacements of the cohesive and dense models were also significantly reduced compared with the loose model.

Figure 6b presents displacement time histories at the top of the Type 1 retaining wall (just below the sound wall) for the three different backfill types (loose, dense, and cohesive) during a large comparable filtered El Centro event. Plotted below these motions is the time history of base acceleration for the model with dense backfill. The final permanent displacement of the dense backfill was 50 to 60 percent of the final permanent displacement of the cohesive backfill. The loose backfill displacement was typically 60 to 70 percent of the displacement of the cohesive backfill.

From Figure 6 it is clear that permanent displacements of the Type 1 system are generally smaller than those for the MSE system. For the loose backfill, the permanent displacement at the top of the MSE wall was four times greater than the permanent displacement at the top of the Type 1 wall. For the dense backfill, the permanent displacement at the top of the MSE wall was three times that of the Type 1 wall. With cohesive backfill, however, permanent displacements were similar for both types of walls.

Displacement Mechanisms of Type 1 and MSE Systems with Sound Walls

Figure 7 plots the sequence of incremental permanent displacements at three positions over the height of the wall (LPT1, LVDT2, and LVDT1 in Figure 2a, and LPT2, LVDT2, and LVDT1 in Figure 2b) for the loose models subjected to San

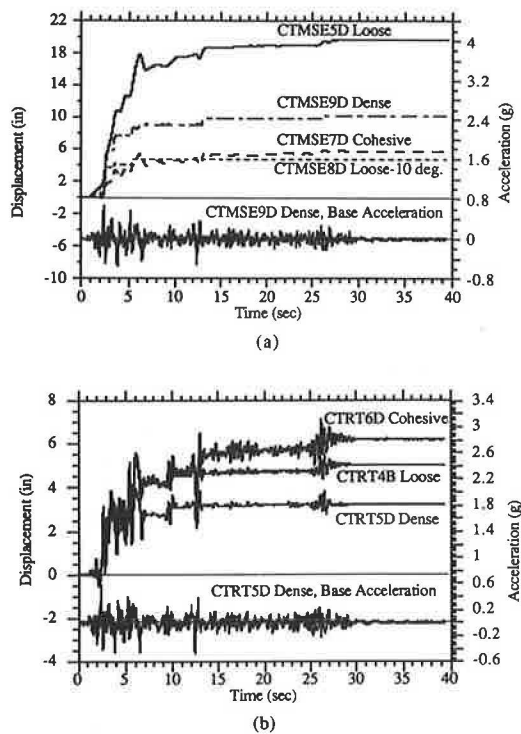


FIGURE 6 Top of retaining wall displacements during a filtered El Centro $\times 5$ event for *a*, four MSE and *b*, three Type 1 models.

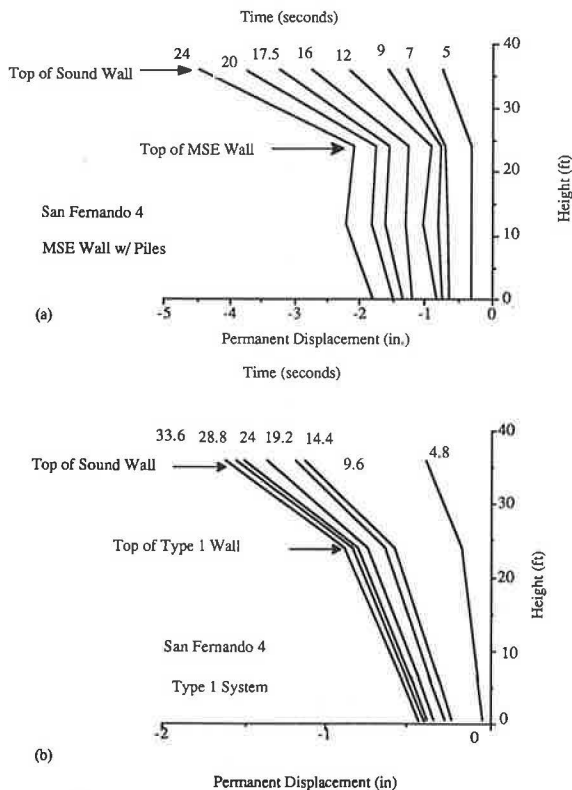


FIGURE 7 Permanent displacement profiles during a San Fernando $\times 4$ event for the loose *a*, MSE and *b*, Type 1 models.

Fernando $\times 4$. In all cases the line connecting the top two points should be straight, reflecting the absence of inelastic behavior in the model sound walls. The line connecting the bottom two points should be curved.

The permanent incremental displacements at the top of the sound wall for the MSE models shown in Figure 7a are closely tied to the soil-pile interaction. For the loose and dense models, pile slippage is followed by the sand filling the vacated space and the pile tips not returning to the original position. This results in accumulated rotation of the sound wall. For the cohesion models, enlarged holes generally allowed the sound wall to rotate back near its original position. The curvature of the face of the MSE wall should be concave to the right, consistent with a shear deformation mode of the soil. Further discussion of MSE displacement mechanism is given by Casey et al. (13).

For the Type 1 model the permanent incremental displacement of the top of the sound wall in Figure 8b was greater than the top of retaining wall displacement, and one can observe a continuing rotation of the Type 1 wall. The actual displaced shape and the Type 1 retaining wall below the sound wall should curve such that slope compatibility is matched at the retaining wall-sound wall connection. This curvature would therefore always be concave to the left in the figures and create a curvature consistent with the final induced residual moments.

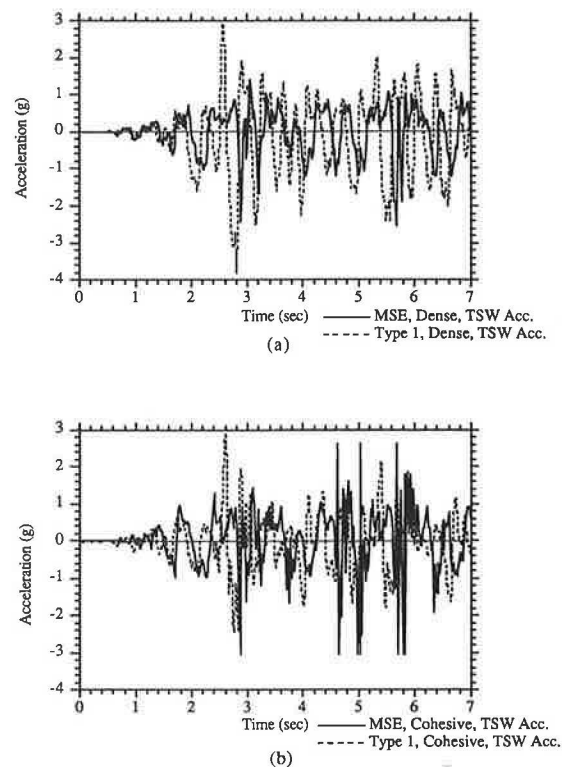


FIGURE 8 Top of sound wall accelerations for the *a*, dense and *b*, cohesive Type 1 and MSE models due to filtered El Centro $\times 5$.

EXPERIMENTALLY DETERMINED YIELD ACCELERATIONS

By analyzing the acceleration recorded by ACC4, in the backfill 2 in. behind the face of the retaining structure, it was possible to determine a cutoff acceleration, which appears to be associated with permanent deformation of the retaining structure. This cutoff acceleration did not appear to be exactly constant. Several of the apparent cutoff accelerations were averaged together as described by Casey et al. (13). The cutoff accelerations are presumed to be an estimate of the yield acceleration (5). The yield acceleration data determined by this method are summarized as follows.

For the MSE system the loose, loose-10°, dense, and cohesive models had yield acceleration ranges of 0.18 to 0.24 g, 0.22 to 0.27 g, 0.26 to 0.33 g, and 0.34 to 0.41 g, respectively. For the Type 1 system the loose, dense, and cohesive models had yield acceleration ranges of 0.22 to 0.36 g, 0.28 to 0.34 g, and 0.27 to 0.35 g. With the exception of one data point from the loose backfill, the Type 1 deduced yield accelerations for all three backfill types ranged from 0.27 to 0.35 g.

SOUND WALL ACCELERATION COMPARISONS

The filtered El Centro $\times 4$ base motion, imposed on each of the models, represents a severe earthquake with base accelerations as high as 0.7 g. During the interval from 1 to 7 sec the base acceleration had peaks up to 0.7 g, and from 7 to 28 sec the measured base acceleration peaks reached 0.15 g. Results from this motion will be compared for all systems.

The acceleration at the top of the sound wall for these two soil retaining systems differed because of the nature of the sound wall attachment to each retaining wall and filtering of the base motion by the wall/backfill systems. The face plates in the MSE system cannot develop shear or moment, hence lateral displacements at the face of the wall are dominated by elastic and permanent shear strains distributed within the reinforced soil mass. The permanent deformations absorb energy and lower the apparent natural frequencies of vibration. For the Type 1 system the lateral deformations are influenced by the shear and flexural stiffness of the cantilever retaining wall and sliding along the base.

The sound wall with the Type 1 wall is cast monolithically with the concrete retaining wall and hence acts as an elastic extension of the cantilever wall with a nearly fixed base. Therefore, the accelerations induced at the top of the sound wall result in elastic amplifications of the transverse and rotational accelerations at the top of the Type 1 retaining wall accompanied by relatively low damping.

The response of the MSE sound wall, slab, and piles (sound wall system) depends highly on the soil-pile interaction. In the dense and loose models the pile skin friction was exceeded and the piles began to pull out when the effective inertial force acting on the sound wall away from the backfill reached a critical level. At the top of the sound wall this phenomenon was shown to result in a capping of the positive acceleration. As the sound wall moves back toward the backfill, the large resistances provided by the pile tip bearing stiffness are reactivated. This sudden change in stiffness induced high-

frequency and large-amplitude accelerations at the top of the sound wall. The resulting acceleration record was nonsymmetric. The slippage of the piles helped to dissipate energy.

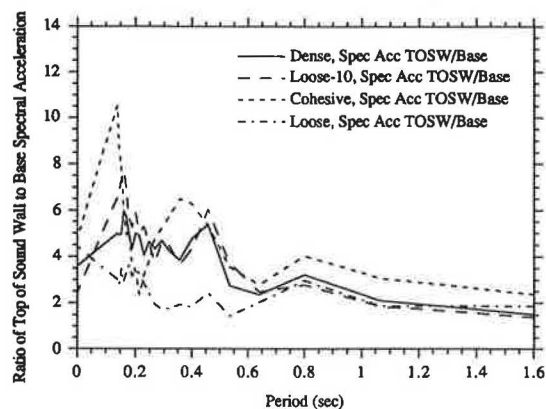
Figure 8a presents 7 sec of the top of sound wall acceleration time histories due to filtered El Centro $\times 5$ for the dense models of both the MSE and Type 1 systems. The lack of symmetry on the positive and negative sides is evident for both systems. The positive accelerations for the MSE system are clearly capped at less than 1 g, and several time intervals show extended positive excursions (which will contribute energy dissipation) where some combination of slipping of the piles and sliding of the MSE wall are occurring. The positive peaks for the Type 1 system show little evidence of capping, and the Type 1 maximum positive acceleration is approximately twice the maximum MSE positive acceleration. Essentially all the negative peaks for both systems are sharp. The maximum negative peaks for the MSE system at approximately 2.8 and 5.7 sec are very high frequency associated with the stiffening described earlier.

A third type of behavior possible with the MSE sound wall system was observed in the cohesive model (Figure 8b). In the cohesive backfill the lateral forces from the piles worked to enlarge the holes that held the piles. Since the material was cohesive, the enlarged holes did not refill, and skin friction was lost after a few large acceleration pulses. In these models the effectiveness of the piles was lost, and the sound wall slab was able to lift up and upon returning the slab struck the backfill soil surface. The impacts caused very high acceleration pulses to travel through the sound wall.

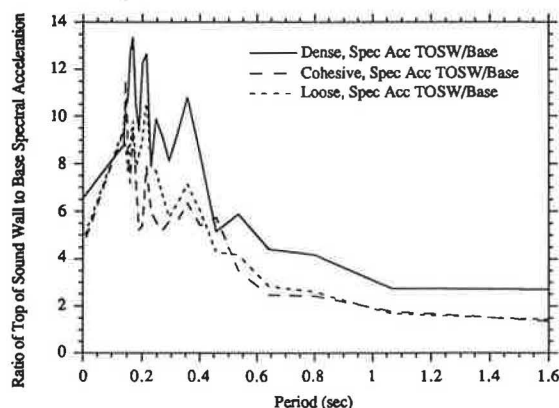
The impacts are clearly seen in Figure 8b, which presents the same top of sound wall acceleration comparisons for the cohesive models as Figure 8a does for the dense models. Very high frequency acceleration amplitudes reach the limit of the recorders on both the positive and negative sides for the MSE system, and the peak amplitudes exceed the acceleration peaks recorded for the Type 1 system. The large accelerations developed at the top of the sound wall due to the impacts may induce large moments at the base of the sound wall. However, even if the high moments exist (no strain gauges were present on the sound wall for the MSE tests), the accelerations are of such short duration that they do not result in high velocities or high displacements. The velocity spectrum of the cohesive model was not significantly higher than that of the dense or loose-10° models.

Figures 9a and 9b present the amplifications of the acceleration spectra for the MSE and Type 1 systems from the base of the retaining wall to the top of the sound wall. Excepting the cohesive model, the maximum amplifications for the MSE system in the range of interest (period less than 0.4 sec) are about 5. The larger amplification for the cohesive model may be associated primarily with lift-off and impact of the slab. The amplifications for the Type 1 system are generally much greater than for the MSE system.

The amplification was also calculated for each earthquake by dividing the peak top of sound wall acceleration by the peak base motion. Figure 10a shows these amplification factors as a function of the peak base acceleration. For each earthquake there are only two data points, one for the positive and one for the negative peaks of the base and sound wall accelerations. The amplification does not appear to be a strong function of the base motion, hence a horizontal line is drawn

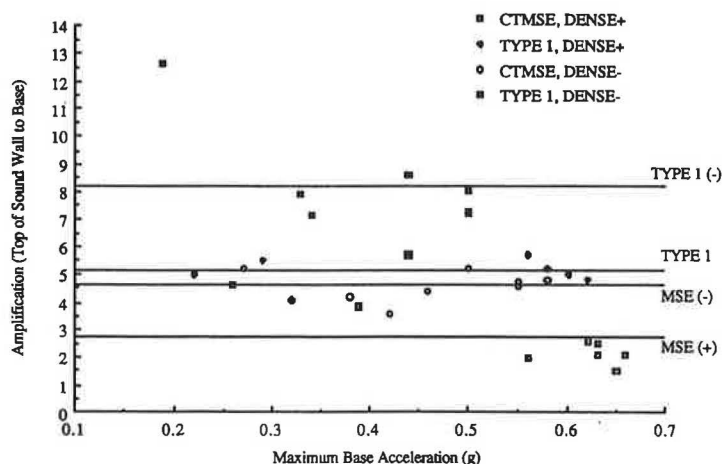


(a)

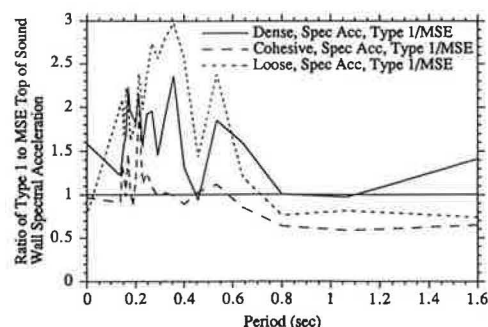


(b)

FIGURE 9 Amplification of spectral acceleration from the base to the top of sound wall in the *a*, MSE and *b*, Type 1 models.



(a)



(b)

FIGURE 10 *a*, Amplification of acceleration from base to top of sound wall for all models and all events; *b*, ratio of top of sound wall acceleration spectra, Type 1 divided by MSE, due to filtered El Centro $\times 5$.

in Figure 10a representing the average amplification for each case. The positive amplifications are smaller than the negative amplifications due to the unsymmetrical resistance for both systems. The Type 1 amplifications are 1.8 to 1.9 times larger than the corresponding MSE amplifications.

Finally, the ratios of Type 1 to MSE top of sound wall acceleration spectra are presented in Figure 10b for the dense, cohesive, and loose models. In general, the Type 1 spectra amplitudes are 1.5 to 3 times greater than the MSE spectral amplitudes over the period range of interest (0.2 to 0.4 sec).

CONCLUSIONS

1. Sound walls superimposed on the Type 1 walls experienced maximum accelerations approximately twice as large as those experienced by sound walls superimposed on MSE systems. This was primarily caused by the monolithic connection between the Type 1 wall and the sound wall and the lower amount of energy dissipated by the backfill behind a Type 1 system.

2. Permanent displacements of MSE walls with sand backfills were clearly related to the competence of the backfill and the amplitude and number of acceleration pulses exceeding the yield acceleration. Displacements at the top of the MSE retaining wall after a large event were three to four times larger than those included at the top of Type 1 walls. Cohesive backfill models did not follow the same trends as the two sand models.

3. The sound wall-slab system with the MSE system needs to be physically separated from the top face plate to avoid striking.

4. An improved anchor at the rear of the slab should be found in place of the piles to minimize the striking and gradual tilting problems.

ACKNOWLEDGMENTS

This work was carried out with funding from the Federal Highway Administration and Caltrans. The continued review and comments on Ken Jackura are gratefully acknowledged.

REFERENCES

1. N. Mononobe and H. Matsuo. On the Determination of Earth Pressure During Earthquake. *Proc., 2nd World Conference on Earthquake Engineering*, Tokyo, 1929.
2. H. B. Seed and R. V. Whitman. Design on Earth Retaining Structures for Dynamic Loads. *Proc., ASCE Specialty Conference: Lateral Stresses in the Ground*, Cornell University, Ithaca, N.Y., 1970.
3. R. Richards, Jr., and D. G. Elms. Seismic Behavior of Gravity Retaining Walls. *Journal of the Geotechnical Engineering Division*, ASCE, April 1979.
4. N. A. Newmark. Effects of Earthquakes on Dams and Embankments. *Geotechnique*, Vol. 15, 1965.
5. A. Bracegirdle. Seismic Stability of Reinforced Earth Retaining Walls. *Bulletin of the New Zealand National Society for Earthquake Engineering*, 1980.
6. M. D. Bolton and R. S. Steedman. Centrifugal Testing of Microconcrete Retaining Walls Subjected to Base Shaking. *Proc., International Conference of Soil Dynamics and Earthquake Engineering*, Southampton University, England, July 1982.
7. L. A. Ortiz, R. F. Scott, and J. Lee. Dynamic Centrifuge Testing of a Cantilever Retaining Wall. *Earthquake Engineering and Structural Dynamics*, 1983.
8. G. N. Richardson and K. L. Lee. Seismic Design of Reinforced Earth Walls. *Journal of the Geotechnical Engineering Division*, ASCE, Feb. 1975.
9. R. B. Nagel. *Seismic Behavior of Reinforced Earth Wall*. Master of Engineering report. University of Canterbury, Christchurch, New Zealand, 1985.
10. W. E. Wolfe and D. Rea. *Earthquake Induced Deformations in Reinforced Earth Walls*. Mechanics and Structures Department, School of Engineering and Applied Science, University of California, Los Angeles, May 1990.
11. G. N. Richardson. Earthquake Resistant Reinforced Earth Walls. *Proc., ASCE Symposium on Earth Reinforcement*, Pittsburgh, Pa., 1978.
12. B. L. Kutter, J. A. Casey, and K. M. Romstad. Centrifuge Modeling and Field Observations of Dynamic Behavior of Reinforced Soil and Concrete Cantilever Retaining Walls. *Proc., 4th U.S. National Conference on Earthquake Engineering*, Vol. 3, EERI, May 20–24, 1990, Palm Springs, Calif., pp. 663–672.
13. J. A. Casey, D. Soon, B. L. Kutter, and K. M. Romstad. Modeling of Mechanically Stabilized Earth Systems: A Seismic Centrifuge Study. *Proc., ASCE Geotechnical Engineering Congress*, Geotechnical Special Publication 27, Vol. 2, Boulder, Colo., June 1991, pp. 839–850.
14. G. S. Chang. *Centrifugal and Numerical Modeling of Soil-Pile-Structure Interaction due to Seismic Activity*. Ph.D. dissertation. University of California, Davis, 1991.

Publication of this paper sponsored by Committee on Transportation Earthworks.

Response of Tension Piles to Simulated Seismic Motion in Saturated Fine Sand

MICHAEL W. O'NEILL, CUMARASWAMY VIPULANANDAN, AND MAURICIO OCHOA

A laboratory model study of tension piles subjected to simulated seismic loading through the soil was conducted. The objective of the study was to assess the magnitude of biased (static) tension load that can be sustained by displacement-type piles driven into medium dense, saturated fine sand during seismic events typical of those in Southern California. The prototype pile characteristics modeled in this study consisted of a closed-end, or plugged, impact-driven pipe pile, 20 to 40 in. in diameter, 20 to 40 ft long (or top 20 to 40 ft of a longer pile). An acceleration record for a particular magnitude 5.8 seismic event, the Oceanside, California, earthquake of July 13, 1986, measured at an offshore deep soil site 45 mi (74 km) from the epicenter, was selected and scaled to higher magnitudes to simulate more severe earthquake loading conditions on the pile. A 21-in.-high by 20-in.-diameter pressure chamber was used to contain the saturated soil and to simulate isotropic effective stresses and drainage conditions. The model test pile was an instrumented, steel, closed-end tube, 1 in. in diameter and 16 in. long, that was loaded through a spring-mass system to simulate feedback from a simple superstructure with a known natural period. Pile-head movements, pile load versus depth, and pore water pressures in the soil were measured during the experiments. Both the simulated seismic record and soil permeability were scaled to model the effect of drainage distance and its effect on pore water pressure generation and dissipation. Contour plots of stability conditions (sustained tension resistance and small pile movements), mobility conditions (sustained resistance associated with substantial pile movements), and failure conditions (total loss of pile capacity) for the model pile were developed from the tests. The effect of distance between the pile and event epicenter on stability was considered analytically.

A laboratory study of tension piles in submerged, fine sand subjected to simulated seismic loading has been conducted to assess the magnitude of biased (static) tension load that can be sustained by displacement-type piles. Biased tension loads may be present on piles that support structures subjected to large static overturning moments including hydraulic structures and bridges, tension-leg offshore platforms, and pile-anchored floating bridges. The prototype pile characteristics modeled in this study consisted of a closed-end, impact-driven pile, 20 to 40 in. in diameter, 20 to 40 ft long (or top 20 to 40 ft of a longer pile), and driven in a fine, uniform, clean siliceous sand at relative densities ranging from 55 to 70 percent. These relative densities were selected to represent the range for medium dense sand. Values biased toward the high side of the normal range for medium dense sands (33 to 67 percent) were used because the test sand was not aged and

would behave similarly to aged prototype sand at relative densities lower than that of the test sand.

The soil-pile model system was excited to simulate the vertical, horizontal, and combined vertical and horizontal components of an earthquake at a deep soil site under water. The rationale of the investigation was that the interaction of the excited soil and the pile would induce shearing stresses at the interface of the soil and pile, which, along with the stress waves in the soil itself, would produce excess pore water pressures and perhaps reductions in effective stress at the pile wall because of grain reorientation in the sand. Such phenomena would reduce the uplift capacity of the pile and either cause the pile to pull out under a biased tension load lower than its static axial capacity or produce a permanent postevent reduction in uplift capacity. The practical problem that originally motivated the study was concern for the stability of pile foundations for tension-leg offshore platforms. The results are also applicable to floating bridge foundations in deep water.

MODELING

Event Selection

The phenomenon was studied by selecting a particular seismic event in which acceleration time histories had been measured at an offshore deep soil site. The event chosen for study was the Oceanside, California, event of July 13, 1986 (1), a magnitude 5.8 earthquake whose epicenter was 45 mi (74 km) southeast of the instrumentation site. Accelerations were measured on the shallow sea floor, 250 ft below mean sea level. Low peak accelerations of the vertical component (3 to 4 mg) and the combined horizontal component (20 to 28 mg) (Figure 1) during this event suggested that piles would not suffer a loss of capacity. Therefore, the actual earthquake was scaled to higher magnitudes (i.e., Richter magnitude 8.0 for the vertical component of motion and Richter magnitudes of 7.0, 7.5, and 8.0 for the resultant component of horizontal motion).

The earthquake scaling procedure involved (a) transforming the time history of the component of motion into the frequency domain, (b) scaling the Fourier amplitude spectrum of the original time history to match a spectrum, termed the "target spectrum" (2), that would represent a higher magnitude event (for instance, magnitude 8.0), and (c) transforming the scaled spectrum back into the time domain while preserving the phase relationship of the unscaled (original)

M. W. O'Neill and C. Vipulanandan, Department of Civil and Environmental Engineering, University of Houston, Houston, Tex. 77204-4791. M. Ochoa, McBride-Ratcliff and Assoc., 7720 Langtry, Houston, Tex. 77040.

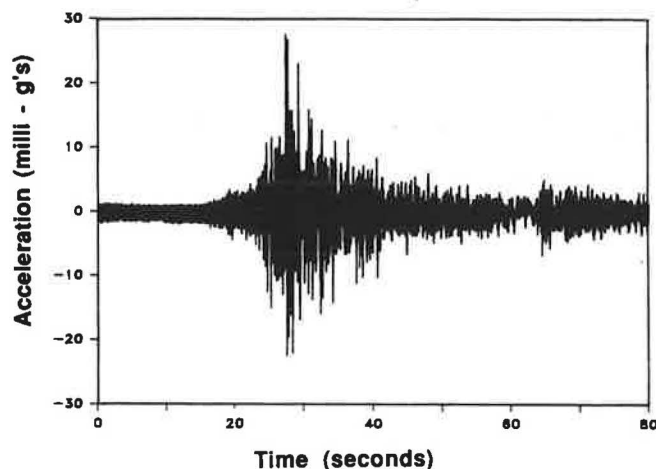


FIGURE 1 Combined X and Y components of Oceanside earthquake of July 13, 1986 ($M = 5.8$).

record to maintain the same earthquake source mechanism. The selection of the target spectrum depended on the level of intensity (in terms of the modified Mercalli intensity), distance from the epicenter, approximate soil conditions, and direction of motion (vertical or horizontal). Original, target, and scaled (computed) spectra for the combined horizontal motion (magnitude 8.0) are shown in Figure 2. Because the duration of significant shaking is influenced by the magnitude of the seismic event, the time segment of strong shaking was doubled (with duplicate acceleration histories) to produce a duration of strong shaking consistent with the magnitude of the target spectrum. Finally, the scaled acceleration time history (Figure 3) was converted to a displacement time history that was used to control the motion of a pressurized test chamber into which the model pile was driven.

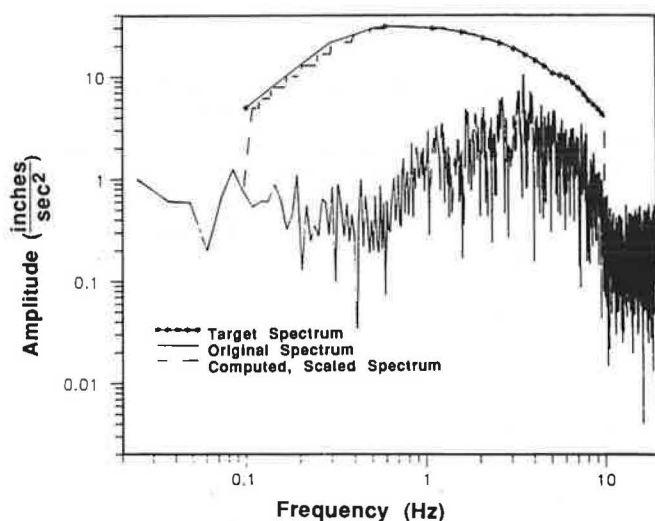


FIGURE 2 Original, target, and computed (scaled, $M = 8.0$) spectra (horizontal motion) of Oceanside earthquake.

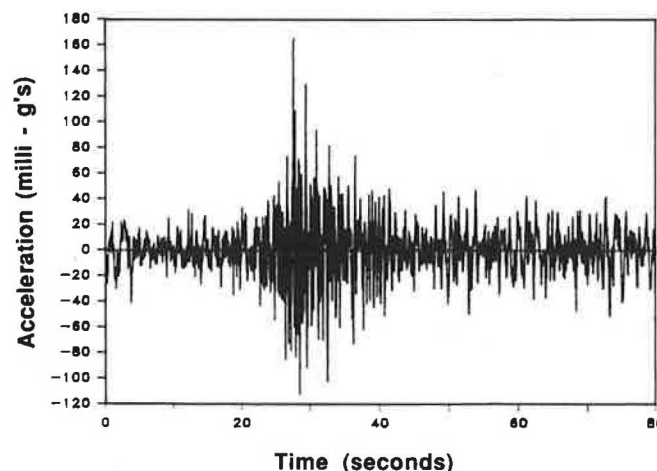


FIGURE 3 Combined scaled ($M = 8.0$) horizontal record of Oceanside earthquake.

Testing Apparatus

A closed-loop hydraulic testing machine (Figure 4) was used to apply the programmed seismic motion to the soil contained in a pressurized test chamber. The chamber was the largest chamber that could be accommodated by the machine: 21 in. high and 20 in. in diameter (Figure 5). Preliminary studies were conducted with buried accelerometers in the chamber to ensure that the shear strain amplitudes produced within the soil by the motion of the chamber within the testing machine were equal to those that would have occurred in situ during the simulated seismic event.

The model test pile, which was driven by impact into pressurized, submerged, very fine sand in the chamber, was a steel, closed-end cylindrical tube, 1 in. in diameter, 16 in. long, and with a wall thickness of 0.05 in. The pile was instrumented internally with three levels of strain gauges to sense axial load distribution.

Movement at the pile head was monitored by a single LVDT. Two miniature pore water pressure transducers were also buried within the chamber to sense the buildup of pore water pressure in the soil 0.5 in. (1 radius) from the wall of the pile ("near field") and 6.0 in. (12 radii) from the pile wall ("far field"). A flexible cable was attached to the head of the pile, which protruded through a port in the chamber, through which biased (static) tension load was applied continuously by means of a deadweight-and-spring system. The purpose of the weight-and-spring loading system was to simulate the presence of a simple superstructure of known natural frequency, such as a floating structure, that feeds axial load back into the pile during the seismic event as the pile's motion excites the structure. The spring constant was varied so that the natural frequency of the loading system (simulated superstructure) varied from 0.1 sec to 1.0 sec. This period varied from lower than to higher than the predominant period of the simulated, time-scaled seismic event. The principal effect of superstructure feedback was to provide excursions of pile head load of typically 10 to 20 percent during shaking. During some vertical-motion-only shaking tests with high initial biased loads, these

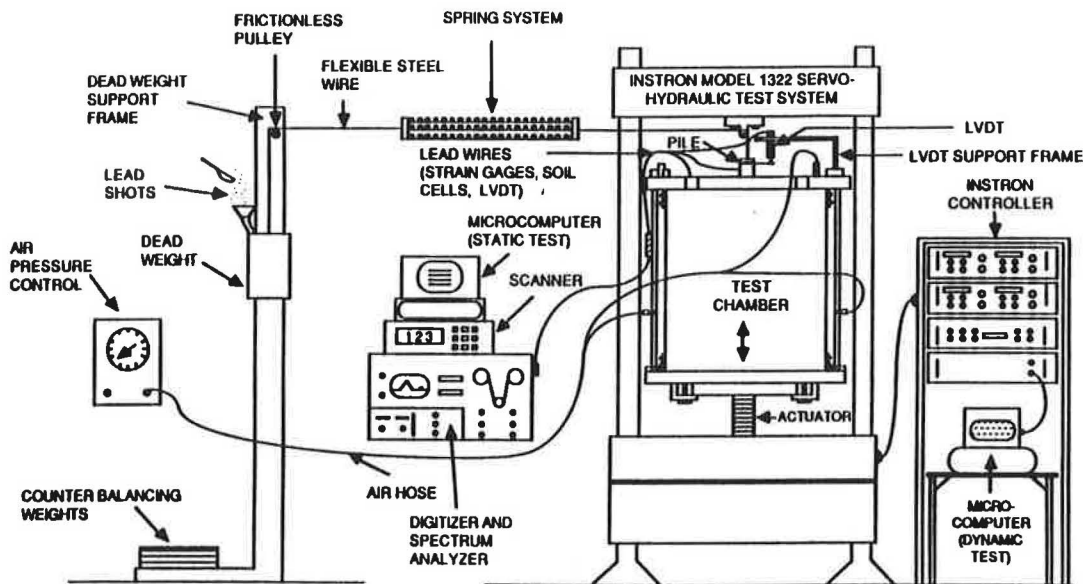


FIGURE 4 Schematic of overall testing arrangement.

excursions were sufficient to cause pile pullout without the generation of pore water pressure within the soil.

The simulated seismic records were applied through the base of the chamber: through vertical motion to simulate the vertical component of seismic motion, through rotary motion to simulate the resultant horizontal component, and through a combination of vertical and rotary motion to simulate the entire event.

Model to Prototype Scaling

In addition to scaling the magnitude of the earthquake upward, it was also desirable to establish geometric scaling between the model and prototype. Such scaling was then combined with the earthquake scaling to produce reasonable similitude between the model tests and the response of a pile under biased tension loading during a strong seismic event at a deep soil site. The analysis performed to establish geometric similitude rules was partially based upon the characteristic of the chamber that known effective stresses can be applied at the boundaries. This analysis included both static and dynamic components.

Static scaling rules were used to establish both a length scale, N , and values for chamber pressures. Two applied isotropic chamber pressures, 2.5 and 5.0 psi, simulated a range of depth-average, ambient horizontal effective soil stresses corresponding to pile penetrations of 20 and 40 ft, respectively (3). The pressure and penetration scaling is illustrated in the following, in which L = pile penetration, σ'_h = horizontal effective stress, m = model, p = prototype, K_0 = lateral earth pressure coefficient, and γ' = buoyant unit soil weight:

Let $L_p = 40$ ft, and let the length scale factor $N = 40$; let σ'_h at $0.67 L_p = \sigma'_h$ at $0.5 L_m$ (horizontal effective stresses against the prototype and model piles at the depth of mean load transfer assuming a triangular distribution of lateral stress with depth in the prototype and a constant value in the model); let the prototype sand have $K_{op} = 0.48$; and let γ' (model and prototype) = 55 pcf.

Then σ'_h at $0.67 (40 \text{ ft}) = 0.67 (40 \text{ ft}) 55 (0.48) = 708 \text{ psf} = 5.0 \text{ psi} = \text{chamber stress}$, and $N L_m (0.5) (5 \text{ psi}) = L_p (0.67) (5 \text{ psi}) = 40 (0.67) (5)$, from which $L_m = 1.33 \text{ ft}$.

Since $N = 40$, the diameter of the prototype pile is 40 in. A similar procedure can be followed to show that an isotropic

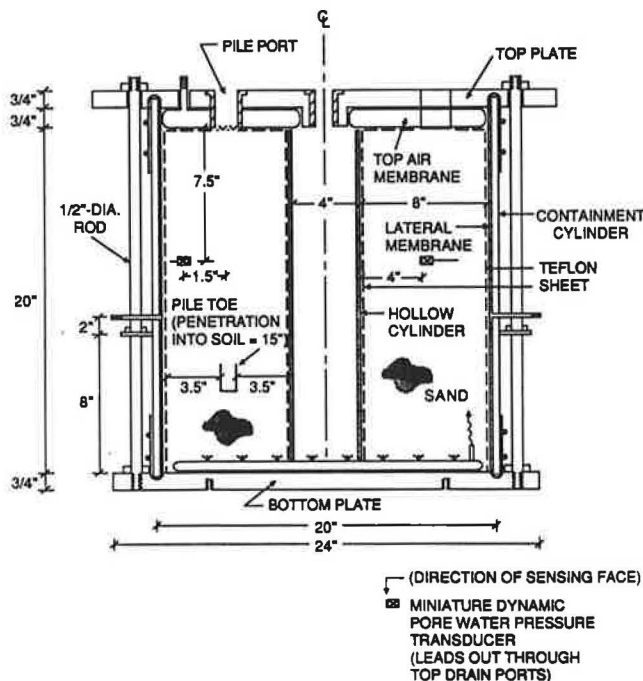


FIGURE 5 Schematic elevation of test chamber (rotational motion).

chamber pressure of 2.5 psi and $L_m = 1.33$ ft (16 in.) models a 20-ft prototype pile with a diameter of 20 in.

It was also desirable to scale time and soil hydraulic conductivity characteristics to affect model-to-prototype similitude with respect to stress changes and pore water pressure diffusion rates during application of the modeled seismic event. The test chamber drains only at the top surface of the sand, which was considered characteristic of prototype conditions. The choice of the scaling factor for time was conditioned simultaneously by two practical considerations: (a) the capabilities of the available closed-loop hydraulic testing machine to track the applied displacement time history and (b) the finest soil (and lowest hydraulic conductivity) that could be found that did not possess cohesive characteristics and that could be saturated by gravity, as required by the design of the testing chamber. A mixture of a very fine sand and finely ground glass beads, termed microfine sand, was used as the model sand. The two time scaling factors resulting from dynamic stress and diffusion considerations were both approximately equal to 7. That is, time was compressed by a factor of 7 and accelerations were multiplied by a factor of 7. Details of time scaling are described by O'Neill et al. (3). Time scaling resulted in simulated superstructures with natural frequencies of 0.7 to 7 sec. By using microfine sand (having a coefficient of permeability of 1.25×10^{-3} cm/sec) as the model sand and a time scaling factor of 7, the coefficient of permeability of the prototype soil was approximately 10^{-2} cm/sec.

During most of the tests involving only simulated vertical soil motion (Phase 1), the dynamic scaling rules were not observed. However, a few tests were conducted following these rules to verify conclusions drawn from the majority of the tests in Phase 1. In tests focusing on the behavior of piles subjected to simulated horizontal motion and combined horizontal and vertical motion (Phase 2), these scaling rules were followed for all shaking tests.

TEST PROCEDURES AND RESULTS

Estimation of Static Capacity

A relation between penetration resistance during driving and static uplift capacity obtained from loading tests was derived experimentally to infer the percentile of the static capacity applied by any given biased load in the simulated seismic loading (dynamic) tests. Dynamic tests were performed under conditions identical to those that existed in the static tests by applying the magnitude-scaled or magnitude-and-frequency-scaled displacement time histories for the selected seismic event to the soil while the pile was held under biased uplift load. For those piles that did not fail during the simulated seismic event, static loading was performed to failure after the simulated event to define the postevent capacity.

Typical Results

A total of 44 tests were conducted by varying the mode of the loading, the intensity of the scaled earthquake, the magnitude of the biased static load, and the natural frequency of the simulated superstructure. Time history measurements of

(a) load on the pile at three locations (the pile head, a depth of 7 in., and 1.0 in. above the pile toe), (b) pore water pressures for near and far fields, and (c) pile head movement were made for all tests in the program. Measurements for a typical test in which the pile was completely pulled out of the chamber during the simulated seismic event ($M = 8.0$, horizontal and vertical components applied) are shown in Figures 6–8. The time scale shown is the actual test time. In a prototype the time values would be multiplied by 7. In that test, the loss of capacity produced by the generation of excess pore water pressure coupled with the dynamic load excursion on the pile head of about 10 percent of the static bias combined to produce complete and catastrophic failure just at the completion of shaking. Liquefaction (manifested physically by sand boiling) took place about 2 sec after completion of the simulated seismic event (14 sec in the prototype).

The failure mechanism of the pile during an event with strong horizontal shaking can be explained as follows. Shear-

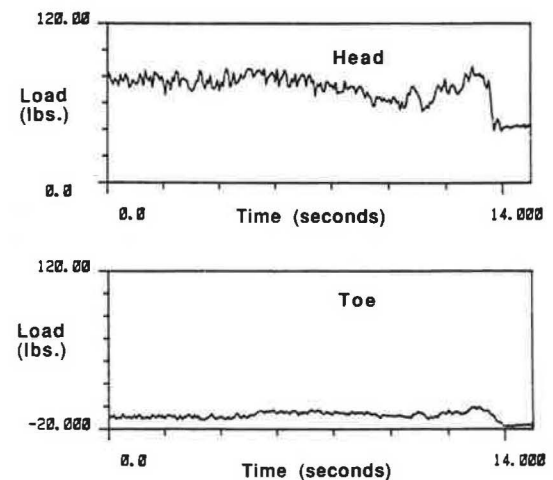


FIGURE 6 Time history measurements of dynamic load on pile for a typical test.

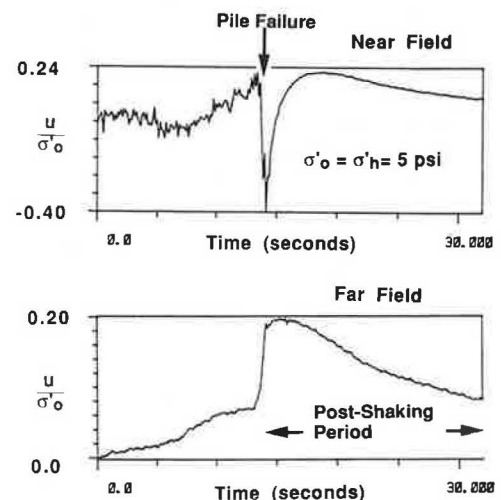


FIGURE 7 Time history measurements of near and far field pore water pressures for a typical test.

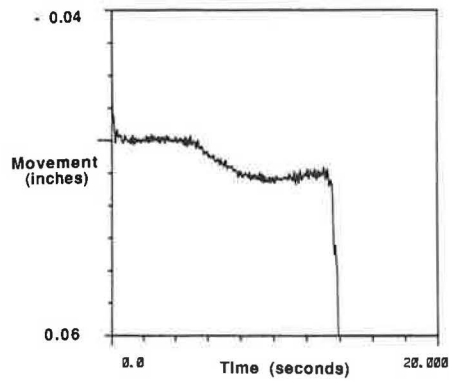


FIGURE 8 Time history measurements of pile head movement for a typical test.

ing strains in the soil generated primarily by the sudden repetitive pullouts of the pile (in response to the superstructure feedback) and additional shearing strains in the soil generated by the horizontal component of the seismic event induced buildup of pore water pressures in the soil to a level high enough to promote significant degradation of skin friction through reduction of effective normal stresses and to allow the pile to displace upward. This action took place before liquefaction could occur in the free field. Evidence exists that failure started at or near the toe of the pile and progressed rapidly up the pile. Once the pile moved significantly upward, the effective stress in the soil beneath the toe was reduced to the point at which the soil liquefied under the toe, and liquefaction spread rapidly into the mass of soil around the pile. This occurrence has important implications relative to potential rapid progressive failure in pile groups, particularly where the piles are short.

No failures were observed under a purely vertical component of loading unless the static biased load plus the feedback load from the superstructure became equal to the static uplift capacity of the pile. This observation is consistent with the observation that no excess pore water pressures developed before pullout failure in the vertical-motion-only tests. Therefore, the horizontal component of motion is by far the most destructive.

INTERPRETATION

Pile Behavior During Seismic Event

On the basis of the experimental results, interpreted contour plots were developed for stability conditions (sustained load and small pile movement), mobility conditions (sustained load associated with substantial pile movement), and failure conditions (total loss of pile capacity) for a displacement pile driven in medium dense submerged sand with a coefficient of permeability of 10^{-2} cm/sec, loaded with a biased tension load, and subjected to a simulated seismic event that occurred 45 mi (74 km) from the earthquake epicenter (Figures 9–11). In these plots, the number in parentheses represents the total measured (unscaled) pile movement during shaking. By inspection of all static tests, it was judged that a pile movement

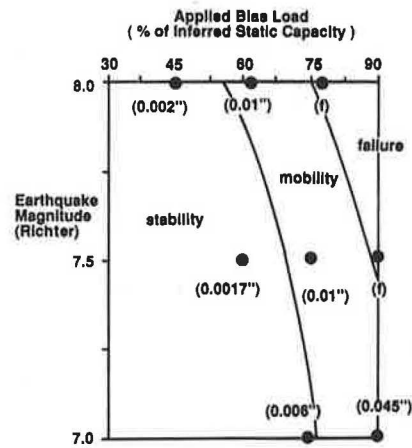


FIGURE 9 Stability, mobility, and failure conditions; horizontal loading; confining pressure: 2.5 psi; epicentral distance: 74 km; relative density: 55 percent.

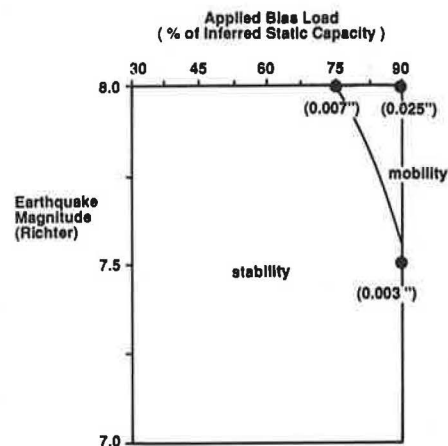


FIGURE 10 Stability and mobility conditions, horizontal loading, confining pressure: 5 psi, epicentral distance: 74 km, relative density: 55 percent.

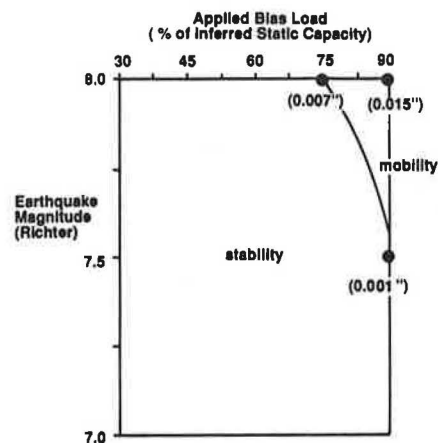


FIGURE 11 Stability and mobility conditions, horizontal loading, confining pressure: 2.5 psi, epicentral distance: 74 km, relative density: 70 percent.

of 0.007 in. (movement of 0.05 in. in the prototype based on a dynamic scaling factor of 7) represented an upper bound to ensure pile stability, and piles that moved less than that amount vertically were judged stable. Movement in excess of 0.007 in. but less than total extraction represented a "mobility" condition between stability and complete failure. On the basis of this criterion, the contour lines separating stability and mobility conditions were drawn. The contour line between failure and mobility conditions was simply drawn by joining approximately the points in the plot in which failure was visually observed, applying judgment in recognition of the coarseness of the grid.

The effect of distance between the pile site and event epicenter on stability and mobility conditions is also considered in Figure 12, which applies to a relative density of 55 percent and chamber pressure of 2.5 psi (simulated toe depth of 20 ft). Ratios of peak ground accelerations for distances of 15 mi (25 km) and 30 mi (50 km) to peak ground accelerations for the distance of 45 mi (74 km), for example, $a_g^{25 \text{ km}}/a_g^{74 \text{ km}}$ [using the predictive attenuation equation proposed by Joyner and Boore (4)], were used to multiply the measured pile movements given in Figure 9. The criterion of maximum pile movement of 0.007 in. to ensure pile stability was then used to define the contour line between stability and mobility conditions.

Postevent Pile Capacity

The results of static uplift tests conducted to failure after the simulated seismic event on piles that did not fail after being subjected to horizontal or combined motion are summarized in Figure 13. Included in that figure are the results of tests conducted at initial soil relative density of 55 percent. It is obvious that the strong motion produced a permanent loss of capacity that varied from very minor ($M = 7$) to very significant ($M = 8$ with loads above 60 percent of static capacity).

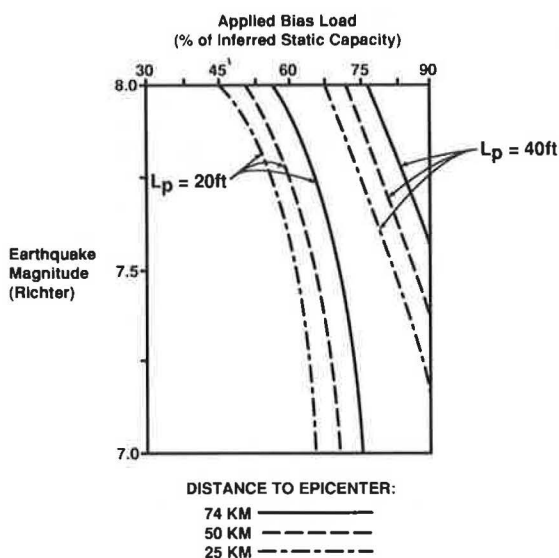


FIGURE 12 Stability-mobility contours for variable epicentral distance (relative density = 55 percent).

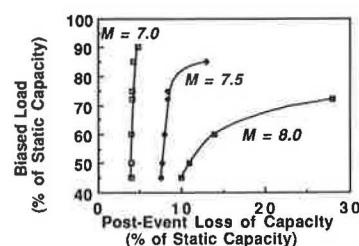


FIGURE 13 Loss of static capacity following strong ground motion (relative density = 55 percent).

DESIGN INFERENCES

Figures 9–12 suggest a design hypothesis for piles for ordinary conditions at medium dense sand sites in which the superstructure is not assumed to be ductile, which is a superstructure that will fail if an individual pile fails. For piles under biased tension loads that anchor superstructures having fundamental periods near the fundamental period of seismic motion, it is desirable to maintain a "stability" condition.

For stability of short piles (≤ 20 ft long) or for the upper 20 ft of longer, flexible piles in loose to medium dense sand (relative density = 55 percent) in which progressive failure is possible, it is suggested that the static biased load plot on or to the left of the appropriate contour line for $L_p = 20$ ft in Figure 12 (derived from chamber pressure of 2.5 psi, which simulates mean effective stresses over the top 20 ft of the soil profile). For example, if the design event is of Richter Magnitude 7.75 and the epicentral distance is 50 km, it is observed in Figure 12 that the stable static biased load that can be sustained for $L_p = 20$ ft is 60 percent of the static uplift capacity of the pile. Stated in other terms, the pile should be designed for a factor of safety against pullout of $1/0.60 = 1.67$ times that which would exist for nonseismic design, provided that other factors, such as hydraulic loading simultaneous with seismic loading, are not significant.

For $L_p = 40$ ft (or the upper 40 ft of longer piles) the contour lines separating mobility from stability in Figure 12 occur at higher normalized biased loads. Such lines could be considered for designing long, rigid piles in which progressive failure cannot occur. It was not possible to develop contours of stability-mobility for varying epicentral distances for $D_r = 70$ percent, because not enough tests were conducted at high biased loads in the chamber when that relative density was employed. However, one can use Figure 11 to ascertain the permissible static biased load for a 45 mi (74 km) (or greater) epicentral distance. This figure indicates stability for all Richter magnitudes up to 8 provided that the added factor of safety against static uplift capacity is 1.33 or higher. Further research is clearly needed at smaller epicentral distances in medium dense sands, for longer piles, and for nondisplacement piles.

Phenomenologically, it is clear from a comparison of Figures 10 and 11 that the pile foundation of a biased-tension-loaded bridge or hydraulic structure should consist of fewer, longer piles rather than more, shorter piles to develop the maximum resistance to pullout failure during earthquakes.

This design hypothesis is based on the assumption that the magnitude of the structural feedback forces has been modeled correctly in this study for a particular case. This will have been correct only if the superstructure behaves as a simple mass-spring system that responds only to the vertical motion of the pile. Other sources of dynamic superstructure loading, such as wave and inertial loadings, may cause the magnitude of pile loading to be different from the simple feedback loading reproduced in these experiments. In the absence of information on this effect, it is suggested that the added factor of safety be applied not to the static biased load but rather to the sum of the static biased load and the peak dynamic load applied to the pile by the superstructure during the seismic event.

CONCLUSIONS

The following conclusions have been drawn from this study:

1. For the earthquake studied, the capacity of the soil to sustain applied uplift loads from a driven displacement pile was not substantially affected by the action of the vertical component of the simulated seismic event. However, the pile motion produced feedback in the simple mass-spring structure to which it was attached, which periodically increased the load on the pile during the simulated event. Additional loading as a result of superstructure feedback produced failure for the case of applied high-biased loads (90 percent of the pile's static capacity).
2. When the combined horizontal component of motion was added, both superstructure feedback and increased pore water pressures developed, resulting in the behavior described in Figures 9–12.
3. The capacity of the soil to sustain static uplift loads after the seismic event was not affected significantly by the action of the horizontal component of a magnitude 7.0 event. Re-

ductions in capacity occurred in stronger events, however, as shown in Figure 13.

4. The interaction of the soil and overlying water was not investigated in this study. For deep water sites, further loss of capacity may occur because of pore water pressure buildup from this effect.

ACKNOWLEDGMENTS

This study was performed by the Department of Civil and Environmental Engineering of the University of Houston under contract to the Minerals Management Service; U.S. Army Engineer Waterways Experiment Station; Exxon Production Research Company; Unocal, S & T Division; Amoco Production Company; and Texaco, U.S.A. The authors express their appreciation to the sponsors of this project.

REFERENCES

1. G. E. Sleaf and D. Engi. Seafloor Response for Two Southern California Earthquakes. *Proc., 1987 SEM Spring Conference on Experimental Mechanics*, Houston, Tex., pp. 747–753.
2. M. D. Trifunac. Preliminary Empirical Model for Scaling Fourier Amplitude Spectra of Strong Acceleration in Terms of Modified Mercalli Intensity and Recording Site Conditions. *Earthquake Engineering and Structural Dynamics*, Vol. 7, 1979, pp. 63–74.
3. M. W. O'Neill, C. Vipulanandan, and M. Ochoa. *Response of Tension Piles to Simulated Seismic Motion in Saturated Fine Sand*. Report UHCEE-90-09, Department of Civil and Environmental Engineering, University of Houston, Houston, Tex., 286 pp.
4. W. B. Joyner and D. M. Boore. Measurement, Characteristics and Prediction of Strong Ground Motion. State-of-the-Art Report. In *Proc., Specialty Conference on Earthquake Engineering and Soil Dynamics II*, ASCE, June 1988, pp. 43–102.

Publication of this paper sponsored by Committee on Foundations of Bridges and Other Structures.

Dynamic Centrifuge Modeling of Geotechnical Structures

BRUCE L. KUTTER

The basic principles of dynamic centrifuge model testing are explained and some advantages and disadvantages of centrifuge modeling are described. Two examples of centrifuge model tests relevant to the performance of transportation structures during earthquakes are described: (a) a study of Struve Slough Bridge, which collapsed in the Loma Prieta Earthquake, and (b) mechanisms of liquefaction and development of sand boils. Two themes emerged from the examples cited. First, the results from centrifuge testing often provide an improved understanding of the deformation and failure mechanisms. Second, the improved understanding provides a basis for the development of simplified but adequate methods of analyzing full-scale geotechnical structures.

The similitude of the scale model testing is significantly enhanced in a centrifuge because the increased self weight produces identical stresses in model and prototype. Schofield (1) summarizes the principles of dynamic centrifuge modeling. Two recent volumes (2,3) containing about 80 papers indicate the broad scope of applications of centrifuge modeling.

The deformation of an element of soil depends on stress, strain, and time. The behavior of elements of soil under three-dimensional stress states and under cyclic loading is not fully understood. Additional questions arise regarding prediction capabilities for complex boundary value problems (e.g., embankments, bridge abutments, dams, pile foundations, retaining walls, consolidation, and seepage through aquifers) under complex loading conditions such as an earthquake. We have little data to show that our existing design procedures result in safe and economical designs. Large earthquakes such as the 1906 San Francisco earthquake occur so infrequently that it is difficult to obtain full-scale data to study them.

Direct modeling, in which researchers attempt to exactly simulate a particular prototype, has not often been the chosen approach of physical modelers. The model tests are usually treated as real events in themselves, and the results are interpreted accordingly. Using this approach, the centrifuge can provide data to directly observe failure mechanisms, calibrate design or analysis procedures, and conduct parametric studies. Physical models can be subjected to extreme loading conditions to study the response of structures during major earthquakes. Model tests are repeatable and economical, unlike the failures caused by real earthquakes.

Comparisons with full-scale field data are undoubtedly the most direct means of verification of a design or analysis procedure. No assumptions regarding particle size effects, strain rate effects, or the effects of confining pressures are needed

if the actual prototype is tested. Full-scale data may be obtained in controlled field tests or by back analysis of the behavior or failure of an uncontrolled event. Difficulties with full-scale data are their cost and nonrepeatability. In the case of earthquake loading, the earthquakes studied are usually smaller than the design earthquake.

The high cost of full-scale tests precludes the possibility of conducting many experiments that cover the full range of variation of all important parameters. For example, laterally loaded piles may be in groups with different geometry, they may penetrate to various depths through layered soils, and they may be loaded with inclined eccentric loads. The matrix of possible parameters is very large compared with the number of full-scale tests that may be conducted.

In a sense, obtaining data for verification of analysis procedures by back analysis of the failure of a prototype is even more expensive. The failures usually involve significant property damage and loss of lives. Furthermore, the data obtained from unplanned failures are often difficult to interpret because of the uncertainty in determining the exact conditions before failure, the precise nature of the loading causing failure, and the absence of sufficient instrumentation to provide detailed data regarding the sequence of important events leading to the failure.

Model tests provide the luxury of repeatability. The generality of findings based on full-scale data is unknown. Changes in structure dimensions, soil profiles, and earthquake motion characteristics have a significant impact on response, and the impact cannot be adequately assessed by analysis of a few full-scale events.

Soils have stress-dependent stiffness, strength, and dilatancy. Geotechnical models are often tested on a centrifuge to obtain stresses in a small model identical to those that occur in a large prototype. Testing models on a centrifuge accounts for the stress dependency, improving the similarity between model and prototype. This makes extrapolation of data to field situations more accurate than is possible for scale model tests conducted in earth's gravity.

The centrifuge also permits certain gravity-driven phenomena to be accelerated in time. For example, consolidation of a clay layer that takes 1 year is modeled in about a 1-hr test at a centrifugal acceleration of 100 g.

CENTRIFUGE MODELING LAWS

The scale factor for length may be expressed as $L^* = 1/N$. The asterisk on a quantity refers to the scale factor for that

Department of Civil Engineering, University of California, Davis, Calif. 95616.

quantity. Hence, L^* is the ratio of length in the model to length in the prototype. N is an arbitrary scale factor. In geotechnical centrifuge modeling, the vertical and horizontal length scale factors are identical.

When dealing with coarse-grained soils, it is sometimes suggested that the size of the particles should be scaled. As pointed out by Bolton and Lau (4), however, fine material at a similar density is likely to be stronger and more dilatant than coarse material. Partly for this reason, the same soil (at the same density and water content) is used in model and prototype. This also ensures that intergranular contact forces will be the same in model and prototype (since both are subject to the same stresses), helping to ensure that the soil properties will be the same in model and prototype. If the same soils are used in model and prototype, the scale factor for density is $\rho^* = 1$.

The scale factor for gravity is $g^* = N$. That is, gravity is N times larger in the model than in the prototype. If a model is made 100 times smaller than the prototype (i.e., $N = 100$), and it is tested in a gravity field that is 100 times greater than earth's gravity, the stresses due to gravity loading would be identical in model and prototype. Of course, it is not really feasible to produce a large gravitational field, but a centrifuge can be used to provide a large acceleration field. The inertia forces produced by spinning a model around an axis are similar to the gravitational forces that develop in a large prototype.

From the scale factors for length, gravity, and density, the scaling relationships for other physical quantities such as mass, force, stress, strain, and time can be derived. For example, the scale factor for mass follows from the relation that a density times a volume must equal a mass ($m = \rho L^3$):

$$m^* = \rho^* L^{*3} = (1)(N^{-1})^3 = N^{-3} \quad (1)$$

From Newton's law of gravitation, the scale law for force is

$$F^* = m^* g^* = (N^{-3})(N) = N^{-2} \quad (2)$$

The scale factor for stress must then be

$$\sigma^* = F^*/L^{*2} = (N^{-2})(N)^2 = 1 \quad (3)$$

This confirms that if the same materials are used in model and prototype, and if gravity is increased in the same proportion that length dimensions are reduced, the stresses obtained in model and prototype will be identical.

If strains within the model are only a function of the stresses, it follows that the strains will also be identical in model and prototype:

$$\varepsilon^* = 1 \quad (4)$$

Of course, the strength and stiffness of a soil are not only a function of the current stresses in the soil; they are also a function of the stress history. In the development of a model, then, it is necessary to simulate the stress history. This may be accomplished by appropriately preconsolidating a soil layer in the laboratory and attempting to simulate the complete construction sequence during the testing of a centrifuge model.

If the relationship between stress and strain is time dependent, the scaling of stresses and strains is more difficult. The assumption of rate-independent mechanical properties is embedded in the preceding derivation of scale factors.

Also, embedded in terms such as stress and strain are the assumptions of continuum mechanics; particle size effects are not considered. It seems plausible that as long as the ratio of model dimensions to the particle dimensions is "very large," the soil may be assumed to be a continuum. But how large is "very large"? The answer to this question depends on the type of problem being studied; ideally it would be answered for every model study.

The scale factors for time are discussed in the following for three important categories of problems: static, diffusion, and dynamic. In a static problem (for example the settlement of a footing on dry sand), the scale factor for time is not important. The rates of application and duration of loading need not be precisely scaled.

In a diffusion problem (such as consolidation, heat flow, or contaminant transport) the problem is governed by a differential equation of the form

$$\partial u / \partial t = c_v \partial^2 u / \partial z^2 \quad (5)$$

In Equation 5, u may represent pore pressure, temperature, or pollutant concentration. t represents time, and c_v is a material property: the coefficient of consolidation or diffusion coefficient. z represents a spatial coordinate that scales like any length dimension. The pore water pressure is a hydrostatic stress, and it follows the previously derived scale law for stress: $u^* = \sigma^* = 1$. By inspection of Equation 5,

$$u^* t^{*-1} = c_v^* u^* L^{*-2} \quad (6)$$

$$t_{\text{dif}}^* = L^* c_v^{*-1} = (N^{-1})^2 c_v^{*-1} = N^{-2} c_v^{*-1} \quad (7)$$

If the same materials are used in model and prototype, c_v will be the same in model and prototype, and $c_v^* = 1$. Therefore, for diffusion problems,

$$t_{\text{dif}}^* = N^{-2} \quad (8)$$

The time required for diffusion processes to occur in the model is N^2 times less in the model and prototype.

Alternatively, the model can be thought of as a simulation of a prototype with a different soil, one with a higher diffusion coefficient. In other words, the diffusion coefficient scales as $c_v^* = N^{-1}$. Fine (impermeable) sand can be thought to represent a coarse sand, or a model with silicon oil as a pore fluid may represent the same soil with water as a pore fluid. If c_v is scaled by a factor of N , the time scale factor for diffusion problems becomes

$$t_{\text{dif}}^* = N^{-1} \quad (9)$$

In dynamic problems it is important that the acceleration of the model increases in the same proportion as the gravitational acceleration. Therefore

$$a^* = g^* = N \quad (10)$$

TABLE 1 SCALE FACTORS FOR CENTRIFUGE MODEL TESTS

Quantity	Symbol	Units	Scale Factor
Length	L	L	N^{-1}
Volume	v	L^3	N^{-3}
Mass	M	M	N^{-3}
Gravity	g	LT^{-2}	N
Force	F	MLT^{-2}	N^{-2}
Stress	σ	$ML^{-1}T^{-2}$	1
Moduli	E	$ML^{-1}T^{-2}$	1
Strength	s	$ML^{-1}T^{-2}$	1
Acceleration	a	LT^{-2}	N
Time (dynamic)	t_{dyn}	T	N^{-1}
Frequency	f	T^{-1}	N
Time (diffusion) *	t_{dif}	T	N^{-1} or N^{-2}

The diffusion time scale factor depends on whether the diffusion coefficient (e.g., coefficient of consolidation) is scaled. If the same soil is used in model and prototype, $t_{dif}^ = N^{-2}$.

Since acceleration has units of L/t^2 ,

$$t^{*2} = L^*/a^* = N^{-2} \quad (11)$$

$$t_{dyn}^* = N^{-1} \quad (12)$$

Dynamic events occur N times faster in the model than in the prototype. Clearly, unless the coefficient of consolidation is scaled, we have different time scale factors depending on the type of phenomena that is occurring in the model. In most cases, it is clear that the problem is dominated either by dynamic loading or by diffusion. If it is so clear, a modeler simply chooses the appropriate factor. On the other hand, the liquefaction of permeable soils may result in simultaneous dynamic generation of pore pressures (due to cyclic shear strain) and dissipation of pore water pressure, which is governed by diffusion. In this case, it is necessary to scale the coefficient of consolidation. Table 1 summarizes the centrifuge scaling laws.

Figure 1 shows sketches of the shaker mounted on the small centrifuge at Davis. This figure includes a model of a bridge with a pile foundation. The container is made from aluminum and has Plexiglas side walls that permit viewing of a cross

section of the model by photography or video cameras. The shaker is mounted on a swinging platform that hangs downward in earth's gravity and gradually swings up as the centrifugal acceleration is increased. The net g -vector, due to addition of earth's gravity and the radial centrifugal acceleration, remains perpendicular to the platform, so the sample will not spill as the bucket swings up.

When the centrifuge acceleration reaches the desired level, and after the pore pressures in the sample are given sufficient time to come into equilibrium, a simulated earthquake can be triggered. At Davis, this is accomplished by pressing a key on a computer. The computer then sends the desired displacement history in analog form to an electronic servocontroller, which in turn sends command signals to the servovalve. The servocontroller receives feedback from a displacement transducer on the model container and performs corrections to compensate for errors. A typical acceleration time history and the corresponding spectral accelerations for the base motion are shown in Figure 2. This figure shows that the desired motion corresponds very well with the actual achieved base motion. The desired acceleration time history shown in Figure 2 was obtained from measured accelerations at Corralitos during the 1989 Loma Prieta earthquake. These data were integrated twice, filtered, and base line corrected to obtain the desired displacement history.

The models are typically instrumented with accelerometers, strain gauges, pore water pressure transducers, and displacement transducers. The same computer that controls the shaker also records data from the experiments. Sixteen channels can be recorded simultaneously. If desired, additional simulated earthquakes may be triggered before stopping the centrifuge. The additional earthquakes may be scaled versions of the initial motion, or they may be completely different motions, such as a sine wave, El Centro, or San Fernando earthquake simulations.

SEISMIC RESPONSE OF TRANSPORTATION STRUCTURES

Some of the recent transportation-related studies at Davis are briefly outlined: modeling of the response of the Struve Slough Bridge during the Loma Prieta earthquake and liquefaction of stratified level ground.

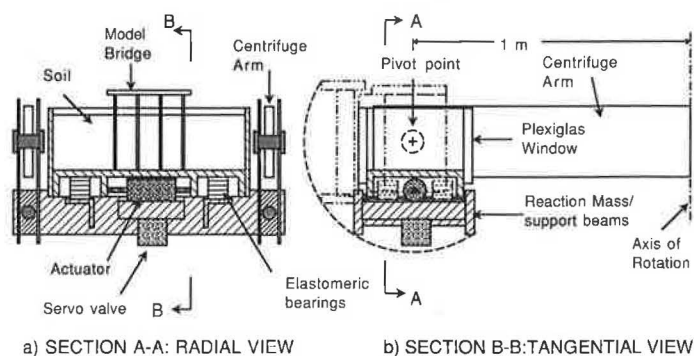


FIGURE 1 Earthquake simulator on the small centrifuge at Davis: a, view looking radially inward; b, side view showing how the bucket swings up as the centrifuge speed increases.

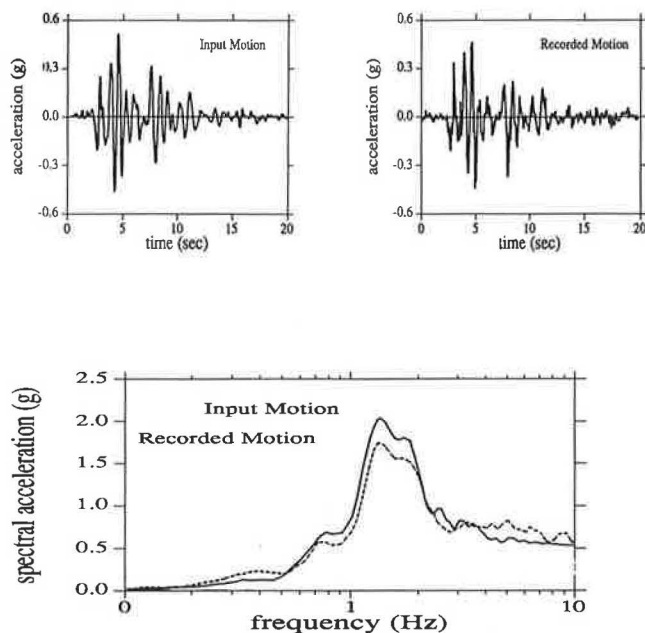


FIGURE 2 Comparison of desired and achieved accelerations: top left, desired (input) time history; top right, recorded time history; and bottom, a comparison of 5 percent damped response spectra.

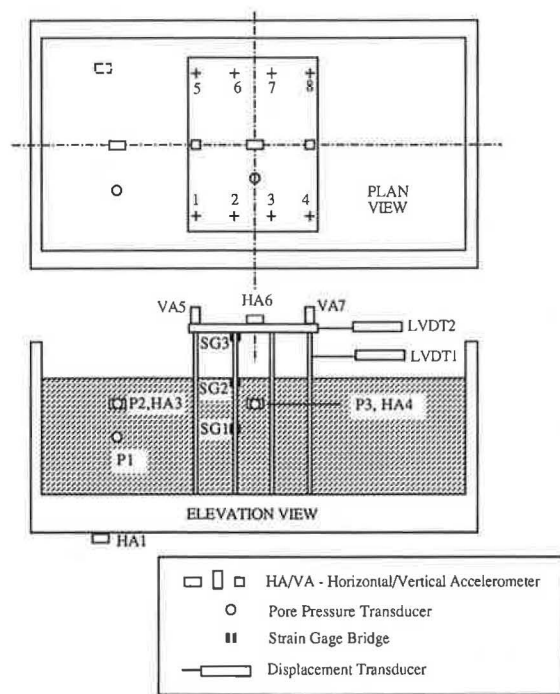


FIGURE 3 Instrument locations for model simulation of Struve Slough Bridge.

Modeling the Failure of the Struve Slough Bridge

The series of tests described in the following demonstrates how the centrifuge can be used to calibrate and develop a method of analyzing a soil-structure interaction problem. Cafe (5) describes the research on Struve Slough Bridge in more detail.

Figure 3 shows the model in the centrifuge container. This test was conducted at a centrifuge acceleration of 60 g . The spacing of the model piles is 5.1 cm (3.06 m), the diameter is 0.6 cm (0.36 m), and length is 21.3 cm (12.8 m), of which 6 cm (3.6 m) extends above the soil. (The dimensions are given as model dimensions with prototype dimensions in parentheses.) The model container is 56 cm (33.6 m) long and 28 cm (16.8 m) wide. Figure 4 shows a sketch of one bent of the actual bridge. The Struve Slough Bridge is approximately 230 m long, consisting of two separate bridges 10.4 m wide on Highway 1 in Watsonville, California. Each bridge consisted of 22 bents equally spaced at 11.3 m. The skew of the bents was not considered in the model tests. Each bent is supported by four Raymond Can step-tapered piles, which are each extended up to the bridge deck with 0.4-m diameter pile extensions. From the surface downward, the soil profile at midspan consists of 9.1 m of very soft peat with some clay, 4.4 m of soft silty clay with peat, 10.7 m of stiff silty clay, and a layer of medium dense sand with gravel (into which the piles were driven).

Preliminary foundation analyses assuming classical beam on elastic foundation theory were conducted on the prototype piles. It was found that the lateral deflections of the pile below the very soft peat layer were insignificant. It was therefore decided to physically model the piles as being fixed at the base of the peat; the model piles were screwed into an alu-

minum bar and fixed to the base of the model container. The 9.1 m of peat was the only soil layer included in the model. This soil was collected at the site in disturbed samples and placed in the model at a moisture content of 93 percent.

The model piles were made of 3.2-mm-diameter annealed stainless steel rods and covered in 6.4-mm-diameter soft rubber tubing. This composite pile design was used in order to approximately simulate the correct bending stiffness, moment capacity, and diameter of the prototype piles. The models were instrumented with accelerometers, pore pressure transducers, and displacement transducers. One pile was instrumented with three sets of strain gauges to monitor the bending of the pile at three locations.

In the Loma Prieta earthquake, one of the bridge decks completely collapsed, and some of the broken piles punched through the bridge deck. The other bridge was severely damaged. Failure of the pile extensions at the connection to the bridge deck was obvious, and it appeared that some of the

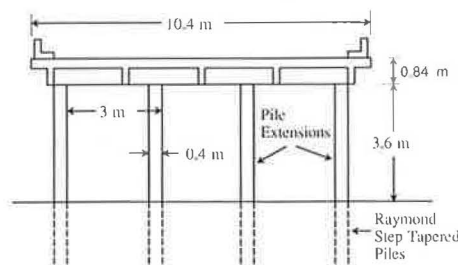


FIGURE 4 Typical cross section of the actual Struve Slough Bridge.

piles may have failed at some depth as well. Large gaps formed around the piles at the ground surface, ranging between about 12 to 25 cm near the middle of the bridge where the peat deposit was the thickest. Similar gaps were also observed to form around the piles in the centrifuge tests.

The analytical model developed to numerically predict the bridge response is shown in Figure 5. The solution was obtained using a linear finite element program called BEAM1DYN. Because of the large spacing of the prototype piles, group effects were neglected. Each pile and extension was modeled as a series of beam elements with a lumped mass. The mass of the bridge deck was attached to the top element of the pile. Viscous damping was introduced as shown at each node. The earthquake motion was introduced at the base of the piles and at springs at each node within the soil. The value of the springs was determined on the basis of an equation provided by Vesic (6).

The unique feature of the new procedure is that the input motions of the soil along the pile, $u_s(i)$, are each different. $u_s(i)$ represents the time history of displacement at the i th node. The values of $u_s(i)$ were calculated for the free field shear beam using the computer program SHAKE (7). A motion of the base of the centrifuge model container obtained from one of the centrifuge model earthquakes was input to a SHAKE analysis of a layer of peat. The analysis provided the acceleration time history at several points within the layer. These accelerations were integrated twice to obtain a displacement record, and after appropriate baseline corrections the displacement history was used as input to BEAM1DYN.

The Young's modulus of the peat (based on a variety of tests) was taken to be 110 kPa, and the Poisson's ratio was assumed to be 0.3. The unit weight of the peat was only 10.3 kN/m³. Figure 6 compares the displacement of the pile extension relative to the base motion measured in the centrifuge test (LVDT1) and the value predicted by BEAM1DYN using the input motion shown in Figure 2. The peak values of the displacement are reasonably predicted, but the frequency content is not precisely matched. The magnitude of displacement

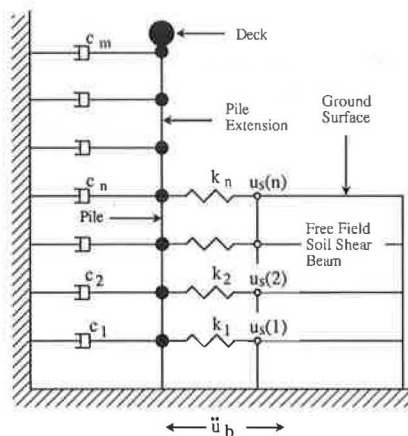


FIGURE 5 Schematic representation of the analytical model used in the computer program BEAM1DYN to predict the response of the Struve Slough Bridge model.

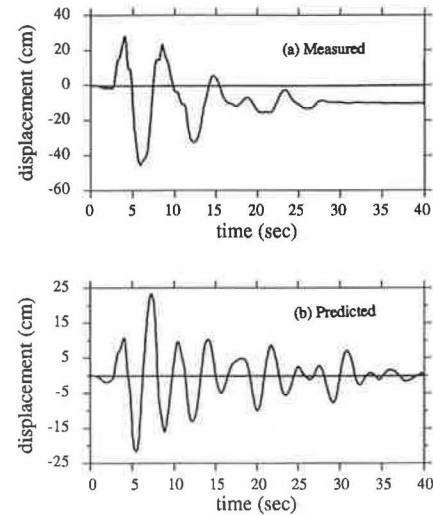


FIGURE 6 Comparison of predicted and measured displacement response: a, measured in the centrifuge test by LVDT1; b, predicted using BEAM1DYN.

is consistent with the field observation that gaps of 12 to 25 cm formed around the prototype piles after the Loma Prieta earthquake. It appears that the damping in the model test was somewhat larger than that simulated in the prediction. The difference in apparent damping is attributable to nonlinearity, which is present in the experiment, but not in the analysis.

Figure 7 compares the peak positive and negative bending moment distribution along the length of a pile as measured in the centrifuge and predicted using BEAM1DYN. The agreement is remarkable, providing some verification of the proposed analytical model. It should be added, however, that some trial and error selection of parameters, especially for the shear modulus and damping parameters for the peat, was required. The need for trial and error adjustment of the parameters points to the usefulness of the centrifuge for "calibrating" a numerical model.

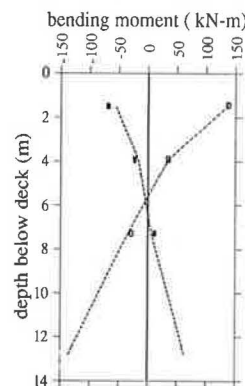


FIGURE 7 Distribution of maximum and minimum bending moment along the length of the pile and pile extension. Experimental data are given by the points, and the predicted moment distribution is represented by the dotted line.

Liquefaction and Sand Boil Mechanisms

Liquefaction and sand boils can cause significant damage to pavements. Such damage was caused by the 1989 Loma Prieta earthquake at the Oakland International Airport, in the Marina District in San Francisco, at the approach to the Oakland Bay Bridge, at the Port of Oakland, and in the city of Santa Cruz.

Centrifuge tests have been conducted to investigate the mechanisms and consequences of liquefaction by many researchers. Some examples of this work are Scott (8), Schofield (1), and Whitman et al. (9). In this paper some recent work involving liquefaction and sand boils in a layered soil is presented. This work is more completely presented by Kutter and Fiegel (10) and Fiegel (11). The work presented here is part of the author's contribution to VELACS, a collaborative project involving many universities [Arulanandan et al. (12)].

The model tested is shown in Figure 8. It consists of a relatively impermeable silica flour (silt) layer overlying a layer of Nevada sand ($D_{50} = 0.15$ mm, $D_r = 60$ percent). The layer of silt was thickest around the edges of the sample to prevent leakage along the sides of the model. The silt surface represented a level prototype, but the interface between the silt and sand was sloped to produce the thinnest silt section at the center of the sample. The sample was shaken with a base acceleration history similar to that recorded in the El Centro earthquake but with the acceleration scaled to a peak of 0.65 g. During this event, the pore pressures increased to equal the total overburden stress at all locations in the sand and silt.

The excess pore pressures in the sand rapidly dropped off after shaking stopped. This pore pressure dissipation is associated with settlement of the sand. The settlement of the sand results in expulsion of water that collects at the interface since the silt is relatively impermeable. The collection of water at the nonlevel interface produces an unstable situation. This is shown in Figure 9 by the surface displacement contours as recorded by the LVDTs. During shaking, most of the LVDTs record a small settlement, but the contours show that after some time, the center of the sample begins to bulge upward. This bulging can be explained by the fact that the silt layer was thinnest at the center of the sample. The water that col-

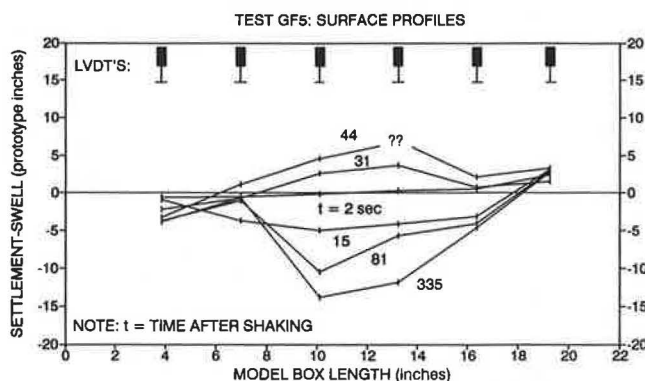


FIGURE 9 Profiles of surface displacement at various times after the beginning of shaking. The surface first settled, then heaved in the middle, and ultimately settled again.

lects at the interface flows along the interface to the lightest silt section.

Figure 10 shows the mechanism described. The bulging continues until a crack forms in the overlying silt. Once a crack forms, the water begins to leak through, and if the flow velocities are sufficient, silt and sand in the vicinity of the crack are eroded and carried to the surface in the form of boils.

Figure 11 shows one of the boils observed in the tests. The irregular layer of dark material near the surface of the silt is the initial ground surface. All of the material above this dark line was carried to the surface by the boil. A swirl of sand has penetrated up toward the surface and a layer of sand has been deposited around the mouth of the boil. Because of the process of preparation of the sample, a natural layering is noticeable within the silt. These layers curve downward in the

NOTE: SILT IS 1" THICK AND SAND IS 2 1/4" THICK AT THE CENTER OF THE MODEL

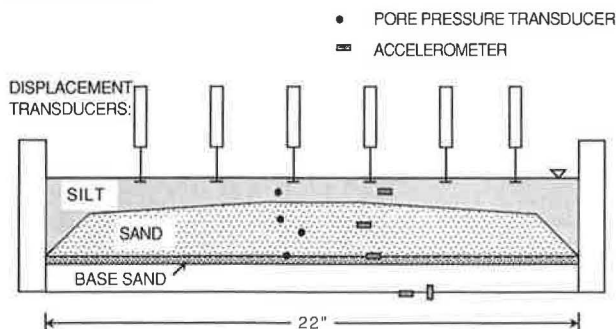


FIGURE 8 Centrifuge model used to study the mechanisms of liquefaction.

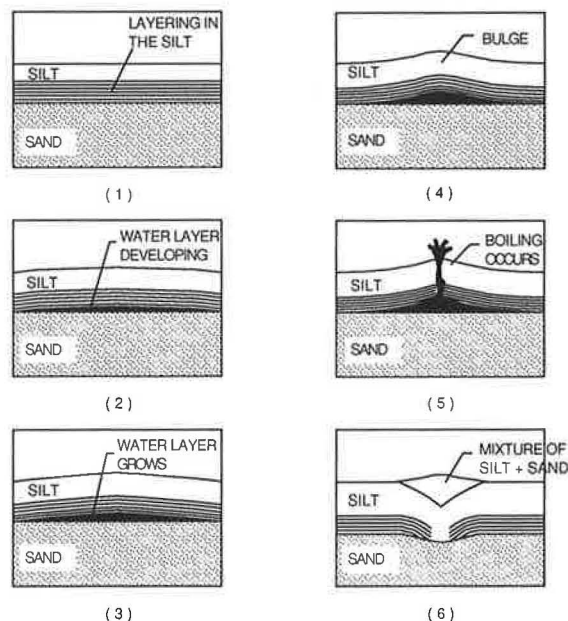


FIGURE 10 Possible sequence of events involving surface heave and eruption of sand boils.

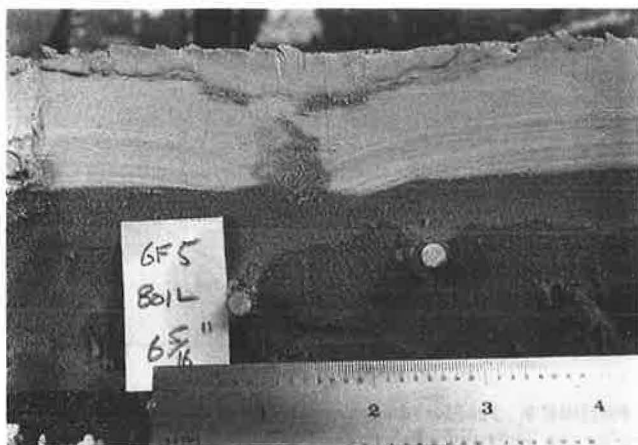


FIGURE 11 Sand boil exposed during excavation after the centrifuge test.

vicinity of the boil because of erosion of underlying silt and sand at the interface by water flowing toward the boil.

CONCLUSIONS

The well-established scaling laws for model testing on a centrifuge have been summarized, and some difficulties have been mentioned. Identical stresses in model and prototype permit the stress-dependent material properties of soils to be accurately simulated.

A new procedure for dynamic analysis of the lateral behavior of piles has been presented and calibrated using centrifuge test data. A mechanism of liquefaction of layered soils is clear after studying a few carefully planned centrifuge model tests. By careful dissection of the sample and consideration of the detailed measurements that are possible, a complex mechanism becomes understandable.

From the examples of centrifuge model tests presented, the centrifuge is shown to be useful in the following ways.

1. Analytical models can be developed on the basis of observed behavior in centrifuge tests.
2. Numerical procedures can be calibrated by comparison of predictions and measurements.

3. Surprising mechanisms, such as local surface heave observed in the liquefaction tests, can be discovered.

ACKNOWLEDGMENTS

Patricia Cafe, Gregg Fiegel, and Yuji Miyamoto conducted the experiments presented. Karl Romstad collaborated on the test on the Struve Slough Bridge. The work presented was sponsored by California Universities for Research in Earthquake Engineering and the National Science Foundation.

REFERENCES

1. A. N. Schofield. Dynamic and Earthquake Geotechnical Centrifuge Modelling. *Proc., International Conference on Recent Advances in Geotechnical Earthquake Engineering and Soil Dynamics*, Vol. 3, University of Missouri, Rolla, 1981, pp. 1081–1100.
2. H. Y. Ko and F. G. McLean (eds.). *Centrifuge 91*. A. A. Balkema, Rotterdam/Brookfield, 1991.
3. J. F. Corte (ed.). *Centrifuge 88*. A. A. Balkema, Rotterdam/Brookfield, 1988.
4. M. D. Bolton and C. K. Lau. Scale Effects Arising from Particle Size. In *Centrifuge 88* (J. F. Corte, ed.). A. A. Balkema, Rotterdam/Brookfield, 1988, pp. 127–131.
5. P. F. M. Cafe, *Dynamic Response of a Pile-Supported Bridge on Soft Soil*. Master's thesis. University of California, Davis, 1991.
6. A. S. Vesic. Bending of Beams Resting on Isotropic Elastic Solids. *Journal of the Engineering Mechanics Division*, ASCE, Vol. 87, No. EM2, 1961, pp. 35–53.
7. P. B. Schnable, J. Lysmer, and H. B. Seed. *SHAKE: A Computer Program for Earthquake Response Analysis of Horizontally Layered Sites*. Report UCB/EERC-72/12. Earthquake Engineering Research Center, University of California, Berkeley, 1972, 102pp.
8. R. F. Scott. Solidification and Consolidation of a Liquefied Sand Column. *JSSMFE*, Vol. 26, No. 4, Dec. 1986, pp. 23–31.
9. R. V. Whitman, P. C. Lambe, and J. Akiyama. Consolidation During Dynamic Tests on a Centrifuge. Preprint 82-063. ASCE National Convention, Las Vegas, Nev., April 1982.
10. B. L. Kutter and G. L. Fiegel. Mechanism of Sand Boil Formation in Layered Soils as Observed in Centrifuge Tests. *Proc., Third Japan U.S. Workshop on Earthquake Resistant Design of Lifeline Facilities and Countermeasures for Soil Liquefaction* (T. D. O'Rourke and M. Hamada, eds.), NCEER, SUNY, Buffalo, N.Y., 1991, pp. 279–292.
11. G. L. Fiegel. Master's thesis. University of California, Davis, in preparation.
12. K. Arulanandan et al. VELACS Check Tests. In preparation for submission to ASCE Journal of Geotechnical Engineering.

Publication of this paper sponsored by Committee on Foundations of Bridges and Other Structures.

Overview of Evaluation of Pile Foundation Stiffnesses for Seismic Analysis of Highway Bridges

GARY M. NORRIS

Methods for the assessment of the nonlinear variation in pile foundation stiffnesses are presented. Values of such lateral and vertical/rotational stiffnesses are intended for use for boundary element springs of a structural dynamic model of a highway bridge undergoing seismic analysis. Conflicts between the FHWA and Applied Technology Council approaches to foundation stiffness evaluation as well as deficiencies in these methods are noted. The methodology presented is demonstrated relative to a number of field case studies that have backcalculated values (or other responses) with which to compare. Such field case studies involve both failing and nonfailing soil responses, different soil conditions, a wide range of deflection amplitudes, and different types of loading (ambient level tests, full-scale, push-back, quick-release bridge tests, and response during earthquake excitation).

Foundation flexibility is taken into account in the structural dynamic modeling of a pile-supported highway bridge by incorporating boundary element springs of stiffness values comparable with those of the soil-pile foundation systems they replace. Typically, the lateral and rotational stiffnesses of the foundations are required for the seismic analysis of a highway bridge.

Whereas the bridge designer undertakes the dynamic analysis of the structure, the geotechnical engineer should direct the evaluation of the foundation stiffnesses needed in the analysis. Given the nonlinear variation of the soil modulus, the dependence of such modulus values on the stress path and the near-field soil strain (associated with superposed free-field and inertial interaction responses), and the necessity of evaluating such modulus dependence from relatively meager subsurface data, such geotechnical expertise is critical. Since the geotechnical engineer evaluates the site-dependent free-field ground surface motions or response spectrum to be used as input to the structure, he already has knowledge of the level of free-field strains that will develop in the different soil layers.

What is needed for realistic structural dynamic modeling is an accurate assessment of both the ground surface motions and the foundation stiffnesses along the length of the structure so that the dynamic analysis leads to an appropriate distribution of seismic forces to the structure. Unfortunately, the bridge design group often chooses to do a fixed base (i.e., infinitely stiff springs) response evaluation or, alternatively, undertakes the evaluation of the foundation springs for what it considers a worst-case soil condition. Neither approach is to be encouraged because each can lead to significant inac-

curacies. In fact, it is not presently known whether an evaluation of the foundation springs for spatially varying soil conditions using linear "design level" stiffnesses with limiting force or moment capacity is sufficient for the task. It may be that a full equivalent linear stiffness analysis, similar in principle to the use of strain compatible shear moduli in a ground response analysis, is required.

Geotechnical input into pile foundation stiffness evaluation is necessary if the potential for a commonly overlooked mechanism of failure is to be assessed. There can be situations where, because of softening of the soil profile associated with either cyclically degrading clay or developing but unrealized liquefaction in sand, the combination of the inertial interaction load from the superstructure and the reduced strength of the soil results in a foundation failure as seen, for instance, in Mexico City in 1985. Accordingly, there might not be free-field soil failure (e.g., liquefaction) or failure initiating with the superstructure, but rather a soil-foundation interaction failure that might be overlooked given the traditional division of work between the bridge design and geotechnical groups within a highway department. Such consideration of soil-foundation interaction failure can be treated in the context of a geotechnical pile foundation stiffness evaluation as shown in the published Meloland, Oakland Outer Harbor, and Cypress case studies.

This paper provides an overview of the author's equivalent linear lateral and rotational pile foundation stiffness evaluation procedures (1) and some field case studies (1-4).

UNCOUPLED STIFFNESSES AND DIFFERENCES IN ASSOCIATED EFFECTS

It is assumed that the lateral and rotational responses of a pile group can be uncoupled and treated independently (Figure 1a) provided that there are no batter piles in the group. Accordingly, the lateral response of the group derives from the soil-pile interaction of the piles near ground surface (together with the lateral resistance of the pile cap and any embedded portion of the pier shaft). The rotational resistance of the group, on the other hand, is dominated by the axial (i.e., vertical) response of the piles about the corresponding axis of rotation. The soils at depth provide the significant part of the axial and, hence, the rotational stiffness of the group.

The associated near-field zones of soil that govern in lateral versus vertical/rotational stiffness evaluation are shown in Figure 1b. The soil modulus variation in these different zones

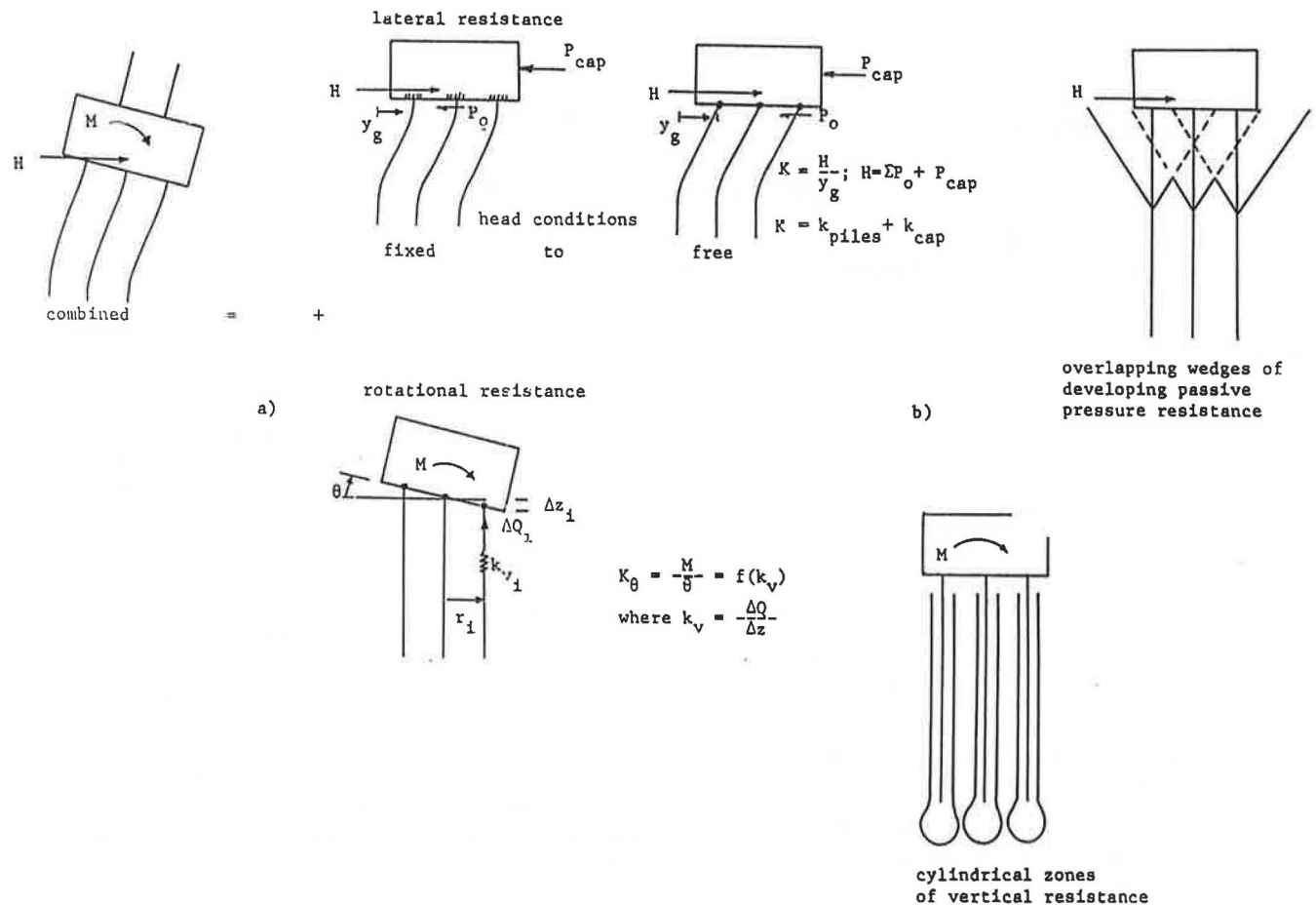


FIGURE 1 (a) Uncoupled lateral and rotational responses and (b) associated zones of soil-pile interaction.

governs the respective pile foundation stiffness evaluations. Furthermore, pile group interference effects, head fixity conditions, and the pile cap contribution are different for the different modes. Group interference due to the progressive overlap of developing passive wedges can be significant for lateral response, whereas there is negligible interaction of cylindrical zones and point pressure bulbs with respect to vertical and, hence, rotational pile group response (Figure 1b). Pile head fixity, ranging from a pinned to a fully fixed condition, has little effect with respect to the rotational stiffness of the pile group; therefore, a pinned condition is assumed. On the other hand, lateral stiffness will vary significantly depending on the assumed head fixity condition (Figure 1a). In fact, the head fixity of a given pile group may vary from being fixed to tending toward a free or pinned head response with an increasing lateral load.

It is assumed here that the soil settles away from the base of the pile cap and that, because of a concurrent lateral response (i.e., the development of soil gaps along the vertical faces of the cap), there is no pile cap contribution to rotational stiffness. On the other hand, with the soil gap closed, there will be a developing passive wedge in front of the leading face of the pile cap resulting in a notable pile cap contribution to lateral resistance. However, such lateral pile cap resistance should not include the shear along its base because, even if

the soil does not settle away from the cap, the soil moves laterally with the cap because of the soil deformation associated with the lateral movement of the underlying piles. Accordingly, it is inappropriate to evaluate the lateral stiffness of the pile cap by treating it as an embedded shallow foundation with base shear as proposed by FHWA (5). Furthermore, the choice of the soil modulus value for cap resistance should be made in conjunction with the level of the lateral deflection of the cap, which is equal to that of the piles at pile top. Given the difference in the width of the pile cap versus the individual pile, the same displacement implies that decidedly different soil strains (proportional to the deflection divided by the width of the member) and, hence, modulus values occur in the controlling zones of the soil in front of the cap versus the individual pile.

BEAM-ON-ELASTIC FOUNDATION FORMULATION

Lateral and rotation pile group stiffnesses rely on first assessing the nonlinear variation in lateral and vertical pile responses. This is best achieved by using the well-accepted beam-on-elastic foundation (BEF) formulation, in which soil-pile reactions are characterized by a continuous bed of springs.

Given the uncoupling of the lateral and rotational responses of the pile group, different sets of springs are used to characterize the lateral (i.e., p - y) and the vertical (t - z) soil-pile reactions (Figure 2).

One significant difference between the lateral and vertical pile responses is that the piles are under an initial static vertical load. Therefore, of the two different pile head responses,

- The horizontal load-displacement (P_o - y_o) response (or the associated pile head stiffness, $k = P_o/y_o$) from p - y behavior and
- The vertical load change-displacement (ΔQ - Δz) response (or the associated vertical pile head stiffness, $k_v = \Delta Q/\Delta z$) from t - z behavior,

the vertical will be different in unload versus load behavior in accordance with the subsequent inertial interaction loading of the pile group (Figure 2b). The consequences of this are considered in a later section.

LATERAL STIFFNESS EVALUATION

Currently available p - y curve formulation (5) has several limitations relative to its use in highway bridge seismic pile foundation analysis. Such formulation was not meant to be par-

ticularly accurate in the small deflection range, nor are such p - y curves appropriate for an embedded pile head (i.e., with the pile top occurring at the base of the cap at, say, 5 to 10 ft below the ground surface). Likewise, available p - y curve formulation does not account for differences in the pile bending stiffness (EI), the pile shape, and the pile head fixity. Whereas strain wedge (SW) model formulation (3,4) will account for all of these factors, such refinement may not be warranted given the subsequent modification due to pile group interference effects and due to existing differences in opinion as to the contribution of the pile cap (1,5).

A simple but realistic p - y BEF analysis that addresses both the small deflection and embedment issues is the equivalent linear subgrade modulus profile approach (1). Accordingly, one assesses the design level subgrade modulus, $E_s (= p/y)$ profiles [i.e., $E_s = f(x)$ (Figure 3a)] given the modulus variation f as characterized in the literature (Figure 4a). However, only that portion of the profile from the pile top and down is used to assess the isolated pile stiffness, k , whereas that variation over the height of the pile cap is used to evaluate the contribution of the pile cap, k_{cap} . Such a design level modulus profile applies at a given value of strain in the soil in the developing passive wedge in front of the pile (or pile cap), which reflects a pile head (or cap) deflection, y_o (or y_g), of 0.1 in./ft of pile (or cap) width B . At a lesser value of deflection, the soil strain is less and the modulus profile is stiffer

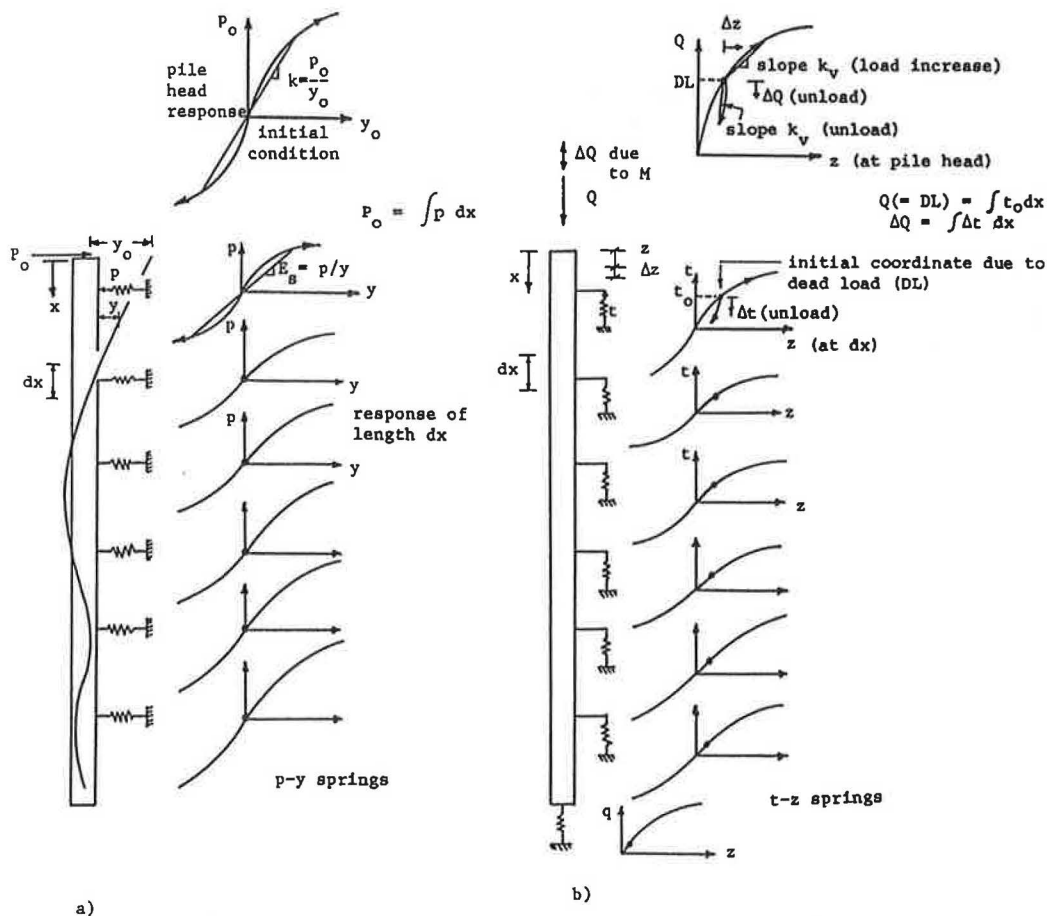


FIGURE 2 BEF characterization for (a) lateral and (b) vertical single pile response.

(Figure 3b) where such a modulus profile amplification value is assessed from Figure 4b given the deflection y_o (y_g) and pile (or cap) width B of interest.

The stiffness, K , of the pile group at a deflection y_g of the pile cap (the same as the deflection at the top of the piles) is

$$K = k_{\text{piles}} + k_{\text{cap}} \quad (1)$$

where K_{piles} is the stiffness of the n number of piles in the group considered collectively, and k_{cap} is the stiffness generated because of the lateral resistance along the vertical side of the front of the pile cap and any embedded portion of the pier shaft. The stiffness of the piles, k_{piles} , is n times the stiffness of the average group pile, k_{gp} , or n times the stiffness of the isolated pile, k , times a group reduction factor, e_g , that takes into account group interference effects, that is

$$k_{\text{piles}} = nk_{\text{gp}} = e_g nk \quad (2)$$

The factor e_g applies at the same load per pile to the group pile as to the isolated pile and, therefore, at a displacement y_g of the pile in the group as compared with the pile top displacement, y_o , of the isolated pile, that is,

$$k_{\text{gp}} = e_g k$$

where k_{gp} applies at displacement y_g (i.e., $k_{\text{gp}} = P_o/y_g$), k applies at displacement y_o (i.e., $k = P_o/y_o$), and

$$y_o = e_g y_g \quad (3)$$

The relationship between (k, y_o) of the isolated pile and (k_{gp}, y_g) of the pile in the group is shown in Figure 5. Factor e_g is a function of pile spacing and is equal to 0.354, 0.503, 0.639, 0.765, 0.885, and 1 for pile spacing, S , of 3, 4, 5, 6, 7, and 8 pile diameters, B , respectively.

From BEF theory, the stiffness of the single isolated pile, k , at a pile top displacement, y_o , can be expressed as

$$k = \frac{EI}{(A_{y_o} \text{ or } C_{y_o})T^3} \quad (4)$$

where EI is the bending stiffness of the pile in units of F/L^2 , A_{y_o} (or C_{y_o}) is the dimensionless BEF coefficient of displacement for free (or fixed) head conditions, and T is the relative stiffness factor of the pile in units of L . The equation for T and the value of coefficients A_{y_o} and C_{y_o} are established from a collection of published solutions (1) for different shaped E_s profiles.

The pile cap stiffness, k_{cap} , due to a uniform horizontal translation, y_g , of the pile cap is

$$k_{\text{cap}} = \frac{P_{\text{cap}}}{y_g} \quad (5)$$

where

$$P_{\text{cap}} = \int p \, dx \quad (6)$$

is the force associated with the integration of the line load force, p (in units of F/L), over the height of the cap and any embedded portion of the pier shaft. Note that p of the p - y curve is

$$p = E_s y \quad (7)$$

(Figure 2a) as in the fashion of the laterally loaded pile but that $y = y_g$ and $E_s = fx$ (see Figure 3a) where f (Figure 4a) now corresponds to the deflection $y_{g,\text{design}} = 0.1 \text{ in.} \times B(\text{ft})/1 \text{ ft}$, where B is taken as the width of the pile cap. Using the appropriate modulus amplification curve of Figure 4b, one

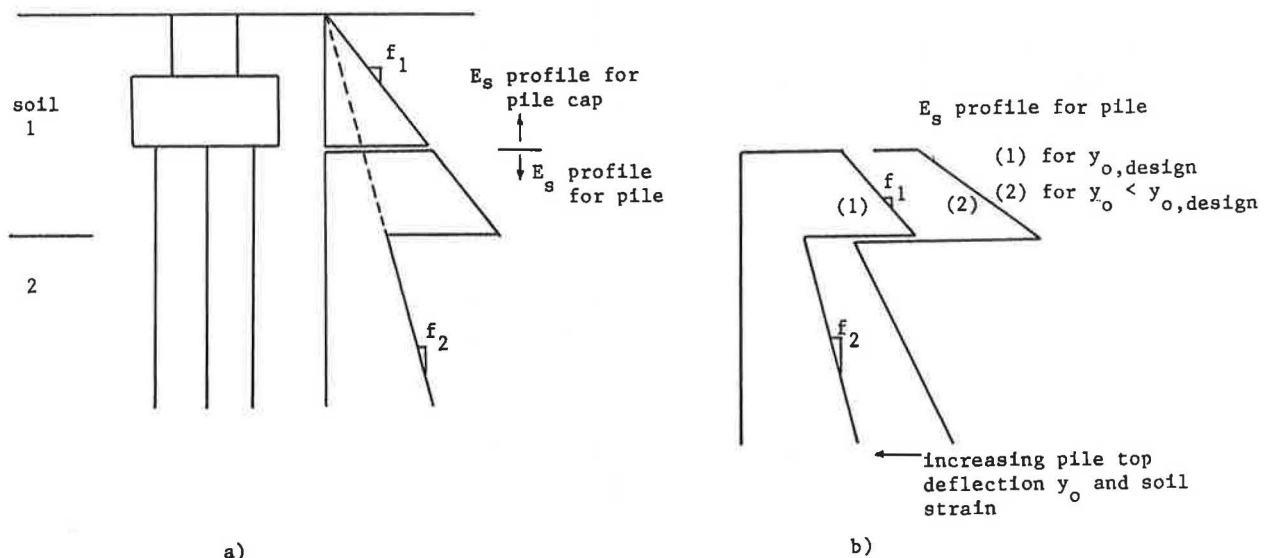


FIGURE 3 Subgrade modulus profile for laterally loaded pile response: (a) variation with depth and (b) change with decreasing pile top deflection.

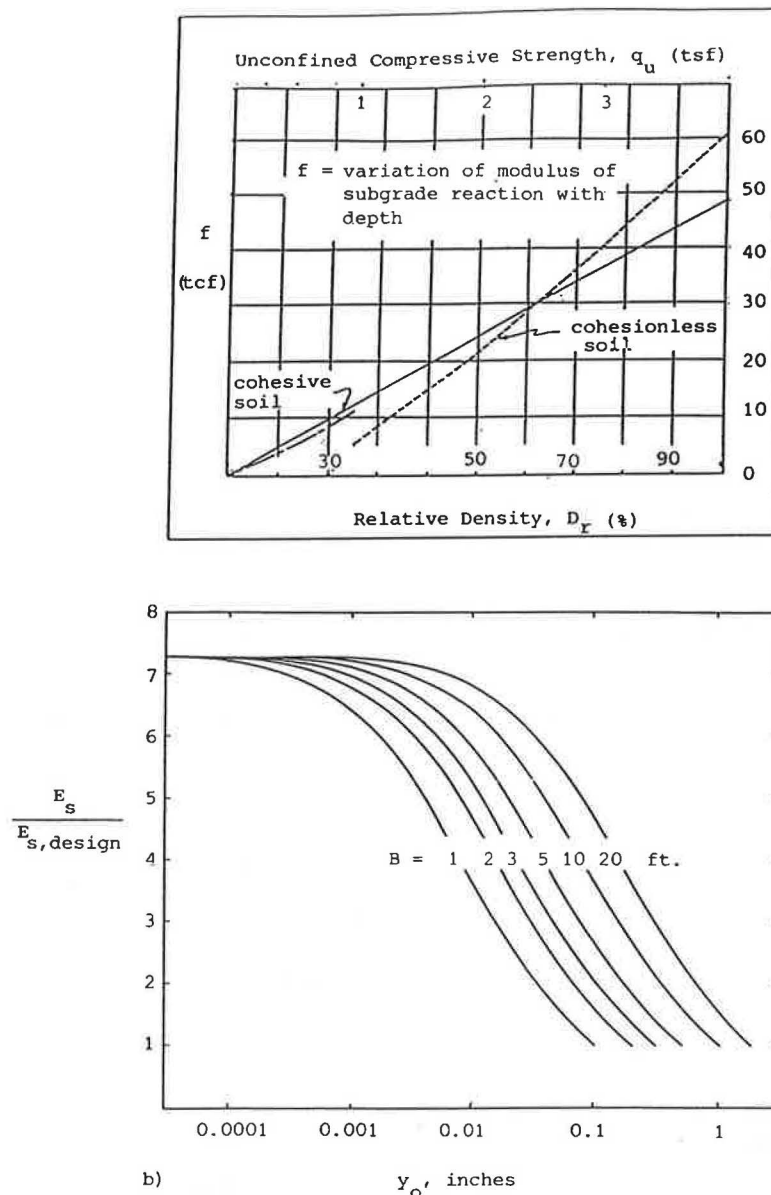


FIGURE 4 (a) Design level subgrade modulus Variation f and (b) subgrade modulus amplification curves (1).

can then obtain the E_s profile for the cap corresponding to the desired value of deflection, y_g , of the pile group. Thereafter, k_{cap} (upon substitution of Equation 7 into Equation 6 and Equation 6 into Equation 5) becomes

$$k_{cap} = (1/y_g) \int E_s y_g dx = \int E_s dx \quad (8)$$

A step-by-step outline of the foregoing procedure as well as sample calculations for the determination of the lateral stiffnesses for Pile Groups 1 and 2 of the Rose Creek Bridge is provided elsewhere (1). Figure 6 compares the predicted range in stiffness variations (from free to fixed head conditions based upon the aforementioned procedure) with best fit values for Piles Groups 1 through 4 backcalculated from system

ID evaluation of bridge response data from full-scale, high-amplitude, push-back, quick-release field tests of the bridge (6). Such bridge tests were carried out over a range in release displacements.

The predicted curves of Figure 6 were obtained using only simple hand calculations and commonly available soil data as provided in the boring logs from the bridge plans. Such equivalent linear stiffness evaluation takes only slightly longer than evaluating just the design level stiffnesses (values at the right end of the curves). In the context of the recommended use of such lateral stiffness (and comparable rotational stiffness) curves, a linear structural dynamic analysis would be undertaken using an assumed set of pile foundation stiffnesses and free-field motion input. Such linear dynamic analysis would be repeated until convergence in the assumed and displace-

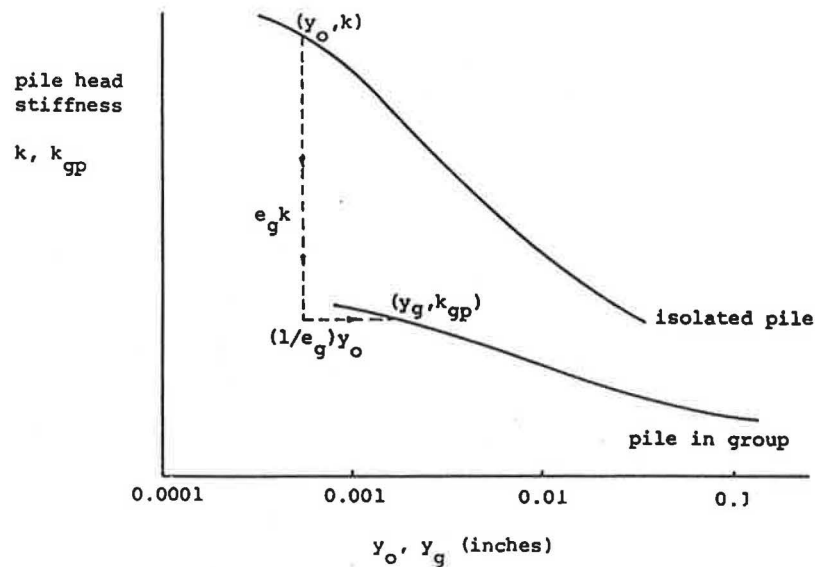


FIGURE 5 Pile head stiffness versus pile top deflection for the single isolated pile (k versus y_o) and the pile in the group (k_{gp} versus y_g).

ment compatible stiffnesses results. (The effect of using displacement compatible versus design level stiffnesses might then be judged.)

The equivalent linear subgrade modulus profile approach is the equivalent of generating the p - y curves with depth but with embedment effects handled directly. In addition, because the modulus amplification curve (Figure 4b) is modeled after the shear modulus reduction curve from soil dynamics, small strain/deflection response is appropriately characterized.

ROTATIONAL STIFFNESS EVALUATION

The rotational stiffness, K_θ , of a pile group is the ratio of the applied moment, M , to the resulting rotation, θ , of the base of the pile cap:

$$K_\theta = M/\theta \quad (9)$$

As discussed earlier, assuming the piles to be pin ended in a rigid pile cap and no cap contribution, the resistance to moment, M , derives solely from the axial response of the (vertical) piles. Given that the pile group is under initial static dead load corresponding to an average pile head force, Q , the moment resistance (equal to M) is the product of the load change, ΔQ_i , in each pile and the distance, r_i , of the pile from the axis of rotation summed over all the piles in the group:

$$M = \sum \Delta Q_i r_i \quad (10)$$

Given that the vertical axial stiffness at the pile head is $k_{vi} = \Delta Q_i / \Delta z_i$, where Δz_i is the pile head displacement, then $\Delta Q_i = k_{vi} \Delta z_i$, so that Equation 10 can be expressed as

$$M = \sum k_{vi} \Delta z_i r_i \quad (11)$$

The relationship between the pile head displacement, Δz_i , and the rotation, θ , is

$$\Delta z_i = r_i \theta \quad (12)$$

Substituting Equation 12 into Equation 11 yields

$$M = \sum k_{vi} r_i^2 \theta \quad (13)$$

and substituting Equation 13 into Equation 9 yields

$$K_\theta = \sum k_{vi} r_i^2 \quad (14)$$

Due to the initial dead load, Q , on the piles, there are different vertical stiffnesses, k_{vi} , in load versus unload response associated with moment, M (Figure 2b). Consequently, the axis of rotation of a regular arrangement of piles is not the symmetrical center of the group. (The axis is shifted toward the stiffer unload piles.) Furthermore, once the moment is reversed, the piles that have unloaded reload and the piles that have undergone a load increase unload so that the axis shifts from its original position to a new one. Figure 7, for instance, shows the Q - z travel paths of the piles of a two-row pile group and the associated M - θ response of the group under cyclic θ excitation (Figure 7a). (Points numbered 1 through 14 in Figures 7a and 7e correspond to those in Figure 7d.) However, in two to three cycles, the M - θ response stiffens in association with the piles tending toward the same (stabilized) unload-reload Q - z travel path (x - y in Figure 7d) corresponding to a centrally located axis of rotation. The stabilized stiffness, $K_\theta = M/\theta$ (Figure 7e), is of interest here. Given that the stabilized rotational stiffness of the pile group is a function of the stabilized unload-reload axial pile stiffness, k_{ulr} (slope x - y in Figure 7d), Equation 14 (for stabilized response) becomes

$$K_\theta = \sum k_{ulr,i} r_i^2 \quad (15)$$

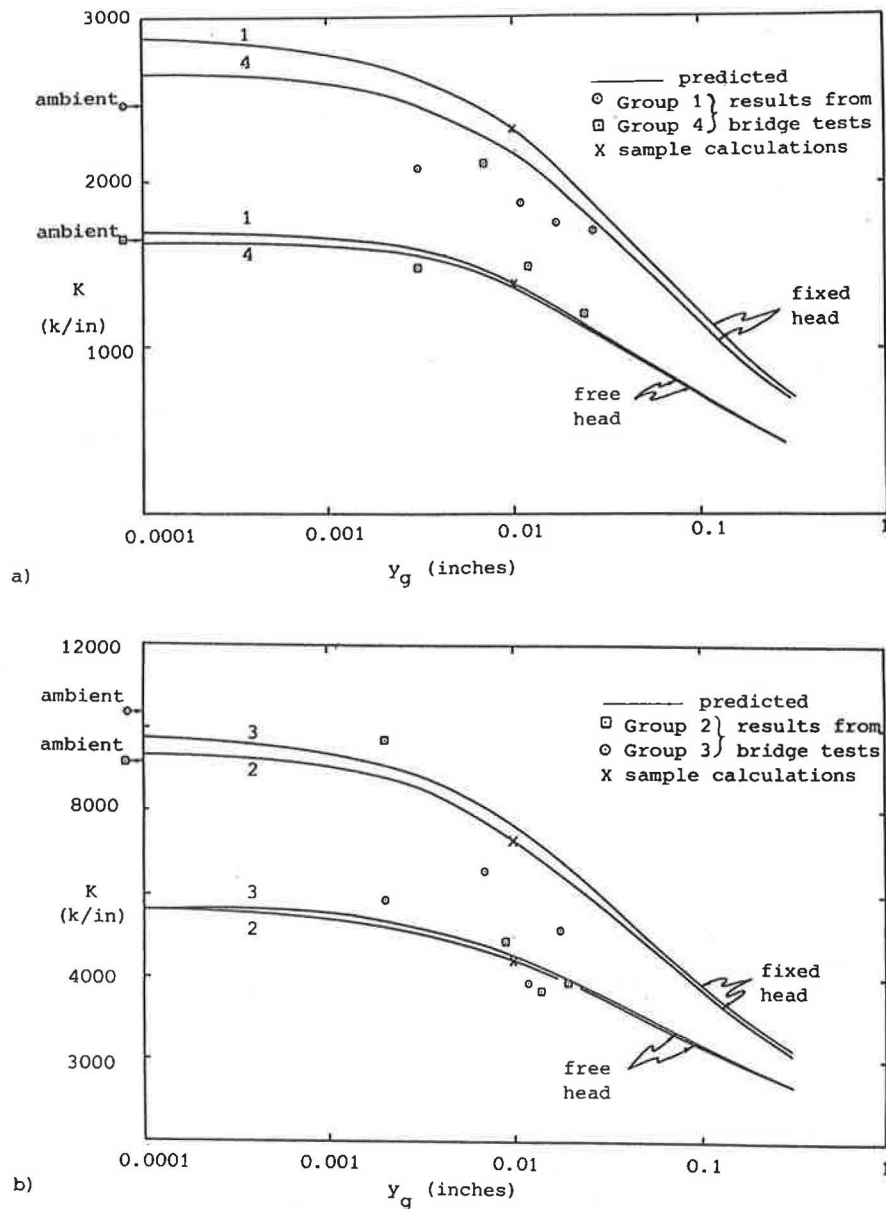


FIGURE 6 Comparison of predicted versus observed (i.e., backcalculated) lateral stiffness results from (a) Pile Groups 1 and 4 and (b) Pile Groups 2 and 3 of the Rose Creek Bridge (1).

Whereas the Q - z travel paths and the M - θ changes of Figures 7d and 7e are shown as straight line segments, they are only the secant slopes of the actual nonlinear variation. Therefore, the value of k_{ulr} actually varies (from one pile row to the next) with the amplitude of unload-reload displacement, Δz_{ulr} ($= r_i \theta$), as shown, for example, in Figure 8 for the piles of Pile Groups 1 through 4 of the Rose Creek Bridge.

Norris (1) presents a method for the assessment of the nonlinear variation in the unload-reload axial pile stiffness, k_{ulr} . The method is based on using Ramberg-Osgood formulation relative to the backbone Coyle-Reese (clay) t - z curves, from which one can then establish the unload-reload t - z response (Figure 2b). This includes the use of small amplitude shear stress-shear strain theory to accurately extend formu-

lation of the Coyle-Reese t - z curves to include nonlinear small amplitude t - z response. Given that using the backbone t - z responses in a Coyle-Reese type of analysis yields the backbone pile head Q - z response (Figure 2b), then, by using the unload-reload Δt - Δz response, one obtains the corresponding ΔQ_{ulr} - Δz_{ulr} pile head response and, therefore, k_{ulr} ($= \Delta Q_{ulr} / \Delta z_{ulr}$). Norris (1) presents a detailed outline of the associated solution procedure, a listing of a very short but useful BASIC program, and a worked example. The k_{ulr} versus Δz_{ulr} responses shown in Figure 8 for Pile Groups 1 through 4 of the Rose Creek Bridge were obtained using this procedure. On the basis of Equation 15, the rotational stiffness variations, k_θ versus θ (Figure 9), for Groups 1 through 4 were assessed. They are compared with values backcalculated from

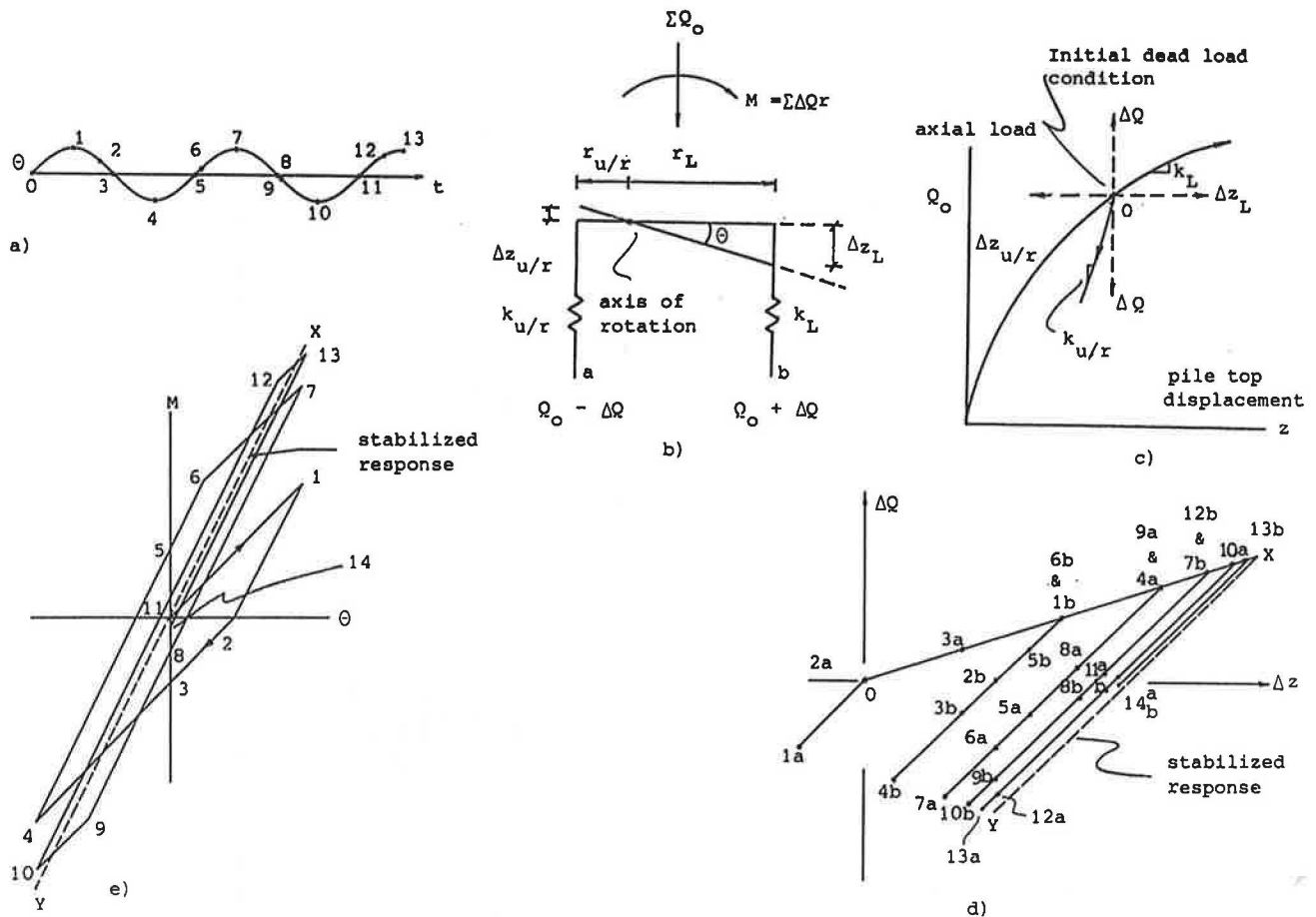


FIGURE 7 (a) Rotational excitation of (b) a two-row pile group given (c) the backbone load-displacement (Q - z) response of the piles with (d) the Q - z travel paths of Row a and b piles in the proximity of the initial condition and (e) the corresponding M - θ response.

the system ID evaluation of bridge response data from the same full-scale, high-amplitude, push-back, quick-release field tests mentioned earlier. The best fit backcalculated rotational stiffness values shown here imply simultaneous adoption of the best fit lateral stiffness values of Figure 6, and vice versa.

An interesting phenomenon is associated with Figures 7d and 7e. Over the two to three cycles necessary for stabilized behavior to develop, (a) permanent rotationally induced settlement develops (equal to the horizontal distance between Point 0 and a point on the x - y line directly to the right of points 14a and 14b of Figure 7d); (b) the spring stiffness, K_θ , increases (i.e., the secant slope between Points 1 and 4, then Points 7 and 10, and then x - y of Figure 7e increases); and (c) a mechanism of damping (as judged by the diminishing area of the M - θ loops of Figure 7e) develops that is not attributable to traditional material or geometric sources. It may be important in future applications to take account of such a response.

STIFFNESS AS A FUNCTION OF NEAR VERSUS FAR-FIELD SOIL RESPONSE

Given that the lateral resistance of the piles derives from the developing passive soil wedges near the ground surface and

that the axial (and, hence, the rotational) resistance of the piles derives from the cylindrical zones of soil over the full length of the piles (Figure 1b), it is clear that the lateral and rotational stiffnesses of the pile group depend on the nonlinear soil properties (a function of the stress or strain level) within these regions thus affected by soil-structure interaction response. However, in an earthquake, the "far" or "free" field soil is also moving. Therefore, for seismic excitation, one should actually take the modulus within a given region to be a function of the total strain, where the total strain is equal to the algebraic sum of the free-field and the inertial interaction strains (with due regard for phase differences). Unfortunately, such an evaluation is not presently feasible, which has led to the development of two conflicting approaches.

FHWA (5) has recommended that pile foundation stiffnesses be assessed on the basis of BEF (p - y and t - z type) analyses. Such nonlinear analyses require soil parameter input that is a function of the relative (or inertial interaction) displacement/strain. Therefore, the resulting lateral or rotational stiffness plotted as a function of relative displacement/rotation would vary as shown by the curve designated "FHWA" in Figure 10a. The Applied Technology Council (ATC) (7), on the other hand, recommends that stiffnesses be assessed on the basis of soil modulus values chosen as a function of the

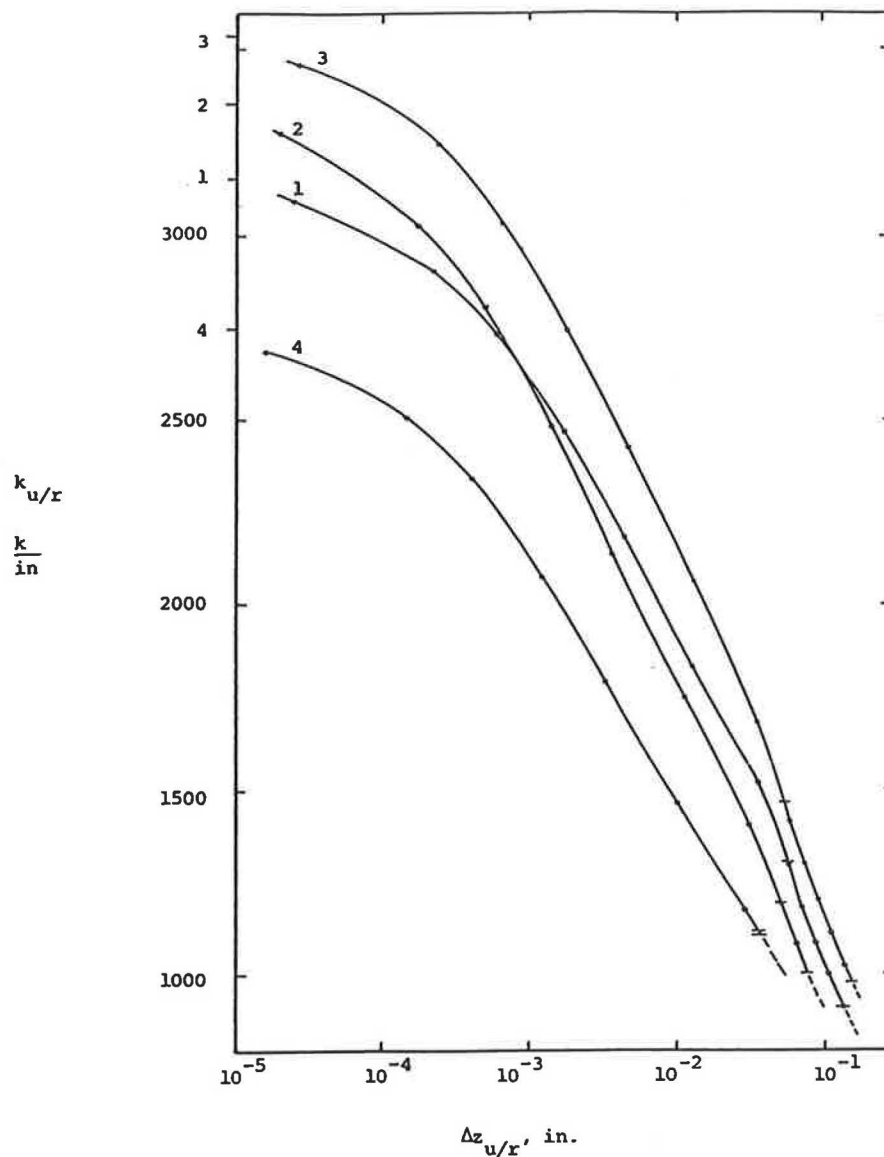


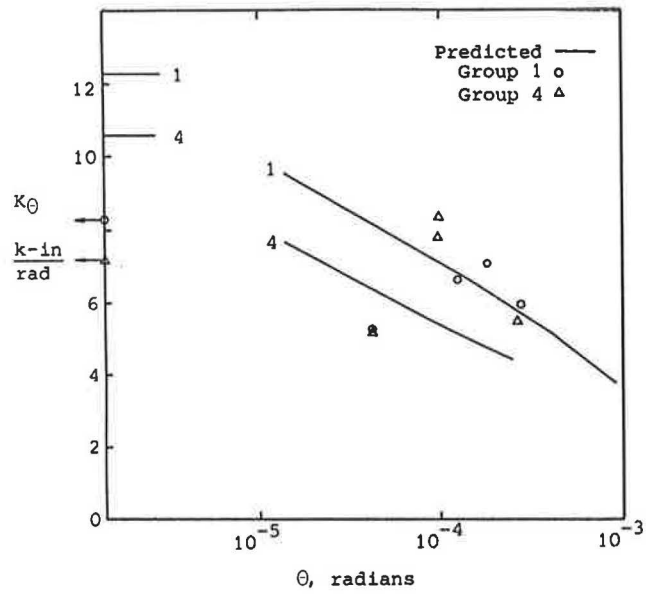
FIGURE 8 Vertical pile head stiffness $k_{u/r}$ versus $\Delta z_{u/r}$ curves for piles of Groups 1-4 from Rose Creek (I).

free-field level of soil strain as assessed, for instance, in a ground response analysis. Such a stiffness would be independent of the relative displacement/rotation and would plot as a horizontal line (a constant value) across Figure 10a. As an expedient, it appears that a combination of the two approaches would be more appropriate. For lower levels of relative displacement (or relative strain), the far- (or free-) field strain would be larger and, therefore, the combined strain would be closer to the free-field value. This implies that the ATC (constant) variation is applicable on the far left-hand side of Figure 10a. At larger levels of inertial interaction displacement/rotation (on the right side of Figure 10a), the relative strain dominates and the FHWA approach should be used. At the intersection of the ATC and FHWA variations, the free-field and relative strains are equal, and the combined strain will depend on the phase difference between the two

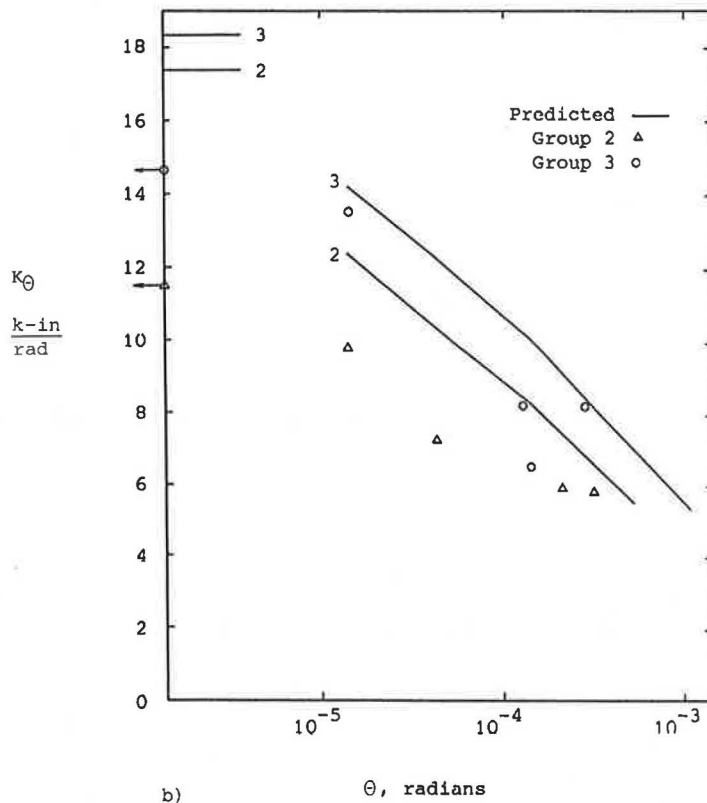
components. At present, the author assumes a direct transition from the ATC to the FHWA variation, as shown in Figure 10b.

In the comparison of the predicted and backcalculated lateral and rotational stiffnesses of Figures 6, 8, and 9 from the Rose Creek Bridge field tests, only relative strains were induced in the soil, and, therefore, no horizontal (ATC-type) cap on the predicted curves was used. Depending on the level of free-field motions to be considered, a cap would need to be superposed. Such discussion points out the possibility for error if backcalculated stiffnesses from full-scale bridge tests are used in seismic without modification.

Analysis of the Oakland Outer Harbor Wharf (3), an instrumented structure that was shaken in the Loma Prieta earthquake, provides an example of the need for such a distinction between the free-field and near-field soil strains. Fig-



a)



b)

FIGURE 9 Comparison of predicted versus observed (i.e., backcalculated) rotational stiffness values for (a) Pile Groups 1 and 4 and (b) Pile Groups 2 and 3 of the Rose Creek Bridge (I).

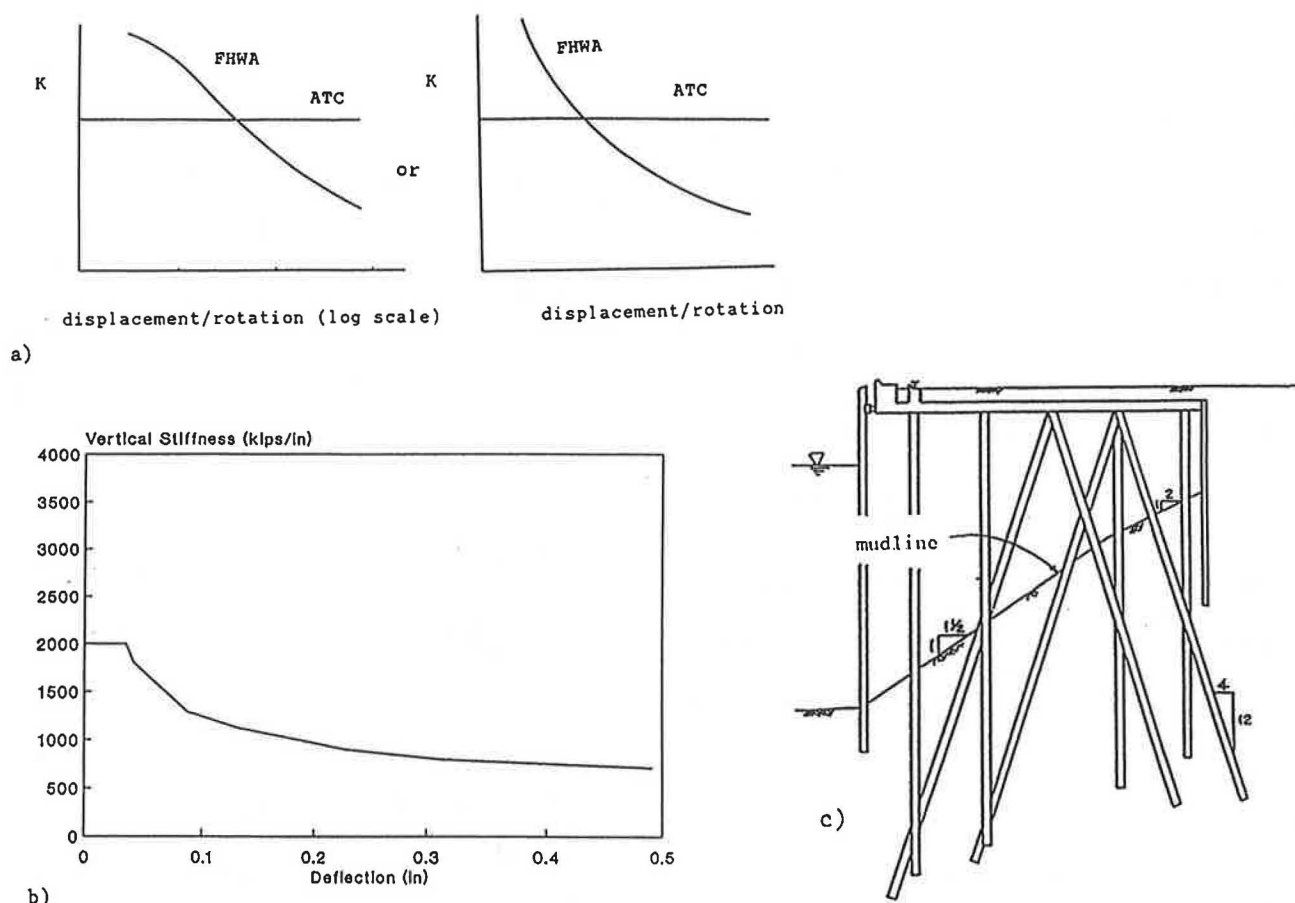


FIGURE 10 (a) Stiffness variation by FHWA versus ATC approaches; (b) proposed pile stiffness variation, as shown here for axial stiffness of all 18-in.-square prestressed concrete piles at (c) Oakland Outer Harbor for the Loma Prieta earthquake.

ure 10c is a cross section of the wharf, which is basically a long, free-standing pile group with batter piles. However, because of the flexibility of the wharf deck and the presence of batter piles, recorded transverse free-field motions were applied to a three-dimensional finite element model of the unsupported length of the piles and deck through lateral and vertical springs (a pair for each pile) at the mudline. Curves of the type shown in Figure 10b were developed (one vertical/axial stiffness curve for all piles and different lateral stiffness curves, not shown, depending on the force/moment condition at the mudline applicable to each pile). Several finite element runs were required before displacement compatible spring stiffnesses were assumed. Once this was accomplished, a comparison of the predicted and the recorded transverse accelerations at recording stations on the deck yielded a nearly perfect match. However, in obtaining compatible stiffnesses, it was noticed that the resulting vertical stiffness values all fell along the level portion of the vertical stiffness curve (Figure 10b) while the lateral stiffness values all fell on the descending portion of their respective curve. By contrast, use of stiffness values significantly different from such compatible values resulted in poor to very poor correlation between the recorded and the predicted accelerations on the deck.

SOIL-PILE FOUNDATION INTERACTION FAILURE

As mentioned earlier, if a soil from which a pile foundation derives some or all of its support softens significantly (or fails in part), a soil-foundation interaction failure may ensue. Such a softening response can occur in a loose to medium sand with developing porewater pressure that may not be sufficient to cause liquefaction but may be high enough to cause trouble. Likewise, under high static loads (e.g., friction piles in Mexico City), cyclic degradation of clay under seismic loading can lead to large displacements.

While it is possible to accommodate porewater pressure buildup in a lateral stiffness analysis by reducing the subgrade modulus profile of Figure 3a at each depth on the basis of the ratio of the reduced vertical effective stress to the original effective stress, once a zone liquefies, particular attention should be paid to whether the piles can take the bending/shear deformation across that layer. The load on such a pile would then include the inertia effects of the soil above the liquefied zone.

Nonstable rotational stiffness, on the other hand, develops when the piles of one or more rows reach axial pile capacity

in either tension or compression. Once moment, M , causes such a response, the piles of that row plunge or pull out, that is, they experience a large plastic displacement, Δz , at a constant axial resistance, $Q = Q_{ult}$, until moment, M , reverses. The Q - z travel paths of such piles never stabilize, and both the Q - z response of the piles and the M - θ behavior of the group become a function of the pattern (as well as the magnitude) of the inertial interaction loading (i.e., the θ or M versus time, t , response as well as the θ or M amplitude). Consequently, the rotational stiffness, K_θ , of the pile group cannot be assessed a priori, that is, without knowledge of the free-field motion, because the pattern of inertial interaction loading, M versus t , or excitation, θ versus t , is dependent on the response of the superstructure to the free-field response.

Norris (2) provides an analysis of such nonstable rotational behavior of the central pier pile group of the Meloland Overcrossing during the 1979 Imperial Valley earthquake, including a comparison of the evaluated stiffness with the back-calculated value from system ID analysis of the recorded response of the bridge (8). By contrast, the rotational stiffness of the same foundation as tested under nonseismic conditions (9) is some 20 times higher. Norris et al. (4) provide a similar analysis of the lateral and rotational stiffnesses of the pile foundations of the Cypress Viaduct during the Loma Prieta earthquake.

SUMMARY

The information presented is an overview of recent studies (1–4) of a methodology for lateral and rotational stiffness evaluation and field case study comparisons. The methodology is an alternative to stiffness evaluation approaches adopted by FHWA and ATC. Of course, it is the author's strong belief that such evaluation should be undertaken or overseen by a geotechnical engineer given his appreciation for the level of free-field soil strains, soil's nonlinear stress-strain behavior, and the possibility of developing pore pressures in sand or cyclic degradation of clay under seismic excitation, or both.

The recommended lateral stiffness evaluation procedure is an equivalent linear subgrade modulus profile approach that is intended to be more accurate than existing p - y curve analysis at seismic levels of excitation. The proposed procedure accounts for the embedment of the pile heads, the group interference effect, and the pile cap contribution in contrast to other approaches, which only allude to these effects (or, in the case of the pile cap, wrongly assess a base shear resistance). This nonlinear stiffness evaluation procedure requires only hand computations (assuming prior knowledge of free-

field strains) and takes only slightly longer than the time necessary to establish the so-called design level stiffness.

The basic rotational stiffness evaluation procedure assumes nonlinear stabilized response, from which it is a simple matter to evaluate the corresponding level of (permanent) rotationally induced settlement that occurs. The dead load on the structure influences whether nonstable behavior occurs as the result of compressional or tensile pile capacity failure. If nonstable rotational behavior develops, the Q - z travel paths that result are a direct function of the pattern as well as the amplitude of inertial interaction loading as demonstrated elsewhere for the case of the Meloland Overcrossing. Whereas some may wish to avoid nonstable behavior altogether, a more practical approach might be to design to accommodate a certain amount of deformation (as with abutment wall movement).

REFERENCES

1. G. M. Norris. Foundation Stiffness Evaluation for Seismic Analysis of Highway Bridges. *Proc., 23rd Symposium on Engineering Geology and Soils Engineering*, Logan, Utah, April 1987, pp. 375–394.
2. G. M. Norris. A Seismic Analysis: Meloland Overcrossing During the 1979 Earthquake. *Soil Properties Evaluation from Centrifugal Models and Field Performance*. Geotechnical Special Publication 17, ASCE, 1988, pp. 88–117.
3. G. Norris et al. *Soil-Foundation-Structure Behavior at the Oakland Outer Harbor Wharf*. Report 91-2. Center for Civil Engineering Earthquake Research, University of Nevada, Reno, June 1991.
4. G. Norris et al. *Seismic, Lateral and Rotational Pile Foundation Stiffnesses at Cypress*. Report 91-3. Center for Civil Engineering Earthquake Research, University of Nevada, Reno, July 1991.
5. I. Lam and G. R. Martin. *Seismic Design of Highway Bridge Foundations*. Reports FHWA/RD-86/101, FHWA/RD-86/102, and FHWA/RD-86/103. FHWA, U.S. Department of Transportation, June 1986.
6. B. M. Douglas and J. A. Richardson. Maximum Amplitude Dynamic Tests of a Highway Bridge. *Proc., 8th World Conference on Earthquake Engineering*, Vol. 6, 1984, pp. 889–896.
7. *Tentative Provisions for the Development of Seismic Regulations for Buildings*. ATC 3-06. Applied Technology Council, 1978.
8. B. M. Douglas, G. M. Norris, L. Dodd, and J. Richardson. Behavior of the Meloland Road Overcrossing During the 1979 Imperial Valley Earthquake. *Proc., 16th Joint Meeting of the U.S./Japan Panel on Wind and Seismic Effects*, UJNR, May 1984, 27 pp.
9. E. A. Maragakis, B. M. Douglas, and S. Vrontinos. Experimental and Analytical Soil-Structure Interaction Studies of Meloland Road Overcrossing. Accepted for 1992 ASCE Structures Congress.

Publication of this paper sponsored by Committee on Foundations of Bridges and Other Structures.

Seismic Highway Bridge Design Using Spectra Specific to Washington State

CARLTON HO AND GEORGE TSIATAS

The Washington State Department of Transportation adopted recommendations for seismic response spectra to replace the AASHTO guidelines. The replacement spectra were based on input and soil amplification representative of the geologic conditions of the Pacific Northwest. A deep subduction zone earthquake was used as the source event rather than a shallow strike-slip earthquake typical of that used in the development of the AASHTO guidelines. Soil data from 123 boring logs from actual bridge sites in Washington State were processed, and nine soil groups representative of the soil conditions in the region were identified, based on similarities of standard penetration test data. Soil amplification spectra were derived for the nine soil groups. These were compared with spectra provided by current guidelines and similar works. They were also correlated with damage from previous earthquakes in the area.

The Pacific Northwest of the United States is acknowledged as a major seismically active region. Two recent events in this region (1949, M 7.1; 1965, M 6.5) resulted in numerous ground failures and considerable structural damage in the heavily populated Puget Sound basin. The recurrence interval of M 6 events in this region has been estimated to be between 5 and 10 years (1,2). The potential occurrence of a greater than M 8 earthquake has been suggested (3).

The Washington Department of Transportation (WSDOT) is currently updating seismic guidelines for highway bridges. Before 1989, WSDOT used AASHTO's 1983 seismic guidelines (4). These guidelines were developed for general use on the basis of research relying on data from California earthquakes. Source mechanisms, wave propagation paths, and site geology of Washington State earthquakes differ significantly from those of California earthquakes.

Seismic activity in Washington State is produced by subduction of the Juan de Fuca plate under the North American plate producing deep focus events (3). Overlying the thick base rock are sizable deposits of glacial material left during the multiple advances and retreats of the Cordilleran ice sheet. These deposits are often heavily overconsolidated with a mixture of grain sizes. On the contrary, California earthquakes generally result from lateral strike-slip of the Pacific plate and the North American plate. These earthquakes tend to have shallow foci (≤ 20 km). The Quaternary deposits overlying the intact rock are often lacustrine, marine, or alluvial. These deposits tend to be thinner and less overconsolidated than the glacial deposits of Washington State. As a result, WSDOT commissioned research to develop seismic response spectra

that more accurately represented ground motion resulting from a Washington State earthquake. Soil amplification spectra for nine characteristic soil profiles were derived using 123 boring logs from bridge sites throughout Washington State.

The base spectrum developed using available data on ground motion from Japanese subduction zone earthquakes similar to those occurring in Washington State is shown in Figure 1. These earthquakes generally have larger high-frequency components than do shallow-focus earthquakes. For comparison, the current AASHTO base (Soil Group I) is superimposed on Figure 1. Figures 2 through 4 show the response spectra normalized by input acceleration for the nine soil groups developed. The curves show the base spectrum multiplied by the soil amplification spectra for 0.1, 0.2, and 0.3 scaled input. These are the most likely values of the acceleration coefficient in Washington State. The curves should be multiplied by the corresponding acceleration coefficient to obtain the design spectra. Table 1 gives the nine soil groups that are considered to be representative of the soil types in Washington State. The soil groups were based on standard penetration test (SPT) data because of extensive use in site investigations. This table can be used to characterize any site in Washington State on the basis of this commonly used in situ test; a zonation map is not needed. The specifics on the development of these spectra are described elsewhere (5,6).

EVALUATION OF SPECTRA

The products of the base spectrum and the soil amplification spectra were compared with the appropriate AASHTO guideline curves and the spectra developed by Seed et al. (7). The products were also compared with the curves generated by predictive equations for subduction zone earthquakes and the response from the existing strong ground-motion records from

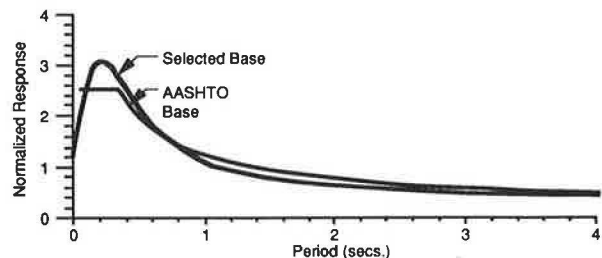


FIGURE 1 Selected base spectrum and AASHTO Soil Type I curve.

C. Ho, Department of Civil and Environmental Engineering, Washington State University, Pullman, Wash. 99164-2910. G. Tsiatas, Department of Civil and Environmental Engineering, University of Rhode Island, Kingston, R.I. 02881.

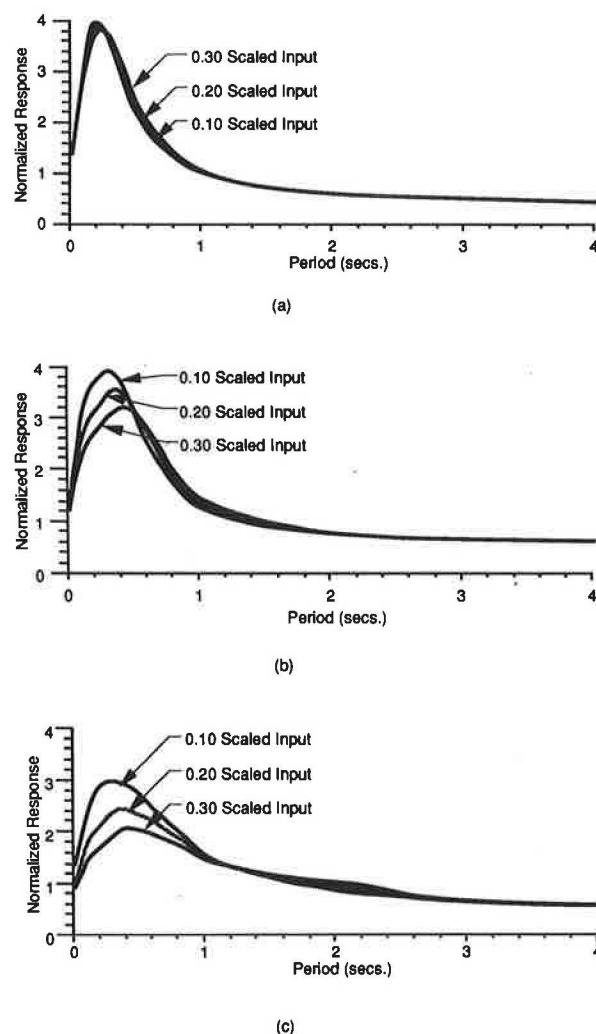


FIGURE 2 Base spectrum multiplied by soil amplification spectra for Groups 1, 2, and 3 (a, b, and c) soils for 0.1, 0.2, and 0.3 scaled input.

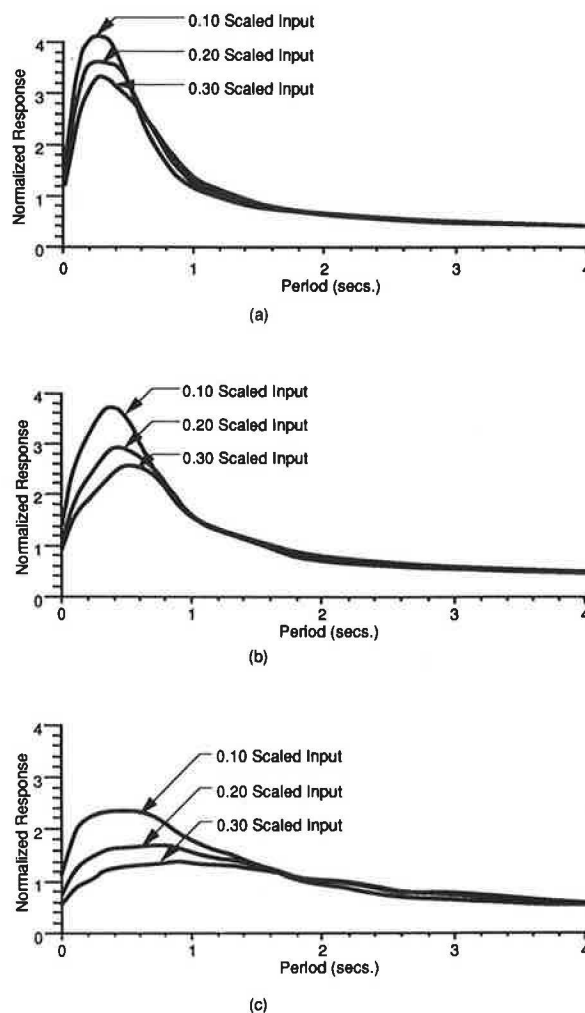


FIGURE 3 Base spectrum multiplied by soil amplification spectra for Groups 4, 5, and 6 (a, b, and c) soils for 0.1, 0.2, and 0.3 scaled input.

the Puget Sound area. Damage from the 1949 and 1965 earthquakes was investigated to determine the correlation between earthquake damage and site soils and to see whether the spectra developed would predict that damage.

A comparison of the spectra developed in this study with the spectra developed by Seed et al. (7) (Figure 5) demonstrates the general trends of the difference of subduction versus shallow earthquakes: larger high-frequency components and smaller long-period components with increasing depth or softness of the deposits, or both. These same trends can also be seen in the spectra developed by Hayashi et al. (8) for Japanese sites (see Figure 6). The Japanese earthquakes that their analysis was based on are subduction zone earthquakes, where larger high-frequency content can be expected. The higher frequencies can be seen in these spectra in the stiff soil category.

The AASHTO curves scaled by the soil factors for three soil conditions are similar to the spectra developed in this study in terms of strengths of records. In that respect, the developed spectra are consistent with the existing codes. The

differences in spectral shapes are from two sources. There are differences in frequency content because deep-focus earthquakes have larger high-frequency content than do shallow-focus earthquakes. There are also differences because of the unique types of soils in Washington State and because of the refinement of the soil groupings. These differences should be expected because the AASHTO curves are based primarily on spectra developed using California earthquakes and soils, which are different from the soils and earthquakes in Washington State.

When comparing the spectra developed in this study with the existing AASHTO curves, it must be noted that the depths specified in this analysis are generally to hard soils (blow counts above 100) and not to bedrock, which is the depth prescribed by the AASHTO guidelines. The depth from hard soils to bedrock varies from zero to around 900 ft in Washington State. The AASHTO curves and corresponding spectra from this analysis are shown in Figure 7. The AASHTO spectrum for stiff soil sites (Group I) very generally corresponds to the base spectrum and Group 1 of this study. There

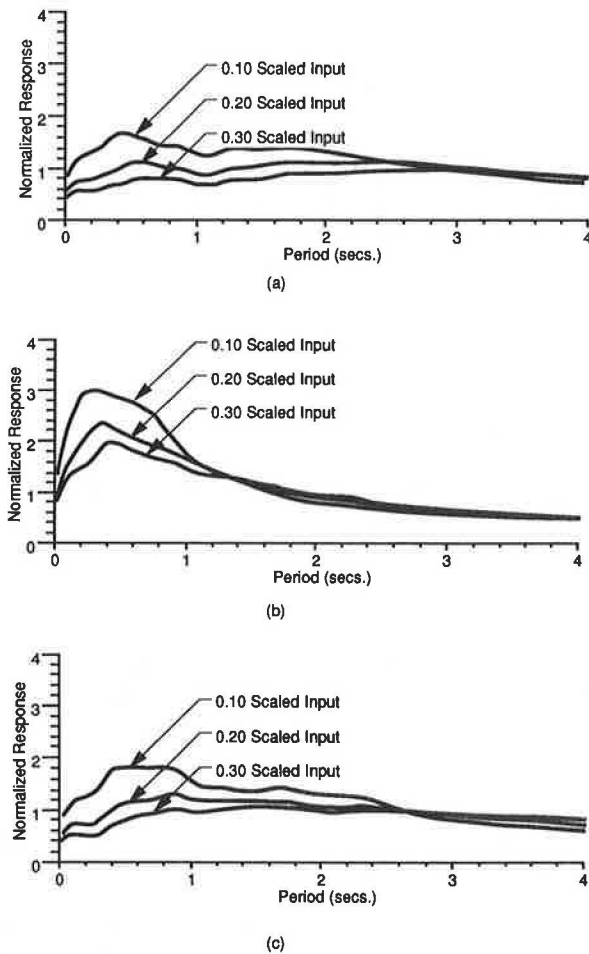


FIGURE 4 Base spectrum multiplied by soil amplification spectra for Groups 7, 8, and 9 (a, b, and c) soils for 0.1, 0.2, and 0.3 scaled input.

are larger high-frequency components in the spectra from this study. This is consistent with studies showing subduction zone ground motions having larger high-frequency content (9). The spectra are very similar above a period of about 1 sec. The AASHTO spectrum for stiff clays and deep cohesionless soils (Group II) corresponds to Groups 2 and 3 spectra in this

TABLE 1 SOIL GROUPS

Group	Description
1	20-50 ft to blow counts of 100 or greater of medium to dense cohesionless soils with up to 5 ft of loose soils (blow counts less than or equal to 10) at the surface. Variable layers of medium and dense soils, with no layers of loose soils beneath the top 5 ft.
2	51-100 ft to blow counts of 100 or greater of medium to dense cohesionless soils with up to 20 ft of loose soils at the surface. Variable layers of medium and dense soils, with no layers of loose soil beneath the top 20 ft.
3	100-300 ft to blow counts of 100 or greater of medium to dense cohesionless soils with up to 30 ft of loose soils at the surface. Variable layers of medium and dense soils, with no layers of loose soil beneath the top 30 ft.
4	10-50 ft to blow counts of 100 or greater of all other soils not in group 1.
5	50-100 ft to blow counts of 100 or greater of all other soils not in group 2.
6	100-300 ft to blow counts of 100 or greater of all other soils not in groups 3, 7.
7	100+ ft to blow counts of 100 or greater of soils consisting primarily of clays or clays and loose sands.
8	COAST SITES, 10-50 ft of loose silt and sand (not necessarily to SPT=100)
9	COAST SITES, 50+ ft of loose silt and sand (not necessarily to SPT=100)

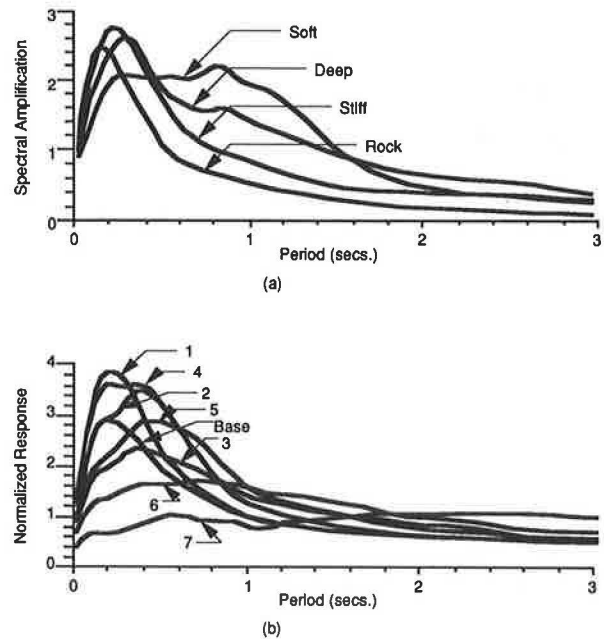


FIGURE 5 Comparison of spectra developed by Seed et al. (7) for four soil conditions (a) and spectra developed in this study for seven soil groups and base accelerations (b).

study. These groups do not include clays, which would generally reduce the higher-frequency response. The AASHTO spectrum for soft to medium-stiff clays and sands includes Groups 5, 6, and 7 in this study. The average of these spectra is very close to the AASHTO guideline curves. These comparisons indicate that the results of this analysis are generally consistent with existing spectra in terms of strengths. The comparisons also address the soil and earthquake factors in Washington State in a more realistic manner.

The spectra developed in this study can also be compared with the predictive equations for subduction zone earthquake ground response. Group 3 spectra are most similar in spectral shape to the Crouse et al. (10) and Vyas et al. (11) spectra for a magnitude 8 earthquake at a depth of 50 km, as shown in Figure 8.

The spectra can also be compared with the responses of the 1949 and 1965 Puget Sound earthquakes. The recording site in Olympia for the 1949 and 1965 events can be classified as a Group 3 site (12). Scaled Group 3 spectra are compared

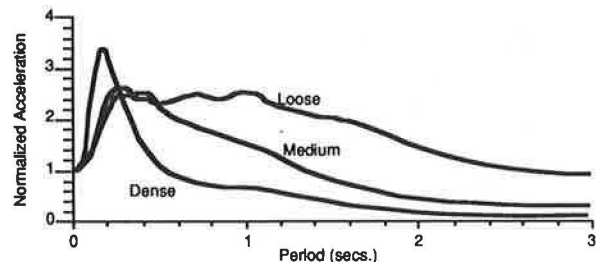


FIGURE 6 Site dependent spectra developed by Hayashi et al. (8) for Japanese earthquakes.

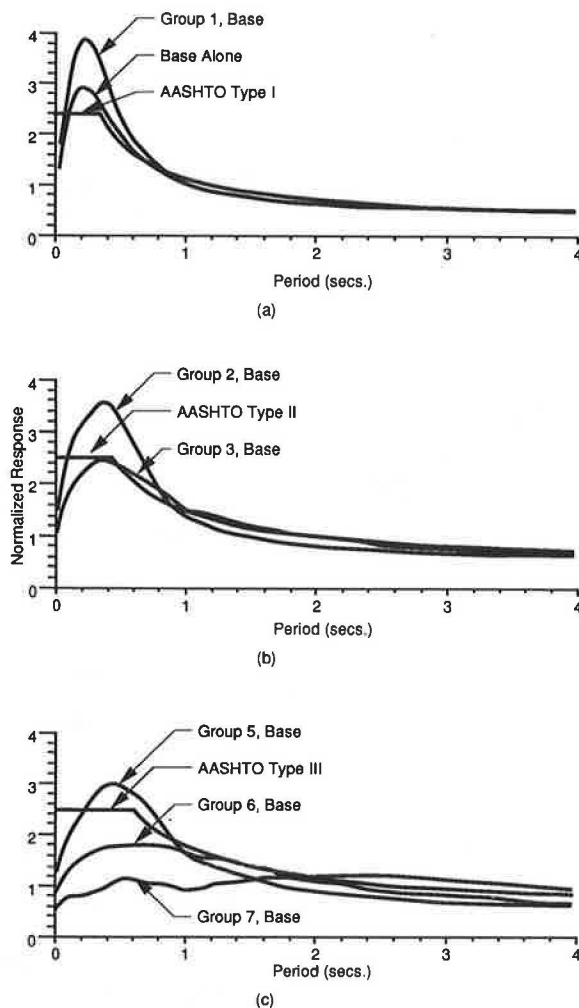


FIGURE 7 Comparison of AASHTO curves with spectra developed in this study: (a) AASHTO Type I with Group 1, (b) AASHTO Type II with Groups 2 and 3, (c) AASHTO Type III with WSDOT 5, 6, and 7.

with the responses from these two events in Figure 9. This actual response is enveloped fairly well by the Group 3 spectra except for the high-frequency response of the 1965 record. This event was almost directly under the recording station. Because of this, the time history may be rich in high-frequency components that would not be seen elsewhere. The recording

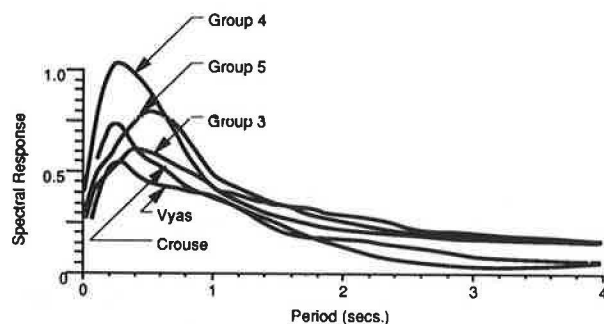


FIGURE 8 Comparison of spectra developed from predictive equations of Crouse et al. (10) and Vyas et al. (11) and spectra developed in this study scaled by 0.3.

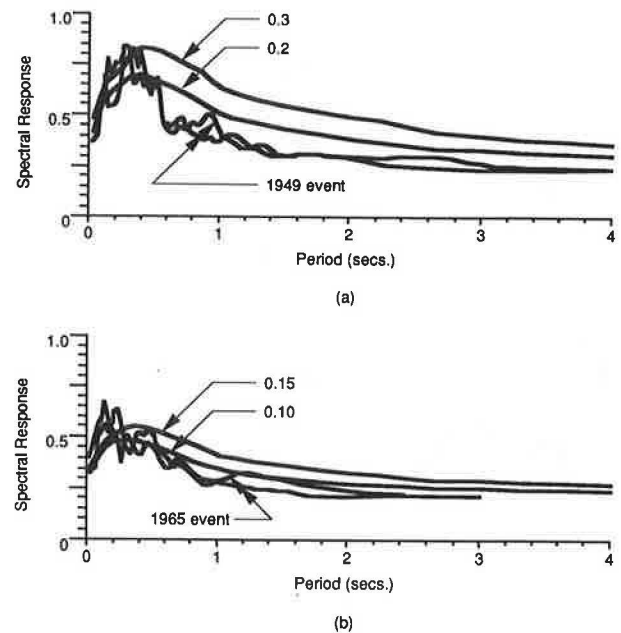


FIGURE 9 Comparison of Group 3 soil spectra developed in this study with horizontal response of Puget Sound earthquakes recorded in Olympia: (a) scaled by 0.3 and 0.2 and the 1949 event, (b) scaled by 0.1 and 0.15 and the 1965 event.

site in Seattle for the 1965 event would be classified as a Group 1 site. The response at this site is enveloped fairly well by the predicted spectra scaled by 0.10 as shown in Figure 10.

It is of value to examine the reported damage in the Puget Sound basin caused by the 1949 and 1965 events and how that damage has been correlated to geologic conditions. The results of this examination can be compared with the spectra developed in this analysis to see if they reflect greater ground shaking for those conditions. Most researchers found some correlation between damage and relative density of soils. Many structures built on artificial fill overlying tidal flats experienced high levels of ground shaking in both the 1949 and 1965 earthquakes (13). Damage was especially severe in the Duwamish River Valley (including Harbor Island) in the Seattle area. In Tacoma and Olympia, settlements of up to 25 cm occurred in the 1949 earthquake. It is not clear if this damage was because of subsidence or vibrational effects because there was evidence of both. Vibrational damage is a function of the period of ground shaking. When the natural period of a struc-

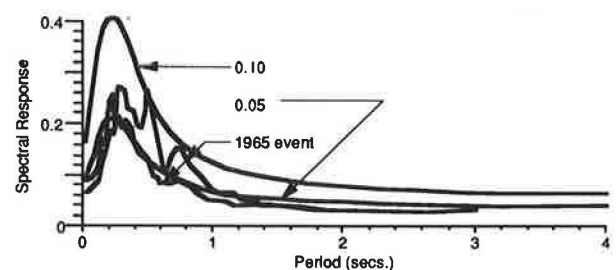


FIGURE 10 Spectra for Group 1 soils scaled by 0.01 and 0.05 and horizontal response of 1965 earthquake recorded in Seattle.

ture coincides with the period of the ground shaking, the probability of damage greatly increases. A general estimate of the natural period of 30- to 50-ft-high buildings in this area is 0.25 to 0.40 sec. Most of these softer sites fall into Groups 4, 5, or 6 depending on the depth to more compact material. Except for the Group 4 spectrum, these spectra have reduced frequency content in the 0.25 to 0.40 sec range compared with more compact sites. There are several possible reasons for the discrepancy between the reported damage and the ground shaking predicted by the spectra in this study. One possible explanation is that the damage in these areas was primarily caused by subsidence (14). Another is that the statistical averaging of the individual sites in the groups necessarily reduces the ordinates of extreme occurrences; in other words, the effects may be modeled in an individual site study but are averaged in a group. A third possibility is that effects other than surficial soils contributed to the damages observed.

The last possibility, that effects other than soils contribute to the severity of ground shaking in this area, has been suggested by several researchers. Anomalies in ground shaking not associated with surficial soils were found in other areas with denser, more stable ground conditions and in areas with artificial fill and unconsolidated natural deposits. Localized destruction on compact Pleistocene deposits occurred on the West Seattle Hill during the 1965 earthquake (15). In Tacoma and Olympia, the worst damage occurred in filled tidal flat areas, but there was also substantial damage on hard gravel uplands (13). Abnormally high intensities occurred in the Chehalis/Centralia area during both the 1949 and 1965 events (15). The severe damage seen in the Duwamish River Valley also varied considerably between areas with apparently similar site characteristics (14).

Various explanations have been forwarded to explain the capricious aspect of ground shaking in these areas. Yount (16) suspects that more severe ground shaking on compact Pleistocene deposits in Seattle was caused by low impedance units overlying bedrock at shallow depths. This explanation would generally be consistent with the results of this study for Group 1 sites. Hawkins and Crossen (13) indicated that clay layers underlying filled river basins might be suspected of causing damage. This analysis indicates a reduction in the amplitude of destructive frequencies on those types of soils.

Another explanation for these anomalies in relative ground shaking is that the highly variable stratigraphy of the underlying bedrock may influence the transmission of earthquake waves. Reflection and refraction may focus energy in certain areas. This idea was forwarded in 1942 by Coombs and Barksdale (17) for damages observed during a 1939 earthquake in the Puget Sound. This concept has received more attention recently with the introduction of sophisticated modeling techniques. Langston and Lee (18) showed the possible effects of focusing in the Duwamish River Valley using a three-dimensional ray-tracing algorithm. They suggested that focusing may be a primary agent in differential ground shaking in this area. This could produce an increase in ground shaking of up to an order of magnitude.

CRITICAL ANALYSIS

The results of this analysis must be examined in the context of the assumptions inherent in the AASHTO guidelines. One

assumption was that ground shaking could be represented by a base spectrum multiplied by a severity coefficient and modified by a soil factor. The severity coefficient map indicates only very general spatial relationships with respect to identified source zones. The earthquake parameters accounted for in the maps are (very generally) source-to-site distance and crustal attenuation. The soil modifiers indicate only the frequency dependent attenuation/amplification properties of the soil column directly beneath the site. The base spectrum, if that assumption is correct, must represent the effects of all other factors that can affect ground shaking at a site, including source characteristics, directivity, and focusing. A broadband spectrum is typically used to account for these variations, but, as was noted in a previous section, effects of focusing alone may cause an order-of-magnitude increase in ground shaking. To specify a base spectrum that would encompass those effects would mean that for most sites the base spectrum would be unreasonably conservative. The solution is to neglect the effects of focusing, directivity, and other parameters that are earthquake- and site-specific and that could (but usually do not) cause more intense ground shaking and to use instead a reasonable average value. This is not outside the intent of the formulators of ATC 3-06 (who produced the AASHTO guidelines) who state, "It is possible that the design earthquake ground shaking might be exceeded during the lifespan of the structure—although the probability of this happening is quite small" (19). The broadband spectrum should encompass most, but not necessarily all, of the anticipated ground response.

Another assumption is that the design response spectrum at a site is directly correlated with the damage an earthquake can cause. Many factors contribute to damage that cannot be represented by this simple frequency-response diagram. The duration of an earthquake is not represented in the response spectrum, except in a very general sense—long-duration earthquakes typically have a broader range of frequency components (20). The duration of an earthquake is a critical factor in structural response in terms of cyclic loading effects. Subduction zone events may have durations up to 4 min. This may be a critical concern and it is addressed in the AASHTO guidelines by suggesting a standard duration of ground shaking of 20 to 30 sec. It was seen in the section on correlation with damage from past earthquakes that on softer sites, ground failure (subsidence) may cause as much damage as do vibrations. Increasing the design coefficient in these areas may result in an increase in the structure's ability to resist lateral motions but does not specifically address damage due to differential settlement.

With the limitations in the AASHTO guidelines in mind, the validity of the assumptions made in this analysis can be examined. The first assumption to consider is that ground response can be modeled by vertical shear waves propagating through horizontal soil layers. Studies comparing down-hole data with analytic response using SHAKE (21) indicate that near surface motions may contain components not predicted with this simple model (22). Wave theory predicts that shear waves become more vertical as they pass through increasingly less-dense materials on their way to the surface (23). For deep focus earthquakes this assumption of vertical shear waves seems reasonable. Nonhorizontally layered bedrock can affect the propagation of earthquake waves through reflection and refraction, which results in nonvertical propagation near the

ground surface. Focusing effects in sedimentary basins can produce long-period surface waves (24) that may be critical in terms of differential movement between bridge piers (25). These long-period effects are accounted for in the AASHTO guidelines in a general way by increasing the base spectrum ordinates at longer periods. Although the effects of focusing can be large, they are very much site- and earthquake-specific and will not affect most sites. Not accounting for them appears consistent with the AASHTO philosophy. The assumption of horizontal soil layers is not unreasonable. Softer soils, which have a greater impact on attenuation/amplification of base motion, are typically horizontally (or nearly horizontally) layered.

A second assumption is that dynamic properties of soils are directly correlated with blow counts and static laboratory test results. Using these correlations requires caution. There are many factors that can affect the blow counts recorded and undrained shear strength test results (26,27). There is significant variability in the values observed in the boring logs, even in apparently homogeneous deposits. Sensitivity studies have been performed in an attempt to bracket the possible response, and it appears that the profile responses are not sensitive to 30 percent variations in calculated shear modulus values except at very soft sites. These soft sites fall into groups that incorporate a wide range of frequency amplification, so this greater variation is accounted for.

Even with consideration of the uncertainties related to these assumptions, the results are consistent with the findings of more sophisticated analyses and give a reasonable first-order estimation of soil amplification effects.

There is some uncertainty related to each of the components of this analysis. It may appear prudent when considering these compounding uncertainties to use mean plus one (or even two) standard deviations in assigning soil amplification multipliers. It is necessary, however, to consider the other parameters that can affect the response and the uncertainties related to each of these. Taking mean plus one standard deviations for all of the parameters that can affect ground shaking would lead to unreasonably large design forces. It seems more rational to use average values for all parameters; if a standard deviation is taken, it should be taken for the entire spectral response. A very rough estimate of the ratios between the response spectrum coefficients and mean plus one standard deviation coefficients might be 1.3 to 1.4 (28).

There is some concern that the very high frequency components (periods less than about 0.2 sec) have not been adequately represented in the selected base spectrum. The 1965 Olympia records contain significant components in this range as indicated in Figure 9. Comparison of spectra developed using shallow-focus and subduction zone earthquakes shows significant differences in this frequency range on rock and stiff soil sites. The spectra developed in this study, however, appear to be consistent with most of the available data. For this reason, the higher-frequency components were not increased. Studies were done to determine what effect these higher frequencies would have on the amplification spectra. There appeared to be no significant effect from including larger high-frequency components (Figure 10).

The results of this study (combined with the generalities involved in the mapping of the severity coefficient) must be considered as a first-order approximation of site response.

Site-specific studies should be considered for critical or unusual structures so that other factors, such as susceptibility to focusing, can be considered in the analysis.

CONCLUSIONS

Response spectra for nine soil groups, developed for the particular conditions of Washington State, have been compared with the existing guidelines, spectra developed from predictive equations, spectra developed from subduction zone earthquakes, and site-specific spectra developed by Seed et al (7). In addition, the response spectra were correlated with damage caused by the recent strong earthquakes in Washington State.

Whereas the base spectrum and soil amplification spectra developed specifically for Washington State are in general agreement with the existing codes in terms of strength of ground shaking, differences in spectral shapes are observed. The differences are consistent with expected differences in frequency content between shallow- and deep-focus earthquakes. The soils in Washington State are diverse, making it logical to divide the types into more groups than those identified by the existing codes. The spectral amplification/attenuation characteristics of these soil groups, however, correspond fairly well with the site-response characteristics of less-refined groupings.

The most substantial differences between the existing codes and the results of this study are at the higher frequencies (periods of less than 0.4 sec). This means the greatest changes in design forces calculated will be to very stiff structures or in the transverse direction in long-span bridges. For other periods of interest, the spectra developed here may provide a slightly higher or lower (but more reasonable) value of relative ground shaking.

This approach should be applied to other regions with subduction zone events. Similar conditions in Northern California, Oregon, and British Columbia warrant its use, if it is not already being done.

ACKNOWLEDGMENT

The work on which this report is based was supported by WSDOT and the U.S. Department of Transportation, Federal Highway Administration. The contribution of Karen Kornher, currently with CH₂MHILL, is gratefully appreciated.

REFERENCES

1. R. S. Clossell. Review of Seismicity in the Puget Sound Region from 1970 through 1978. *U.S. Geological Survey Open-File Report 83-19*, 1983.
2. N. H. Rasmussen, R. C. Millard, S. W. Smith. *Earthquake Hazard Evaluation of the Puget Sound Region, Washington State*. Geophysics Program, University of Washington, Seattle, 1975.
3. T. H. Heaton and S. H. Hartzell. Source Characteristics of Hypothetical Subduction Earthquakes in the Northwestern United States. *Bulletin of the Seismological Society of America*, Vol. 71, No. 3, June 1986, pp. 675-708.
4. *Guide Specifications for Seismic Design of Highway Bridges*. American Association of State Highway and Transportation Officials, Washington, D.C., 1983.

5. G. Tsiasas, R. Fragaszy, C. Ho, and K. Kornher. *Design Response Spectra for Washington State Bridges*. Final technical report, May 1989.
6. C. Ho, K. Kornher, and G. Tsiasas. Ground Motion Model for Puget Sound Cohesionless Soil Sites. *Earthquake Spectra*, Vol. 7, No. 2, May 1991, pp. 237–266.
7. H. B. Seed, C. Ugas, and J. Lysmer. Site-Dependent Spectra for Earthquake Resistant Design. *Bulletin of the Seismological Society of America*, Vol. 66, No. 1, Feb. 1976, pp. 221–234.
8. S. Hayashi, H. Tsuchida, and E. Kurata. Average Response Spectra for Various Subsoil Conditions. Third Joint Meeting, U.S.–Japan Panel on Wind and Seismic Effects, UJNR, Tokyo, May 10–12, 1971.
9. I. M. Idriss. Characteristics of Earthquake Ground Motions. *Proc., ASCE Geotechnical Engineering Division Specialty Conference on Earthquake Engineering and Soil Dynamics*, Pasadena, Calif., June 19–21, 1978, pp. 1151–1265.
10. C. B. Crouse, Y. K. Vyas, and B. A. Schell. Ground Motions from Subduction Zone Earthquakes. *Bulletin of the Seismological Society of America*, Vol. 78, No. 1, Feb. 1988, pp. 1–25.
11. Y. K. Vyas, C. B. Crouse, and B. A. Schell. Regional Design Ground Motion Criteria for the Southern Bearing Sea. *7th International Conference on Offshore Mechanics and Arctic Engineering*, Vol. 1, Houston, Tex., Feb. 7–12, 1988, pp. 187–193.
12. Shannon and Wilson, Inc., and Agabian Associates, *Geotechnical and Strong Motion Earthquake Data from U.S. Accelerograph Stations*. NUREG/CR-0985, Vol. 4.
13. N. M. Hawkins and R. S. Crossen. Causes, Characteristics and Effects of Puget Sound Earthquakes. *U.S. National Conference on Earthquake Engineering*, Earthquake Engineering Research Institute, Oakland, Calif., 1975, pp. 104–112.
14. D. R. Mullineaux, M. G. Bonilla, and J. Schlocker. *Relation of Building Damage to Geology in Seattle, Washington, During the April 1965 Earthquake*. U.S. Geological Survey Professional Paper 575-D, 1967, pp. 183–191.
15. B. Gonen and N. M. Hawkins. *Building Standards and the Earthquake Hazard for the Puget Sound Basin*. Report SM 74-1. Department of Civil Engineering, University of Washington, Seattle, May 1974.
16. J. C. Yount. Geologic Units That Likely Control Seismic Ground Shaking in the Greater Seattle Area. *Proc., Workshop XIV, Earthquake Hazards of the Puget Sound Region, Washington*. U.S. Geological Survey Open-File Report 83-19, 1983, pp. 268–279.
17. H. A. Coombs and J. D. Barksdale. The Olympic Earthquake of November 13, 1939. *Seismological Society of America Bulletin*, Vol. 32, No. 1, 1942, pp. 1–6.
18. C. A. Langston and J.-J. Lee. Effect of Structure Geometry on Strong Ground Motions: The Duwamish River Valley, Seattle, Washington. *Bulletin of the Seismologic Society of America*, Vol. 73, No. 6, Dec. 1983, pp. 1851–1863.
19. *Tentative Provisions for the Development of Seismic Regulations for Buildings*. Applied Technology Council, Publication ATC 3-06, 1978.
20. R. P. Kennedy et al. *Engineering Characteristics of Ground Motion, Task I: Effects of Characteristics of Free-Field Motion on Structural Response*. NUREG/CR-3805, May 1984.
21. P. B. Schnabel, J. Lysmer, and H. B. Seed. *SHAKE, a Computer Program for Earthquake Response Analysis of Horizontally Layered Sites*. EERC 72–12. Earthquake Engineering Research Center, University of California, Berkeley, Calif., Dec. 1972.
22. C. Y. Chang and M. S. Powers. Empirical Data on Spatial Variation of Earthquake Ground Motion. *2nd International Conference on Soil Dynamics and Earthquake Engineering*, on board the liner *Queen Elizabeth II*, New York to Southampton, Vol. 1, June/July 1985, pp. 3–17.
23. K. Kanai. *Engineering Seismology*. University of Tokyo Press, Tokyo, 1983, pp. 83–140.
24. W. B. Joyner and D. M. Boore. Measurement, Characterization, and Prediction of Strong Ground Motion. *Earthquake Engineering and Soil Dynamics II—Recent Advances in Ground-Motion Evaluation*. Geotechnical Special Publication 20, ASCE, June 1988, pp. 43–102.
25. T. C. Hanks and D. A. Johnson. Geophysical Assessment of Peak Accelerations. *Bulletin of the Seismologic Society of America*. Vol. 66, No. 3, June 1976, pp. 959–968.
26. H. B. Seed, I. M. Idriss, and I. Arango. Evaluation of Liquefaction Potential Using Field Performance Data. *Journal of Geotechnical Engineering*, ASCE, Vol. 109, No. 3, March 1983, pp. 458–482.
27. W. A. Weiler. Small-Strain Shear Modulus of Clay. *Earthquake Engineering and Soil Dynamics II—Recent Advances in Ground-Motion Evaluation*. Geotechnical Special Publication 20, ASCE, June 1988, pp. 331–345.
28. N. Donovan. Soil and Geologic Effects on Site Response. *Proc., Second International Conference on Microzonation*, Vol. 1, San Francisco, Calif., Nov./Dec. 1987, pp. 55–80.

Publication of this paper sponsored by Committee on Engineering Geology.

Effects of Stratigraphic and Construction Details on the Load Transfer Behavior of Drilled Shafts

MICHAEL O'NEILL, LYMON REESE, RALPH BARNES, SHIN-TOWER WANG, MARK MORVANT, AND MAURICIO OCHOA

Drilled shafts are often designed by representing soil layers as ideal geomaterials, such as clay, sand, or rock, and using simple correlation factors to convert measured strength values into values of unit shaft and base resistance. The effects of apparently minor inclusions in layers of otherwise uniform soil and soft rock on load transfer, particularly in shaft resistance, are addressed. Also considered are the effects of the use of polymer drilling slurry and artificial roughening of the borehole on load transfer. Data from the load testing of six full-sized drilled shafts at three sites indicated that thin sandstone layers could increase load transfer by one-third in dense sand and that thin bentonite layers could decrease load transfer by two-thirds in clay-shale. No adverse effects could be detected in shaft load transfer by the use of polymer drilling slurry, and the rifling of a borehole wall in clay-shale increased the shaft load transfer by about 40 percent over that in an unrifled shaft.

Current design procedures for drilled shafts are based primarily on experience that has been accumulated in the testing of full-scale shafts and in the correlation of test results with soil or rock properties obtained in a straightforward manner. In recent years several data bases of loading tests and corresponding soil and rock properties have been established and have been used effectively to develop design procedures and parameters (1–3). However, these procedures do not directly address the issue of apparently minor variations in the subsurface conditions that are often neglected in establishment of design loads. For example, Tomlinson (4) cited variations in average unit shaft (side) resistance of from 0.4 to in excess of 5.0 tsf in similar chalk formations in the United Kingdom due to locally present flints and fissures that affect both the shaft load transfer and the strength indicated in the laboratory. To provide more information on this phenomenon and information on the effects of certain construction details (namely, rifling of the borehole and use of polymer drilling slurry) on load transfer, the results of six loading tests on full-sized drilled shafts at three test sites in three geological settings are presented in this paper.

The three test sites are all characterized by the presence of fairly thick layers of geomaterial that can be characterized in

a straightforward manner with SPT or triaxial compression tests. However, interbedded with some of the layers are thin layers and seams, usually no thicker than 4 in. and making up less than 10 percent of the vertical profile of the major layer, of either harder or softer material (or both). The extent to which this interbedding affects load transfer is examined.

SITE A—MONTGOMERY FORMATION

The Montgomery Formation is a Pleistocene-aged deltaic terrace of the Texas Gulf Coast region. It consists mainly of layers of submerged silty fine sands with occasional layers of clay and sandy clay. Within the fine sand layers are occasionally found seams of cemented sand, locally called weak sandstone. These seams are normally too thin to sample and test in the laboratory but appear to have compressive strengths in the range of 60 to 150 ksf. They can normally be penetrated during drilled shaft construction with an auger but occasionally require the use of a core barrel.

During the design phase for a major interchange between U.S. Highway 290 and the Sam Houston Tollway, located approximately 17 mi northwest of downtown Houston, Texas, two test shafts were constructed and tested to assist in finalizing the design parameters (5). The site conditions and test shaft profiles are shown in Figure 1. The drilled shaft denoted Shaft 1 was purposely situated in an area of the interchange in which sandstone seams were known to exist, whereas the shaft denoted Shaft 2 was constructed in an area where the seams were known to be absent. The two test shafts were separated by about 1,500 ft, so that the soil layering was somewhat different at each test shaft location, as shown in Figure 1. *N* values in Figure 1 and the figures that follow represent uncorrected values, and *c_u* values are undrained shear strength values obtained from *UU* triaxial compression tests.

Each shaft at this site was constructed under bentonitic slurry controlled as recommended by Reese and O'Neill (3). Slurry samples from the bottom of the borehole just before concreting indicated the following:

- Unit weight: 64.3 and 69.3 pcf for Shafts 1 and 2, respectively;
- Sand content (by volume): Shaft 1, < 1 percent; Shaft 2, 11 percent; and

M. O'Neill, Department of Civil and Environmental Engineering, University of Houston, Houston, Tex. 77204-4791. L. Reese and S.-T. Wang, Lymon C. Reese and Associates, Austin, Tex. 78718. R. Barnes, Southwestern Laboratories, Inc., Dallas, Tex. 75222. M. Morvant, Louisiana Department of Transportation and Development, Baton Rouge, La. 70804-9245. M. Ochoa, McBride-Ratchliff and Associates, Houston, Tex. 77040.

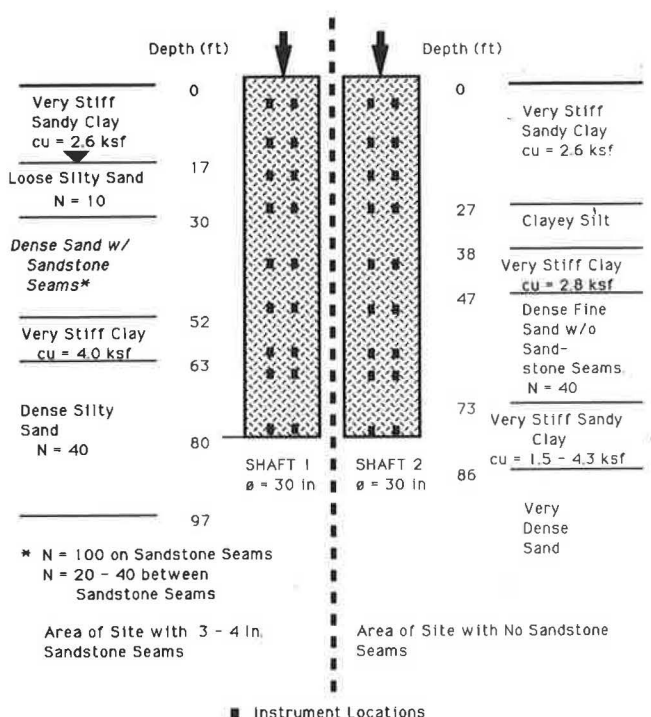


FIGURE 1 Soil and shaft profiles: test shafts at US-290/Sam Houston Tollway test site.

- Marsh funnel viscosity (sec/quart): Shaft 1, 37; Shaft 2, 49.

The slurry was displaced directly with tremie-placed, high-slump concrete, which is the standard procedure in the area. For these shafts, as well as the other four shafts described herein, concrete slump was in the range of 6 to 7 in., and the time between opening the borehole and completion of concreting was 5 to 7 hr.

Load-settlement relations for both shafts on the first cycle of loading are shown in Figure 2, which also contains the load-settlement curves for all other tests described in this paper. In all tests reported in this paper, loading was according to the quick test method, in which load increments of approxi-

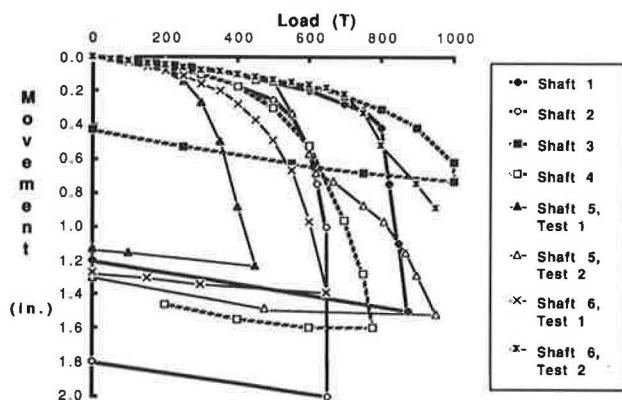


FIGURE 2 Load versus settlement: for test shafts.

mately 7 percent of the anticipated failure load are applied every 5 min. A second cycle of loading was applied to each shaft immediately after the completion of the first cycle to study potential loss of capacity due to large interface strains. In both shafts the second cycle of loading produced load-settlement relations almost identical to those on the first cycle, except that a slight increase of base resistance occurred in Shaft 1.

Shafts 1 and 2 (and Shafts 3, 4, and 5, described later) were instrumented with Mustran cells (6) to measure distribution of load along the shafts, and a load cell and displacement transducers at the shaft heads. Mustran cell locations are shown schematically in Figure 1. For the highest load applied to Shafts 1 and 2 for the first loading cycle, measured load distribution relations are shown in Figure 3. It is clear that load transfer was identical between shafts except for the depth range of roughly 30 to 52 ft. In that range, unit shaft load transfer was slightly more than twice as high in Shaft 1 as in Shaft 2. The major layer corresponding to the dense sand with interbedded sandstone seams in Shaft 1 (30 to 52 ft) was found at 47 to 73 ft in depth in Shaft 2. The ratio of shaft load transfer in these two corresponding layers was still about 2. Since differences in load transfer were minor elsewhere, it is argued that the differences in slurry composition in the two shafts had very little effect on shaft load transfer.

Base resistance in these two shafts will be described in a separate section.

SITE B—LIME HILLS FORMATION

The Lime Hills Formation is a component of the Wilcox Group, a heterogeneous system of formations deposited in Eocene times. It consists mainly of calcareous clay, silty clay, and seams and lenses of fine sand, some of which are cemented. Lignite seams also appear near the top of the formation. During the design phase of the I-20/I-49 interchange, 4 mi west of downtown Shreveport, Louisiana, two test shafts, here denoted Shaft 3 and Shaft 4, were constructed and load tested (7). The soil profiles at the location of each test shaft are indicated on Figure 4. Shaft 3 was placed in an area within the footprint of the interchange where thin seams of both sandstone and lignite were found, and Shaft 4 was placed in

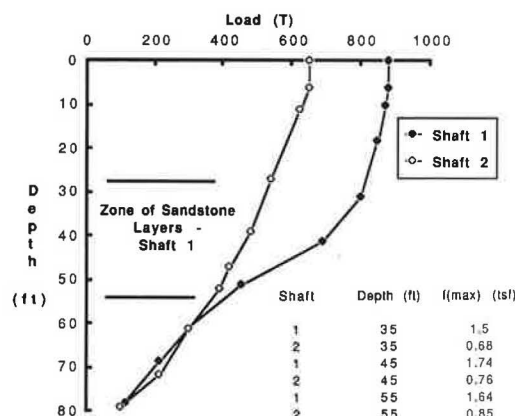


FIGURE 3 Load versus depth: Shafts 1 and 2.

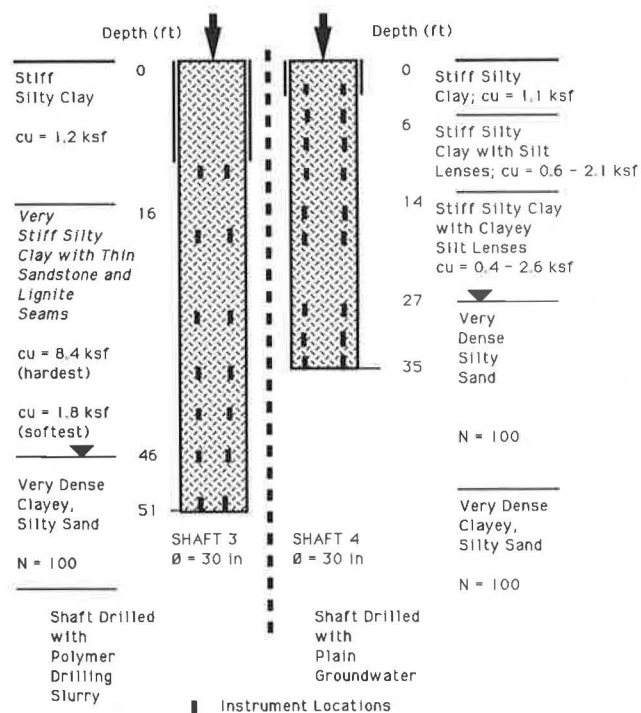


FIGURE 4 Soil and shaft profiles: Test Shafts 3 and 4 at I-20/I-49 Interchange test site.

an area where no such inclusions existed. The lignite was somewhat softer and more brittle than the clay, whereas the sandstone was somewhat stronger than the clay in which it was included. No samples could be obtained for definitive strength tests. Each shaft was designed to penetrate to a very dense sand layer found consistently, but at varying elevations, over the site. The elevation of the soil surface at Shaft 3 was 9 ft below that at Shaft 4, so that the surface of the very dense sand was about 20 ft lower at Shaft 3 than at Shaft 4. As with Shafts 1 and 2, the test locations were about 1,500 ft apart.

The piezometric surface appeared to be at the top of the very dense sand at both test locations, and the overlying strata were dry. Shaft 4 was drilled first, without the use of casing (other than surface casing) or drilling slurry. When the very dense sand was penetrated, some groundwater flowed into the borehole to about the top of the sand layer, but the hole remained stable, which indicates the presence of at least some cohesion in the sand. The shaft was concreted using tremie methods. To avoid a collapse of Shaft 3, the entire hole was drilled under polymer drilling slurry, in this case a PHPA emulsion. During drilling, the expected thin sandstone and lignite seams, not encountered in Shaft 3, were found within the clay between depths of 16 and 46 ft. After completion of the borehole the polymer slurry was allowed to remain unagitated for 30 min to allow sand to settle out, following which the base was cleaned and the shaft concreted using tremie methods. Bottomhole samples of the slurry taken after 30 min of settling indicated a unit weight of 62.5 pcf, a sand content of < 1 percent, and a Marsh funnel viscosity of 30 sec/quart. Shaft 3 was cased in the top 11 ft, and bond was broken between the casing and soil to account for later excavation at

that location. Both shafts were instrumented with Mustran cells at the locations indicated.

Load-settlement curves for the two test shafts are shown in Figure 2. Clearly, Shaft 3 carried the greater load with the lesser settlement. The reason for the higher capacity appears to be increased unit load transfer in the stiff clay layer with sandstone and lignite seams, greater contact area along the sides of the shaft, and higher unit base resistance (described later). Measured load distribution relations for Shafts 3 and 4 at the maximum load applied are given in Figure 5. No significant effect of the sandstone and lignite seams can be presumed in Shaft 3, however, since the clay matrix was about 50 percent stronger at Shaft 3 than at Shaft 4, which is the approximate difference in unit load transfer. It appears that the stiffer sandstone and softer lignite in effect each canceled the strengthening or weakening effect of the other.

SITE C—EAGLE FORD FORMATION

The Eagle Ford Formation is a Cretaceous-aged marine deposit consisting mainly of laminated clay shales. Embedded within the Eagle Ford are occasional seams of calcite and bentonite. The bentonite seams, which are seldom more than 3 in. thick, are much softer than the shale. During installation of drilled shafts, this formation can normally be penetrated, without the use of casing or slurry, using soil augers, owing to the horizontal bedding and frequency of the laminations (10 to 20 to the inch).

Two test shafts were installed at the site of the GTE World-wide Operations headquarters building in Irving, Texas, 15 mi northwest of downtown Dallas (8). Two objectives were established for the testing: (a) determine the effect of the presence of thin bentonite seams on the shaft resistance in the clay-shale and (b) determine whether simple rifling of the borehole could increase shaft resistance substantially. One other important detail is noted: about 20 ft of overburden soils had been removed at the location of the test shafts, exposing unweathered clay-shale, only about 1 week before the shafts were installed and 3 weeks before the shafts were load tested.

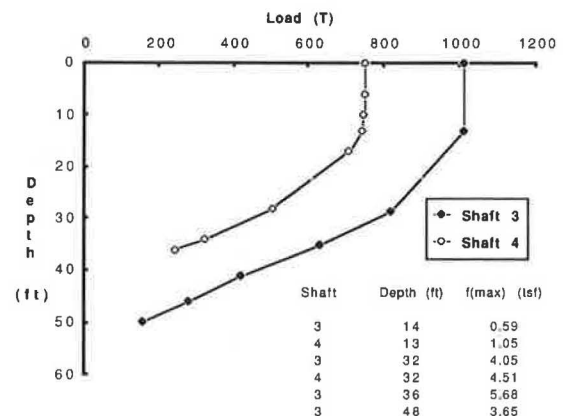


FIGURE 5 Load versus depth: Shafts 3 and 4.

Figure 6 shows the geomaterial and shaft profiles for the two test shafts. Bentonite seams appeared within the clay-shale formation in the depth range of 36 to 41.5 ft. The general groundwater surface was well below the base elevation of the test shafts, although a few seeps from perched water were encountered at various elevations during drilling. The geomaterial profiles can be considered identical at both shaft locations, because the shafts were only about 20 ft apart.

Shaft 5 was drilled with normal drilling procedures (without casing or drilling fluid), except that the top 26 ft was cased off and bond broken between the shaft and soil. This permitted the test section to include the zone with bentonite seams. Shaft 5 was instrumented with Mustran cells at the locations indicated. Shaft 6, on the other hand, was drilled using normal procedures and then rifled using a simple 1-in. long side cutter affixed to the drilling auger. Rifling was done on a pitch of about 3 ft, and two separate passes were made so that two separate rifled grooves, estimated to be about 0.75 in. deep, were developed on the borehole wall. Shaft 6 was not instrumented. Both Shafts 5 and 6, however, were cast with voids beneath their bases so that it would be possible to produce failure in side resistance at loads below the capacity of the available testing system (1,000 tons). Each void was vented to the atmosphere to prevent air pressure buildup. With the void it was possible to determine the average unit shaft load transfer in the contact zone for Shaft 6.

Load-settlement relations for two cycles of loading are shown in Figure 2. A reference of zero settlement is used for the beginning of each test, although the accumulated deflection of the shafts at the beginning of the second cycle of loading was about 5 in., as the shafts were pushed slowly down to a

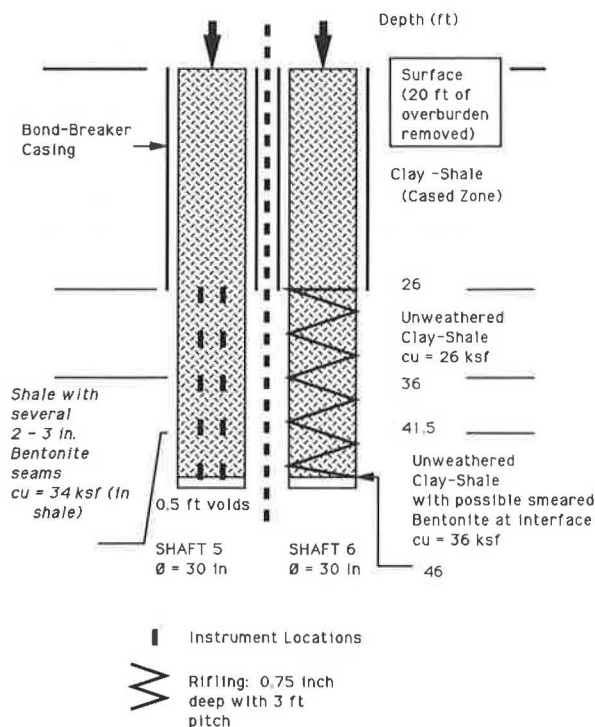


FIGURE 6 Soil and shaft profiles: Test Shafts at GTE test site.

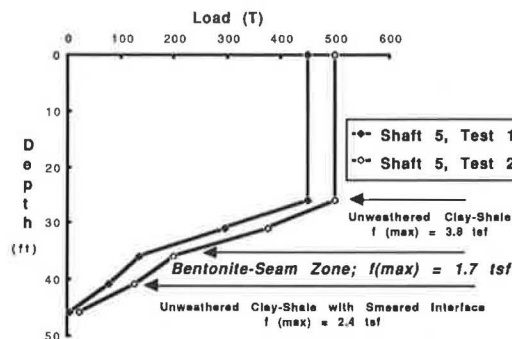


FIGURE 7 Load versus depth: Shaft 5, load and reload.

point at which the shaft base was just above the bottom of the borehole prior to unloading and beginning the second cycle of loading. Cyclic loading was used to observe whether degradation of side shear occurred with large deformations during relatively rapid loading. Both shafts were considerably stiffer during reloading than during initial loading despite the fact that no base resistance existed during either sequence. This behavior, which is not typical of drilled shafts in the Eagle Ford shale, appears to be because the shale had been recently unloaded by excavation of overburden, resulting in the opening of the horizontal laminations, which were apparently again closed by the initial loadings. It is also evident that Shaft 6 carried considerably more load during initial loading than did Shaft 5 at a given settlement, once the settlement exceeded about 0.1 in. This phenomenon is apparently due to the effects of borehole rifling.

The load distribution at failure for both loading cycles in Shaft 5 (denoted Test 1 and Test 2) are shown in Figure 7. Reduced load transfer is seen in the zone in which the bentonite seams are embedded and also below that zone, compared with the load transfer in the zone of unweathered shale above. The only explanation for the reduced load transfer in the zone below the bentonite zone is that bentonite clay cuttings were carried down with the auger and smeared on the sides of the borehole for some distance below the deepest bentonite seam. It is also seen in Figure 7 that little difference in shaft load transfer occurred between the two cycles of loading despite the fact that the accumulated shear displacement was more than 5 in. for Test 2.

COMPARATIVE SIDE AND BASE UNIT LOAD TRANSFER RELATIONS

Representative relations between unit shaft load transfer (shear stress), f , and local shaft movement, w , from among the first cycle loadings on the instrumented shafts at Sites A and C, are shown in Figure 8. The f - w curves for comparable layers for Shafts 1 and 2, with and without sandstone seams, clearly indicate that the sandstone seams had a major reinforcing effect on the dense sand at the site, although more deflection was required to mobilize the full resistance when the sandstone seams were present. On the other hand, in Shaft 5, the bentonite seams clearly reduced the ultimate load transfer, but their presence also significantly reduced the local settle-

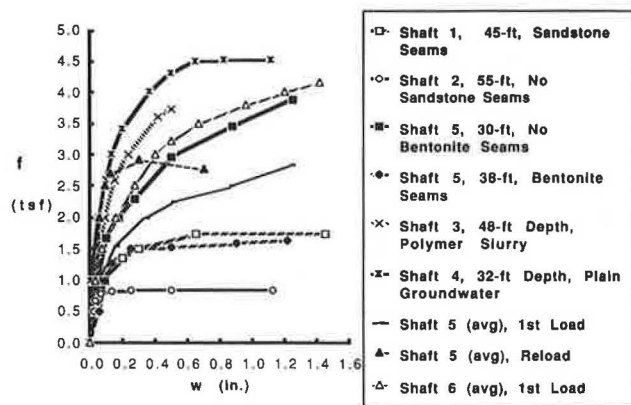


FIGURE 8 Comparative unit side load transfer relations.

ment required to mobilize full shaft resistance. In the unweathered clay-shale, full unit shaft resistance had not yet been mobilized at a settlement of 1 in.

Comparative f - w relations are also shown in Figure 8 for the lower very dense sand layer at Site B. The relations are almost identical, indicating no discernible difference in shaft behavior between drilling with natural groundwater and drilling with polymer slurry.

For Site C the average shaft unit load transfer relations over the entire depth of contact are compared for the two shafts in Figure 8, since no depthwise determination of f - w curves was possible in Shaft 6. The initial average f - w relations are of similar shape for both shafts, except that f values are about 40 percent larger at corresponding values of w for Shaft 6, the rifled shaft, for $w > 0.1$ in. Comparative f - w relations are shown for Shaft 5 during initial loading and reloading, indicating the result of the effect speculated earlier that initial loading had closed laminations that had opened during site excavation. No loss of ultimate shaft resistance can be observed between the two loadings.

Relations of net unit base load transfer (q) to base settlement (w) measured for Shafts 1 through 4 are given in Figure 9. Shaft 1 (founded in dense sand) developed an ultimate unit base resistance of 19 tsf at a settlement of 3 in., or 10

percent of the shaft diameter. According to Reese and O'Neill (3), a value of 24 tsf would be expected on the basis of the SPT N value. Their correlative expression for base resistance is $q(ult) (tsf) = 0.6N \leq 45$ tsf. The difference is minor and the cause of the difference is unknown. It may have been associated with the relatively small size of the test shaft, the need to use bentonitic slurry, and the difficulty of cleaning the bases of relatively small shafts constructed under slurry. The base of Shaft 2 at Site A was in a sandy clay material. The ultimate base resistance was 22 tsf, developed at a movement of about 1.25 in., or 4 percent of the shaft diameter. According to Reese and O'Neill (3), a value of 16 tsf would have been expected on the basis of an average value of c_u of 3.5 ksf in the base layer. The correlative expression for base resistance is $q(ult) = 9 c_u$. The small overprediction of capacity may have been because the sandy clay drained slightly during loading.

Shafts 3 and 4 were both founded in a very dense sand. Drilling reports indicated that the sand was siltier at Shaft 3, although the SPT blow counts at both locations were identical. The interpreted ultimate base resistance for Shaft 4 is approximately 53 tsf, compared with 45 tsf predicted by Reese and O'Neill (3). However, for Shaft 3 the ultimate base resistance is only 22 tsf, about half of the predicted value, and it occurred at a settlement of 0.5 in., or 1.7 percent of the shaft diameter, which is characteristic of undrained or partially drained behavior, perhaps due to the presence of silt at that location.

Shafts 5 and 6 were not designed to evaluate base resistance. However, Shaft 5 was pushed during Test 2 until approximately 57 tsf of base resistance was developed, with no indication that bearing capacity failure was impending.

EXPERIMENTALLY DERIVED CORRELATIVE FACTORS

A number of procedures exist whereby predictions of ultimate unit shaft and base resistance can be made. Reese and O'Neill (3), whose work is representative, cite several expressions for shaft and base resistance. Those for base resistance have already been indicated.

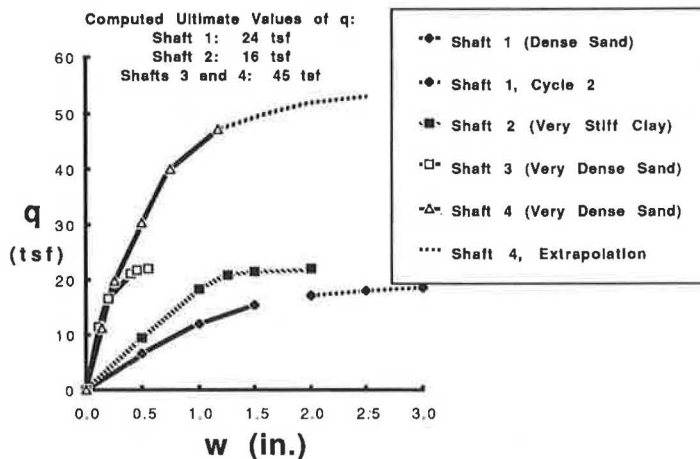


FIGURE 9 Unit base load transfer relations.

For shaft resistance, four expressions are used for soil and soft rock:

$$f_{\max} = \alpha c_u \text{ (in clay)} \quad (1)$$

where $\alpha = 0.55$ except in the top 5 ft and bottom diameter of the shaft, where $\alpha = 0$;

$$f_{\max} = [1.5 - 0.135 (z)^{0.5}] \sigma'_v = \beta \sigma'_v \text{ (in sand)} \quad (2)$$

where z = depth in feet and σ'_v = vertical effective stress;

$$f_{\max} = \kappa q_u \text{ (in very soft shale)} \quad (3)$$

where q_u is the unconfined compressive strength of shale cores and κ is a correlation factor, traditionally taken as 0.15; and

$$f_{\max} = \mu [q_u (\text{psi})]^{0.5} \text{ (in harder shale)} \quad (4)$$

where μ is typically recommended to be 2.5.

Equation 4 was adapted from Horvath and Kenney (9) and is predicated on massive rock with no weak seams and no special roughening of the borehole wall. Generally, in shale, f_{\max} is evaluated from both Equations 3 and 4, and the smaller value is used.

Values of correlative parameters α , β , κ , and μ backcalculated from the loading tests described in this paper are given in Table 1. Values for these parameters recommended by

TABLE 1 SUMMARY OF CORRELATIVE FACTORS FOR UNIT SHAFT RESISTANCE

Site	Shaft	Layer	Avg. $f(\text{max})$ (tsf)	Correlative Factors			
				α	β	κ	μ
290/Tollway	1	Dense sand with sandstone seams (depth = 30 - 52 ft)	1.6	-	0.88 [0.64]	-	-
	2	Dense sand without sandstone seams (depth = 47 - 73 ft)	1.0	-	0.42 [0.45]	-	-
	1	Very stiff sandy clay (depth = 0 - 17 ft)	0.60	0.46 [0.55]	-	-	-
	2	Very stiff sandy clay (depth = 0 - 27 ft)	0.62	0.48 [0.55]	-	-	-
120/149	3	Very dense sand (depth = 46 - 51 ft) (polymer slurry)	3.7	-	1.3 [0.56]	-	-
	4	Very dense sand (depth = 27 - 35 ft) (plain water)	4.7	-	2.4 [0.74]	-	-
	3	Very stiff silty clay with sandstone / lignite seams (depth = 16 - 46 ft) (polymer slurry)	2.5	[insufficient soil test data to evaluate correlative factors]			
	4	Very stiff silty clay with no sandstone / lignite seams (depth = 6 - 27 ft) (plain water)	1.5	[insufficient soil test data to evaluate correlative factors]			
GTE	5	Unweathered shale (depth = 26 - 36 ft)	4.2	-	-	0.16 [0.15]	3.1 [2.5]
	5	Shale / bentonite seams (depth = 36 - 41 ft)	1.7	-	-	0.049 [0.15]	1.1 [2.5]
	5	Shale / smeared face (depth = 41 - 46 ft)	2.0	-	-	0.056 [0.15]	1.3 [2.5]
	5	Average (26 - 46 ft) (unrilled)	2.9	-	-	0.10 [0.15]	2.0 [2.5]
	6	Average (26 - 46 ft) (rilled)	4.2	-	-	0.15 [0.15]	2.8 [2.5]

[] Indicates value computed from data base in Reese and O'Neill (3)

Range of correlative factors from data base in (3):

α - [] value $\pm 25\%$

β - [] value $+50\%/-25\%$

κ - [] value $\pm 25\%$

μ - [] value $+100\%/-25\%$

Reese and O'Neill (3), which were evaluated from analysis of a data base of 41 large test shafts, are shown in brackets immediately below the values derived from the tests. At Site A, the sandstone seams increased β to a value about one-third greater than is normally recommended, whereas the value is very close to that recommended where sandstone seams were absent. At Site B β was 2.5 to 3.5 times the value recommended in the lower dense sand, probably because the sand possessed some cohesion or cementation. No clear adverse effect of the use of the polymer slurry is seen. At Site C, Factor κ was about as recommended and Factor μ was slightly greater than is recommended in the unweathered shale with no rifling. Where bentonite seams were encountered and in the zone immediately below, these factors were considerably below the recommended values. Rifling increased the average shaft load transfer by 40 percent over the unrifled shaft and restored Factors κ and μ to their recommended values (or slightly above) in spite of the presence of the bentonite seams.

CONCLUSIONS

The following conclusions can be drawn from analysis of the full-scale loading tests described in this paper. It is not suggested that they can be generalized to other sites, but they serve to point out the magnitude of the effects of relatively minor anomalies in the subsurface profile and in the method used to construct the shafts on the load transfer behavior in drilled shafts.

1. Inclusions of sandstone seams no thicker than 3 to 4 in. and making up less than 10 percent of the thickness of the layer increased the β factor for a dense sand layer by about one-third over that in a comparable layer without such inclusions.

2. Thin, hard sandstone and soft, brittle lignite seams included within the same layer of stiff clay appeared to have mutually canceling effects.

3. The use of polymer slurry during construction appeared to produce load transfer and settlement behavior comparable with construction under plain groundwater.

4. Inclusions of bentonite seams no thicker than 3 in. and composing less than 10 percent of the thickness of the layer decreased the κ and μ factors by about two-thirds compared with similar factors in that part of a clay-shale formation not containing the bentonite seams. Load transfer in the zone below the bentonite layers also appeared to be adversely affected.

5. Unloading of horizontally laminated clay-shale by removal of about 1.25 tsf of overburden pressure before the

construction of drilled shafts caused drilled shaft settlements at full mobilization of side load transfer to be much larger than is normally expected.

6. Rifling of the borehole wall by using a simple side cutter on the drilling auger increased unit side resistance by about 40 percent in clay-shale.

ACKNOWLEDGMENTS

The authors are indebted to the following agencies and companies, which sponsored or coordinated the tests described in this paper: Harris County Toll Road Authority, Louisiana Department of Transportation and Development, Bell Bottom Foundation Company, GTE Realty Company, and H. C. Beck, Inc. The authors also acknowledge the valuable assistance of Edmundo Majano and Roy Henson of the University of Houston in acquiring and reducing much of the data.

REFERENCES

1. J. H. Long and S. Schimel, Drilled Shafts—A Database Approach. *Proc., Foundation Engineering: Current Principles and Practices*, Vol. 2, ASCE, June 1989, pp. 1091–1108.
2. F. H. Kulhawy, T. D. O'Rourke, J. P. Stewart, and J. F. Beach. Transmission Line Structure Foundations for Uplift-Compression Test Loading; Load Test Summaries. *Appendix to EPRI Final Report EL-2870*, Electric Power Research Institute, June 1983.
3. L. C. Reese and M. W. O'Neill. *Drilled Shafts: Construction Procedures and Design Methods*. Report FHWA-HI-88-042. Federal Highway Administration, U.S. Department of Transportation, July 1988.
4. M. J. Tomlinson. Piles in Weak Rock (preface). *Geotechnique*, Vol. 26, March 1976, pp. 1–4.
5. W. R. Barker and L. C. Reese. *Instrumentation for Measurement of Axial Load in Drilled Shafts*. Report 89-6. Center for Highway Research, The University of Texas at Austin, Austin, Nov. 1969.
6. L. C. Reese, M. W. O'Neill, and S.-T. Wang. *Drilled Shaft Tests, Interchange of West Belt Toll Road and US 290; Harris County, Texas*. Final report. Lyman C. Reese and Associates, Inc., Austin, Tex., July 1988.
7. S.-T. Wang, L. C. Reese, M. W. O'Neill, and E. Majano. *Axial-Load Tests of Drilled Shafts on I-49/I-20 Interchange; Route I-49; Caddo Parish, Louisiana*. Lyman C. Reese and Associates, Inc., Austin, Tex., March 1991.
8. *Field Load Tests; Full-Sized Drilled Shafts: GTE TELOPS*, Irving, Texas. Report 89-1015. Southwestern Laboratories, Inc., Dallas, Tex., Dec. 1989.
9. R. G. Horvath and T. C. Kenney. Shaft Resistance of Rock-Socketed Drilled Piers. *Proc., Symposium on Deep Foundations*, ASCE, Oct. 1979, pp. 182–214.

Publication of this paper sponsored by Committee on Foundations of Bridges and Other Structures.

Comparison of Measured and Computed Drilled Shaft Capacities Based on Utah Load Tests

RICHARD PRICE, KYLE M. ROLLINS, AND EDWARD KEANE

Fourteen load tests were performed at a number of bridge sites in Utah in an effort to reduce foundation costs. Soil profiles generally consisted of cohesionless materials. Failure loads were determined from load-settlement data using four methods, including Davisson's method, double tangent method, 1 in. criterion, and the Hirany and Kulhawy's method. Hirany and Kulhawy's method typically failure loads 30 percent higher on the average than Davisson's method. Load capacities were computed using equations proposed by Reese and O'Neill/FHWA, Meyerhof, and Reese et al. Good agreement between measured (Davisson's method) and computed capacities was generally found for the FHWA and Meyerhof methods, but the Reese et al. method significantly underpredicted capacity. The design methods were generally more than 25 percent conservative in comparison with the Hirany and Kulhawy failure load interpretation. In three cases involving dense gravels and weathered shale the design equations resulted in computed capacities that were only 20 to 30 percent of the measured failure load.

In an effort to reduce construction costs, the Utah Department of Transportation has performed a number of load tests on drilled shafts. Since the measured capacities were generally higher than estimates based on design equations, it was possible to increase design loads for each shaft. The costs of load testing proved to be insignificant when compared with savings that were realized by reducing the size and number of drilled shafts needed. It is estimated that the testing program resulted in cost savings of more than \$890,000 in the first 2 years. Unfortunately, load testing cannot be performed for each project, and reliance must be placed on load prediction equations. Reasonable capacity prediction equations are necessary to provide safe yet economical shaft foundations for highway structures.

OBJECTIVES AND SCOPE OF INVESTIGATION

Since the inception of the Utah load testing, Reese and O'Neill (1) prepared a drilled shaft handbook with new design recommendations for nationwide use. This work was prepared for the Federal Highway Administration in cooperation with the Association of Drilled Shaft Contractors. In addition, a new procedure for interpreting axial load test data was proposed by Hirany and Kulhawy (2).

It was determined that a review and summary of the existing load test information would be valuable for (a) establishing a computer data base on the performance of drilled shafts in Utah that could be updated with future tests, (b) evaluating the variation in load capacity on the basis of various load test interpretation procedures, (c) determining the suitability of various design equations for Utah soil conditions, and (d) making recommendations for future load testing procedures.

Since the load test data set was not used in the development of any of the design methods, it provides an independent check on the various design methods proposed for use. Load test data can easily be compared with calculated values based on design methods. By comparing load test data with these methods, one can better determine which method is more applicable for a given circumstance.

In this study, four methods were used for determining failure load from the load versus settlement test data. The procedures are Davisson's Method (3), the double tangent method (4,5), Hirany and Kulhawy's Method (2), and Terzaghi's simple procedure (6), which defined failure at a settlement of 1 in. The results from each interpretation procedure were compared with three prediction methods. The load prediction equations included those proposed by Reese and O'Neill (1), Meyerhof (7), and Reese et al. (8).

DESCRIPTION OF DATA BASE CHARACTERISTICS

A total of 14 load tests were available for evaluation, and additional tests are presently under way. In each case the function of the foundation was to support a bridge or overpass.

Geotechnical Conditions

The subsoils at the test sites generally consisted of granular materials deposited by stream flow along with some man-made fill. Clay layers were encountered in only two of the tests. Subsoils encountered at these sites ranged from very loose to very dense sand and gravel with some silt and cobbles. SPT N values ranged from 10 to 80 but were typically between 20 and 40 blows/ft. A fairly typical boring log in the alluvial deposits is shown in Figure 1. Most of the shaft tips were founded in soil; however, in three cases, the shaft tips were

R. Price, RB&G Engineering, P.O. Box 711, Provo, Utah 84603. K. M. Rollins, Civil Engineering Department, Brigham Young University, 368 CB, Provo, Utah 84602. E. Keane, Materials and Research Division, Utah Department of Transportation, 4500 S. 2700 W., Salt Lake City, Utah 84119.

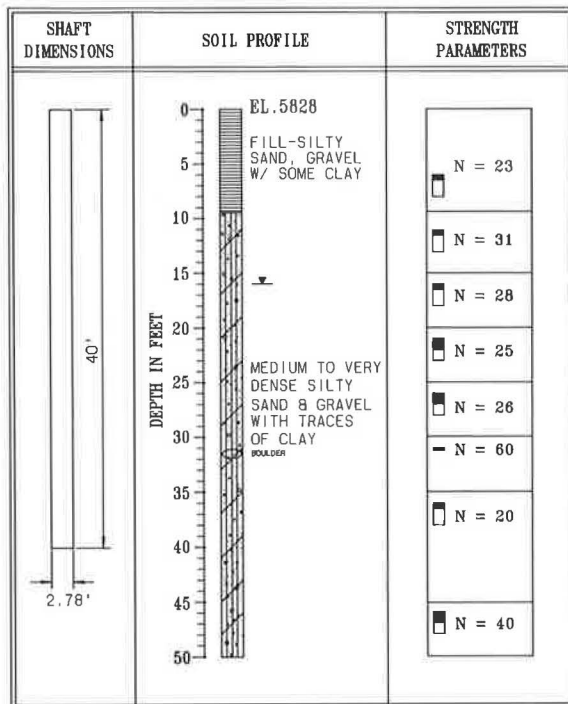


FIGURE 1 Typical boring log in granular alluvial soils at Test Site 6, F-493-North.

terminated in shale bedrock. Borehole logs showing soil type and groundwater elevation were available for each structure along with SPT N values, gradations, and limited shear test results. Unconfined compressive strength data were obtained for the shafts founded in shale. At Test Site 10, the unconfined compressive strength of the shale was between 1 and 2 tsf, whereas at the site for Tests 11 and 12 the compressive strength varied from 300 to 3,000 psi.

Drilled Shaft Types and Construction

Each drilled shaft was cast-in-place portland cement concrete with reinforcement provided by rebar cages. In each case the

holes were excavated with rotary drilling machinery. Excavations in granular soils below the water table were carried out using casing, which was subsequently removed. In most cases, however, the dry method of construction was used. The top of each test shaft was finished smooth and level to within $\pm \frac{1}{32}$ in. The unconfined compressive strength, f'_c , was typically between 4,000 and 5,000 psi. Table 1 gives the location and dimensions of the test shafts. Where concrete volumes were known, an equivalent diameter was determined on the basis of the volume of concrete placed, and this diameter was used in subsequent calculations. Whereas this procedure is an approximation, it accounts for overages in excavation diameter assuming that the shaft wall is relatively uniform with depth.

Load Testing Procedure

Hydraulic load cells were used to apply the desired loads, and the load frame was capable of applying loads of just over 1,100 tons. Each test shaft was placed between two larger reaction shafts that anchored the load frame. The average of two extensometer readings was used to monitor settlement at the top of the shaft.

Test-Shafts F-493-South and F-501-1 were loaded in 25-ton increments at 3-min intervals. All three of the C-630 shafts were loaded in 50-ton increments at 2.5-min. intervals, and the remainder were loaded in 50-ton increments at 3-min. intervals. Settlement readings were taken immediately before increasing the load. Test shafts with the word "skin" on the end of the location are specially cast shafts with compressible material at the tip to prevent end bearing, thus measuring skin resistance only.

Instrumentation

To evaluate the total load being carried at different depths along the shaft, vibrating wire strain gauges were installed at regular depth intervals in several of the test shafts. The gauges were attached to the rebar cage in sets of 3 at each depth and protected. Figure 2 shows the load in the pile as a function

TABLE 1 SUMMARY OF DRILLED SHAFT GEOMETRIES INCLUDED IN THE DATA BASE

Ref.	Structure	Effective Depth (Ft.)	Diameter (Ft.)	Equivalent Dia. (Ft.)
1	F-435-East	23.3	2	2.09
2	F-435-West	20.6	2	2.08
3	F-438	40.8	3	3.08
4	F-489	40	2	
5	F-489-Skin	40	2	
6	F-493-North	40	2.5	2.78
7	F-493-South	40	2.5	3.14
8	F-495-North	40	2.5	2.62
9	F-495-South	40	2.5	3.82
10	F-501-1	33	2	
11	F-501-2	33	2	
12	C-630Skin	14	2	
13	C-769-1	38.5	3	
14	C-769-2	28	3	

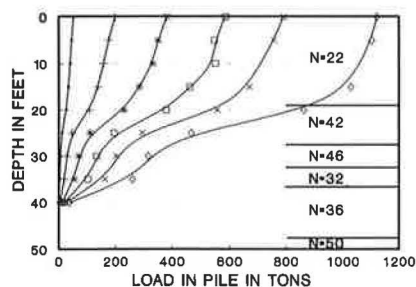


FIGURE 2 Load in pile versus depth below ground for Load Test 5, F-489, SKIN.

of depth for Load Test 5 along with the SPT N values at each depth. This shaft was designed to have skin friction, and this is borne out by the strain gauge data. Whereas a few of the strain gauge readings provided useful information, the majority were unreliable and exhibited increasing inconsistency with increasing load. Readings made little to no sense when the applied load approached 400 tons, which was well before failure. The cause of the problem is undetermined.

LOAD TEST INTERPRETATION

Description of Methods Used

To evaluate the predictions of ultimate capacity given by the various design methods, the ultimate capacity must first be determined from the field load test. Four methods for interpreting the ultimate load were used: Davisson's double tangent, Hirany and Kulhawy, and Terzaghi's 1 in. of settlement criteria.

Davisson's Method

The Davisson method (3) is a graphical method that defines the ultimate capacity as that load corresponding to the settlement that equals the elastic compression of the shaft plus 0.15 in. plus a factor equal to the diameter of the shaft in inches divided by 120. In computing the elastic compression, the modulus of elasticity, E_c , of the concrete was evaluated using the equation $E_c = 57,000(f'_c)^{0.5}$ (psi), and the shaft area was based on the effective diameter. Figure 3 shows an example of this method using the data from Load Test 1.

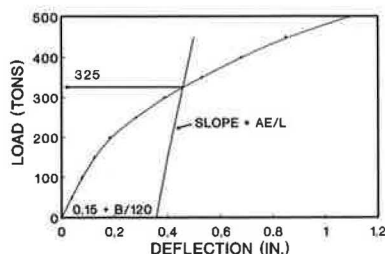


FIGURE 3 Failure load interpretation using Davisson (1972) method.

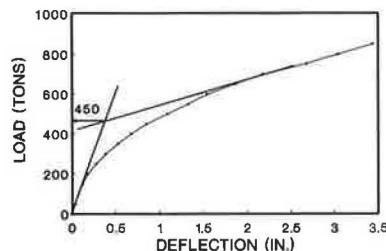


FIGURE 4 Failure load interpretation using double tangent method.

Double Tangent Method

The double tangent method (4) is a graphical method that defines the ultimate capacity as the load corresponding to the intersection of lines drawn tangent to the initial and failure portions of the load-settlement curve. This method involves subjectivity in determining the failure slope. An example of the method for Load Test 1 is shown in Figure 4.

One in. of Settlement

A typical parameter for design of shallow foundations is to limit settlement to 1 in. Terzaghi (6) also suggested that this value be used in determining the ultimate capacity of drilled shaft foundations. In evaluating the load test data, defining ultimate capacity as the load corresponding to 1 in. of settlement was also considered.

Hirany and Kulhawy's Method

After a detailed review of 41 methods proposed in the literature for determining failure loads from load tests, Hirany and Kulhawy (6) proposed that the ultimate capacity be defined at the beginning of the final straight line portion of the load-displacement curve. This point was found to correspond to a displacement of 4 percent of the shaft diameter, and this value has been used as the failure criterion. Failure displacements would therefore be defined at displacements of 1 and 2 in. for shaft diameters of 2 and 4 ft. Figure 5 shows an example of this method, again using the data from Test 1. Hirany and Kulhawy indicate that if the failure load is divided by a factor of safety of 2, the average displacement is about

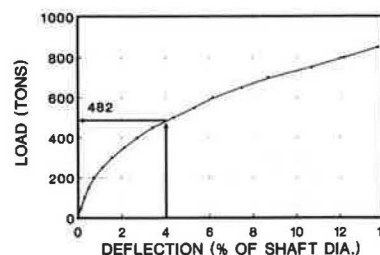


FIGURE 5 Failure load interpretation using Hirany and Kulhawy (1989) method (4 percent of shaft diameter).

TABLE 2 SUMMARY OF MEASURED AND COMPUTED CAPACITIES USING VARIOUS METHODS FOR EACH DRILLED SHAFT IN THE DATA BASE

SUMMARY SHEET								
Test Locations		Load Test Results				Prediction Methods		
		(Tons)				(Tons)		
Ref	Site	Hirany and Kulhawy	Davisson	Double Tangent	1*	FHWA	Reese	Meyerhof
1	F-435-E	490	325	450	480	244	162	262
2	F-435-W	355	220	200	355	226	150	339
3	F-438	1100	905	730	1000	716	382	811
4	F-489	1020	995	570	1100	302	238	226
5	F-489SKIN	> 1100	> 1100	610	> 1100	234	134	76
6	F-493-N	580	365	390	500	395	295	330
7	F-493-S	650	445	480	570	495	336	464
8	F-495-N	505	325	325	455	265	158	328
9	F-495-S	915	565	535	710	533	376	561
10	F-501	> 1100	> 1100	625	> 1100	291	205	372
11	C-630SKIN	1010	645	355	1100	662	N.A.	N.A.
12	C-630	1015	600	355	1100	837	N.A.	792
13	C-769-1	770	550	295	680	443	333	289
14	C-769-2	520	338	280	455	262	262	232

0.4 percent of the shaft diameter or about 10 percent of the failure displacement. This method is simple and non-subjective, yet it takes into account the shape of the load-displacement curve. It does not, however, account for elastic compression of the shaft. This factor is not critical for the Utah data base, since all shafts are less than 40 ft long.

Comparison of Methods

A summary of the ultimate capacity as determined by each of the four methods is given in Table 2. In addition, a comparison of the average ultimate capacity for each method is shown graphically in Figure 6. On the average, the double tangent method yielded the lowest failure load and was about 70 percent of the average Davisson failure load. The 1-in. criterion, on the other hand, yielded a failure load 26 percent higher on average than the Davisson failure load. The capacity values obtained with the 1-in. settlement criterion and the Hirany and Kulhawy method were typically within about 10 percent of one another. The agreement of the last two methods results because the Hirany and Kulhawy failure criterion

(4 percent of the shaft diameter) is about equal to 1 in. for the shaft diameters under consideration. The primary reason for the higher loads with the latter two methods is that the methods define failure at a somewhat higher deformation. In two cases, failure as defined by all but the double tangent method was not achieved, although the total applied load exceeded just over 1,100 tons. In these two cases the double tangent method estimated the failure load at around 600 tons, which is a conservative estimate considering that deformations were very low at this load.

If the failure load interpreted with the Hirany and Kulhawy 4 percent criterion is divided by a factor of safety of 2, the allowable load typically corresponded to a deformation of 1 percent of the shaft diameter. This is about 2.5 times greater than the 0.4 percent average reported for the data base used by Hirany and Kulhawy (2).

DESIGN METHODS

Three design methods were used to predict ultimate capacities: Reese and O'Neill/FHWA, Meyerhof, and Reese. Each method for computing ultimate capacity, Q_u , uses the following basic equation:

$$Q_u = Q_s + Q_b \quad (1)$$

where Q_s equals shaft resistance and Q_b equals base or tip resistance.

Reese and O'Neill/FHWA Method

The Reese and O'Neill/FHWA method (1) is a semiempirical method developed by Reese and O'Neill on the basis of a

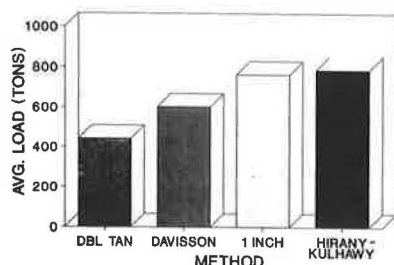


FIGURE 6 Comparison of average load determined by various failure load interpretation methods.

large data base of drilled shaft load tests. The method establishes design procedures for shafts in sands, clays, and rock. Side resistance in clay is calculated by multiplying the product of the shear strength and surface area by the factor α , whereas side resistance in sand is calculated by multiplying the product of the surface area and the average effective stress by a factor β . The factor α is 0.55 for all points along the shaft except from ground surface to a depth of 5 ft, and the bottom one diameter of the drilled shaft or one stem diameter above the top of the bell, where α is zero.

The factor β is obtained from the equation

$$\beta = 1.5 - 0.135\sqrt{z} \quad 1.2 \geq \beta \geq 0.25 \quad (2)$$

where z is the depth below the ground surface in feet. Limiting values of load transfer in side resistance have been set at 2.75 tsf for clays and 2.0 tsf for sands. These limits are not theoretical but are the largest values that have been measured. It is interesting to note that the β factor is independent of sand density or shear strength.

The ultimate unit end bearing pressure, q_b , for drilled shafts in saturated clay is calculated using the equation

$$q_b = N_c \cdot c_{ub} \quad q_b \leq 40 \text{ tsf} \quad (3)$$

In Equation 3,

$$N_c = 6.0 \cdot \left[1 + 0.2 \cdot \left(\frac{\text{length}}{\text{base diam.}} \right) \right] \quad N_c \leq 9 \quad (4)$$

and c_{ub} is the average undrained shear strength of the clay computed one to two diameters below the base.

The net ultimate unit end bearing pressure, q_b , for drilled shafts in sand (tsf) is 0.6 times the N_{SPT} (uncorrected), with a limit of 45 tsf. When base diameters exceed 50 in., q_b is reduced by a factor of q_b divided by the base diameter.

Meyerhof's Method

The Meyerhof method (7) is an empirical procedure based on load test data and allows computation of capacity in sands and clays. The ultimate unit skin friction f_s of drilled shafts in sands is computed using the equation

$$f_s = \frac{N}{100} \leq 0.5 \text{ tsf} \quad (5)$$

where N is the standard penetration blow count along the shaft. This is half of the skin friction specified for driven piles in sands. Skin friction in clays is taken as zero when the base is resting on soil significantly stiffer than the soil around the stem. For shafts in soils with no soil of exceptional stiffness below the base, the average cohesion is reduced by a factor of 0.15 to 0.6 and applied to the area of the shaft 5 ft beneath the ground surface to 5 ft above the base or top of bell.

The ultimate tip bearing pressure, q_u , in tsf is calculated with the following equation:

$$q_u = \frac{0.133 \cdot \bar{N} \cdot D}{B} \leq q_1 \quad (6)$$

where

$$\bar{N} = C_N \cdot N,$$

N = standard penetration resistance (blow/ft) near shaft tip,

$$C_N = 0.77 \log_{10} 20/p \quad (\text{for } p \geq 0.25 \text{ tsf}),$$

p = effective overburden stress at shaft tip (tsf),

D = depth drilled into granular bearing stratum (ft),

B = width or diameter of shaft (ft), and

q_1 = limiting point resistance (tsf), equal to $1.33N$ for sand and N for nonplastic silt.

According to Meyerhof, the ultimate tip resistance for driven piles in sands is three times the value allowed for drilled shafts in similar materials. Tip resistance values for clays are taken as 9 times the undrained strength near the base as with the other methods.

Reese et al. Method

The Reese et al. method (8) is a forerunner of the FHWA method discussed previously. This method is felt to be somewhat conservative relative to the newer FHWA method. In clay, the skin friction is obtained by multiplying the undrained strength by an α factor, which varies from 0 to 0.5 depending on the method of construction. For skin friction in sand, Reese multiplies the average effective stress by a lateral pressure factor K and by the tangent of the friction angle of the sand. K is 0.7 from the ground surface to a depth of 25 ft, 0.6 from 25 to 40 ft, and 0.5 for depths exceeding 40 ft.

End bearing in clay is computed as it is with the FHWA method. In sand the following equation is used:

$$Q_p = \frac{q_p}{\alpha_p} A_p \quad (7)$$

where

q_p = 0 for loose sand, 16 tsf for medium dense sand, and 40 tsf for dense sand; and

α_p = base reduction factor to limit base settlement to 1 in. = $0.6B$ (B in feet).

Capacity Computation Results

A simple spreadsheet program was developed to facilitate computations for each shaft and reduce the potential for errors. Figure 7 shows a typical spreadsheet printout containing soil profile information, capacity estimates for each method, and various factors that were used in the calculations. Table 2 presents a summary of results for each of the methods used. A review of this table indicates that Reese's method generally yields the lowest estimate of the ultimate capacity and is typically 60 percent of the maximum value predicted by the three methods. Meyerhof's method gave the maximum computed capacity in 64 percent of the cases, whereas the FHWA procedure yielded the highest capacity in 36 percent of the cases. On the average, the difference between the capacity computed by the FHWA and the Meyerhof procedures was about 20 percent.

TEST F-493 - NORTH #6

LENGTH 40
DIAM. 2.78

					FHWA		REESE			MEYERHO		
GAMMA	SOIL	DEPTH	AREA	Po'	B	Qs	K	PHI	Qs	N	Qs	
120	SAND	0	9.5	83.0	0.285	1.2	28.4	0.7	34	11.2	23	19.08
120	SAND	9.5	16	56.8	0.765	1.018	44.2	0.7	36	22.1	29	16.46
57.6	SAND	16	20	34.9	1.018	0.927	33	0.7	36	18.1	29	10.13
57.6	SAND	20	35	131.0	1.291	0.792	134	0.6	35	71	25	32.75
52.6	SAND	35	40	43.7	1.573	0.673	46.2	0.6	33	26.8	20	8.734
57.6	SAND	40	0	0.0	1.063	0	0	0.7	36	0	30	0
			0	0.0	0.487	0	0	0.7		0		0
			0	0.0	0.487	0	0	0.7		0		0
			0	0.0	0.487	0	0	0.7		0		0
			0	0.0	0.487	0	0	0.7		0		0
			0	0.0	0.487	0	0	0.7		0		0
TOTAL SIDE						286		149		87		
TOTAL TIP						109		146		N br	25	23
Q ult.						395		295			330	

* NOTE: All Q values are in Tons.

FIGURE 7 Typical spreadsheet printout containing required input data and computed capacity for each prediction method.

Ease of Application

Because it is simple and straightforward for the design engineer and yields reasonable results, the FHWA method is favored over the other methods presented in this study. The β factor needed for unit skin resistance in sand is simple to apply, and the α factor for clays is a constant or zero. For unit tip resistance, the uncorrected N value is multiplied by a constant with a limiting value and in clays is almost always nine times the undrained cohesive strength of the clay. With a knowledge of the blow counts for sands and the undrained strength for a soil profile, one can quickly calculate the estimated ultimate load capacity of a drilled shaft.

COMPARISON OF COMPUTED AND MEASURED CAPACITY

Comparisons between the computed and measured load capacities are a function of both the load test interpretation procedure and the prediction equation. Comparisons are presented for the three computation procedures and both the Davisson method and the Hirany and Kulhawy method (similar values to the 1-in. criterion).

Plots comparing the measured ultimate capacity using Davisson's method (x-axis) and the calculated ultimate capacity (y-axis) for the FHWA, Meyerhof, and Reese et al. procedures are presented in Figures 8, 9, and 10, respectively. Boundaries representing 25 percent conservative and 25 percent unconservative estimates of the load capacity are shown to provide perspective regarding the degree of error in the computed values.

A review of Figures 8 through 10 indicates that the FHWA method probably provides the best agreement with measured values but the Meyerhof method also provides relatively good agreement. The Reese et al. procedure typically underestimated the measured capacity by more than 25 percent and, therefore, represents a more conservative estimate of capacity. For three cases the measured capacity was four to five

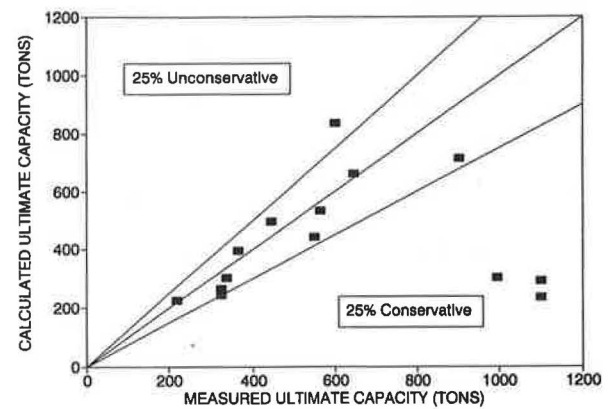


FIGURE 8 Comparison of measured capacity using Davisson method (1972) and computed capacity using FHWA method (1987).

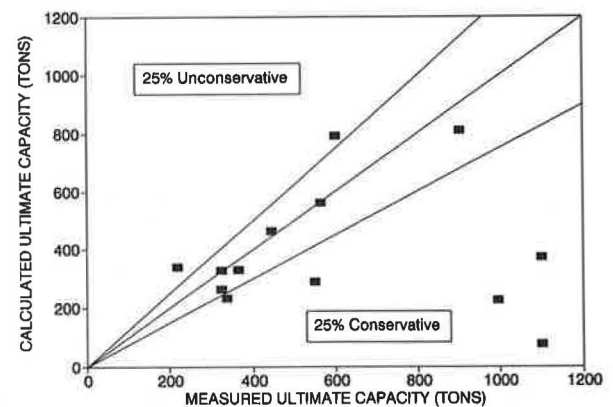


FIGURE 9 Comparison of measured capacity using Davisson method (1972) and computed capacity using Meyerhof method (1976).

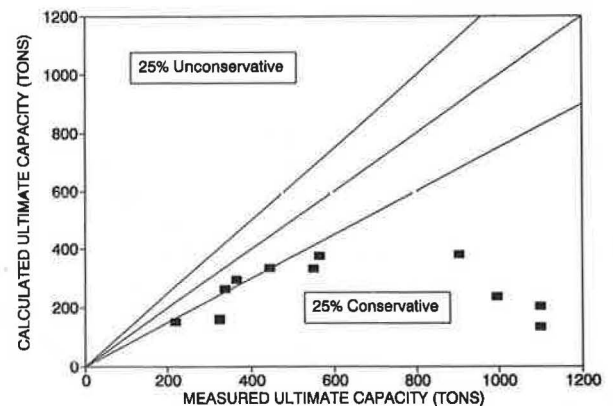


FIGURE 10 Comparison of measured capacity using Davisson method (1972) and computed capacity using Reese et al. method (1976).

times higher than the computed capacity regardless of the design equation used. In two of these cases, the soils were relatively dense sandy gravels (Load Tests 4 and 5) and the higher resistance can generally be attributed to side friction. The third shaft penetrated into weathered shale, and the higher resistance can be attributed to increased base resistance.

Comparisons between computed capacity and measured load capacity based on Hirany and Kulhawy's technique are presented in Figures 11 through 13. As indicated previously, the Hirany and Kulhawy (4 percent shaft diameter) interpretation is the least conservative of the various interpretation methods used. Because the FHWA design method is based on a failure load at a settlement of 5 percent of the shaft diameter, the computed capacities would be expected to be somewhat unconservative. The results in Figure 11, however, show the opposite. Almost all the load tests were more than 25 percent conservative. The Meyerhof method was similar to the results for the FHWA method, whereas the Reese method was more conservative. The results in Figures 11 through 13 indicate that increases in computed capacities of 25 percent or more are justifiable in cases where the higher deformation level associated with the Hirany and Kulhawy failure criteria can be tolerated.

CONCLUSIONS

Three methods for predicting the ultimate load capacity for drilled shafts (FHWA, Reese's, and Meyerhof's) were evaluated with load test data. Four load test interpretation methods were used in the comparison: Davisson's, double tangent, Hirany and Kulhawy's, and 1 in. of settlement. On the basis of the results, the following conclusions are possible.

1. The load test interpretation suggested by Davisson generally yields ultimate capacities about 37 percent higher than those from the double tangent method. The Hirany and Kulhawy interpretation procedure produces ultimate capacities typically 25 percent higher than the Davisson method because failure is defined at a higher deformation level.

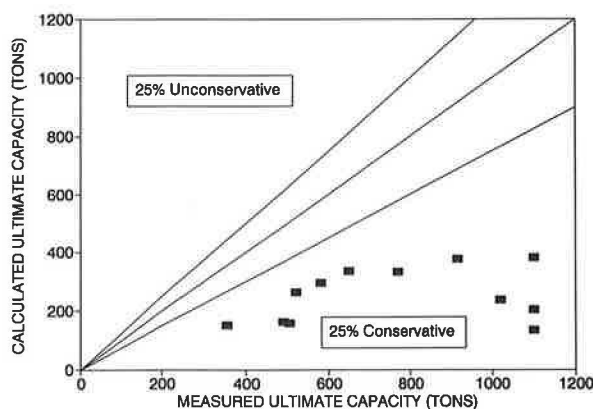


FIGURE 11 Comparison of measured capacity using Hirany and Kulhawy (1989) method and computed capacity using FHWA method (1987).

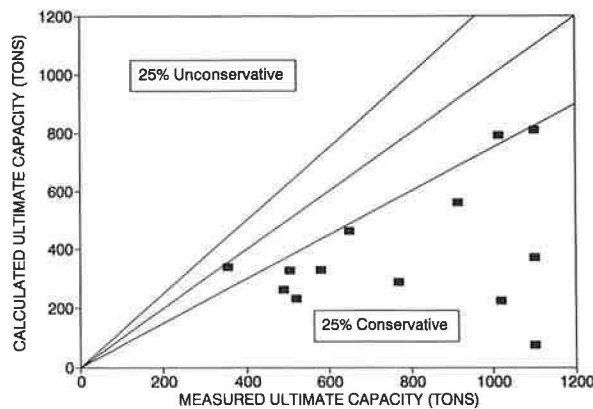


FIGURE 12 Comparison of measured capacity using Hirany and Kulhawy method (1989) and computed capacity using Meyerhof method (1976).

2. Whereas the Davisson method is a common interpretation procedure, the higher capacities provided by the Hirany and Kulhawy method may be acceptable if somewhat greater shaft deformations are tolerable (about 1 in. for 2-ft-diameter shafts at failure, 0.25 in. with $FS = 2$).

3. Of the three prediction methods used, the FHWA method yielded the most favorable results for both ease of application and correlation with measured load capacity (on the basis of Davisson's method). In no case did the FHWA method overestimate measured capacity by more than 25 percent, and there were few cases where it was more the 25 percent conservative.

4. The Meyerhof equation also predicted load capacities in good agreement with measured capacities, but Reese's method typically underpredicted measured values by more than 25 percent.

5. In comparison with the Hirany and Kulhawy interpretation, almost all the computed capacities were more than 25 percent conservative, suggesting that modifications of the design equations may be appropriate for gravelly soils.

6. Additional load tests should be performed in gravelly soils to allow appropriate modifications of existing design equations.

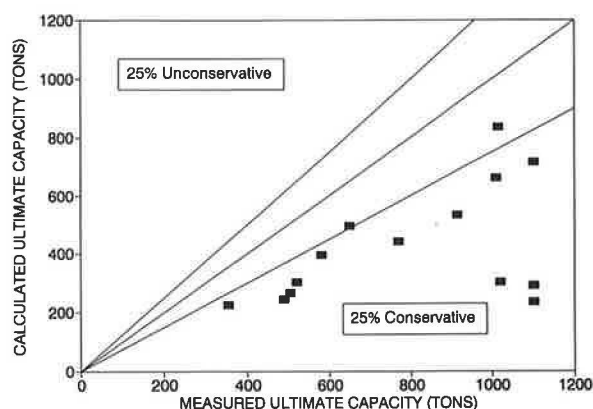


FIGURE 13 Comparison of measured capacity using Hirany and Kulhawy method (1989) and computed capacity using Reese et al. method (1976).

ACKNOWLEDGMENTS

This work was funded by a grant from the Utah Department of Transportation and supplementary support from the Association of Drilled Shaft Contractors. This support is gratefully acknowledged.

REFERENCES

1. L. C. Reese and M. W. O'Neill. *Drilled Shafts: Construction Procedures and Design Methods*. Federal Highway Administration, U.S. Department of Transportation, McLean, Va., 1987.
2. A. Hirany and F. H. Kulhawy. Interpretation of Load Tests on Drilled Shafts, Part 1: Axial Compression. *Proc., Foundation Engineering Congress*, Vol. 2, ASCE, Evanston, Ill., 1989, pp. 1132–1149.
3. M. T. Davisson. High Capacity Piles. *Proc., Innovations in Foundation Construction*, ASCE, Illinois Section, 1972.
4. C. I. Mansur and J. M. Kaufman. Pile Tests, Low-Sill Structure, Old River, Louisiana. *Journal of the Soil Mechanics and Foundation Division*, ASCE, Vol. 82, No. SM5, Oct. 1956, pp. 1079–11079-33.
5. H. D. Butler and H. E. Hoy. *User's Manual for the Texas Quick-Load Method for Foundation Load Testing*. Report IP 77-8. Federal Highway Administration, U.S. Department of Transportation, 1977.
6. K. Terzaghi and R. B. Peck. *Soil Mechanics in Engineering Practice* (corrected printing of 2nd ed.) John Wiley and Sons, New York, 1968.
7. G. G. Meyerhof. Bearing Capacity and Settlement of Pile Foundations. *Journal of the Geotechnical Engineering Division*, ASCE, Vol. 102, No. GT3, March 1976, pp. 195–228.
8. L. C. Reese, F. T. Touma, and M. W. O'Neill. Behavior of Drilled Piers Under Axial Loading. *Journal of the Geotechnical Engineering Division*, ASCE, Vol. 102, No. 5, May 1976, pp. 493–510.

Publication of this paper sponsored by Committee on Foundations of Bridges and Other Structures.

Dynamic Testing of Drilled Shafts

MOHAMAD HUSSEIN, FRANK TOWNSEND, FRANK RAUSCHE, AND GARLAND LIKINS

Concerns about the construction of drilled shafts lead to the need for further testing. To confirm the basic design, a static test is often performed to verify capacity. The ultimate capacity will be the lesser of the soil resistance and the structural strength, affected by the integrity of the shaft. Because of the high costs associated with static tests, however, they cannot be justified economically to verify integrity. Several integrity testing techniques exist, but many require substantial preparation, which translates into extra cost. Lower-cost alternatives to static testing and integrity inspection are presented that can be applied to any drilled shaft or driven concrete pile selected for testing after construction. The capability of this technology on a true Class A prediction event is demonstrated.

Dynamic testing of drilled shafts for bearing capacity (1,2) and integrity (3,4) provides a reliable and economical alternative to static load testing. These methods have been used worldwide for many years because of their low costs and time-saving advantages. Integrity testing using the low strain pulse-echo method is particularly fast and cost-effective, allowing the method to be used for essentially all shafts on a site. If bearing capacity needs to be confirmed, high strain testing methods involving dropping a weight on the shaft are used. The speed of this test and its relatively low cost allow a much larger percentage of the shafts to be tested than with any other method.

The case history reported here (5,6) was initiated by the Association of Drilled Shaft Contractors, Inc. (ADSC), and the Florida Department of Transportation and was conducted at and under the supervision of the University of Florida in Gainesville. To promote the use of drilled shafts, ADSC has supported efforts to demonstrate the reliability of dynamic testing methods as an affordable method for verification of the adequacy of the shafts. A load test shaft and two reaction shafts were monitored dynamically for integrity evaluation. The test shaft was also subjected to high strain dynamic testing and then to a full-scale static load test for comparison of capacity.

SITE DETAILS

Both the north and south reaction shafts (NRS and SRS, respectively) were 30 in. in diameter and 44 ft long. The load test shaft (LTS) was constructed with a 28-in. OD casing to

20 ft and then advanced to 45 ft with a 24-in. auger (area reduction to 73 percent of the 28-in.-diameter section). This detail was not communicated to the testing engineer until after the integrity test revealed this "defect." All shaft details are shown in Figure 1 along with a representative soil boring. The soil profile consisted of 30 ft of sand (SPT N values 6 to 13) over an approximately 6-ft clay layer ($N \approx 10$) under which limestone (unconfined compression strength $q_u = 13.6$ tsf) was encountered.

LOW STRAIN INTEGRITY TESTS

All three shafts were tested before the static test (the LTS was also tested after the high strain tests) to evaluate structural integrity using the pile integrity tester (PIT) and so-called low strain methods. In this test, a small hand-held hammer was used to strike the shaft and generate a low force or low strain stress wave. An accelerometer was attached to the top of the shaft, and the signal was amplified and digitized for further analysis using the PIT software. Results of several blows were integrated to velocity, averaged, digitally applied exponentially over time, and then plotted. Figure 2 shows the signal before and after amplification for the LTS and demonstrates that reflections from major cross section changes or the shaft bottom were enhanced and more easily interpreted using this amplification function. Figure 3 shows the processed results of low strain tests conducted on the LTS before and after the high strain tests. Since results were similar, it was concluded that the high strain test (discussed subsequently) did not damage the shaft. The test was also performed with an instrumental hammer, allowing computation of both force and velocity. These signals were converted by Fourier transformation to the frequency domain yielding the mobility curve. These results are beyond the scope of this paper. A thorough discussion of the testing method, analysis, and limitations is presented elsewhere (4).

The PIT velocity-depth results shown in Figure 1 are prepared by first converting the time scale to a length scale using the typical value of 13,000 ft/sec for the wave speed. After the input pulse, the curve for a uniform shaft should be free of sharp variations until the reflection from the shaft bottom. For the LTS (Figure 1), the positive velocity increase at 23 ft is interpreted as a cross section reduction and matches the designed reduction at the end of the 28-in. casing. The next major velocity increase is at 46 ft, which corresponds approximately to the design length (changing the assumed wave speed from 13,000 to 12,700 ft/sec would change the apparent length to the design value of 45 ft). If the shaft length is accurately known, the wave speed can be calculated if a clear

M. Hussein, Goble Rausche Likins and Associates, Inc., 8008 South Orange Avenue, Orlando, Fla. 32809. F. Townsend, University of Florida, Room 345, Weil Hall, Gainesville, Fla. 32611. F. Rausche, Goble Rausche Likins and Associates, Inc., 4535 Emery Industrial Parkway, Cleveland, Ohio 44128. G. Likins, Pile Dynamics, Inc., 4535 Emery Industrial Parkway, Cleveland, Ohio 44128.

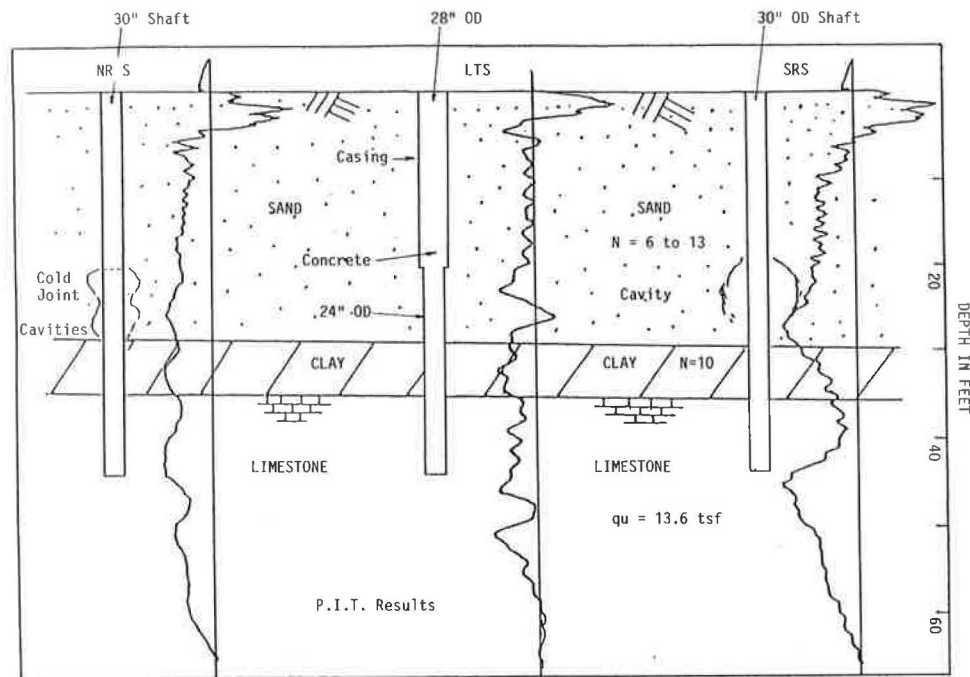


FIGURE 1 Pile and soil profiles along with PIT results.

toe reflection is observed. In this example, the time between impact and toe reflection leads to the previously mentioned wave speed of 12,700 ft/sec, which is well within commonly observed bounds of 10,000 to 15,500 ft/sec. However, this reflection occurs also at twice the depth of the cross-sectional reduction, and the second reflection could be caused by (a) reflection from the shaft bottom, (b) a secondary reflection from the midlength reduction, or (c) a combination of both. The greater negative amplitude near the shaft bottom for the test performed after the high strain testing are indicative of higher soil stiffness (Figure 3). The dynamic loading test cycles apparently compressed the soil under the shaft bottom and produced a stiffer strength response.

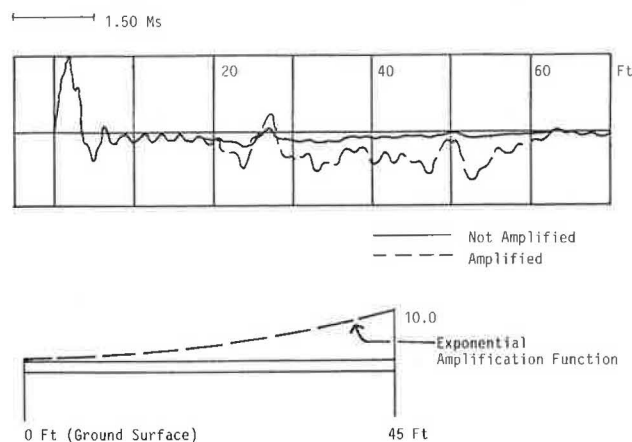


FIGURE 2 Top, pile top velocity histories (LTS) showing effects of data amplification; bottom, exponential amplification function versus shaft length.

The results of the PIT tests for the uniform reaction shafts also are shown in Figure 1. In neither case do the records indicate sharp cross-sectional reductions. The NRS test result shows a clear reflection from the shaft bottom. The SRS result shows a definite positive change in slope at this location, which for longer shafts with relatively high resistance is often interpreted as positive proof of the shaft length indicator. Although all shafts show some negative reflections, the negative reflection from about 25 ft in SRS was interpreted as a bulge or an increased cross section with subsequent return to the nominal diameter within the clay zone. The larger negative section in the PIT curve for the SRS between depths of 20 and 25 ft corresponds to the depth in which an observed high concrete take occurred during construction. All three shafts show a relative velocity increase near the limestone, indicating perhaps less overage in the shaft diameter due to the strength of this soil material.

HIGH STRAIN CAPACITY TESTS

The LTS was subjected to dynamic testing conforming to ASTM D4945 before static loading. High strain dynamic tests

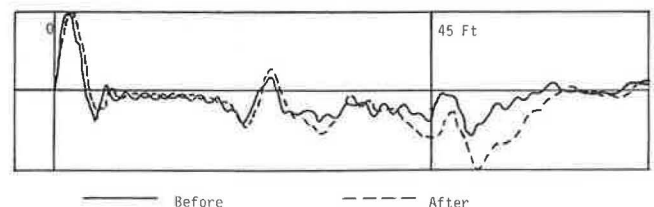


FIGURE 3 LTS velocity histories before and after high strain tests.

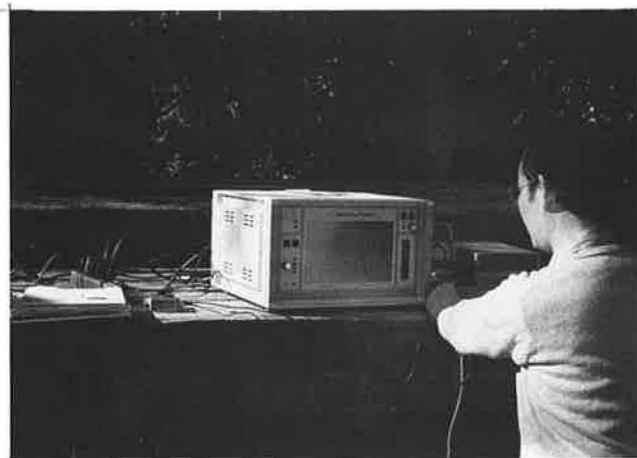


FIGURE 4 Clockwise from top left: Pileco 19.5-kip ram, GCPC Pile Driving Analyzer PIT low strain testing, instrumented pile, and cushion and striker plate.

were accomplished using a 9¾-ton drop weight supplied by Pileco of Houston. The weight was placed in a short set of swinging leads and operated by a small crane. The test consisted of four impacts with 3-, 7-, 8-, and 8-ft drop heights (i.e., with potential energies of 79.5, 136.5, 156, and 156 kip-ft). The weight struck a 3-in.-thick steel striker plate placed on top of an 8-in.-thick plywood cushion covering the top of the shaft. This configuration was designed by wave equation techniques to mobilize the expected soil resistance without causing damaging impact stresses. The impact assembly, cushion, and pile preparation are shown in Figure 4.

Dynamic capacity testing of the LTS involved the measurement of strain and acceleration approximately 3.5 ft below the shaft top. "Windows" were cut into the steel casing and the transducers were bolted directly to the concrete. The signals from the transducers were conditioned and converted to force and velocity by a Pile Driving Analyzer (PDA). The PDA was initially developed in the late 1960s for impact-driven piles and is a field testing and data acquisition system. It has worldwide acceptance in evaluating pile capacity, driving stresses, pile integrity, and hammer performance according to the Case method (7). It has also been used to evaluate

cast in situ shafts since 1973, with current extensive use on drilled shafts by many organizations worldwide (8). A variety of drilled shafts, auger piles, and even barrettes have been tested with the PDA (1,2).

The measured force and velocity traces are shown in Figure 5 for the four impacts. The corresponding maximum stresses at the pile top ranged from 0.96 to 1.54 ksi. Energies transferred to the pile top were 7.3, 13.1, 20.4, and 21.9 kip-ft, or up to 14 percent of the potential energies. Clearly, transfer efficiencies improved (from 9 to 14 percent) as the pile top cushion compressed. Substantial amounts of energy were lost because of winch inertia and pulley friction (ram suspended by two-part line). The Case method (a closed form solution evaluated by the PDA) predicted capacity for the four blows ranging from 564 to 679 kips (average of 637 kips). These records were then subjected to further analysis by CAsE Pile Wave Analysis Program (CAPWAP) (9), a program that calculates the total static resistance and its distribution and, on the basis of these values, a predicted static load-deflection curve for the shaft top. CAPWAP capacities for the four blows ranged from 610 to 665 kips (average 644 kips). CAPWAP also determined average quakes (elastic displacements) of

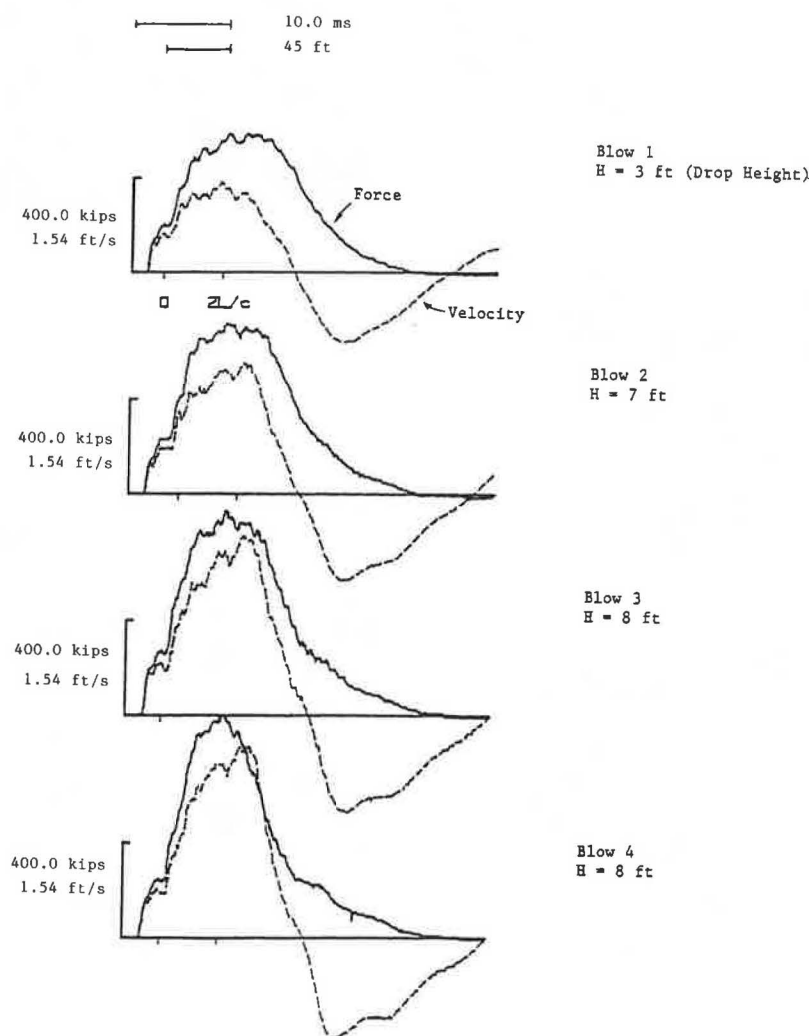


FIGURE 5 Measured pile top force and velocity for high strain capacity tests.

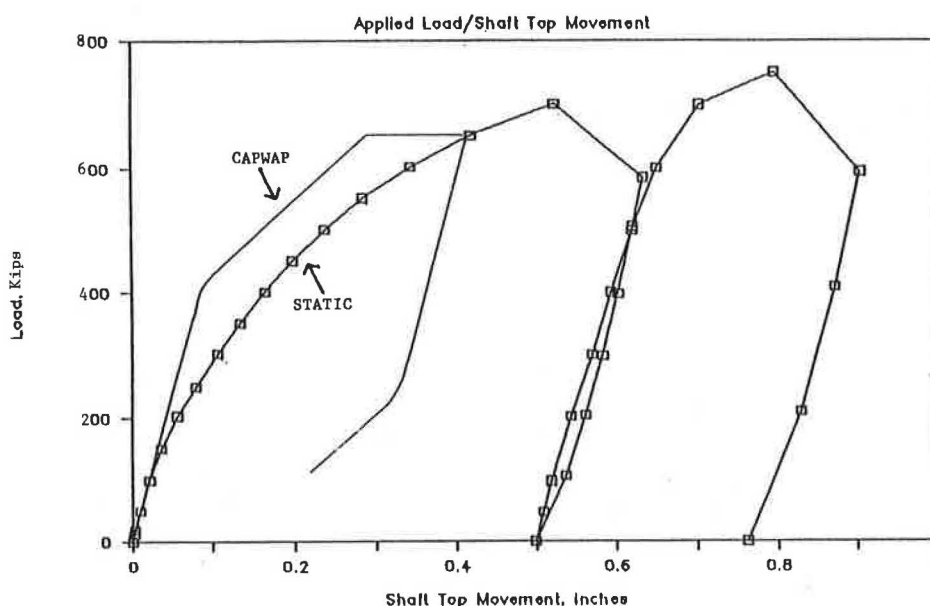


FIGURE 6 CAPWAP versus static load/top movement.

0.06 and 0.18 in. for skin and bottom, respectively, and Smith damping constants of 0.18 and 0.14 sec/ft. These results were reported to the University of Florida before obtaining knowledge of the static test results.

The LTS was subjected to a static load test after the dynamic tests were completed. The load test procedure followed the quick test method of ASTM D1143. The resulting load-deflection curve is shown in Figure 6. The shaft was loaded to a maximum load of 700 kips. If the Davisson limit load criterion is applied, the resulting failure load would be 600 kips. The shaft capacity predicted both dynamically and statically is in close agreement. A second static test cycle was then conducted to a maximum load of about 750 kips. CAPWAP load-deflection curves calculated from all four blows and the two curves from the static tests (after subtracting the creep movements) are combined in Figure 6.

CONCLUSIONS

Dynamic testing using low strain impacts by a hand-held hammer was successful in detecting planned and unplanned area changes in the constructed shafts. These area changes were independently discovered by the test engineer and verified through construction records. Thus, these methods can be of invaluable assistance in the quality assurance of drilled shaft foundations.

High strain dynamic testing for capacity evaluation did not cause damage to the shaft, as evidenced by the low strain integrity tests conducted both before and after the dynamic load tests. This result is not surprising since even the high strain impact stresses were less than 1.6 ksi in compression and 0.1 ksi in tension.

The dynamic loading apparatus performed well. A relatively low percentage (14 percent) of the hammer's potential energy was actually transferred to the shaft, probably because of losses in the cushion and the winch hoisting system. The

dynamic pile top records were easily acquired and evaluated with existing equipment and methods already well proven on driven piles. The bearing capacity calculated from the dynamic tests was in good agreement with the results from the static load test. Dynamic testing of drilled shafts has already been applied to numerous cast in situ shafts worldwide with good success and represents a cost-effective, quick alternative to static tests.

REFERENCES

1. F. Rausche and J. Seidel. Design and Performance of Dynamic Tests of Large Diameter Drilled Shafts. *Second International Stress Wave Conference*, Stockholm, Sweden, 1984.
2. J. Seidel and F. Rausche. Correlation of Static and Dynamic Pile Tests on Large Diameter Drilled Shafts. *Second International Stress Wave Conference*, Stockholm, Sweden, 1984.
3. F. Rausche, G. Likins, and M. Hussein. Pile Integrity by Low and High Strain Impacts. *Proc., Third International Conference on Stress Wave Theory to Piles*, Ottawa, Ontario, Canada, May 1988.
4. F. Rausche, R. K. Shen, and G. Likins. Comparison of Pulse Echo and Transient Response Pile Integrity Test Methods. Presented at the 70th Annual Meeting of the Transportation Research Board, Washington, D.C., Jan. 1991.
5. *Dynamic Tests of Drilled Shafts Performed at the Kanapaha Site on April 5, 1990*. Goble Rausche Likins and Associates, Inc.
6. F. C. Townsend, J. F. Theos, and M. Shields. *Good Testing of Instrumented Drilled Shaft*. FDOT Report FL/DOT/RMC/0496-2927. Tallahassee, Fl., 1991.
7. F. Rausche, G. G. Goble, and G. E. Likins. Dynamic Determination of Pile Capacity. *Journal of Geotechnical Engineering*, ASCE, 1985.
8. B. H. Fellenius, (ed.). *Proc., Third International Conference on Stress Wave Theory to Piles*. Ottawa, Ontario, Canada, May 1988.
9. G. E. Likins, M. Hussein, and F. Rausche. Design and Testing of Pile Foundations. *Proc., Third International Conference on Stress Wave Theory to Piles*, Ottawa, Ontario, Canada, May, 1988.

Publication of this paper sponsored by Committee on Foundations of Bridges and Other Structures.

Lateral Subgrade Modulus of Sands for Deep Foundations

DANIEL O. WONG

The common practice of designing laterally loaded deep foundations is either by means of the lateral subgrade modulus concept or by the lateral load transfer method. The lateral subgrade modulus for sands is a function of several factors including deflection, which itself is usually an unknown. The lateral load transfer method is readily available to analyze laterally loaded deep foundations by using p - y curves. However, p - y curves are complicated mathematical relations and by no means offer a simple representation of the pile-soil interaction. The concept of the equivalent subgrade modulus for sands, in which the nonlinear pile-soil characteristics are implicitly taken into account, is presented. Relationships of equivalent subgrade modulus versus dimensionless lateral load factor for sands are developed, and a design procedure is proposed. Comparison of solutions by the proposed design procedure and the lateral load transfer method is favorable.

The design of laterally loaded deep foundations typically requires the prediction of lateral deflection and induced bending moment of the foundation elements under applied loads. The analyses can be performed by means of the lateral subgrade modulus concept. The lateral subgrade modulus is a linear relationship of soil pressure and deflection. However, the lateral subgrade modulus is a function of depth for cohesionless soils (1). McClelland and Focht (2) also showed that soil responses to lateral loading are dependent on depth and pile deflection. A representative value of the lateral subgrade modulus may be assumed for a particular problem (3). A more rational approach to analyzing laterally loaded piles is to model the soils by uncoupled, nonlinear load transfer functions, widely known as p - y curves. A p - y relationship is a mathematical representation of the soil reaction and the lateral pile deflection per unit length at a particular location along the pile. A linear subgrade modulus with respect to depth can be obtained by an iterative procedure using p - y data (4). Numerical procedures using finite difference or finite element algorithms have been developed to incorporate the p - y criteria in the analyses of laterally loaded piles (5,6). However, such procedures require extensive numerical procedures such that the linear subgrade modulus method may be preferred in preliminary computations or for relatively simple design cases. Furthermore, a single subgrade modulus for a particular problem usually provides a better overall feeling or understanding of the pile-soil interaction than a series of p - y curves. Attempts have been made in the past to develop a simplified method for analyses of laterally loaded piles (7). The work presented offers a unique subgrade modulus for sands describing the pile-soil interaction for a specific laterally loaded pile condition.

The development of the equivalent subgrade modulus, k_{eq} , for sands under lateral loads is described. The equivalent subgrade modulus is a pile-soil relationship incorporating implicitly the effects of the lateral load and the nonlinearity of pile-soil interaction. A parametric study was conducted to develop the appropriate equivalent subgrade modulus by backcalculating with Broms's equation (3) using the required deflection obtained from a numerical model for the laterally loaded pile problem—COM 624 (6). Such methodology was used successfully to develop the equivalent subgrade modulus for laterally loaded piles in clays (8). Among the parameters investigated in this study are lateral load, pile stiffness, and soil properties. Both submerged and above-water conditions are considered. The design curves of k_{eq} versus the dimensionless lateral load factor for cohesionless soils are subsequently developed and a simple design procedure is proposed. Solutions for maximum pile deflection and maximum bending moment for laterally loaded piles in sands can be readily solved with accuracy comparable with the load transfer method.

BROMS'S EQUATIONS AND NONDIMENSIONAL SOLUTIONS

Presented in this section are the brief synopses of Broms's equations and the nondimensional solutions for solving laterally loaded piles in sands.

Broms's Equations

Broms (3) stated that for piles with the dimensionless depth of embedment of ηL larger than 4.0, the magnitude of the lateral deflection at the ground surface is unaffected by a change of the embedment length, L . η is defined as

$$\eta = \left(\frac{k}{EI} \right)^{0.2} \quad (1)$$

where k is the coefficient of subgrade reaction, assumed to be a function of relative density of soil only, and EI is the bending stiffness of the pile.

Terzaghi (1) has shown that the horizontal coefficient of subgrade reaction k_h at depth Z , for a pile with diameter B , in sand can be found as

$$k_h = k \frac{Z}{B} \quad (2)$$

Broms recommended that the lateral deflection at the ground surface, y_o , for a free-head long pile ($\eta L > 4.0$) be calculated as

$$y_o = \frac{2.40P}{k^{0.6}(EI)^{0.4}} \quad (3)$$

where P is the applied lateral load at the ground surface.

For a fully restrained long pile, where the slope at the pile head remains zero, the deflection at the ground surface is determined by

$$y_o = \frac{0.93P}{k^{0.6}(EI)^{0.4}} \quad (4)$$

Nondimensional Solutions

Nondimensional solutions for laterally loaded piles require an iterative procedure to achieve convergence of the relative stiffness factor, T , which is the reciprocal of η in Equation 1:

$$T = (EI/k)^{0.2} \quad (5)$$

The lateral deflection, y , and bending moment, M , of the pile can be obtained from the following equations:

$$y = A_y \frac{PT^3}{EI} + B_y \frac{MT^2}{EI} \quad (6)$$

$$M = A_m PT + B_m M \quad (7)$$

where A_y and B_y are deflection coefficients due to the applied lateral load P and the applied moment M , respectively, and A_m and B_m are moment coefficients due to the applied lateral load P and the applied moment M , respectively.

Depending on the value of the maximum depth coefficient, Z_{max} , the deflection and moment coefficients can be obtained at any depth along the pile. Coefficient charts are available in Matlock and Reese's paper (4). Z_{max} is defined as

$$Z_{max} = \frac{L}{T} \quad (8)$$

In the absence of an applied moment at the pile head, the maximum deflection and moment coefficients can be found in Table 1.

Using the maximum coefficients in Table 1, the maximum deflection and maximum moment of piles under the lateral loads can be calculated from Equations 6 and 7, respectively.

Both Broms's equations and the nondimensional solutions describe the soil resistance by a modulus k , which, as mentioned previously, is a function of the depth and magnitude of the lateral load. The estimation of the k value is usually a challenge to practicing engineers but is essential to the accuracy of the solution. This paper presents a representative k value, which implicitly accounts for the effects of pile depth, pile diameter, and the applied lateral loads, to be used directly in the Broms and nondimensional equations.

LOAD TRANSFER RELATIONSHIPS FOR SANDS

Nonlinear lateral load transfer relationships, termed p - y curves, are often used to represent the soil responses subjected to lateral loading. A brief description of four procedures to construct p - y curves for piles in sands, as presented by Murchison and O'Neill (9), is presented in the subsequent paragraphs. Details of the four procedures can be found in their respective references.

Procedure of Reese et al.

Reese et al. (10) introduced a p - y method based on the results of a series of field tests. A p - y curve constructed from this method consists of four segments as shown in Figure 1. The first segment is a linear relationship with a slope of kZ up to a point that can be determined by an empirical relationship, where Z is the depth of interest. k is a soil modulus and can be determined from the standard penetration test blow count. Correlations shown in Figures 2 and 3 are recommended. Figures 2 and 3 are modified by Murchison and O'Neill (9) from Gibbs and Holtz (11) and Meyer and Reese (12), respectively. The second segment is a parabola and terminates at a deflection of $B/60$, where B is the diameter of the pile. The curve continues in a straight line with a slope empirically determined and terminates at a deflection of $3B/80$ with soil resistance reaching an ultimate value, p_u . p_u remains unchanged as deflection increases for the fourth segment in the p - y curve. The ultimate soil resistance per unit of depth, ρ_u , can be calculated as the lesser value of Equations 9 and 10 and modified by an empirical parameter involving the pile, soil, and loading conditions.

$$p_u = \gamma z[B(K_p - K_a) + ZK_p \tan \phi \tan \beta] \quad (9)$$

$$p_u = \gamma BZ[K_p^3 + 2K_o K_p^2 \tan \phi + \tan \phi - K_a] \quad (10)$$

TABLE 1 SUMMARY OF MAXIMUM DEFLECTION AND MOMENT COEFFICIENTS DUE TO LATERAL LOAD ONLY (4)

Z_{max}	A_y		A_m	
	Free-head	Restrained-Head (Slope=0.0)	Free-head	Restrained-Head (Slope=0.0)
10	2.435	0.820	0.772	0.930
4	2.445	0.829	0.767	0.930
3	2.723	0.968	0.704	0.970
2.2	4.011	1.268	0.557	1.060

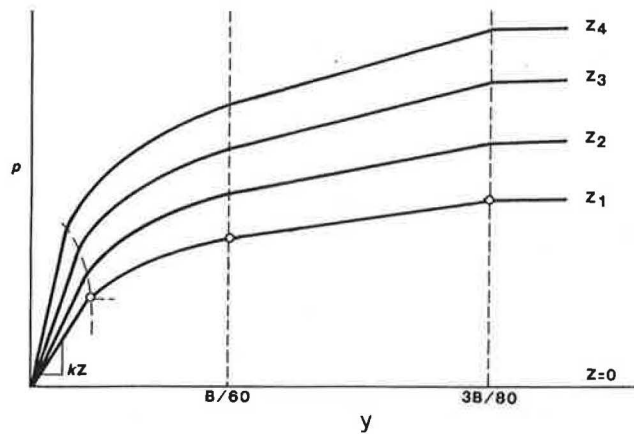


FIGURE 1 Characteristic shape of a family of p - y curves for procedure of Reese et al. (10).

where γ is the unit weight of soils and K_a and K_p are Rankine active and passive coefficient, respectively. K_o is the at-rest earth pressure coefficient, ϕ is the frictional angle, and β is determined as $45 + \phi/2$.

Bogard and Matlock's Procedure

This method (13) called for a modification of the first method by simplifying the calculation of p_u and using nondimensional charts to generate p - y curves. p_u can be determined as the minimum of the values given in Equations 11 and 12.

$$p_u = (C_1 Z + C_2 B) \gamma Z \quad (11)$$

$$p_u = C_3 B \gamma Z \quad (12)$$

The parameters C_1 , C_2 , and C_3 are related to the angle of internal friction of sands. The p - y curves are subsequently constructed using normalized charts.

Scott's Procedure

Scott (14) idealized the p - y curve into two linear segments. The first straight line segment terminates at a resistance value p_k with a slope of kZ . p_k can be determined from design curves of normalized resistance versus angle of internal friction; k can be found from the relationship presented in Figure 3. The second straight line segment starts with p_k with an empirically determined slope of $kZ/4$. There is no ultimate soil resistance value defined in this method.

Murchison and O'Neill Procedure

The p - y relationship characterized by this procedure (9) is a continuous hyperbolic tangent curve. This method is a reformulation of Parker's recommendation (15) on his experimental and analytical study of small diameter piles in sands. Murchison and O'Neill suggested that the characteristic p - y curve can be represented as

$$p = \eta A p_u \tanh \left[\left(\frac{kZ}{A \eta p_u} \right) y \right] \quad (13)$$

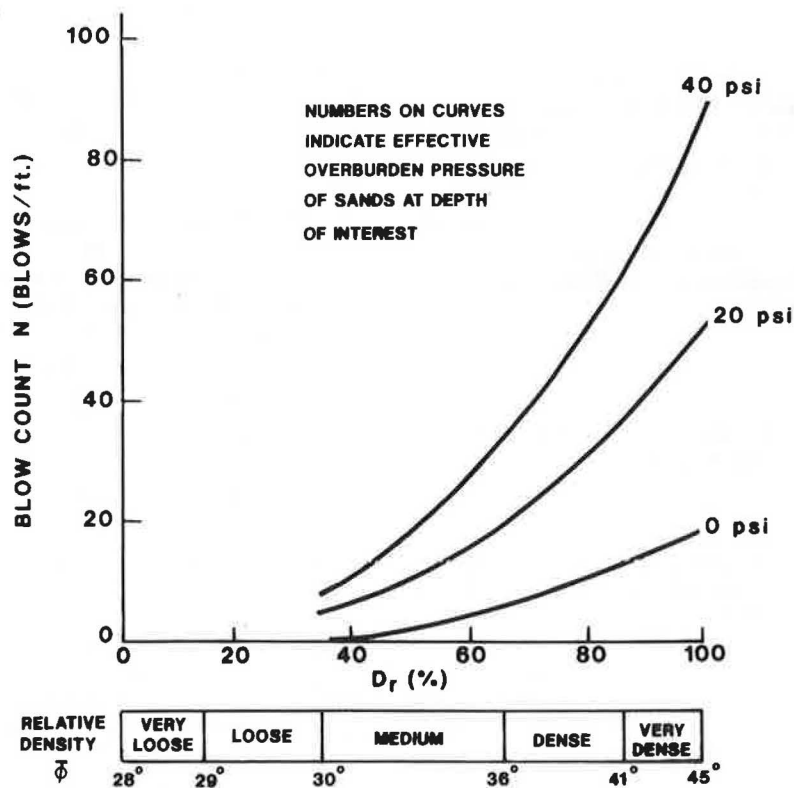


FIGURE 2 SPT blow count versus angle of friction and relative density of sands (9).

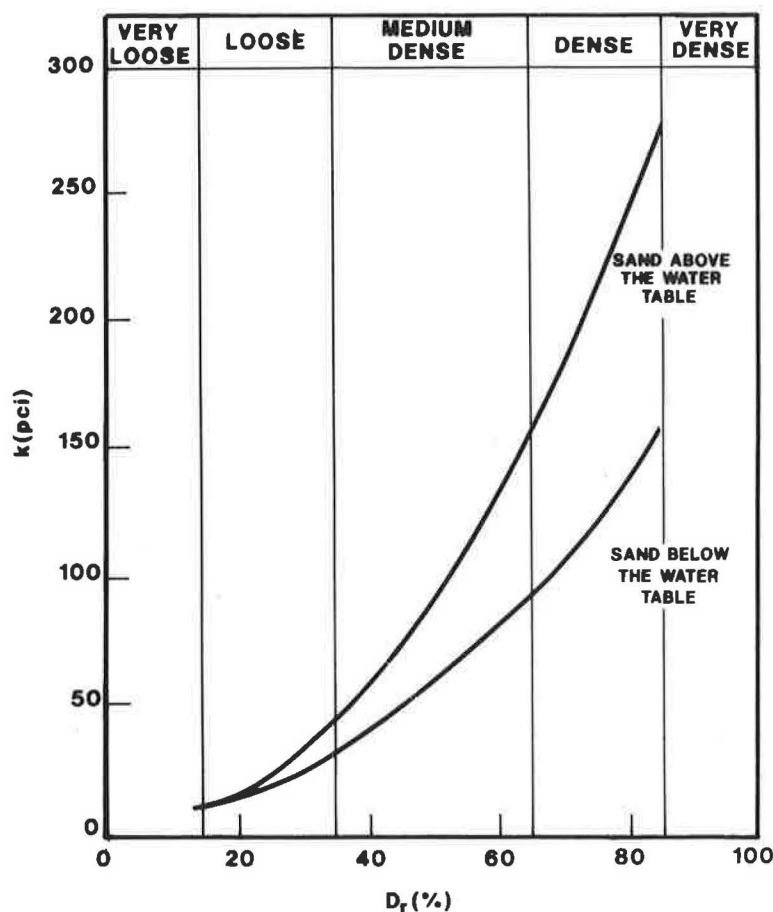


FIGURE 3 k versus relative density (9).

where p_u is the unmodified ultimate soil resistance found in Equations 9 and 10. η is taken as 1.5 for uniformly tapered piles and 1.0 for circular, prismatic piles. A is a factor related to the diameter of pile, B , and depth Z as

$$A = 3 - 0.8Z/B \geq 9 \quad \text{for static loading} \quad (14)$$

The shape of the p - y curve generated from this procedure is similar to that from the procedure of Reese et al. except that it is not a piecewise curve but a continuous analytical function.

PARAMETRIC STUDY

A parametric study was performed on hypothetical problems to determine a representative lateral subgrade modulus, called the equivalent lateral subgrade modulus (k_{eq}), under specific pile-soil conditions. The same methodology was successfully used to develop the lateral equivalent subgrade modulus for piles in clays (8). The method involves calculating the lateral deflection of a hypothetical pile, y_o , under specific soil and loading conditions by employing a numerical computer solution COM624 (6). The equivalent lateral subgrade modulus,

k_{eq} , can be determined by rewriting Equations 3 and 4 as follows:

$$k_{eq} = \frac{4.302 P^{1.67}}{(EI)^{0.67} y_o^{1.67}} \quad \text{for free-head pile} \quad (15)$$

$$k_{eq} = \frac{0.886 P^{1.67}}{(EI)^{0.67} y_o^{1.67}} \quad \text{for restrained-head pile} \quad (16)$$

where P is the applied lateral load and EI is the bending stiffness of pile.

A wide range of subgrade modulus was selected to represent a full spectrum of soil parameters in this study. Table 2 summarizes the selected soil parameters for cohesionless soils above and below the water table. The pile parameters investigated in the study are given in Table 3.

To perform the required numerical analyses using COM624, the lateral pile-soil interaction is modeled by the p - y curves, which may be constructed by one of the four procedures described in previous sections. Murchison and O'Neill (9) concluded that their proposed procedure was the most accurate of all four procedures. However, the conclusion of accuracy was based on a small data base and the relative comparison of the four procedures. The recent design manual sponsored by the Federal Highway Administration (16) recommends the

TABLE 2 SUMMARY OF SOIL PARAMETERS

	Sand Above the Water Table			Sand Below the Water Table		
	29	33	39	29	33	39
Frictional Angle ϕ (deg.)						
Subgrade Modulus k (pci)	25	95	225	20	60	125

TABLE 3 SUMMARY OF PILE PARAMETERS

Pile Material	Pile Diameter B (in.)	Young's Modulus E (psi)	Moment of Inertia I (in ⁴)
Concrete	36	3×10^6	82447.9
Steel	12	3×10^7	1017.9

use of the Reese et al. procedure for obtaining p - y curves. It appears that this procedure is more widely used and conservative. On the basis of this discussion and the advantage of being internally generated in COM624, the Reese et al. procedure was used to construct p - y curves in this parametric study.

EQUIVALENT SUBGRADE MODULUS

From the results of the parametric study described in the previous section, the relationships of the equivalent subgrade modulus, k_{eq} , versus the dimensionless lateral load factor $P\beta/kB^2$ were developed, in which P is the applied lateral load and

$$\beta = (kB/4EI)^{0.25} \quad (17)$$

where k is the subgrade modulus determined from Figure 3. EI is the bending stiffness of the pile, and B is the pile diameter.

Figures 4 and 5 show the relationships of k_{eq} versus the dimensionless lateral load factor for sands above the water table under a free-head and a restrained-head condition, respectively. Figures 6 and 7 show the relationship for sands below the water table under a free-head and a restrained-head condition. The k_{eq} under any particular conditions would not exceed the threshold value of k , which constitutes the initial slopes of the p - y curves at any depth Z by the product of kZ .

DESIGN PROCEDURE

The design curves to obtain k_{eq} are shown in Figures 8 and 9 for cohesionless soils above and below the water table, re-

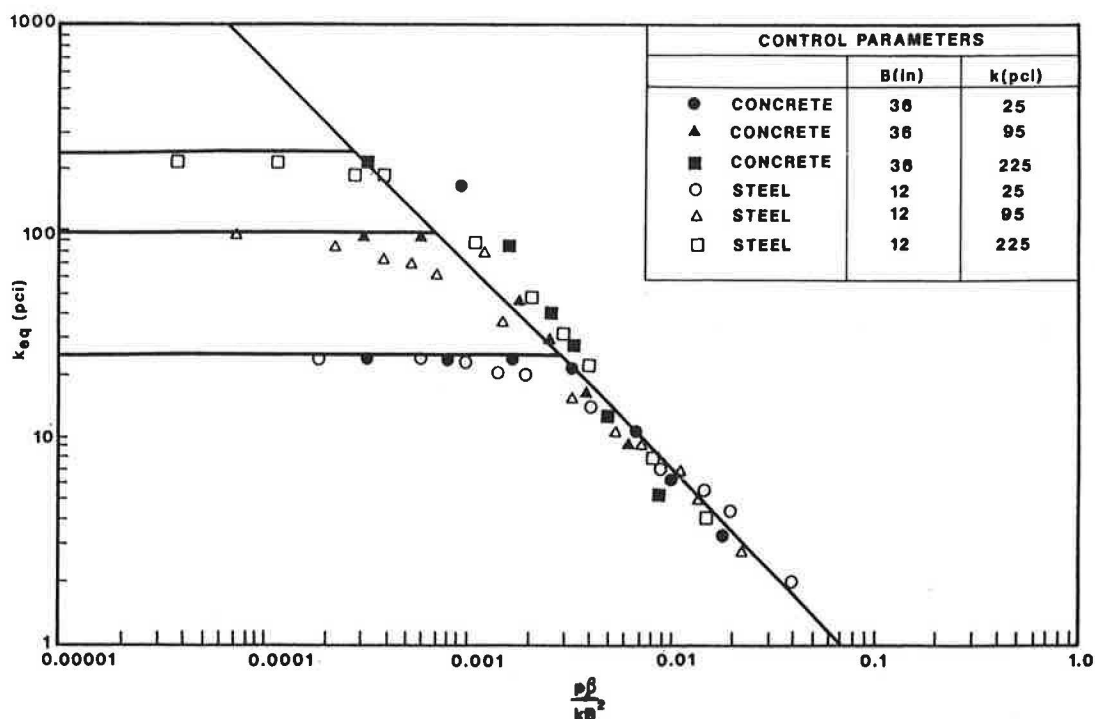


FIGURE 4 k_{eq} versus dimensionless lateral load factor for sands above the water table, free-head conditioning.

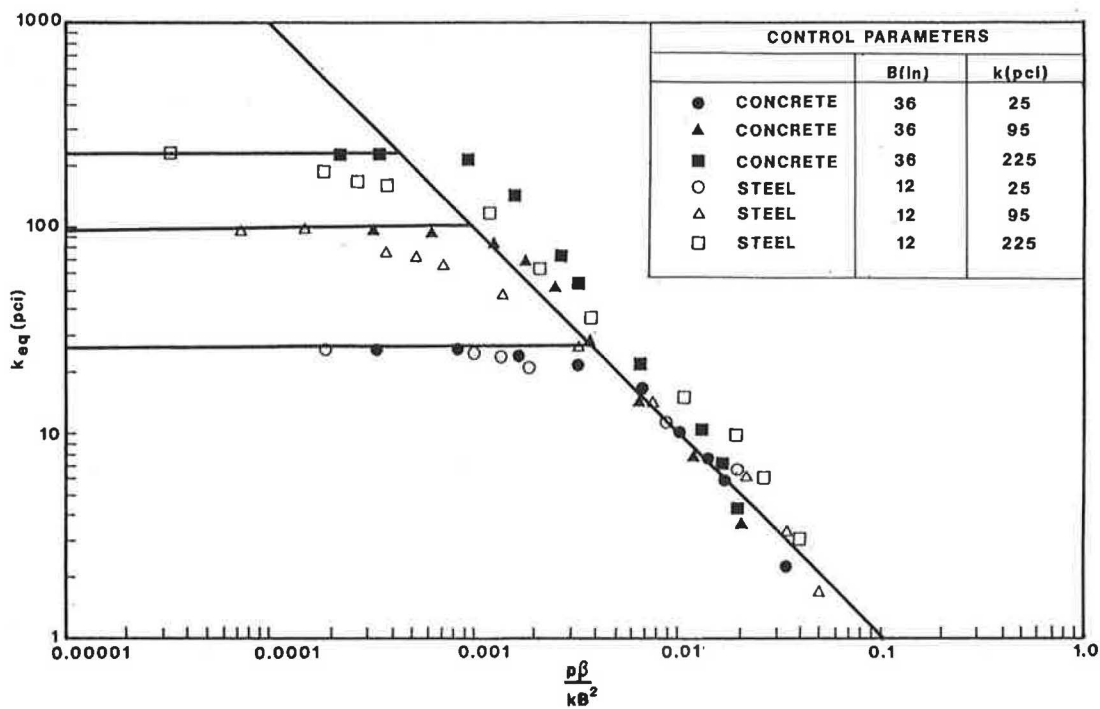


FIGURE 5 k_{eq} versus dimensionless lateral load factor for sands above the water table, restrained-head conditioning.

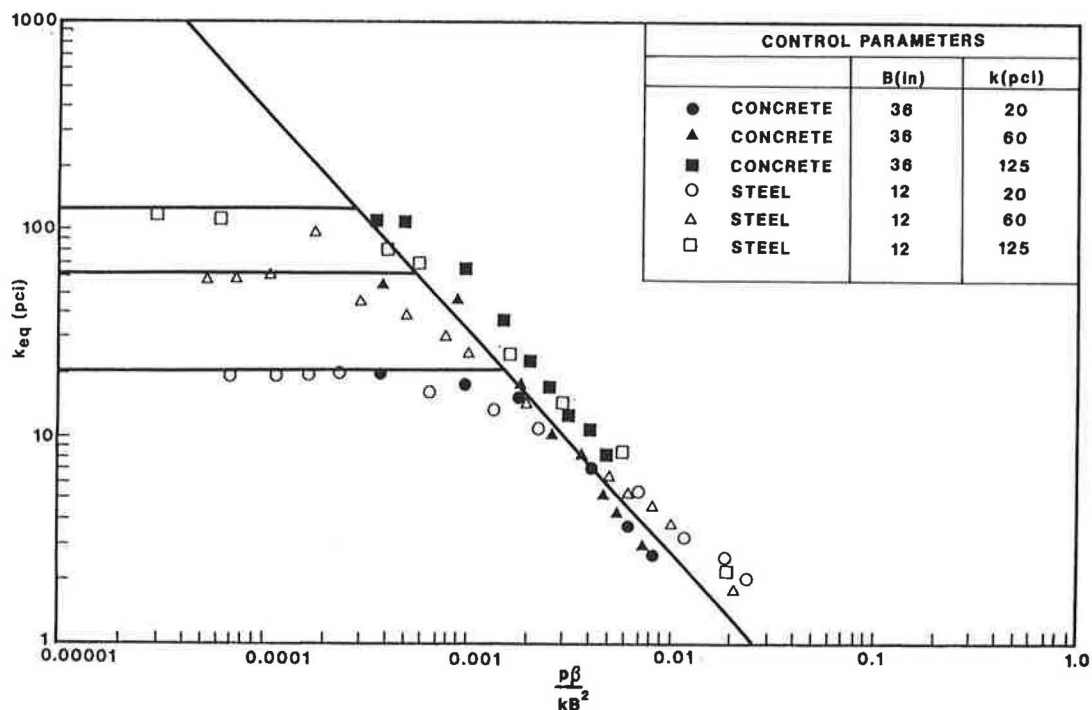


FIGURE 6 k_{eq} versus dimensionless lateral load factor for sands below the water table, free-head condition.

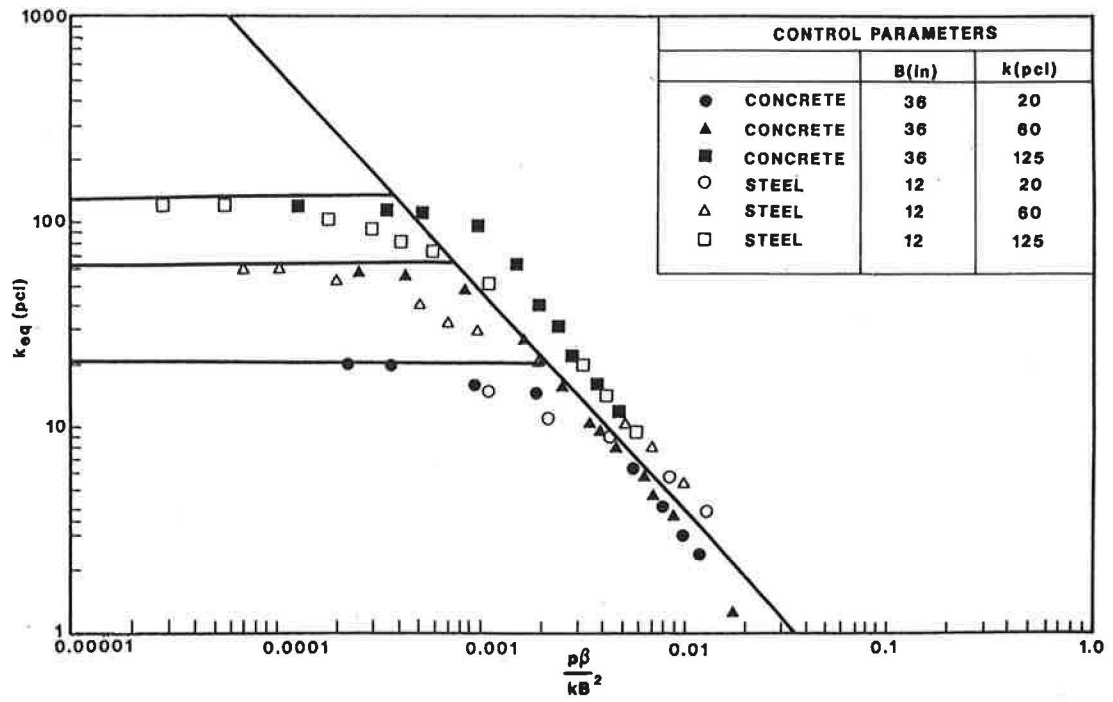


FIGURE 7 k_{eq} versus dimensionless lateral load factor for sands below the water table, restrained-head condition.

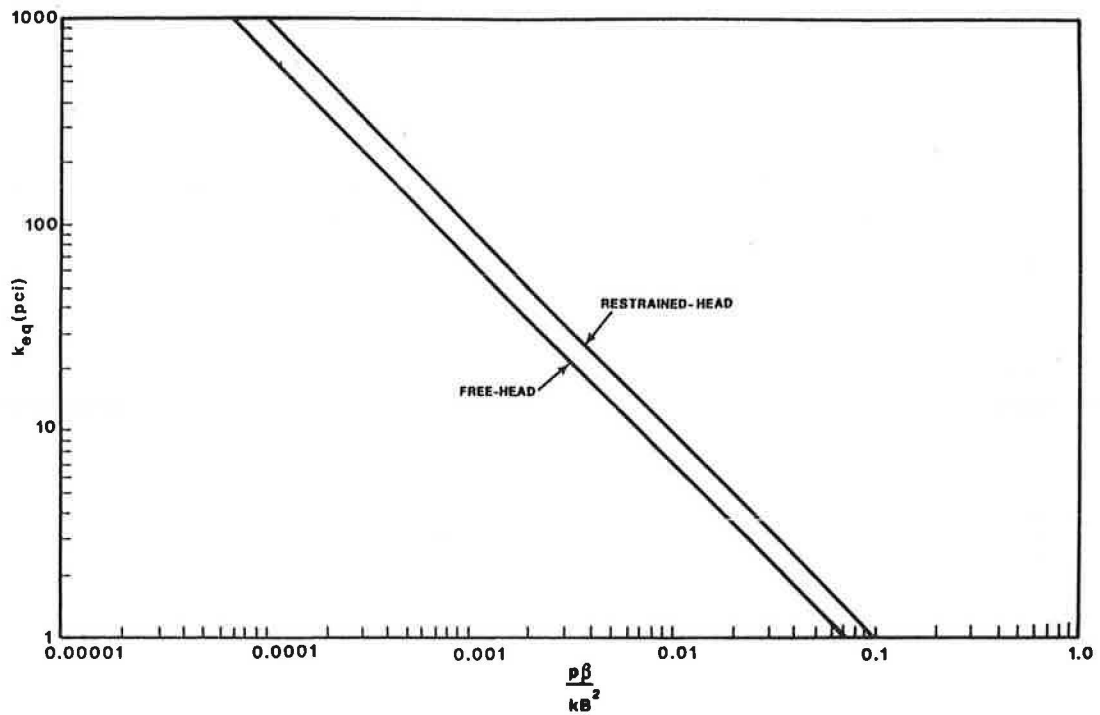


FIGURE 8 Design curves of k_{eq} versus dimensionless lateral load factor for sands above the water table.

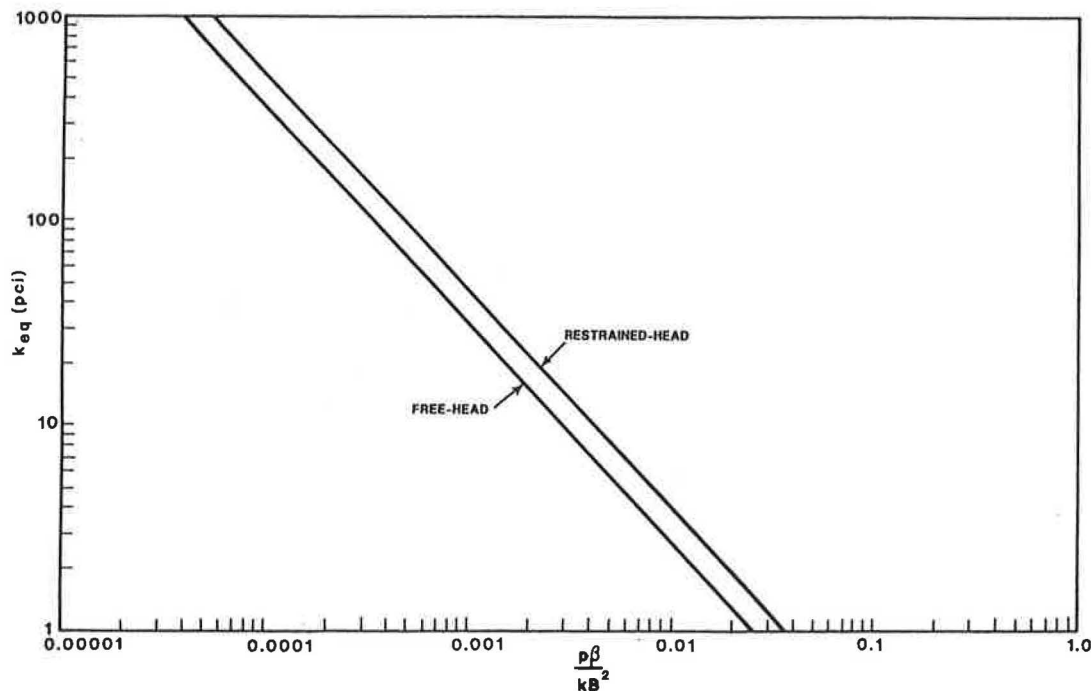


FIGURE 9 Design curves of k_{eq} versus dimensionless lateral load factor for sands below the water table.

spectively. The horizontal lines in Figures 4 through 7 represent the threshold values of k for sands of various relative densities. These lines are omitted in Figures 8 and 9, but the threshold values should be checked before a modulus is chosen from the design curves. The checking mechanism will be further discussed in the following paragraph. A simple design procedure is proposed to analyze laterally loaded piles in sands as follows:

1. Characterize the subsurface soil with a threshold subgrade modulus, k , using the relationships presented in Figures 2 and 3.
2. Obtain coefficient β using Equation 17.
3. Calculate the dimensionless lateral load factor, $P\beta/kB^2$.
4. Determine the equivalent subgrade modulus, k_{eq} , from either Figure 8 or Figure 9. Depending on given subsurface and boundary conditions, check $k_{eq} \leq k$. If $k_{eq} > k$, use $k_{eq} = k$.
5. Calculate the maximum deflection of pile from Equations 3 or 4 by substituting k_{eq} into k .
6. Determine the maximum moment from Equation 7 with all the necessary parameters obtained from Table 1 and Equation 5.

The nondimensional equation (Equation 6) can also be used to determine the maximum deflection of the pile by using the equivalent modulus k_{eq} . However, only Broms's equations (Equations 3 or 4) are considered for the subsequent sections of this paper.

This paragraph demonstrates the simplicity of the proposed design procedure by following Steps 1 to 6 to solve an example problem. Given a pipe pile of 20-in. OD and $\frac{3}{8}$ in. in wall

thickness driven into submerged sands ($\phi = 30$ degrees), k in Step 1 can be found in Figures 2 and 3 as 30 pci. Obtain β in Equation 17 as $8.186 \times 10^{-3} \text{ in.}^{-1}$ using E of 3×10^7 psi and I of 1,113.5 in.⁴ Determine $P\beta/kB^2$ for a lateral load P of 15 kips as 0.01. Obtain a k_{eq} of about 2.8 pci from Figure 9. The maximum deflection and maximum moment are found to be 1.20 in. and $1.2 \times 10^6 \text{ in.-lb}$ using Equations 3 and 7, respectively, for free-head conditions.

To examine the effectiveness of the proposed design procedure, a study was conducted to compare results obtained by computer analyses using COM624 and by following the proposed procedure. Three cases were established for the comparison study: (a) steel pipe pile 20 in. in diameter and $\frac{3}{8}$ in. in wall thickness driven in submerged sands and loaded laterally under free-head condition; (b) 24-in.-diameter drilled pier, dry sands, and restrained-head condition; and (c) 48-in.-diameter drilled pier, submerged sands, and free-head condition. Table 4 summarizes the important parameters for these three cases. Figures 10 and 11 compare the maximum deflections and maximum moments, respectively, by COM624 and the proposed design method. The comparisons indicate a less than 10 percent discrepancy in results within the range of various controlled parameters used in this study.

CONCLUSIONS

The relationships of equivalent subgrade modulus and dimensionless lateral load factor are established for laterally loaded piles in sands above and below the water table. A simple design procedure using the concept of the equivalent subgrade modulus is proposed to find the maximum deflection

TABLE 4 PARAMETERS FOR COMPARISON STUDY

Case	Pile Material	Pile Diameter B (in.)	Pile-Head Condition	Frictional Angle (deg.)	Soil Condition
A	Steel	20*	Free	30	Submerged
B	Concrete	24	Restrained	35	Dry
C	Concrete	48	Free	36	Submerged

* with 3/8 in. wall thickness

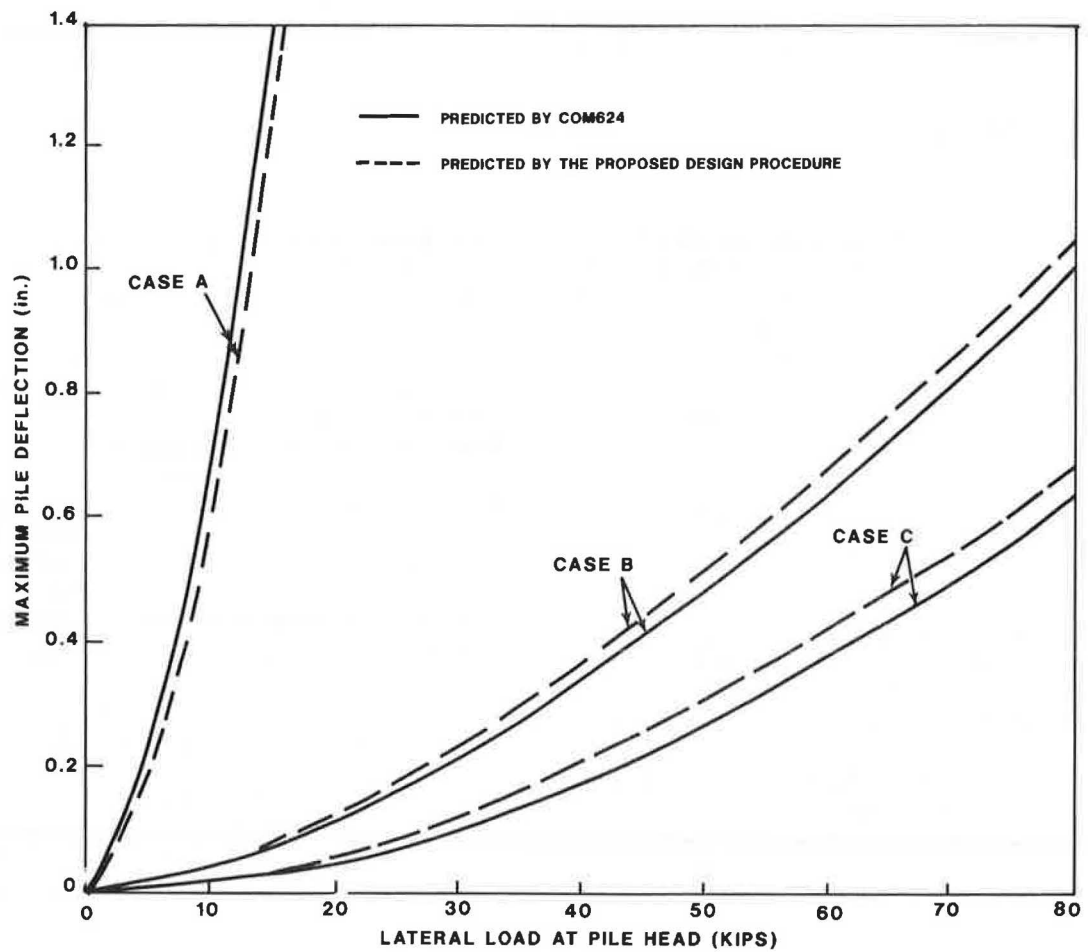


FIGURE 10 Comparison of maximum deflections by COM624 and proposed method.

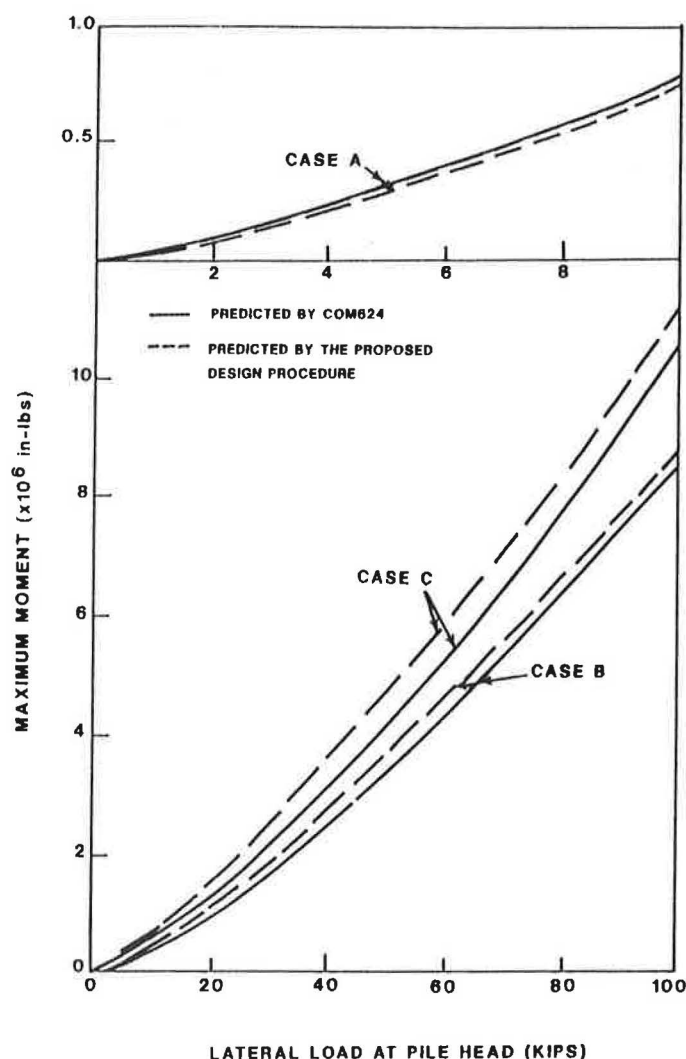


FIGURE 11 Comparison of maximum moments by COM624 and proposed method.

and maximum moment for practical problems. A comparison study indicated that the results obtained by the proposed procedure compared well with those determined by the computer using numerical solution COM624.

LIMITATIONS

The proposed equivalent lateral subgrade modulus and the design procedures were developed on the basis of the range of controlled parameters outlined in Tables 2 and 3. The findings of this study are only applicable for cohesionless soils. Similar results and procedures for cohesive soils can be found in a companion paper (8). Potential users of the proposed design curves and procedures are urged to recognize all the limitations.

ACKNOWLEDGMENTS

The author would like to thank all the reviewers who provided many useful comments to this paper.

REFERENCES

1. K. Terzaghi. Evaluation of Coefficients of Subgrade Reaction. *Geotechnique*, Institution of Civil Engineers, Vol. 5, London, 1955, pp. 297-326.
2. B. McClelland and J. A. Focht, Jr. Soil Modulus of Laterally Loaded Piles. *Transactions*, ASCE, Vol. 123, 1958, pp. 1049-1086.
3. B. B. Broms. Lateral Resistance of Piles in Cohesionless Soils. *Journal of the Soil Mechanics and Foundations Division*, Vol. 90, No. SM3, 1964, pp. 123-156.
4. H. Matlock and L. C. Reese. Generalized Solutions for Laterally Loaded Piles. *Journal of the Soil Mechanics and Foundations Division*, Paper 2626, Vol. 86, No. SM5, 1960, pp. 63-91.
5. H. Matlock and T. A. Haliburton. *A Program for Finite-Element Solution of Beam-Columns on Nonlinear Supports*. Austin, Tex., 1964.
6. L. C. Reese and W. R. Sullivan. *Documentation of Computer Program COM 624, Geotechnical Engineering Software SS80-1*. Geotechnical Engineering Center, The University of Texas at Austin, Austin, 1975, pp. 663-649.
7. L. T. Evans, Jr., and J. M. Duncan. *Simplified Analysis of Laterally Loaded Piles*. Report UCB/ET/82-04. University of California at Berkeley, Berkeley, 1982.

8. D. O. Wong. Subgrade Modulus of Laterally Load Piles in Clays. Presented at 70th Annual Meeting of the Transportation Research Board, Washington, D.C. 1991.
9. J. M. Murchison and M. W. O'Neill. Evaluation of p - y Relationships in Cohesionless Soils. *Analysis and Design of Pile Foundations* (J. R. Myer, ed.), ASCE, 1984, pp. 174-191.
10. L. C. Reese, W. R. Cox, and F. D. Koop. Analysis of Laterally Loaded Piles in Sand. *Proc., Sixth Annual OTC*, Vol. 2, Paper 2080, Houston, Tex., 1974.
11. H. J. Gibbs and W. G. Holtz. Research on Determining the Density of Sands by Spoon Penetration Testing. *Proc., Fourth International Conference on Soil Mechanics and Foundation Engineering*, London, Vol. 1, 1957, pp. 35-59.
12. B. J. Meyer and L. C. Reese. *Analysis of Single Piles Under Lateral Loading*. Research Report 244-1. Center for Transportation Research, The University of Texas at Austin, Austin, 1979.
13. D. Bogard and H. Matlock. *Simplified Calculation of p - y Curves for Laterally Loaded Piles in Sand*. Earth Technology Corporation, Inc., Houston, Tex., 1980.
14. R. F. Scott. *Analyses of Centrifuge Pile Tests: Simulation of Pile Driving*. Research Report, API OSAPR Project 13. California Institute of Technology, Pasadena, Calif., 1980.
15. F. Parker, Jr., and L. C. Reese. *Experimental and Analytical Study of Behavior of Single Piles in Sand Under Lateral and Axial Loading*. Research Report 117-2. Center for Highway Research, The University of Texas at Austin, Austin, 1970.
16. L. C. Reese and M. W. O'Neill. *Drilled Shafts: Construction Procedures and Design Methods*. FHWA-HI-88-042. Federal Highway Administration, U.S. Department of Transportation, Aug. 1988.

Publication of this paper sponsored by Committee on Foundations of Bridges and Other Structures.

Modeling Soil Reaction to Laterally Loaded Piles

TAKAAKI KAGAWA

A numerical study was made for linearly elastic soil-pile conditions to clarify the lateral soil-reaction behavior of a pile. The apparent lateral stiffness of soil is strongly influenced not only by the soil stiffness but also the geometry and the stiffness of a pile. Also, the apparent lateral stiffness of soil varies significantly with depth, even if the soil stiffness is constant with depth. A new and improved procedure for estimating the lateral soil springs that can be used with the beam-on-Winkler foundation model of a soil-pile system is presented. With these soil springs the beam-on-Winkler foundation model can reproduce with excellent accuracy the pile responses computed from the corresponding continuum system. Although limited to linearly elastic soil-pile conditions, the results may be expanded to nonlinear soil conditions.

Piles have been used extensively to improve the foundation performance of a wide range of transportation systems. In addition, piles are becoming increasingly popular, since new construction and developments must cope with undesirable subsurface conditions involving weak and compressible soils that have been avoided in the past.

It is evident that pile foundations have a controlling impact on the overall performance of a transportation system. However, the most common design practice has been to represent a pile foundation by a set of simplistic linearly elastic translational and rotational springs, lumped at the pile-cap level. These discrete foundation springs are supposed to represent the embedded portion of the pile and the surrounding soil. Their numerical values should reflect the influence of various key soil-pile factors. Such factors include variations of soil properties with depth, geometrical and stiffness properties of the pile, and the constraining condition at the pile cap, among other factors. Therefore, evaluation of such foundation springs is not straightforward. It requires consideration of soil-pile interaction, which is affected by the stiffness and the geometrical properties of soil and pile. Such foundation springs are often determined from available elasticity solutions that assume homogeneity of soil properties with depth. For critical transportation systems, however, such foundation springs should be determined by performing soil-pile interaction analyses that explicitly account for the soil-pile conditions at the project site. The key conditions are the stress-strain-strength behavior of soils at the site and variations of soil-pile stiffness with depth.

In the last 10 years a number of studies have developed various types of numerical methods for soil-pile interaction analyses of single piles and groups of piles. These methods include the finite-element method, the boundary-element

method, mathematical solutions to wave equations, and the beam-on-Winkler foundation method. The finite-element and boundary-element methods are generally costly and may not be readily available to practicing design engineers. Mathematical solutions are limited to idealized soil-pile conditions. Therefore, the most economical and versatile numerical method for soil-pile interaction analyses tends to be the beam-on-Winkler foundation method.

The beam-on-Winkler foundation method approximates the lateral soil reaction, which is continuous with depth, using a series of isolated lateral soil springs. Therefore, the method neglects the interaction between such soil springs. Because of this simplification the method is numerically efficient. The method has also been shown to yield satisfactory pile responses when it is used with appropriate soil springs. Therefore, the reliability of the method is determined by our ability to predict realistic lateral soil springs to be used with the method.

Evaluation of the lateral soil springs for the beam-on-Winkler foundation model is not an easy task. The lateral soil springs are influenced not only by the stiffness properties of soil but also by the geometry and the stiffness properties of a pile. Rational guidelines are not available to estimate the lateral soil springs, even for linearly elastic soil conditions.

The lateral soil springs for the beam-on-Winkler foundation model were first determined by using the concept of subgrade-reaction moduli. The subgrade-reaction moduli were estimated from field plate-loading tests on clays and sands (1-3) and later from field and laboratory pile-load tests. The lateral soil springs thus determined are still being used in pile design.

The lateral soil springs vary dramatically when the magnitude of pile deflection changes. This change is due mainly to the nonlinear stress-strain effects in soil. Therefore, the lateral soil springs based on the subgrade-reaction theory are associated with the magnitude of pile deflections in a test. Considering the nonlinear nature of the lateral soil reaction, McClelland and Focht (4) proposed to relate the lateral load-deflection (p - y) relations of pile to the stress-strain relations of soil. This method has been revised by various researchers by using field and laboratory pile-load test results (5-8), and the method is well accepted in offshore pile design (9).

These p - y criteria, however, are based on pile-load tests with a narrow range of soil-pile parameters. In addition, it is always difficult to quantify the stress-strain relations of soil adjacent to a pile in field tests. Therefore, these p - y criteria are not necessarily suited to rigorous derivation of the relation between the lateral soil springs (p - y stiffness) and in situ soil stiffness.

Department of Civil Engineering, 2150 Engineering Building, Wayne State University, Detroit, Mich. 48202.

Kagawa and Kraft (10) studied analytically the lateral soil springs of a linearly elastic soil-pile system. The objectives of this study were to (a) clarify for idealized soil-pile conditions the relation between the p - y stiffness and the stiffness of the surrounding soil medium and (b) provide sound bases for interpreting existing criteria and for developing nonlinear p - y relations.

The major objectives of this paper are to (a) expand the concepts introduced by Kagawa and Kraft (10), (b) develop a new and improved procedure for determining such lateral soil springs, and (c) demonstrate the performance of such lateral soil springs. It is hoped that the results of this paper will provide a rational guideline for the estimation of the lateral soil springs to be used with the beam-on-Winkler foundation model for soil-pile interaction analyses.

SOIL REACTION TO Laterally LOADED PILES

Soil-Reaction Coefficient

Figure 1 shows how a pile responds to a horizontal force applied at its pile head for a pile in a linearly elastic, homogeneous medium. Figure 1 includes pile deflections normalized by corresponding ground-level deflections and the soil-reaction coefficient δ defined by

$$p = E_s \delta y \quad (1)$$

where

p = the soil reaction to a unit length of a pile,
 E_s = the Young's modulus of soil, and
 y = pile deflection.

The soil-reaction coefficient δ is a continuous function of depth, and δ represents the interaction between the pile and the continuum soil medium. In addition, δ is indicative of the soil stress that is normal to the pile.

Figure 1 shows that the soil-reaction coefficient starts with a positive value near the ground surface. The δ value decreases with depth, and it may become negative at depth.

Negative δ values occur where tensile normal stresses act in the soil adjacent to the pile.

As shown in Figure 1 for flexible piles, pile deflections vanish rapidly with depth, and the soil reaction to a pile is concentrated at shallow depths. Therefore, the soil at shallow depths participates in soil reaction more effectively than deeper soil. This results in larger δ values at shallower depths for flexible piles. For rigid piles, soil reaction is mobilized more uniformly along the pile shaft, and smaller and more uniform soil-reaction coefficients result. Therefore, the relative deformability of the soil and the pile has a significant impact on δ .

The pile responses in Figure 1 emphasize that a rational evaluation of the lateral soil springs must take full account of soil-pile interaction effects.

Average Soil-Reaction Coefficient

Figure 1 has demonstrated that the soil stiffness against pile deflection is difficult to determine solely from the stiffness properties of soil without considering the soil-pile interaction effects determined by the geometry and the deformation properties of the pile. In addition, the soil-reaction coefficient, which represents the apparent lateral soil stiffness of the pile, varies dramatically with depth.

Figure 1 also suggests that we must exactly follow complex variations of δ with depth when we are to correctly reproduce pile responses using the beam-on-Winkler foundation model. However, the use of a soil-reaction coefficient that is constant with depth would simplify the analysis procedure. Therefore, a soil-reaction coefficient that is constant with depth is introduced in the following. Such a constant profile represents an average behavior of the variation of δ with depth.

To find such an average value $\bar{\delta}$, Kagawa and Kraft (10) and Kagawa (11) considered the pile responses in two separate systems, continuum and beam-on-Winkler foundation models. The soil reaction in the continuum (or exact) system is denoted by p and that of the beam-on-Winkler foundation is denoted by p' . The corresponding pile deflections in these two systems are represented by y and y' .

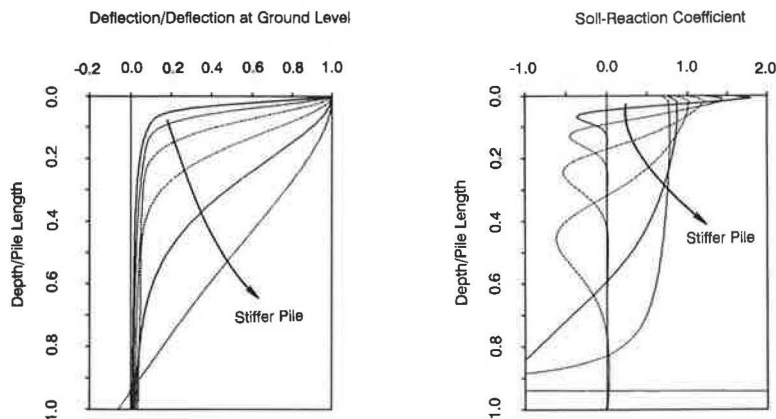


FIGURE 1 Pile deflection and soil-reaction coefficient.

The simplest way of deriving an average would be to assume that the sum of the soil reaction along the pile shaft is identical in the two systems. This condition may be represented by

$$\int_0^H (p - p') dx = 0 \quad (2)$$

in which H = pile length and x = depth. This condition also implies that the resultant lateral soil reaction along the pile in the beam-on-Winkler foundation model equals the pile-head shear. Assuming that the two systems produce the same pile deflections, we can derive the following average:

$$\bar{\delta} = \frac{\int_0^H p dx}{\int_0^H E_s y dx} \quad (3)$$

The next simplest average was derived by equating the work done by the soil reactions in the two systems. The work done by the soil reaction and the pile displacements in these systems under the same external loads may be equated as follows:

$$\int_0^H (py - p'y') dx = 0 \quad (4)$$

This condition is equivalent to the condition that the work done by the soil reaction in the beam-on-Winkler foundation method equals the work done by the pile-head shear. The average can then be obtained as

$$\bar{\delta} = \frac{\int_0^H py dx}{\int_0^H E_s y^2 dx} \quad (5)$$

In contrast to the average in Equation 3, the average in Equation 5 has the pile deflection as a weighting function; therefore, the soil-reaction coefficients at larger pile deflections have greater influence on the average.

Improved Average Soil-Reaction Coefficients

The average in Equation 5 was developed originally for offshore piles that are usually long and flexible. The average has been found adequate to reproduce reliable pile responses in many cases (10,11). The use of $\bar{\delta}$ in Equation 5 with the beam-on-Winkler foundation method, however, will not yield pile responses identical to the corresponding continuum model. The difference in pile responses from these two systems tends to be large for very long and flexible piles. Therefore, the goal of this paper is to obtain the average soil-reaction coefficient $\bar{\delta}$ that yields improved pile responses for a wide range of soil-pile parameters.

The objective of establishing such an average may be mathematically equivalent to minimizing the following weighted error integral:

$$E = \int_0^H W(x)(p - p')^2 dx \quad (6)$$

where p' is the soil reaction in the beam-on-Winkler foundation model, $E_s \bar{\delta} y'$. Assuming that y' equals y , we can minimize this error integral by determining $\bar{\delta}$ from the following condition:

$$\frac{\partial E}{\partial \bar{\delta}} = 0 \quad (7)$$

Equation 7 gives the following average:

$$\bar{\delta} = \frac{\int_0^H W(x)py dx}{\int_0^H W(x) E_s y^2 dx} \quad (8)$$

The average in Equation 8 gives the average in Equation 5 when the weighting function $W(x)$ equals unity. Therefore, the work consideration used in the derivation of the average in Equation 5 was a special case of minimization of the error integral in Equation 6. The true virtue of Equation 8, however, gives us a unified approach to obtaining average $\bar{\delta}$. Equation 8 allows us to devise various averages that satisfy specific purposes.

PERFORMANCE EVALUATION OF AVERAGE SOIL-REACTION COEFFICIENTS

Numerical Procedures

Pile responses have been computed by the computer program PILE, coded specifically for this study, and the performance of several average $\bar{\delta}$'s has been studied to find the best soil-reaction model for the beam-on-Winkler foundation analysis of laterally loaded piles. The program is based on linearly elastic models of soil medium and a pile. A pile was divided into a sufficient number of elements to achieve satisfactory accuracy of computed pile responses. The number of elements used in this study ranged from 70 to 135, depending on pile length. The soil reaction to the pile was evaluated by first constructing the flexibility matrix of the soil medium and then by inverting the matrix to obtain the stiffness matrix for soil reaction. The flexibility coefficients were computed by integrating, over the surface of an incremental length of a pile, Mindlin's solution to a homogeneous, elastic half-space (12). The pile was modeled by the standard, finite-element, beam elements.

The following four different averages of the soil-reaction coefficients were computed for a continuum soil condition:

- $\bar{\delta}$ in Equation 3 (Case 1),
- $\bar{\delta}$ in Equation 5 (Case 2),
- $\bar{\delta}$ in Equation 8 with $W(x) = y$ (Case 3), and
- $\bar{\delta}$ in Equation 8 with $W(x) = p$ (Case 4).

Computed pile responses were then compared with those from the beam-on-Winkler foundation model with corresponding average $\bar{\delta}$.

Case 1 is the simplest average of all. Case 2 assumes unity for the weighting function in Equation 8. Case 3 uses the pile

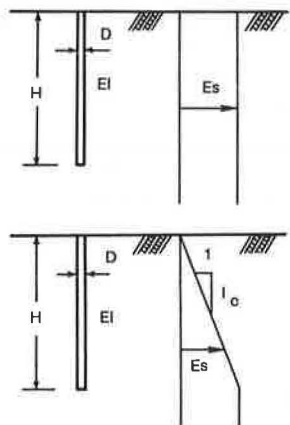
deflection y as the weighting function in the error integral in Equation 8, and Case 4 uses the soil reaction p as the weighting function.

Key Soil-Pile Parameters

The soil-pile conditions used in this study are schematically shown in Figure 2. These involve the cases with soil modulus constant with depth (homogeneous modulus cases) and those with soil modulus linearly increasing with depth (linearly increasing modulus cases). The homogeneous modulus cases may apply to overconsolidated soil conditions in which the soil stiffness does not appreciably change with depth. On the other hand, the linearly increasing modulus cases may be valid for normally consolidated clay and sand sites in which the soil stiffness increases nearly proportionally with depth. The physical properties of such a soil medium are represented by the shear modulus (or Young's modulus) G_s (or E_s) and Poisson's ratio ν for the homogeneous modulus cases and by the rate of increase in Young's modulus with depth I_e and Poisson's ratio ν for the linearly increasing modulus cases. The pile is characterized by the width D , the length H , and the flexural rigidity EI . A brief dimension analysis reveals that pile responses are controlled by the aspect ratio of the pile H/D , Poisson's ratio of soil, and the degree of rotational constraint at the pile head (fixed-head or free-head condition). In addition, the relative deformability of soil and the pile is related to the soil-pile flexibility coefficient defined by

$$K_r = \frac{EI}{E_s H^4} \quad \bar{K}_r = \frac{EI}{E_s D^4} \quad \tilde{K}_r = \frac{EI}{I_e D^5} \quad (9)$$

The soil-pile flexibility coefficients K_r and \bar{K}_r are useful for the homogeneous modulus cases. The soil-pile coefficient \bar{K}_r will be called "local" soil-pile flexibility because the coefficient involves only the soil-pile conditions at a depth. \tilde{K}_r will also be called a local soil-pile flexibility coefficient, and it will be used for the linearly increasing modulus cases. Smaller



(b) Linearly Increasing Modulus Cases

FIGURE 2 Soil-pile conditions: *top*, homogeneous modulus cases; *bottom*, linearly increasing modulus cases.

TABLE 1 RANGES OF KEY PARAMETER VALUES

Key Parameters	Parameter Values
H/D	25, 50, 100 & 200
K_r	$10e-7$ to $10e-2$
\bar{K}_r & \tilde{K}_r	$10e+1$ to $10e+6$
Pile-Head Cond.	Free & Fixed Head
Poisson's Ratio of Soil	0.3, 0.4 & 0.5

soil-pile flexibility coefficients correspond to more flexible pile (or stiffer soil) conditions.

The ranges of values of the dimensionless parameters used in this study are summarized in Table 1. These ranges are expected to cover sufficient variations of soil-pile conditions in practice.

Homogeneous Soil Stiffness Cases

The average soil-reaction coefficients (Cases 1 through 4) have been computed for a variety of soil-pile conditions. Figure 3 shows typical results of such analyses. $\bar{\delta}$ values for Cases 1 through 4 are shown for an aspect ratio of 100, a Poisson's ratio of 0.5, and the free-head condition. $\bar{\delta}$ values from Case 1 are nearly constant even if the soil-pile flexibility coefficient changes from 10^{-7} to 10^{-2} . This indicates that Case 1 does not reflect the soil-pile interaction effects due to the relative deformability of soil and the pile. On the other hand, Cases 2 through 4 yielded $\bar{\delta}$ values that dramatically decrease as the pile stiffness (or the soil-pile flexibility coefficient) increases. This analysis indicated that the Poisson's ratio has a negligible influence on $\bar{\delta}$ values and that the fixed-head condition results in smaller $\bar{\delta}$ values.

Figure 4 compares the lateral pile-head stiffness obtained from the continuum soil cases and from the beam-on-Winkler foundation models with $\bar{\delta}$ from Cases 1 through 4. The figure includes results for the free-head and fixed-head conditions and for aspect ratios of 25 and 100. Figure 4 shows that Case 1 significantly underestimates the lateral pile-head stiffness. A similar conclusion applies to Case 2 for short and flexible piles. On the other hand, Case 4 tends to overestimate the lateral pile-head stiffness for all cases. This tendency is pro-

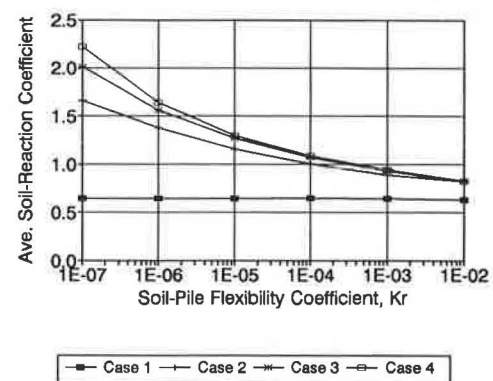


FIGURE 3 Average soil-reaction coefficients for $H/D = 100$ and free-head conditions (homogeneous E_s).

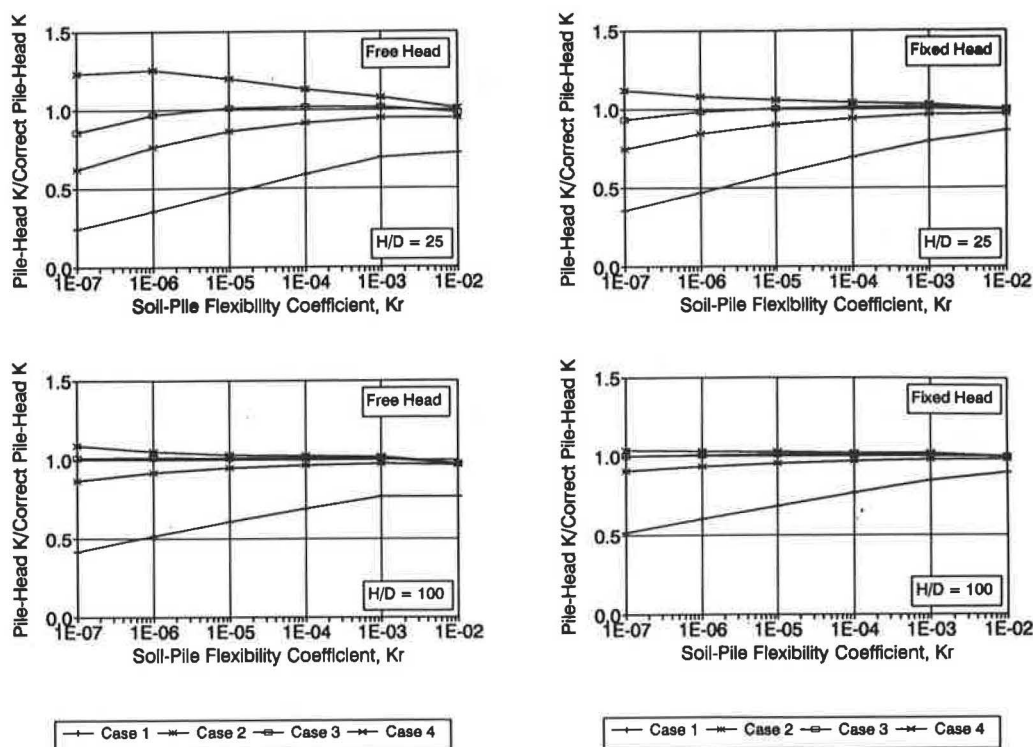


FIGURE 4 Comparisons of pile-head stiffnesses from continuous and beam-on-Winkler foundation models (homogeneous E_s).

nounced for short and flexible piles. Case 3, however, gives excellent predictions of lateral pile-head stiffness.

Similar comparisons are made in Figure 5 for the maximum bending moments in the pile computed by the continuum soil cases and by the beam-on-Winkler foundation models with $\bar{\delta}$ from Cases 1 through 4. In all cases the maximum moment in the pile is overestimated by the beam-on-Winkler foundation models. Case 1 yielded significant overestimation for short and flexible piles with the free-head condition. Cases 2 through 4 provide much better agreements than Case 1, but we cannot neglect this overestimation for short and flexible piles. Case 4 resulted in the best agreement, but the difference in performance between Cases 3 and 4 is very small. Most piles in practice have a soil-pile flexibility coefficient on the order of 10^{-6} to 10^{-3} . For this range of K_r , overestimation is on the order of less than 20 percent.

The comparisons in Figures 4 and 5 indicated that Case 3 gives the best predictions of pile responses for a wide range of soil-pile parameter values. Therefore, the average $\bar{\delta}$ from Case 3 is summarized in Figure 6 for the free-head and fixed-head conditions. Figure 6 includes results for aspect ratios of 25, 50, 100, and 200. The $\bar{\delta}$ values for these aspect ratios are nearly identical except for very rigid piles. This identity resulted from plotting $\bar{\delta}$ against the local soil-pile flexibility coefficient \bar{K}_r .

Natural soil conditions do not involve homogeneous soil stiffness with depth. Therefore, a guideline may be needed for the selection of an appropriate soil modulus for \bar{K}_r when $\bar{\delta}$ in Figure 6 is to be used in design. Such a guideline may be derived by looking at the variation of the numerator of

Equation 8 with depth. This quantity starts with zero at the ground surface and increases with depth. At some depth this quantity reaches its maximum value, and its value will not change after that. The portion of the soil before this quantity reaches the maximum may be considered to actively resist pile deflection. Therefore, the stiffness of this portion of soil can be used in \bar{K}_r . The depth at which the numerator of Equation 8 reaches the maximum will be called the effective pile length for the purpose of estimating \bar{K}_r . The effective pile lengths thus computed are summarized in Figure 7 for a range of soil-pile conditions. Unless a pile is very rigid (i.e., \bar{K}_r exceeds about 10^{-4}), the effective pile length is typically less than 20-pile-diameter depth.

Linearly Increasing Soil Stiffness Cases

A series of parametric studies have also been made for the linearly increasing soil modulus cases. Their results are summarized below.

Figure 8 shows comparisons of the pile-head stiffness computed by the continuum and the beam-on-Winkler foundation models with $\bar{\delta}$ from Cases 1 through 4. As we observed in the homogeneous modulus cases, Case 1 does not provide reliable estimates of pile-head stiffness for all the conditions used in this study. Case 2 yielded best agreements, and Cases 3 and 4 slightly overestimate the pile-head stiffness. The degree of overestimation is on the order of 5 percent.

Figure 9 shows similar comparisons for the maximum pile moments obtained from the continuum and the beam-on-

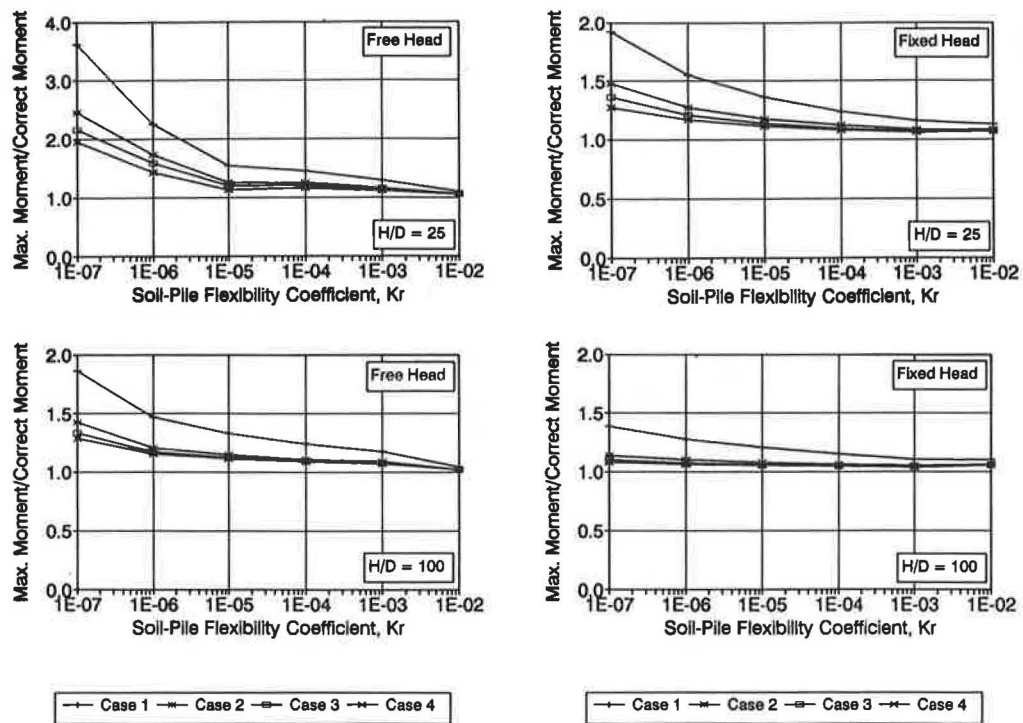


FIGURE 5 Comparisons of pile moment from continuous and beam-on-Winkler foundation models (homogeneous E_s).

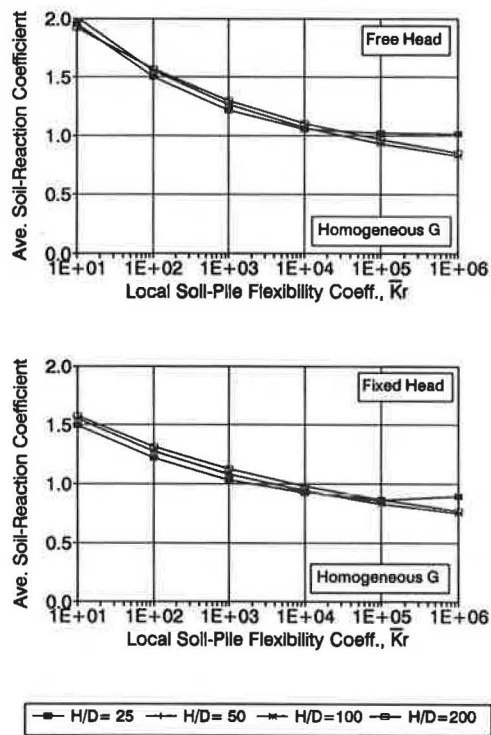


FIGURE 6 Summary of average soil-reaction coefficients (homogeneous E_s).

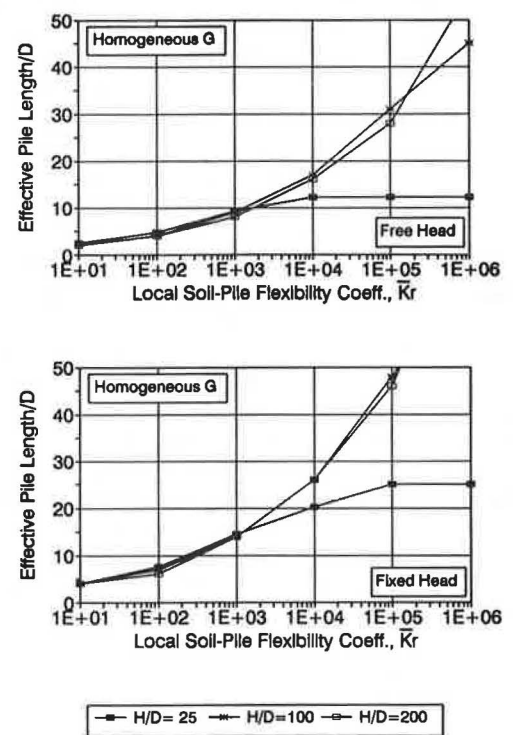


FIGURE 7 Effective pile length (homogeneous E_s).

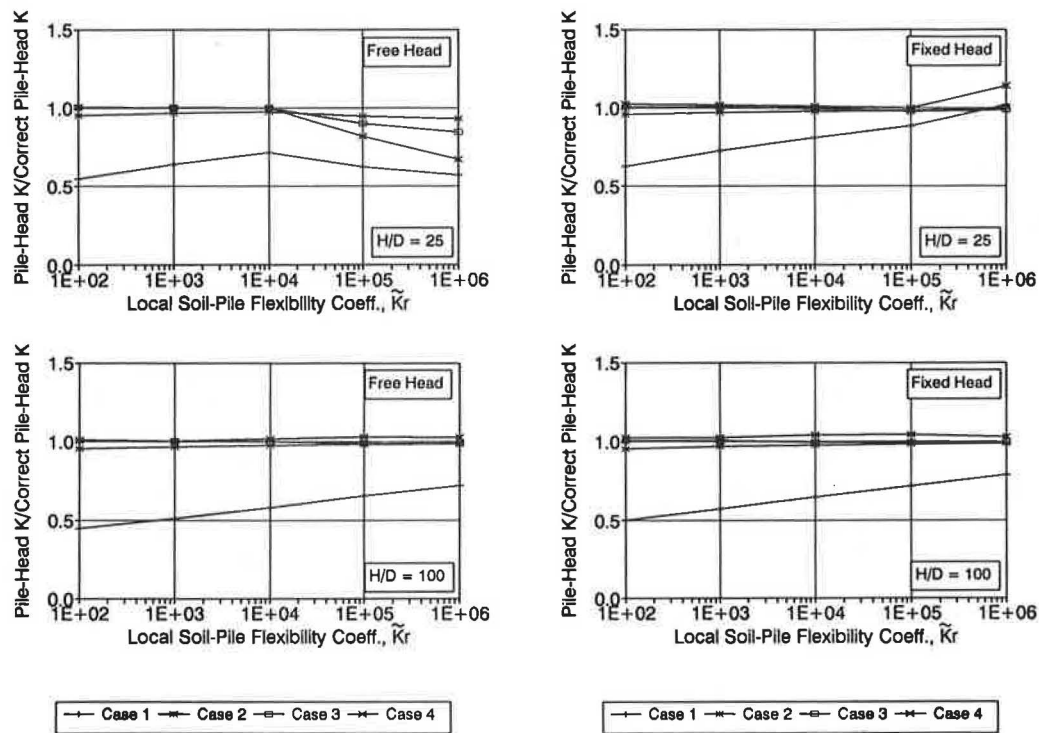


FIGURE 8 Comparisons of pile-head stiffnesses from continuous and beam-on-Winkler foundation models (linearly increasing E_s).

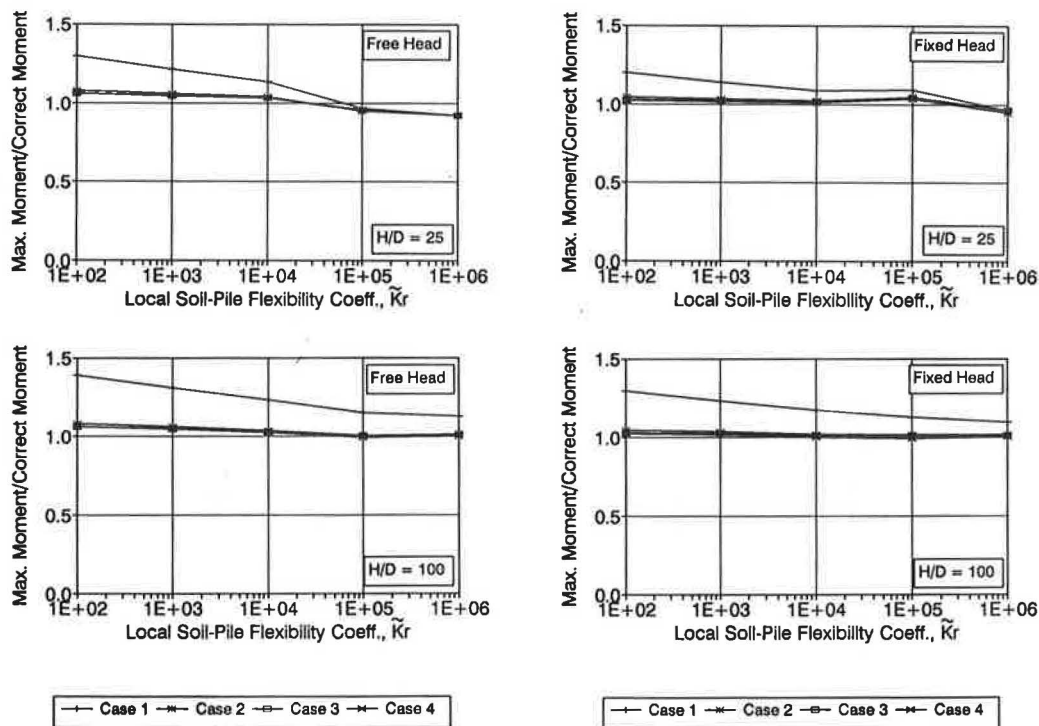


FIGURE 9 Comparisons of pile moment from continuous and beam-on-Winkler foundation models (linearly increasing E_s).

Winkler foundation models. Cases 1 through 4 overestimate the maximum moment in the pile except for very rigid pile (or soft soil) conditions. The degree of overestimation in this case is much less than that in the homogeneous modulus cases (see Figure 5). Cases 2 through 4 estimate almost perfectly the maximum moment in the pile.

Although Case 2 resulted in excellent predictions of pile-head stiffness and pile moments, the overall performance of Case 3 for both the homogeneous and linearly increasing modulus cases is considered to be the best. The average $\bar{\delta}$ from Case 3 is plotted against \bar{K}_r in Figure 10. The figure also includes $\bar{\delta}$ in Figure 7 for comparison. The $\bar{\delta}$'s for the homogeneous cases are less than those for the linearly increasing modulus cases by about 0.2 for both the free-head and fixed-head conditions.

Figure 11 summarizes the effective pile lengths for the linearly increasing modulus cases. The effective pile length is typically less than 15-pile-diameter depth unless the pile is very rigid (i.e., \bar{K}_r exceeds about 10^4).

APPLICATIONS

Results of this study can be readily used in the design analysis of laterally loaded piles. The average $\bar{\delta}$ in Figures 6 and 10 can be used to determine the lateral soil springs for the beam-on-Winkler foundation model of a soil-pile system. For a given set of soil stiffness data, the lateral soil springs can be determined from

$$K = \frac{P}{y} \Delta H = E_s \bar{\delta} \Delta H \quad (10)$$

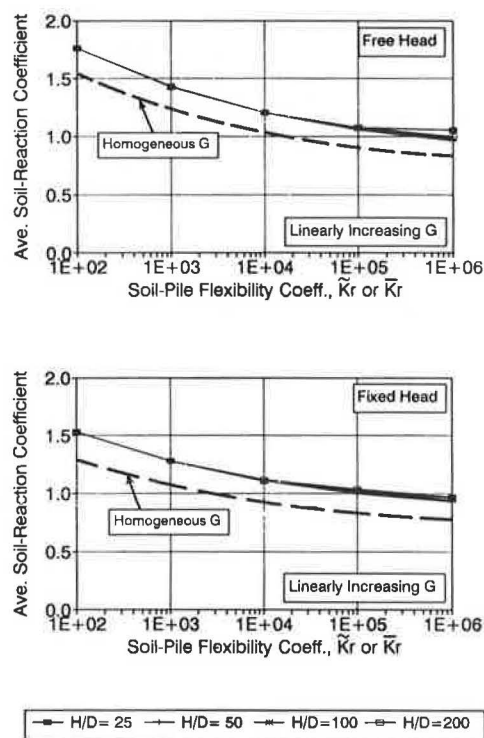


FIGURE 10 Summary of average soil-reaction coefficient (linearly increasing E_s).

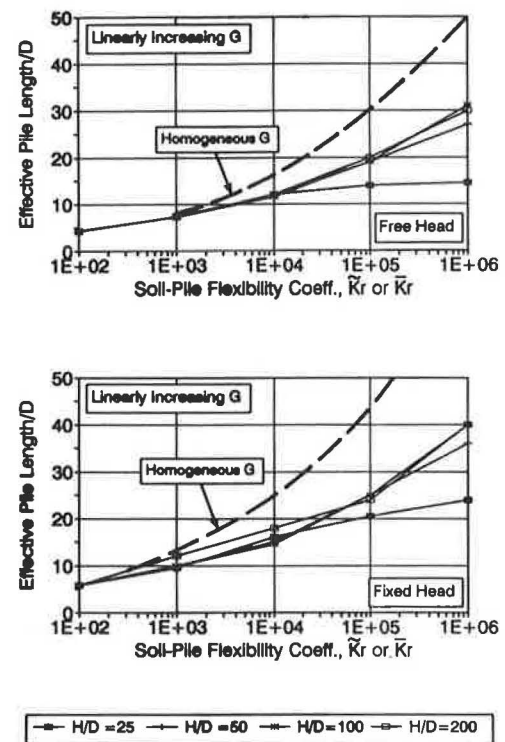


FIGURE 11 Effective pile length (linearly increasing E_s).

where the lateral soil spring K is defined over the incremental pile length ΔH . Evaluation of E_s (Young's modulus of soil) invites discussion, but E_s should be based on a rational estimate of the magnitude of the soil strains involved in the problem under investigation. A typical guideline to serve this purpose is given by (5,10)

$$\gamma = (1 + \nu)/(\alpha D) \quad (11)$$

where

- γ = the representative soil shear strain around the pile,
- ν = Poisson's ratio of soil, and
- α = an empirical factor that typically ranges from 2.0 to, say, 6.0.

The lateral soil springs thus determined can then be used as input to readily available beam-column computer programs.

CONCLUSIONS

A numerical study was made for linearly elastic soil-pile conditions to clarify the lateral soil-reaction behavior of a pile.

The study indicated that the apparent lateral stiffness of soil, represented by the soil-reaction coefficient $\bar{\delta}$, is strongly influenced not only by the soil stiffness but also the geometry and the stiffness of the pile. In addition, $\bar{\delta}$ varies significantly with depth.

The paper presented a new approach for obtaining average soil-reaction coefficients, which are constant with depth even for layered soil conditions, that can be used with the beam-on-Winkler foundation model of a soil-pile system. With this

average soil-reaction coefficient, the beam-on-Winkler foundation model will reproduce with excellent accuracy the pile responses computed from the corresponding continuum system. Therefore, the results of this study can be instantly used by practicing engineers.

Although this study is limited to linearly elastic soil-pile conditions, the results can be expanded to nonlinear soil conditions, as suggested by Kagawa and Kraft (10,13).

REFERENCES

1. K. Terzaghi. Evaluation of Coefficients of Subgrade Reaction. *Geotechnique*, Vol. 5, 1955.
2. B. B. Broms. Lateral Resistance of Piles in Cohesive Soils. *Journal, Soil Mechanics and Foundations Division*, ASCE, Vol. 90, No. SM2, 1964, pp. 27-63.
3. B. B. Broms. Lateral Resistance of Piles in Cohesionless Soils. *Journal, Soil Mechanics and Foundations Division*, ASCE, Vol. 90, No. SM3, 1964, pp. 123-156.
4. B. McClelland and J. A. Focht, Jr. Soil Modulus for Laterally Loaded Piles. *Transactions*, ASCE, Vol. 123, 1958.
5. H. Matlock. Correlations for Design of Laterally Loaded Piles in Soft Clay. *Proc., 2nd Offshore Technology Conference*, Houston, Tex., 1970, pp. 577-594.
6. L. C. Reese, W. R. Cox, and F. D. Koop. Analysis of Laterally Loaded Piles in Sand. *Proc., 6th Offshore Technology Conference*, Houston, Tex., 1974, pp. 473-483.
7. D. A. Brown, C. Morrison, and L. C. Reese. Lateral Load Behavior of Pile Group in Sand. *Journal, Geotechnical Engineering Division*, ASCE, Vol. 114, No. 11, 1988, pp. 1261-1276.
8. C.-F. Tsai, R. F. Scott, D. Steussy, and J. M. Ting. *Full-Scale Pile Vibration Tests*. Earth Technology Corp. and California Institute of Technology, Long Beach and Pasadena, Calif., 1981.
9. *API Recommended Practice for Planning, Designing and Constructing Fixed Offshore Platform* (16th ed.). American Petroleum Institute, Washington, D.C., 1986.
10. T. Kagawa and L. M. Kraft, Jr. Lateral Load-Deflection Relationships of Piles Subjected to Dynamic Loadings. *Soils and Foundations*, Vol. 20, No. 4, 1980, pp. 19-36.
11. T. Kagawa. Dynamic Soil Reaction to Axially Loaded Piles. *Journal, Geotechnical Engineering Division*, ASCE, Vol. 117, No. 7, 1991, pp. 1001-1020.
12. R. D. Mindlin. Force at a Point in the Interior of a Semi-Infinite Solid. *Physics*, Vol. 7, 1936.
13. T. Kagawa and L. M. Kraft, Jr. Lateral Pile Response During Earthquakes. *Journal, Geotechnical Engineering Division*, ASCE, Vol. 107, No. GT12, 1981, pp. 1713-1731.

Publication of this paper sponsored by Committee on Foundations of Bridges and Other Structures.

Bearing Capacity Determination Method for Strip Surface Footings Underlain by Voids

C. W. HSIEH AND M. C. WANG

A method of bearing capacity determination for strip surface footings subjected to vertical central loading and underlain by a continuous circular void with its axis parallel with the footing axis is presented. A nomograph is also presented for ease in application of the developed equations. For equation development, the performance of strip surface footings with and without an underground void was investigated using a plane-strain finite element computer program. In the analysis, the foundation soil was characterized as a nonlinear elastic, perfectly plastic material that obeys the Drucker-Prager yield criterion. A wide range of soil properties, footing widths, void sizes, and void locations including depth to void and void eccentricity was considered. The ultimate bearing capacity values were obtained from the results of analysis and were related graphically with the influencing factors investigated. The bearing capacity equations were then developed through curve fitting to these graphical relationships. The effectiveness of the developed equations was evaluated by comparing the computed bearing capacity values with the model footing test results. Good agreement between the two sets of data was shown. It was therefore concluded that the developed equations together with the nomograph may become an effective tool for analysis and design of strip surface footing underlain by a continuous circular void, at least within the conditions investigated.

Despite its origin, either naturally formed or man-made, an underground void may occur under a foundation. The frequency of its presence under the foundation and the seriousness of its effect on foundation stability have been pointed out in previous papers (1,2). To approach such a problem, options such as filling the void, excavating the overlying soil and placing the foundation below the void, using piles or piers, reinforcing the overlying soil layer, relocating the foundation site, and possibly others are considered. These options are often difficult and very costly to implement. To ensure its long-term stability, the foundation must be originally designed with a thorough understanding of the void effect. In response to this need, many research studies have been conducted (1-9).

There is no methodology currently available for analysis and design of such a foundation system. The core of the methodology requires equations for determination of the ultimate bearing capacity of the foundation. The development of such bearing capacity equations for analysis of strip surface footing underlain by a continuous circular void is presented.

FOOTING PERFORMANCE ANALYSIS

The analysis of strip surface footing performance under vertical central loading was performed using the finite element method. A two-dimensional plane-strain finite element computer program was developed. In the computer program, the footing is characterized as a linear elastic material and the foundation soil as a nonlinear elastic, perfectly plastic material that obeys Hooke's law and the Drucker-Prager yield criterion (10). A hypothetical layer to model possible slips at the interface is placed between the vertical sides of the footing and the soil. The nonlinear solution is accomplished through the use of Reyes's incremental stress-strain relation (11) together with the tangential stiffness method.

The computer program differs from those previously developed by Baus (12), Badie (13), and Azam (14) in that it contains a preprocessor, the main program, and a postprocessor. The preprocessor is for input data preparation, and the postprocessor is for providing the results of finite element analysis in the desired graphical form. The preprocessor adopts a step-by-step procedure using the question-and-answer interactive format to guide the user to provide the necessary input. It contains various subroutines for generating the finite element mesh and for specifying boundary conditions, material properties, external loading, and type of analysis. The program also incorporates the numerical scheme of Siriwardane and Desai (15) for keeping the state of stress during yielding on the yield surface, and the numerical computation uses the Gauss-Jordan elimination method to solve the symmetrical BANDED global stiffness matrix. A detailed description of program development is given by Hsieh (16).

The computer program was validated by using the model footing test data obtained by Baus (12), Badie (13), and Azam (14) and the data published by Siriwardane and Desai (15) and Whitman and Hoeg (17). The finite element analysis was performed using an IBM 4090. The generation of element mesh and other input data preparation was done through a VAX 8550 or a PC, and a VAX 8550 was used to obtain the results of analysis. For plotting software, PLOT 10 was used.

FOUNDATION SYSTEM INVESTIGATED

The strip surface footing analyzed was a reinforced concrete footing with a width varying between 2 in. and 6 ft. Three different soils support the footing—commercial kaolin, silty clay, and clayey sand. The underground void was circular in

C. W. Hsieh, Gannett Fleming, Inc., P.O. Box 1963, Harrisburg, Pa. 17105-1963. M. C. Wang, Department of Civil Engineering, The Pennsylvania State University, University Park, Pa. 16802.

cross section and continuous with its axis parallel to the footing axis. Figure 1 shows a schematic view of the footing/soil/void system together with the symbols used for defining footing size and the size and location of the void. As shown, B , D , E , and W represent footing width, depth to void, void eccentricity, and void diameter, respectively.

In the analysis, the size (W) and location (D and E) of the void were expressed as ratios to footing width (B). Three levels each of void size ($W/B = 0.67, 1$, and 2), void eccentricity ($E/B = 0, 1$, and 2), and numerous levels of depth to void ($D/B = 1$ to 14) were analyzed. The material properties used in the analysis are summarized in Table 1. The concrete footing properties in Table 1 are obtained from Bowles (18), and the properties of silty clay, kaolin, and clayey sand are from Baus (12), Badie (13), and Azam (14), respectively.

ULTIMATE BEARING CAPACITY

Results of the finite element analysis were used to evaluate the mechanistic behavior of the foundation system. Among the behaviors investigated are principal stress distribution, displacement fields, propagation of plastic yielding, deformed configurations of the void, and the footing pressure versus settlement relation. From these data, the ultimate bearing capacity of each condition analyzed was obtained.

The ultimate bearing capacity data were analyzed further with respect to various factors considered including soil type, footing width, void size, and void location. It was found that the effect of soil type and footing width on bearing capacity for footing underlain by a void can be properly considered by nondimensionalizing both the independent and dependent variables: the ratios of q_o/q_{nv} , D/B , W/B , and E/B , in which q_o and q_{nv} are the ultimate bearing capacities of with and without void conditions, respectively (16). Furthermore, the ultimate bearing capacity values can be related with void locations for different void sizes in the form shown in Figures 2 through 6 regardless of soil type. Note that the data in

TABLE 1 PROPERTIES OF FOUNDATION SOILS AND CONCRETE FOOTING USED IN FINITE ELEMENT ANALYSIS

Material Parameters	Kaolin	Silty Clay	Clayey Sand	Concrete Footing
Internal Friction Angle, deg	8.0	13.5	31.0	N/A
Unit Cohesion (psi)	23.0	9.5	1.3	N/A
Initial Modulus in Compression (psi)	2880	677	6100	3.3×10^6
Initial Modulus in Tension (psi)	7000	1505	11300	3.3×10^6
Poisson's Ratio	0.39	0.28	0.32	0.20
Dry Unit Weight, pci	0.058	0.052	0.061	0.087

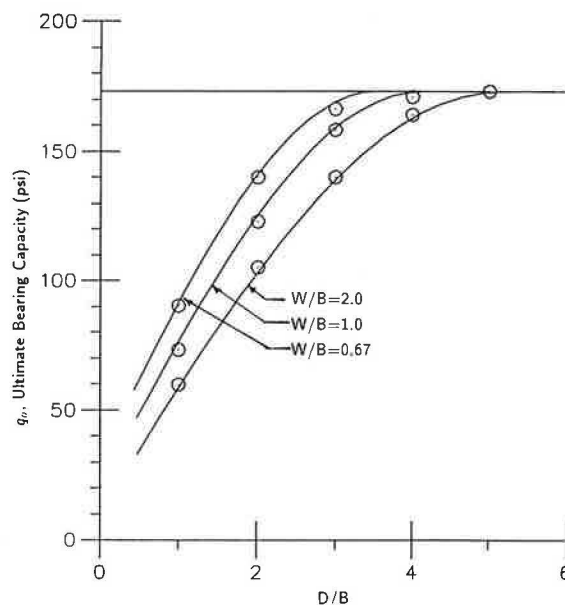


FIGURE 2 Variation of ultimate bearing capacity with D/B for kaolin with $E/B = 0$ and $W/B = 0.67, 1.0$, and 2.0 .

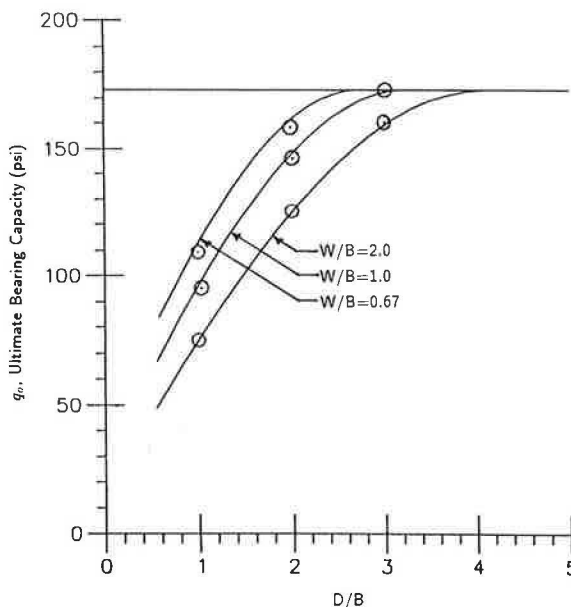


FIGURE 3 Variation of ultimate bearing capacity with D/B for kaolin with $E/B = 1.0$ and $W/B = 0.67, 1.0$, and 2.0 .

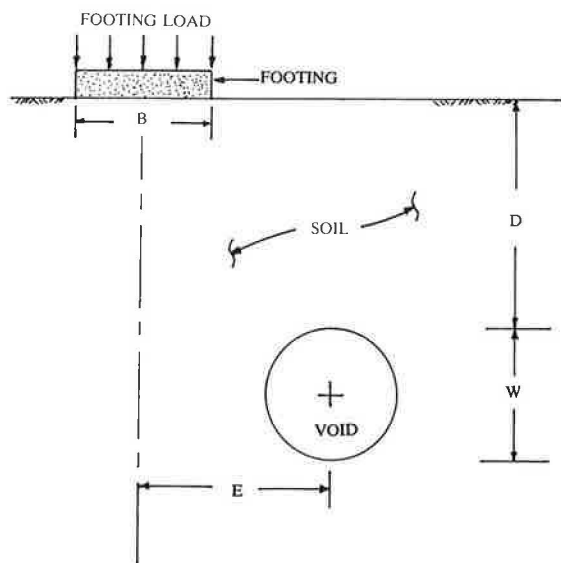


FIGURE 1 Schematic view of footing/soil/void system.

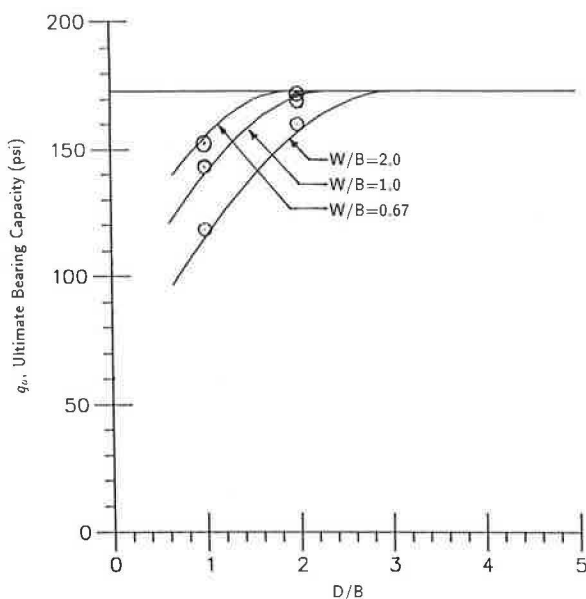


FIGURE 4 Variation of ultimate bearing capacity with D/B for kaolin with $E/B = 2.0$ and $W/B = 0.67, 1.0$, and 2.0 .

Figures 2, 3, and 4 are for kaolin with $E/B = 0, 1$, and 2 , respectively; Figures 5 and 6 are respectively for silty clay and clayey sand with $E/B = 0$. Other figures are available elsewhere (16). Thus, there is a total of nine figures. These graphs form the data base for the development of the ultimate bearing capacity equation.

According to Figures 2 through 6 and the other figures, the ultimate bearing capacity of strip footing varies with void size and location so that the bearing capacity increases as the depth to void increases, void size decreases, and void eccentricity increases, while other factors are constant. The data indicate that there is a depth to void beyond which the presence of a void has no effect on the ultimate bearing capacity. This depth to void, termed as the critical depth (D_c) in previous papers

(1,2), varies with soil type, void size, and void eccentricity. The critical depth to void is an important factor required in the ultimate bearing capacity equation.

EQUATION FORMULATION

The ultimate bearing capacity equation was developed by fitting the graphical relations in Figures 2 through 6 and the other figures. In the fitting process, the main features of the curves were first identified. Functions having such features were then selected to fit the curves. Through trial and error, the function best fitting the curve was adopted. Further, the coefficient, amplitude, and argument of the function were determined for each curve. The various sets of coefficients for all curves were analyzed to determine the variation between each coefficient and the influencing factors.

For the curves in Figures 2 through 6, different functions were tried, such as polynomial, hyperbolic secant, arc tangent, and sine. Of the various functions attempted, the one-quarter-cycle sine function best fit the curves. The function contains two coefficients—one for the intercept on the vertical axis and the other for the amplitude. By using this function, the SAS nonlinear regression analysis was performed to determine the coefficients that best fit each curve. It was found

that the argument in the sine function equals $\frac{\pi D}{2D_c}$, and the coefficients vary with the void size, void location, and shear strength property of soil.

The equation relating the coefficients with void size, void location, and soil strength was developed first by plotting the coefficients against W/B for each E/B and soil type. All the relation curves were then fitted by a factored hyperbolic secant function that has a maximum value equal to q_{nv} , the ultimate bearing capacity value of no-void condition, and is asymptotic to a constant value as W/B approaches infinity. Furthermore, to generalize the equation that fits the curves in Figures 2 through 6, the ultimate bearing capacity is expressed as q_o/q_{nv} . In the analysis, the value of q_{nv} is computed

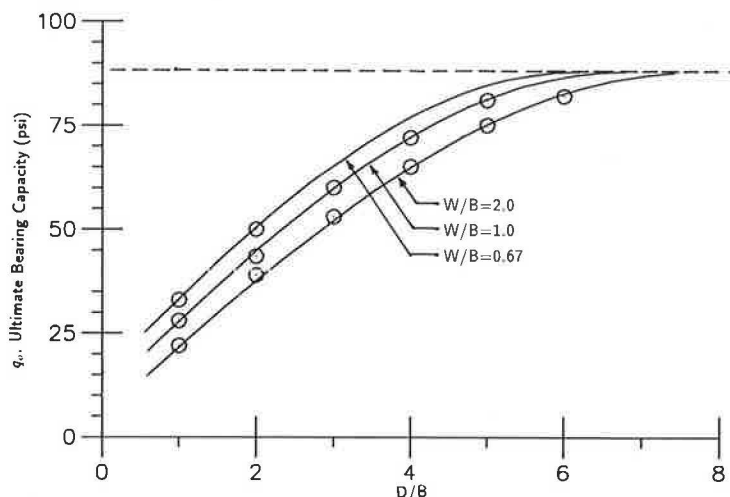


FIGURE 5 Variation of ultimate bearing capacity with D/B for silty clay with $E/B = 0$ and $W/B = 0.67, 1.0$, and 2.0 .

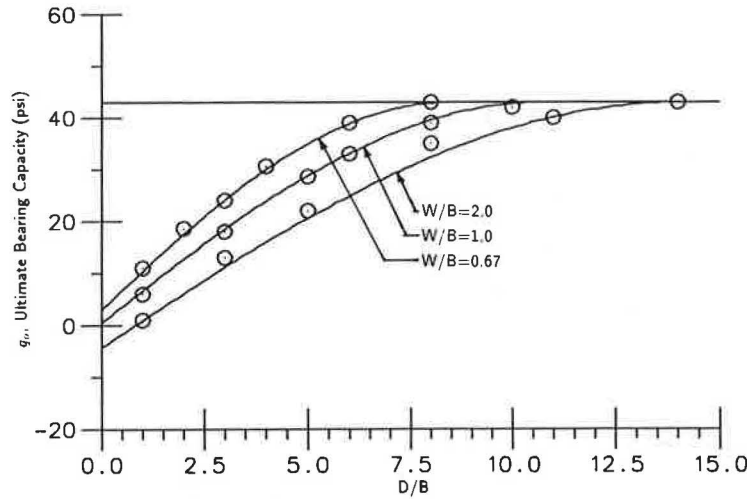


FIGURE 6 Variation of ultimate bearing capacity with D/B for clayey sand with $E/B = 0$ and $W/B = 0.67, 1.0$, and 2.0 .

by using the conventional bearing capacity equation together with Meyerhof's coefficients.

Because the argument of the one-quarter-cycle sine function contains the critical depth to void (D_c), an equation for predicting D_c is required. From Figures 2 through 6 and the others, the critical depth to void for each condition is obtained from the point where the curve reaches the no-void bearing capacity value. The values of D_c thus obtained are plotted against W/B for each level of E/B . The plots reveal that the D_c/B versus $\log(W/B)$ relation can be approximated by a linear function. The coefficients contained in the linear function of D_c/B versus $\log(W/B)$ are then further related with void location and soil strength property.

Details on equation formulation are documented elsewhere (16). The final ultimate bearing capacity equation is as follows, where ζ is the bearing capacity ratio:

$$q_o = \zeta q_{nv} \quad (1)$$

In Equation 1,

$$\zeta = \sin \delta + K(1 - \sin \delta) \quad (2)$$

and

$$\delta = \frac{\pi}{2} \frac{D}{D_c} \quad (3)$$

$$D_c = B[D_1 + D_2 \log(W/B)] \quad (4)$$

$$D_1 = 16.3 \sin 2\phi \cos^2 \phi - 2.93(E/B) \sin 2\phi \quad (5)$$

$$D_2 = 22.5 \sin \phi - 3.5(E/B) \tan \phi \quad (6)$$

$$K = K_p + \text{sech}\{[2.9 - \tan^2 \phi - 0.4(E/B)^2 \cos 2\phi] + [2.5 - 1.5 \tan^2 \phi - 0.58(E/B) \cos^2 \phi] \log(W/B)\} \quad (7)$$

$$K_p = \begin{cases} -0.42 \tan^2 \phi & \text{if } 2cB \geq \gamma B^2 \\ 0 & \text{if } 2cB < \gamma B^2 \end{cases}$$

In the preceding equations, ϕ = internal friction angle of soil, c = cohesion of soil, and γ = unit weight of soil.

NOMOGRAPH AND EXAMPLE

For ease in application of the developed equations one nomograph for determination of K is presented in Figure 7. There are three sets of curves—Figures 7a, b, and c for internal friction angle (ϕ) equal to 10, 20, and 30 degrees, respectively. A minimum of three levels for each variable is also presented in the nomograph for ease in data interpolation when necessary.

As an example of the use of the nomograph and equations, a 5-ft-wide strip surface footing is supported by cohesive soil. The foundation soil has a unit weight, cohesion, and internal friction angle of 130 pcf, 15 psi, and 20 degrees, respectively. A 5-ft diameter continuous circular void having its axis parallel with the footing axis is 3 ft from the footing axis and 10 ft below the footing base. The ultimate bearing capacity of the footing can be determined as follows.

For the conditions given, $B = 5$ ft, $E = 3$ ft, $W = 5$ ft, and $D = 10$ ft, $\gamma = 130$ pcf, $c = 15$ psi, and $\phi = 20$ degrees.

1. Determine D_c and compute δ . From Equations 4, 5, and 6, for $E/B = 0.6$, $W/B = 1$, and $\phi = 20$ degrees,

$$D_c \cong 44 \text{ ft}$$

$$\delta = \frac{\pi}{2} \frac{D}{D_c} \cong \frac{180^\circ}{2} \frac{10}{44} \cong 20.45^\circ$$

2. Determine coefficient K . From Figure 7(b), for $W/B = 1$, $E/B = 0.6$, $\phi = 20$ degrees, and $2cB = 2(15 \times 144)(5) = 21600$, which is greater than $\gamma B^2 = (130)(5)^2 = 3250$,

$$K \cong 0.08$$

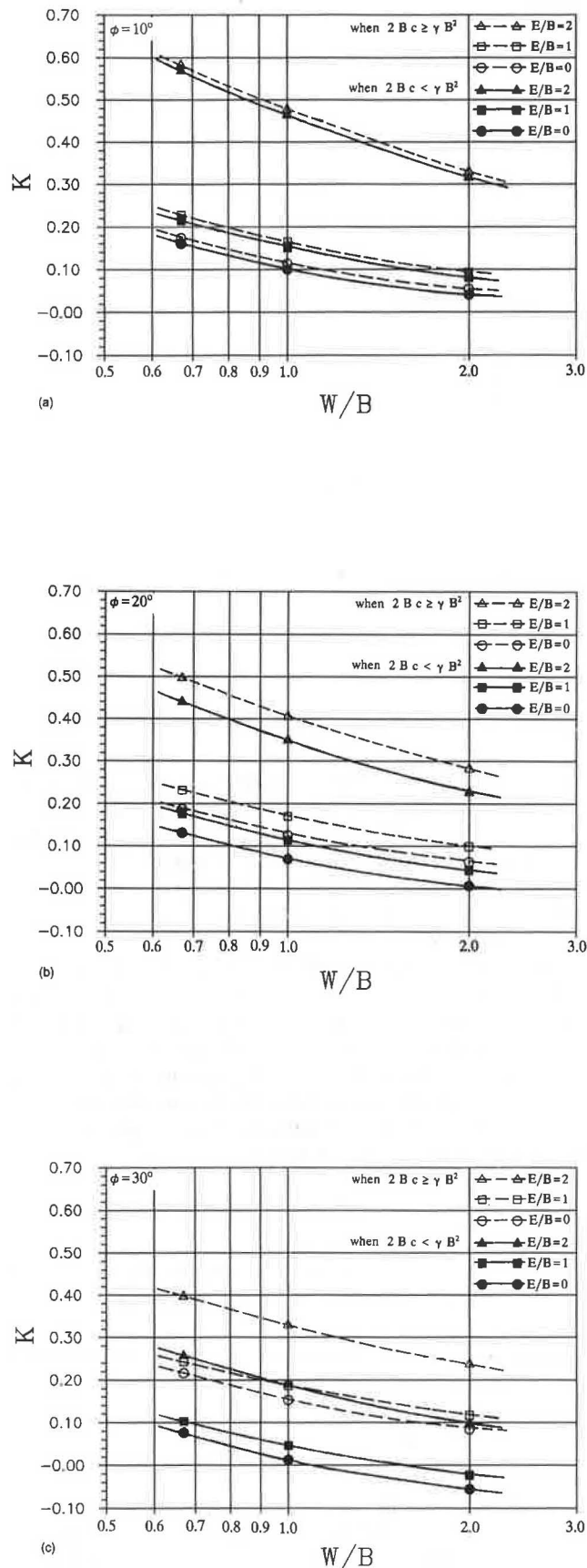


FIGURE 7 Variation of coefficient K with W/B for internal friction angle of (a) 10, (b) 20, and (c) 30 degrees.

3. Compute bearing capacity ratio ζ .

$$\begin{aligned}\zeta &= \sin \delta + K (1 - \sin \delta) \\ &= \sin 20.45^\circ + 0.08 (1 - \sin 20.45^\circ) \\ &\approx 0.40\end{aligned}$$

4. Compute the ultimate bearing capacity of no-void condition, q_{nv} . For $\phi = 20$ degrees, $N_c \approx 14.83$, $N_q \approx 6.40$, and $N_\gamma \approx 2.90$,

$$\begin{aligned}q_{nv} &= cN_c + qN_q + \frac{1}{2} \gamma B N_\gamma \\ &\approx (15)(14.83) + 0 + \frac{1}{2} \left(\frac{130}{1728} \right) (5 \times 12)(2.90) \\ &\approx 229.0 \text{ psi}\end{aligned}$$

5. Compute the required ultimate bearing capacity.

$$\begin{aligned}q_o &= \zeta q_{nv} \\ &= (0.40)(229.0) = 91.6 \text{ psi}\end{aligned}$$

COMPARISONS

To demonstrate the effectiveness of the developed equations, the ultimate bearing capacity of model test footings was computed and compared with the test results obtained by Badie (13) for kaolin and Azam (14) for clayey sand. The model test footing was a steel plate 2.0 in. wide by 5.25 in. long by 0.5 in. thick, tested under the plane-strain loading in a test tank approximately 32 in. high, 60 in. long, and 5.5 in. wide. A circular void was at various locations. The conditions, including void location and soil type used for comparison, test results, and computed bearing capacity values, are given in Table 2. A fairly good agreement between the two sets of data is seen, indicating that the developed equations can provide accurate bearing capacity data for strip surface footing underlain by a continuous void at least within the range of conditions investigated.

SUMMARY AND CONCLUSIONS

The need to develop a methodology for determining the ultimate bearing capacity of shallow foundation underlain by

TABLE 2 COMPARISON BETWEEN COMPUTED ULTIMATE BEARING CAPACITY AND MODEL FOOTING TEST RESULT

Test Soil	D/B	W/B	E/B	Ultimate Bearing Capacity (psi)	
				Computed	Test Result
Kaolin	2.0	2.41	0	95.6	117.4
	3.0	2.41	0	130.9	137.9
	4.5	2.41	0	165.2	164.3
	2.0	2.41	1.5	133.3	125.1
Clayey Sand	2.0	2.41	0	11.5	17.0

an underground void was identified. A method of bearing capacity determination for strip surface footing overlying a continuous circular void with its axis parallel to the footing axis was presented.

For bearing capacity equation development, the performance of strip surface footing subjected to a vertical central loading with and without an underground void was investigated using a plane-strain finite element computer program. In the analysis, the foundation soil was characterized as a nonlinear elastic, perfectly plastic material that obeys the Drucker-Prager yield criterion. To cover a wide range of soil property, three different soils were analyzed—kaolin, silty clay, and clayey sand. A range of footing width, varying void sizes, and void locations including the depth to void and void eccentricity were considered. The ultimate bearing capacity of each condition analyzed was obtained from the footing performance data. These ultimate bearing capacity values were then related graphically with the various influencing factors investigated including void size, void location, and shear strength properties of the soil. The bearing capacity equations were developed through curve fitting of the graphical relationships. For these equations, one nomograph was presented for ease in equation application.

The developed equations were used to determine the bearing capacity of some model test footings, and the results were compared with the test data. A good agreement between the prediction and test data was obtained. On the basis of this comparison, it may be concluded that the developed bearing capacity equation may become an effective tool for analysis and design of strip surface footing underlain by a circular void, at least within the range of conditions considered.

ACKNOWLEDGMENTS

The authors are grateful to the National Science Foundation for its financial support of the research reported in this paper. The authors thank Karen M. Detwiler for painstakingly typing the manuscript.

REFERENCES

1. R. L. Baus and M. C. Wang. The Bearing Capacity of Strip Footing Located Above a Void in Cohesive Soils. *Journal of Geotechnical Engineering Division*, ASCE, Vol. 109, No. 1, 1983, pp. 1–14.
2. A. Badie and M. C. Wang. Stability of Spread Footing Above Void in Clay. *Journal of Geotechnical Engineering Division*, ASCE, Vol. 110, No. 11, 1984, pp. 1591–1605.
3. M. C. Wang and R. L. Baus. Settlement of Footings Above a Void. *2nd Conference on Ground Movements and Structures*, The Department of Civil Engineering and Building Technology, UWIST, 1980.
4. M. C. Wang and A. Badie. Effect of Underground Void on Foundation Stability. *Journal of Geotechnical Engineering*, ASCE, Vol. 111, No. 8, 1985, pp. 1008–1019.
5. M. C. Wang, C. S. Yoo, and C. W. Hsieh. Effect of Void on Footing Behavior under Eccentric and Inclined Loads. *Foundation Engineering: Current Principles and Practices*, Vol. 2, *Proc. of the Congress*, ASCE, 1989, pp. 1226–1239.
6. L. A. Wood and W. J. Larnach. The Behavior of Footings Located Above Voids. *Proc., Eleventh International Conference on Soil Mechanics and Foundation Engineering*, Vol. 4, San Francisco, Calif., 1985, pp. 2273–2276.
7. G. A. H. Abdellah and M. H. Abdalla. The Interaction Between a Tunnel/Cavity and Nearby Structures. *Proc., VI Australian Tunneling Conference*, 1987, Vol. 1, pp. 183–189.
8. M. C. Wang and C. W. Hsieh. Collapse Load of Strip Footing Above Circular Void. *Journal of Geotechnical Engineering*, ASCE, Vol. 113, No. 5, 1987, pp. 511–515.
9. A. Badie and M. C. Wang. Stability of Underground Cavity Subjected to Surface Loads. *International Symposium on Unique Underground Structures*, Denver, Colo., 1990.
10. D. Drucker and W. Prager. Soil Mechanics and Plastic Analysis in Limit Design. *Quarterly of Applied Mathematics*, Vol. 10, No. 2, 1952, pp. 157–165.
11. S. F. Reyes. *Elastic-Plastic Analysis of Underground Openings by the Finite Element Method*. Ph.D. thesis. University of Illinois, Urbana, 1966.
12. R. L. Baus. *The Stability of Shallow Continuous Footings Located Above Voids*. Ph.D. thesis. The Pennsylvania State University, University Park, 1980.
13. A. Badie. *Stability of Spread Footing Supported by Clay Soil with Underground Void*. Ph.D. thesis. The Pennsylvania State University, University Park, 1983.
14. G. Azam. *Stability of Shallow Continuous Footings Supported by Two-Layer Soil Deposits with an Underground Void*. Ph.D. thesis. The Pennsylvania State University, University Park, 1990.
15. H. J. Siriwardane and C. S. Desai. Computational Procedures for Nonlinear Three-Dimensional Analysis with Some Advanced Constitutive Laws. *International Journal for Numerical and Analytical Methods in Geomechanics*, Vol. 7, No. 2, 1983, pp. 143–171.
16. C. W. Hsieh. *Development of Methodology for Stability Analysis of Surface Strip Footing Above Continuous Circular Void*. Ph.D. dissertation. Department of Civil Engineering, The Pennsylvania State University, University Park, 1991.
17. R. V. Whitman and K. Hoeg. Development of Plastic Zone Beneath a Footing. *Report to U.S. Army Engineering Waterways Experiment Station*, Department of Civil Engineering, The Massachusetts Institute of Technology, Cambridge, 1966.
18. J. E. Bowles. *Foundation Analysis and Design* (4th ed.). McGraw-Hill Book Co., New York, 1988.

Publication of this paper sponsored by Committee on Foundations of Bridges and Other Structures.

Vertical Uplift Load-Displacement Relationship of Horizontal Anchors in Sand

BRAJA M. DAS AND VIJAY K. PURI

Small-scale laboratory model test results for the uplift capacity of horizontal rectangular anchors embedded at shallow depths in medium and dense sand are presented. The ultimate uplift capacities obtained from the laboratory model tests are compared with the theory proposed by Meyerhof and Adams. On the basis of model test results, an approximate nondimensional uplift load-displacement relationship is developed. This relationship is useful in the determination of the allowable anchor holding capacity at a given level of vertical displacement of the anchor.

In many instances, horizontal plate anchors are used in the construction of foundations to resist uplifting loads. In most cases they are either square or circular in shape. Generally, the design limitation for plate anchors must address concerns for (a) the allowable uplift capacity, which is estimated by applying a suitable factor of safety to the theoretical ultimate uplift capacity, and (b) the allowable uplift displacement when subjected to allowable load. Several theoretical and experimental studies are available (1-4) for prediction of the ultimate uplift capacity of horizontal plate anchors. Practically all theories, with the exception of that given by Meyerhof and Adams (3), are valid only for circular anchors. Meyerhof and Adams's theory provides relationships for the ultimate uplift capacity of circular and rectangular plate anchors. A review of the existing literature indicates that no serious effort has thus far been made to develop the relationships between uplift load and corresponding displacement of horizontal plate anchors.

Reported herein are some small-scale laboratory model test results on shallow horizontal rectangular plate anchors embedded in sand. The ultimate uplift capacity of those rectangular anchors determined experimentally has been compared with the existing theory of Meyerhof and Adams (3). In addition, a nondimensional relationship for the load and displacement of rectangular plate anchors has been developed.

GEOMETRIC PARAMETERS FOR AN ANCHOR

Figure 1 shows a horizontal plate anchor with length L and width B . The depth of embedment of this plate anchor is D . When the embedment ratio D/B is relatively small and the anchor is subjected to ultimate uplift load (Q_u), the failure

surface in soil located above the anchor extends to the ground surface, and these anchors are referred to as shallow anchors. However, at larger values of D/B , local shear failure in soil located around the anchor takes place; thus, these anchors are referred to as deep anchors. On the basis of several laboratory and field test results, Meyerhof and Adams (3) determined the critical values of the embedment ratio below which shallow anchor conditions for circular and square anchor plates exist. Those values of the critical embedment ratio that are functions of the soil friction angle ϕ are given in the following table.

Soil Friction Angle, ϕ (deg)	Critical Embedment Ratio, $D/B = D/B_{cr}$, for Circular and Square Plate Anchor
30	4
35	5
40	7
45	9

The critical embedment ratio for rectangular anchors can be 40 to 50 percent higher than the square or circular anchors (5).

ULTIMATE UPLIFT CAPACITY

As mentioned earlier, the theory of Meyerhof and Adams (3) is the only analytical expression presently available to estimate

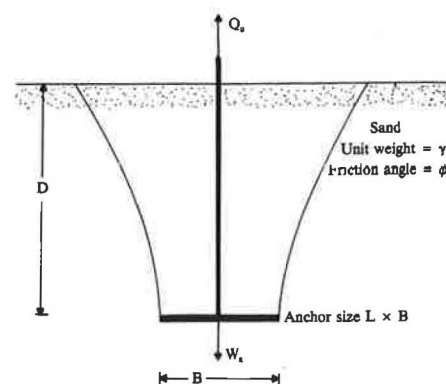


FIGURE 1 Geometrical parameters of shallow horizontal anchor.

the ultimate uplift capacity of rectangular anchors. According to this theory, for shallow rectangular anchors

$$Q_u = \gamma D^2(2SB + L - B)K_u \tan \phi + W + W_a \quad (1)$$

where

- Q_u = gross ultimate uplift capacity,
- γ = unit weight of soil,
- D = depth of embedment,
- B = anchor width,
- L = anchor length,
- K_u = uplift coefficient,
- ϕ = soil friction angle,
- S = shape factor,
- W = effective weight of the soil located immediately above the anchor, and
- W_a = effective weight of the anchor and the rod.

The theoretical variations of the uplift coefficient K_u for various soil friction angles fall within a narrow range and may be taken as 0.95. For shallow anchors, the shape factor increases linearly with the embedment ratio D/B , or

$$S = 1 + m\left(\frac{D}{B}\right) \quad (2)$$

where m is the shape factor coefficient. The variation of the shape factor coefficient m with the soil friction angle ϕ as suggested by Meyerhof and Adams (3) is as follows:

Soil Friction Angle, ϕ (deg)	Shape Factor Coefficient, m
30	0.15
35	0.25
40	0.35
45	0.5

The net ultimate uplift capacity of an anchor can be expressed in a nondimensional form as (6)

$$N_q = \frac{Q_o}{\gamma BLD} \quad (3)$$

where N_q is the breakout factor and

$$Q_o = \text{net ultimate uplift capacity} = Q_u - W_a \quad (4)$$

Combining Equations 1 through 4, for shallow rectangular anchors,

$$N_q = \left(\frac{D}{B}\right)K_u \tan \phi \left\{ \left[1 + 2m\left(\frac{D}{B}\right) \right] \frac{B}{L} + 1 \right\} + 1 \quad (5)$$

The preceding expression is valid for shallow anchors, that is, up to a limit of $D/B = (D/B)_{cr}$.

LABORATORY MODEL TESTS

Laboratory model pullout tests were conducted in a box measuring 0.6 m \times 0.6 m \times 0.6 m. A poorly graded silica sand was used for the tests. The sand had 84 percent passing No.

30 U.S. sieve, 53 percent passing No. 40 U.S. sieve, 7 percent passing No. 60 U.S. sieve, and 3 percent passing No. 200 U.S. sieve.

Three model aluminum plates measuring 50.8 mm \times 50.8 mm, 50.8 mm \times 101.6 mm, and 50.8 mm \times 152.4 mm were used for the tests giving length-to-width ratios (L/B) of 1, 2, and 3. All of the aluminum plates were 3.18 mm thick.

In conducting the model tests, sand was compacted in 25.4-mm-thick layers in the box to a desired height. Uplift force to the plates was applied through a 6.35-mm-diameter steel rod rigidly attached at the center of each plate. The rod was connected to a lever arm attached to the side of the test box. Step loads were applied at the other end of the lever arm. The lever-arm ratio was 1:10. The upward movement Δ of the anchor was measured by a dial gauge.

Two series of tests were conducted by changing the unit weight of compaction of the sand. The average unit weight of compaction for each series and the corresponding angle of friction determined from the standard triaxial tests are given in Table 1. For a given series, the ultimate pullout load for each plate was obtained from embedment ratios varying from 1 to 5. This range of embedment ratio applies to shallow anchor condition.

LABORATORY MODEL TEST RESULTS

Typical variations of the net load Q versus the vertical displacement Δ/B (Δ = vertical displacement) obtained from the present laboratory model tests are shown in Figure 2. Each test was conducted twice, and the Q versus Δ/B plots shown in Figure 2 are the average plots. The net ultimate uplift load Q_o is defined as the load at which sudden pullout occurred, or where the Q versus Δ/B plot showed a practically linear relationship. The net ultimate capacities thus determined for tests in medium (Series 1) and dense (Series 2) sands are shown in Figure 3.

VARIATION OF BREAKOUT FACTOR, N_q

Using the experimental ultimate uplift capacities shown in Figure 3 and Equation 3, the experimental variations of the breakout factors with embedment ratio for all tests have been calculated and are shown in Figures 4 and 5. For comparison purposes, the theoretical variations of N_q calculated using Equation 5, which is based on the theory of Meyerhof and Adams (3), are also shown in these figures. A comparison between the theoretical and experimental curves indicates that the experimental values are slightly higher than those predicted by theory.

TABLE 1 AVERAGE UNIT WEIGHT OF COMPACTION AND CORRESPONDING TRIAXIAL FRICTION ANGLE

Series	Nature of Compaction	Relative Density, D_r (%)	Average Unit Weight of Compaction, γ (kN/m ³)	Friction Angle, ϕ (deg)
1	Medium	47.6	15.79	34
2	Dense	72.9	16.88	40.5

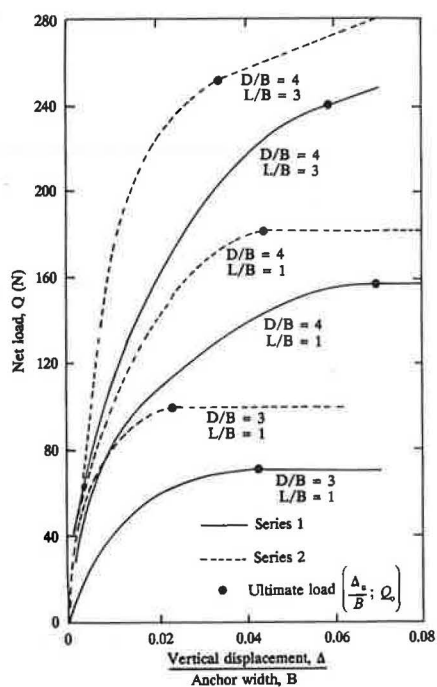


FIGURE 2 Typical variation of Q versus Δ/B .

VARIATION OF Δ_u WITH D/B

Figure 6 shows the variation of the nondimensional ultimate displacement Δ_u/B (Δ_u = anchor displacement at ultimate load) with the embedment ratio of anchors. From this figure, the following general conclusions can be drawn.

1. For similar embedment ratios and anchor plates, the magnitude of the displacement at ultimate load is about 1.5 to 2 times higher in medium sand than in dense sand.

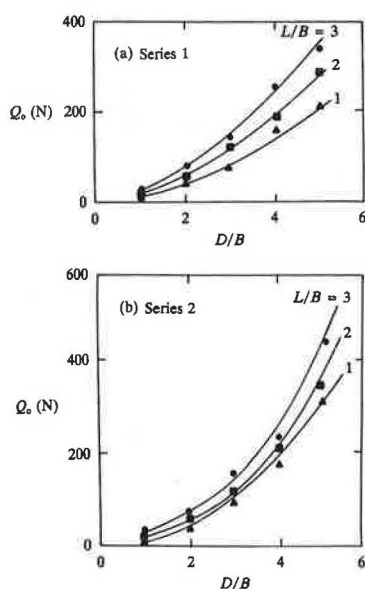


FIGURE 3 Variation of Q_u versus D/B : a, Series 1; b, Series 2.

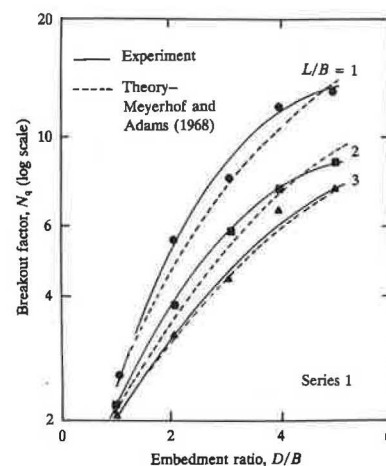


FIGURE 4 Variation of N_q versus D/B , Series 1.

2. For a given anchor plate and type of sand compaction, the magnitude of Δ_u increases with the embedment ratio within the limits of the test (that is, $D/B \leq 5$).

3. For a given embedment ratio and type of sand compaction, the magnitude of Δ_u decreases with increase in the length-to-width ratio (L/B).

NET LOAD VERSUS DISPLACEMENT RELATIONSHIP

On the basis of the experimental net load Q and corresponding displacement Δ relationships obtained from the present tests, it appears that they can be approximated in a nondimensional rectangular hyperbolic form as

$$\bar{Q} = \frac{\bar{\Delta}}{C_1 + C_2 \bar{\Delta}} \quad (6)$$

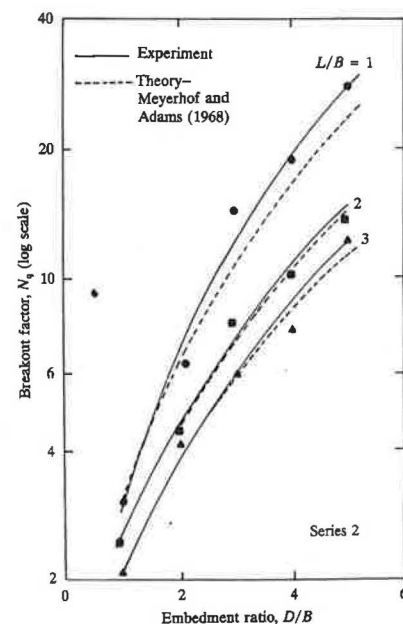
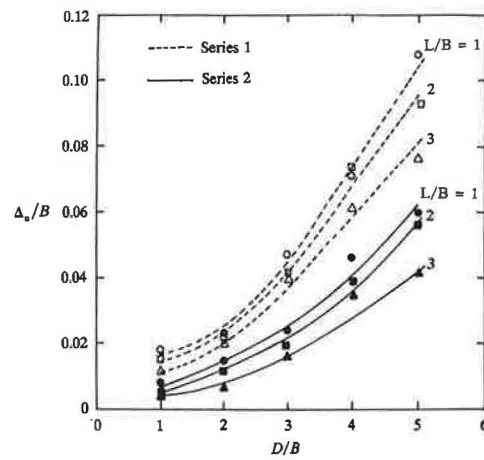
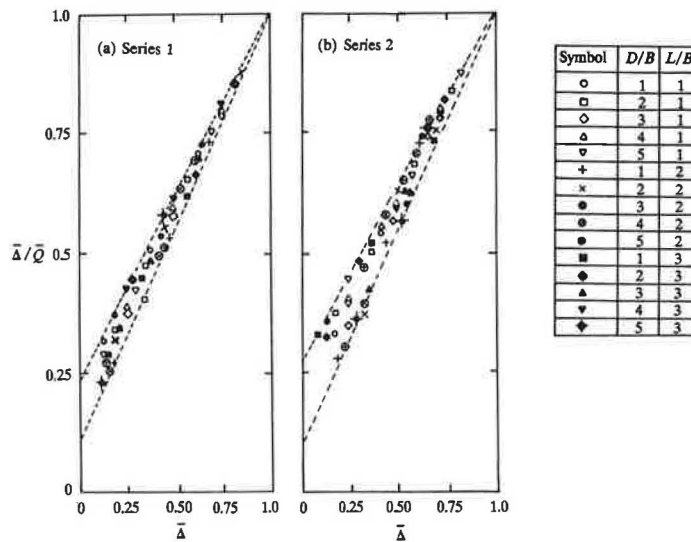


FIGURE 5 Variation of N_q versus D/B , Series 2.

FIGURE 6 Plot of Δ_u/B versus D/B .FIGURE 7 Plot of $\bar{\Delta}/\bar{Q}$ versus $\bar{\Delta}$: a, Series 1; b, Series 2.

where

$$\bar{Q} = \frac{Q}{Q_0},$$

$$\bar{\Delta} = \frac{\Delta}{\Delta_u},$$

Q = net load at an anchor displacement of Δ ,

Q_0 = net load at an anchor displacement of Δ_u , and

C_1, C_2 = constants.

Equation 6 can be arranged in the form

$$\frac{\bar{\Delta}}{\bar{Q}} = C_1 + C_2 \bar{\Delta} \quad (7)$$

The preceding relationship implies that the plot of $\bar{\Delta}/\bar{Q}$ versus $\bar{\Delta}$ will be a straight line. On the basis of the average plots of

Q (net load) versus Δ (uplift displacement) obtained from the laboratory tests (similar to those shown in Figure 2), the variation of $\bar{\Delta}/\bar{Q}$ versus $\bar{\Delta}$ has been plotted in Figure 7. From the plots it can be seen that all points fall in a rather narrow band. The average values of C_1 and C_2 can be given as 0.175 and 0.825, respectively. If these values are substituted into Equation 6, the net load at given displacement Δ can be expressed as

$$Q = Q_0 \left[\frac{\frac{\Delta}{\Delta_u}}{0.175 + 0.825 \left(\frac{\Delta}{\Delta_u} \right)} \right] \quad (8)$$

CONCLUSIONS

The results of a number of laboratory model uplift tests on shallow rectangular anchor plates embedded in sand have

been presented. On the basis of the model test results, the following conclusions can be drawn.

1. The experimental ultimate uplift capacity of rectangular anchor plates is generally in good agreement with those predicted by the theory of Meyerhof and Adams (3).
2. The approximate range of the anchor displacement Δ_u at ultimate load can be estimated from Figure 6.
3. On the basis of present model tests, an approximate nondimensional load-displacement relationship has been developed (Equation 8).

REFERENCES

1. A. Balla. The Resistance to Breaking-Out of Mushroom Foundations for Pylons. *Proc., 5th International Conference on Soil Mechanics and Foundation Engineering*, Vol. 1, 1961, pp. 569–576.
2. L. G. Mariupolskii. The Bearing Capacity of Anchor Foundations. *Soil Mechanics and Foundation Engineering*, Vol. 3, No. 1, 1965, pp. 14–18.
3. G. G. Meyerhof and J. I. Adams. The Ultimate Uplift Capacity of Foundations. *Canadian Geotechnical Journal*, Vol. 5, No. 4, 1968, pp. 225–244.
4. C. J. Veesaert and S. P. Clemence. Dynamic Pullout Resistance of Anchors in Sand. *Proc., International Symposium on Soil-Structure Interaction*, Rourkee, India, 1977, pp. 389–397.
5. G. G. Meyerhof. Uplift Resistance of Inclined Anchors and Piles. *Proc., 8th International Conference on Soil Mechanics and Foundation Engineering*, Moscow, Vol. 2.1, 1973, pp. 167–172.
6. A. S. Vesic. Breakout Resistance of Object Embedded in Ocean Bottom. *Journal of the Soil Mechanics and Foundations Division*, ASCE, Vol. 97, No. SM9, 1971, pp. 1183–1205.

Publication of this paper sponsored by Committee on Foundations of Bridges and Other Structures.